

# In silico optimisation of cancer treatment schedules

Dissertation

zur Erlangung des Doktorgrades  
der Naturwissenschaften

vorgelegt beim Fachbereich Physik  
der Johann Wolfgang Goethe-Universität  
in Frankfurt am Main

von  
Harald Christoph Kempf  
aus Hanau

Frankfurt 2012  
(D 30)

Vom Fachbereich Physik der Goethe-Universität als Dissertation angenommen.

Dekan: Prof. Dr. Michael Huth

Gutachter: Prof. Dr. Marcus Bleicher  
Prof. Dr. Michael Meyer-Hermann

Datum der Disputation: 25. April 2013

## **Erklärung**

Ich versichere hiermit, dass ich die vorliegende Arbeit selbständig verfasst, keine anderen als die angegebenen Hilfsmittel verwendet und sämtliche Stellen, die benutzten Werken im Wortlaut oder dem Sinne nach entnommen sind, mit Quellen- bzw. Herkunftsangaben kenntlich gemacht habe.

Frankfurt am Main, den 29. August 2012

# Abstract

The central goal of this investigation is to describe the dynamic reaction of a multicellular tumour spheroid to treatment with radiotherapy. A focus will be on the triggered dynamic cell cycle reaction in the spheroid and how it can be employed within fractionated radiation schedules.

An agent-based model for cancer cells is employed which features inherent cell cycle progression and reactions to environmental conditions. Cells are represented spatially by a weighted, dynamic and kinetic Voronoi/Delaunay model which also provides for the identification of cells in contact within the multicellular aggregate. Force-based interaction between cells will lead to rearrangement in response to proliferation and can induce cell quiescence via a mechanism of pressure-induced contact inhibition. The evolution of glucose and oxygen concentration inside the tumour spheroid is tracked in a diffusion solver in correspondence to *in vitro* or *in vivo* boundary conditions and a corresponding local nutrient uptake by single cells. Radiation effects are implemented based on the measured single cell survival in the linear-quadratic model. The survival probability will be affected by the radiosensitivity of the current cycle phase and the local oxygen concentration. Quiescent cells will reduce the effective dose they receive as a consequence of their increased radioresistance. The radiation model includes a fast response to fatal DNA damage through cell apoptosis and a slow response via cell loss due to misrepair during the radiation-induced G2-block. A simplified model for drug delivery in chemotherapy is implemented.

The model can describe the growth dynamics of spheroids in accordance to experimental data, including total number of cells, histological structure and cell cycle distribution. Investigations of possible mechanisms for growth saturation reveal a critical dependence of tumour growth on the shedding rate of cells from the surface.

In response to a dose of irradiation, a synchronisation of the cell cycle progression within the tumour is observed. This will lead to cyclic changes in the overall radiation sensitivity of the tumour which are quantified using an enhancement measure in comparison to the expected radiosensitivity of the tumour. A transient strong peak in radiosensitivity enhancement is observed after administration of irradiation. Mechanisms which influence the peak timing and development are systematically investigated, revealing quiescence and reactivation of cells to be a central mechanism for the enhancement. Direct redistribution of cells due to different survival in cell cycle phases, re-activation of quiescent cells in response to radiation-induced cell death and blocking of DNA damaged cells at the G2/M checkpoint are identified as the main mechanisms which contribute to a synchronisation and determine the radiosensitivity increase. A typical time scale for the development of radiosensitivity and the relaxation of tumours to a steady-state after irradiation is identified, which is related to the typical total cell cycle time.

A range of clinical radiotherapy schedules is tested for their performance within the simulation and a systematic comparison with alternative delivery schedules is performed, in order to identify schedules which can most effectively employ the described transient enhancement

effects. In response to high-dose schedules, a dissolution of the tumour spheroid into smaller aggregates can be observed which is a result of the loss of integrity in the spheroid that is associated with high cell death via apoptosis.

Fractionated irradiation of spheroids with constant dose per time unit but different inter-fraction times clearly reveals optimal time-intervals for radiation, which are directly related to the enhancement response of the tumour. In order to test the use of triggered enhancement effects in tumours, combinations of trigger- and effector doses are examined for their performance in specific treatment regimens. Furthermore, the automatic identification and triggering in response to high enhancement periods in the tumour is analysed. While triggered schedules and automatic schedules both yield a higher treatment efficiency in comparison to conventional schedules, treatment optimisation is revealed to be a global problem, which cannot be sufficiently solved using local optimisation only.

The spatio-temporal dynamics of hypoxia in the tumour are studied in response to irradiation. Microscopic, diffusion-induced reoxygenation dynamics are demonstrated to be on a typical time-scale which is in the order of fractionation intervals.

Neoadjuvant chemotherapy with hydroxyurea can yield a drastic improvement of radiosensitivity via cell cycle synchronisation and specific toxicity against radioresistant S-phase cells.

The model makes clear predictions of radiation schedules which are especially effective as a result of triggered cell cycle-based radiosensitivity enhancement. Division of radiation into trigger and effector doses is highly effective and especially suited to be combined with adjuvant chemotherapy in order to limit regrowth of cells.

# Zusammenfassung

Die vorliegende Arbeit befasst sich in ihrer zentralen Fragestellung mit der Reaktion von multizellulären Tumorsphäroiden auf verschiedene therapeutische Maßnahmen aus dem Bereich der Krebstherapie, insbesondere der Strahlentherapie. Tumorsphäroide stellen als komplexes, dreidimensionales Aggregat von Zellen ein hervorragendes *in vitro* System dar, an dem Wachstum und Verhalten eines Tumors unter realistischen Zell-Zell-Wechselwirkungen und dem Einfluss von Nährstoffgradienten studiert werden können.

Das verwendete Model basiert auf einer agentenbasierten Darstellung der Zelle und wurde in der Programmiersprache C++ implementiert. Zell-Agenten durchlaufen einen realistischen Zellzyklus, welcher durch diskrete Zyklusphasen, Wachstum und Teilung definiert ist. Weiterhin reagieren sie auf Umwelteinflüsse, wie Druck durch benachbarte Zellen oder die lokale Nährstoffkonzentration. Die Zellagenten werden räumlich in einer dynamisch-kinetischen, gewichteten Delaunay-Triangulation als wechselwirkende sphärische Körper beschrieben. Die Delaunay-Triangulation erlaubt die effiziente Bestimmung und Aktualisierung von Zell-Zell-Kontakten im System. In der dualen Voronoi-Zerlegung werden Zellen als dreidimensionale Polyeder repräsentiert, so dass sich gewebeähnliche, realistische Kontaktflächen zwischen Zellen bilden. Eine kräftebasierte Wechselwirkung für Zellen auf Grundlage des Johnson-Kendall-Roberts-Modells und physiologischer Parameter wurde implementiert und die resultierende Dynamik wird in der überdämpften Näherung integriert. Die Nährstoffversorgung innerhalb des Tumorsphäroiden erfolgt über Diffusion von der Tumoroberfläche aus einem unbegrenzten Reservoir an Nährlösung mit definiertem Glucose- und Sauerstoffgehalt. Mithilfe eines Diffusions-Algorithmus wird die lokale Konzentration aller diffundierenden Substanzen in Abhängigkeit von den Randbedingungen und der lokalen Nährstoffaufnahme durch Zellen berechnet. Eine Versorgung mit Glukose ist für Zellen überlebenswichtig, während eine lokale Hypoxie oder sogar ein vollständiges Fehlen von Sauerstoff toleriert werden kann und zur Bildung einer therapieresistenten hypoxischen Zellpopulation führt.

Die Effekte einer Strahlendosis sind auf Basis des linearquadratischen Modells für Zellüberleben in Abhängigkeit der Dosis definiert. Gemessene Parameter, welche die Strahlensensitivität der Zellen in verschiedenen Zyklusphasen beschreiben, werden für das linearquadratische Modell verwendet. Darüber hinaus wird die effektive Dosis in Abhängigkeit von der lokalen Sauerstoffkonzentration reduziert. Zellen in Quieszenz zeigen eine erhöhte Strahlenresistenz und reduzieren die erhaltene effektive Dosis um einen konstanten Resistenzfaktor.

Als Reaktion auf einen tödlichen Strahlenschaden können Zell-Agenten im Modell entweder einen schnellen Zelltod in der Apoptose zeigen oder aber einen langsamen durch Mißreparatur nach Blockierung am G2/M-Kontrollpunkt, welche letztendlich ebenfalls die Auflösung der Zelle durch Apoptose induziert. Die bevorzugte Induktion von direkter Apoptose spiegelt dabei schwere DNA-Schäden wieder, die zum Beispiel durch Bestrahlung mit Schwerionen vermehrt erzeugt werden, während der verzögerte Zelltod am G2/M Kontrollpunkt die Folge von minder schweren DNA-Schäden ist, die vermehrt durch Röntgenbestrahlung ausgelöst

werden.

Ein stark vereinfachtes Modell für die Reaktion von Zellen auf chemotherapeutische Medikamente wurde implementiert, um insbesondere die Wirkung von Hydroxyurea auf die Zellpopulation zu beschreiben. Eine Dosis Hydroxyurea ist spezifisch toxisch für Zellen in der Synthesephase des Zyklus und bewirkt darüber hinaus eine Blockade der Transition von der G1-Phase in die Synthesephase, solange eine ausreichend hohe Konzentration vorhanden ist. Im Modell wird vereinfachend angenommen, dass eine hinreichend hohe Konzentration von Hydroxyurea im kompletten Tumor erreicht werden kann, indem die Konzentration in der umgebenden Nährstofflösung beliebig hoch gewählt wird.

Als Observable für die momentane Strahlensensitivität eines Tumors wird das sogenannte "Enhancement" definiert, welches in Relation zur erwarteten durchschnittlichen Strahlensensitivität eines Tumorsphäroiden in der exponentiellen Wachstumsphase definiert ist. Um die Synchronizität der Zellpopulation zu beschreiben, werden verschiedene Messgrößen eingeführt. Als am besten geeignete Größe wird die Shannon-Entropie der Zellzyklusverteilung als Observable für die Synchronizität definiert.

Die entwickelte Simulationsumgebung kann das Wachstum eines Tumorsphäroiden ausgehend von einer kleinen Zahl an malignen Zellen beschreiben. Diese werden als frei schwimmend in einer Nährlösung behandelt und formen als Konsequenz der Zell-Zell-Adhäsion im Verlauf der Proliferation ein kugelförmiges Zell-Aggregat. Das Wachstum des Tumorsphäroiden kann für verschiedene Nährstoffkonzentrationen im umgebenden Medium in Übereinstimmung mit experimentellen Messungen beschrieben werden. Der Tumorsphäroid zeigt in Übereinstimmung mit histologischen Befunden eine typische Schichtung, mit einem äußeren Rand aus aktiv proliferierenden Zellen, einer vermehrt quieszenten Zwischenlage und einem nekrotischen Innenraum, der im späteren Stadium durch die Auflösung von nekrotischen Zellen einen Hohlraum bildet. Sowohl die Dicke der Schicht aus lebenden Zellen als auch die Zellzyklusverteilung stimmen mit experimentellen Beobachtungen überein.

In der Analyse des durchschnittlichen Zellflusses zeigt sich, dass in einem voll entwickelten Tumorsphäroiden als Folge der Zellproliferation ein konstanter Fluss von Zellen in den nekrotischen Kern beobachtet werden kann, sowie eine gleichzeitige Expansion der Oberfläche. Eine Bestrahlung führt zur transienten Umkehr dieses Flusses, so dass sich die Schicht aus überlebenden Zellen effektiv zusammenzieht, bevor der ursprüngliche Fluss durch die Reproduktion wiederhergestellt wird.

Verschiedene Mechanismen, die für die Saturierung des Wachstums von Sphäroiden verantwortlich sein könnten, werden im Modell untersucht. Weder eine Erhöhung der Zell-Zell-Adhäsion, noch die Einführung einer externen zentral wirkenden Kraft auf die äußerste Zell-Lage kann im Modell zu einer vollständigen Saturierung führen oder die zentrale nekrotische Kavität schließen. Dies steht allerdings nicht unbedingt im Widerspruch zu experimentellen Beobachtungen, die üblicherweise in einem Wachstumszeitraum von bis zu 4 Wochen ebenfalls keine volle Saturierung beobachten können. Eine interessante kritische Abhängigkeit wird im Zusammenhang mit dem Verlust von Tumorzellen von der Oberfläche des Sphäroiden beobachtet. Besonders im Zusammenhang mit der Zytokinese während der Mitose wird in Experimenten die vermehrte Ablösung von Zellen aufgrund eines temporären Kontaktverlusts beobachtet. Abgelöste Zellen verlieren sich im Nährstoffmedium und werden mit dessen regelmäßigem Wechsel aus dem System entfernt. In der Simulation wurde dieser Vorgang entsprechend experimentell ermittelter Raten implementiert, so dass Oberflächen-

zellen entweder in zufälliger Zyklusphase oder nur in der Mitose abgelöst und aus dem System entfernt werden. Wird eine Verlustrate gewählt, die unabhängig von der Sphäroidgröße ist, so zeigt sich eine kritische Abhängigkeit des Wachstums von der entsprechenden Rate. Eine Verlustrate in experimentell ermittelter Höhe führt dazu, dass sich Aggregate unter einer kritischen Zellzahl aufgrund ihres Oberfläche-Volumen-Verhältnisses auflösen. Wird die Rate geringfügig reduziert, so kommt es ab einem kritischen Punkt zu einem normalen Wachstum des Sphäroiden. Diese kritische Abhängigkeit könnte von Bedeutung für die Auflösung von Mikrotumoren und Metastasen *in vivo* sein.

Eine detaillierte Untersuchung der Reaktion des Tumorsphäroiden auf Bestrahlung wird durchgeführt, bei der sich zeigt, dass als Folge der Bestrahlung eine drastische Resynchronisation der Zellpopulation im Bezug auf ihr Voranschreiten im Zellzyklus auftritt. Als Hauptursachen für die dosisabhängige Synchronisation werden drei Mechanismen identifiziert: die direkte Änderung der Zellzyklusverteilung als Konsequenz der unterschiedlichen Strahlensensitivitäten von Zellen entsprechend ihrer aktuellen Zyklusphase, die synchrone Reaktivierung von quieszenten Zellen und die Blockierung von Zellen am G2/M Kontrollpunkt als Konsequenz von Strahlenschäden an der DNA. Das synchrone Voranschreiten von Zellen im Zyklus sorgt im Tumorsphäroiden für eine kollektive Entwicklung der Strahlensensitivität, die sich als deutliche Erhöhung der durchschnittlichen Sensitivität gegenüber der erwarteten Sensitivität zeigt (entsprechend einer Erhöhung des „Enhancement“). Die Entwicklung der Strahlensensitivität im Model entspricht dabei qualitativen Beobachtungen im Rahmen von „split-dose“-Experimenten. Ein ausgeprägtes, transientes Maximum in der Strahlensensitivität kann in der Folge einer vorangehenden Bestrahlung beobachtet werden, welches sich für die Nutzung mit einer Folge-Dosis eignet. Die Mechanismen, welche die Form und zeitliche Lokalisation des Maximums beeinflussen, werden in der Konsequenz einer Untersuchung im Hinblick auf die verursachten Veränderung unterzogen. Es zeigt sich, dass die Quieszenz und Reaktivierung von Zellen einen deutlichen Einfluss auf die Reaktion hat, aber das ein Maximum der Strahlensensitivität und anschließende gedämpfte Oszillationen unabhängig von der Wahl der Parameter beobachtet werden können.

Es besteht eine Korrelation der Maxima in der Strahlensensitivität mit der typischen Zellzykluszeit der Zellen, des Weiteren kann ein charakteristischer Zeitraum definiert werden, in dem ein Tumor nach einer Bestrahlung wieder in einen desynchronisierten Gleichgewichtszustand zurückkehrt.

Die begrenzte Sauerstoffversorgung des Sphäroiden über die Oberfläche führt zu einer ausgeprägten Hypoxie im zentralen Bereich, deren Wirkung auf die Effektivität einer Strahlendosis untersucht wird. Gerade bei höheren Einzeldosen von 8 Gy zeigt sich deutlich der Effekt der Strahlenresistenz, der mit der Hypoxie einhergeht.

Verschiedene klinische Bestrahlungsprotokolle werden im Modell auf ihre Wirksamkeit hin überprüft, insbesondere im Hinblick auf die Ausnutzung der beobachteten transienten Erhöhung der Strahlensensitivität, die einer vorausgehenden Bestrahlung folgt. Es zeigt sich, dass hyperfraktionierte Bestrahlungspläne, welche die Gesamtdosis in eine Vielzahl kleinerer Dosen aufteilen, insgesamt eine bessere Reduzierung der Tumormasse bewirken können. Die beobachtete Effizienz der Bestrahlungspläne kann im Model mit Hilfe der Korrelation von Enhancement und der Bestrahlungszeiten erklärt werden. In hypofraktionierten Bestrahlungsplänen, welche eine kleinere Zahl hoher Einzeldosen einsetzen, konnte beobachtet werden, dass der Tumorsphäroid sich in eine Vielzahl kleinerer Zellaggregate auflöst. Der

Zerfall steht in direktem Zusammenhang mit dem Verlust von Zell-Zell-Kontakten, der mit der Auflösung von apoptischen Zellen nach einer Strahlendosis einhergeht.

Eine systematische Analyse verschiedener Fraktionierungen einer Gesamtdosis wird durchgeführt, um optimale Bestrahlungsintervalle zu identifizieren, welche den Enhancement-Effekt ausnutzen. Unter anderem wird die benötigte Dosis zur vollständigen Sterilisation eines Tumorsphäroiden in Abhängigkeit vom verwendeten Bestrahlungsintervall analysiert. Hierbei zeigt sich, dass wider Erwarten eine Vergrößerung des Bestrahlungsintervalls nicht unbedingt zu einer niedrigeren Effizienz führt, was Aufgrund von einem vermehrten angeregten Wachstum in den längeren Bestrahlungspausen unbedingt zu erwarten ist. Tatsächlich ist es in bestimmten Zeiträumen möglich, das Bestrahlungsintervall zu erhöhen, ohne eine größere Dosis zur Sterilisation aufwenden zu müssen. Die typischen Bestrahlungsintervalle für die dieses Verhalten beobachtet werden kann, entsprechen der typischen zeitlichen Position des Enhancement-Maximums und sind damit auf die strahleninduzierten Zell-Zyklus-Effekte zurückzuführen.

Die Auswirkungen einer konstanten Dosis pro Zeiteinheit, welche in unterschiedlichen Fraktionierungen appliziert wird, werden im Modellsphäroiden untersucht. Es zeigt sich, dass eine leicht vom Standardtherapieplan abgewandelte, konstante Fraktionierung von 2.5 Gy/30h signifikant bessere Ergebnisse erzielen kann. Als Ursache für die unterschiedliche Reduktion in Tumormasse der verschiedenen Fraktionierungen werden Zellzyklus-Effekte identifiziert.

Im Hinblick auf eine optimale Nutzung der Enhancement-Effekte werden verschiedene Bestrahlungspläne untersucht, in denen eine konstante Dosis pro Zeiteinheit je in eine Auslöse- und eine Effektdosis aufgeteilt wurde. Es zeigt sich, dass durch das Hervorrufen einer Synchronisation und der verbundenen kollektiven Entwicklung der Radiosensitivität mithilfe der Auslöse-Dosis und anschließende Gabe der Effektdosis zum Zeitpunkt des Maximums eine gute Effizienz der Bestrahlungspläne erreicht werden kann.

Die Möglichkeit der automatische Kalkulation von Dosis und Bestrahlungszeitpunkt in Abhängigkeit von der zeitlichen Entwicklung des Enhancements wird mit verschiedenen Algorithmen untersucht. Des Weiteren wird zum Vergleich der Effizienz eine manuell im Hinblick auf die Ausnutzung des Enhancements optimierte Bestrahlungsserie durchgeführt. Beide Versuchsreihen weisen eine insgesamt höhere Effizienz als die klinischen Standardpläne auf.

Durch Veränderungen in der Struktur und Zellzyklusverteilung des Tumors ändert sich im Verlauf von längeren Bestrahlungsprotokollen der zeitliche Ablauf der Enhancement-Reaktion geringfügig, was eine entsprechende Neuberechnung erforderlich macht. Obwohl diese Neuberechnung sowohl in der automatischen Berechnung, als auch in der manuellen Optimierung berücksichtigt ist, sinkt deren Effektivität im Verlauf der Bestrahlungsserie unter die Effektivität des besten konstant-fraktionierten Bestrahlungsplan ab. Es zeigt sich, dass die Optimierung der Bestrahlungspläne eine globale Optimierung erfordert und nicht allein durch lokale Optimierung erreicht werden kann.

Die zeitliche und räumliche Erhöhung der Sauerstoffkonzentration in Folge einer Strahlendosis wird im Modelltumor untersucht. Eine mikroskopische, diffusions-basierte lokale Erhöhung der Sauerstoffverfügbarkeit wird beobachtet, welche nach einer Bestrahlung für eine Zeitspanne von bis zu 48 Stunden erhalten bleibt. Da die Reoxygenation in allen kapillarnahen Regionen eines makroskopischen Tumors *in vivo* ausgelöst wird, kann der im Modell beschriebene zeitliche Verlauf der Sauerstoffkonzentration in Bezug zu experimentellen Messungen mit Hilfe der Positronen-Emissions-Tomographie gesetzt werden.

Im Hinblick auf eine mögliche synergetische Wechselwirkung wird der neoadjuvante Einsatz von Hydroxyurea in Kombination mit einer Strahlendosis untersucht. In Übereinstimmung mit experimentellen Messungen kann die durch Hydroxyurea hervorgerufene Synchronisation des Zellzyklus eine drastische Erhöhung der Strahlensensitivität hervorrufen, die mit einer entsprechend koordinierten Folge-Dosis genutzt werden kann. Selbst unter der Annahme einer zeitlich stark beschränkten Verabreichung von Hydroxyurea und einer schlechten Reaktionsfähigkeit von Zellen auf ein Absinken der Konzentration von Hydroxyurea zeigt sich ein signifikanter Verstärkungseffekt. Im Zusammenhang mit der fraktionierten Bestrahlung konnte besonders für einige alternative Bestrahlungspläne ein hohes Potential für eine adjuvante Chemotherapie mit Zytostatika prognostiziert werden.

Insgesamt kann das Modell klare Vorhersagen über die Effektivität alternativer Bestrahlungspläne treffen, welche in Tumorsphäroiden *in vitro* verifiziert werden können. Eine Ausnutzung der strahlungs-induzierten Synchronisation und der damit einhergehenden Erhöhung der durchschnittlichen Strahlensensitivität erweist sich in allen untersuchten Fällen als effizienzsteigernd gegenüber Standardprotokollen. Ein simples und spezifisches Bestrahlungsprotokoll, welches mit 2.5 Gy/30h nur geringfügig von der typischen klinischen Fraktionierung abweicht, konnte als hochgradig effektiv im Rahmen des Modelltumors identifiziert werden. Eine Aufteilung der Strahlendosis in eine synchronisations-induzierende Auslöse- und eine nachfolgende, koordinierte Effektdosis kann zu einer drastischen Erhöhung der Effizienz führen. Besonders für Behandlungspläne mit einer höheren Effektdosis, in denen aufgrund der konstanten Dosis pro Zeiteinheit eine längere Behandlungspause zwischen den Bestrahlungsböcken liegt, kann eine adjuvante Chemotherapie zu einer weiteren drastischen Steigerung der Effizienz führen.

# Contents

<b>1</b>	<b>Introduction</b>	<b>14</b>
1.1	Cancer modelling . . . . .	14
1.2	Experimental systems and data basis . . . . .	16
1.3	Clinical treatment planing and optimisation . . . . .	18
1.4	Central questions . . . . .	19
<b>2</b>	<b>Model</b>	<b>20</b>
2.1	Cell behaviour and its abstraction . . . . .	20
2.1.1	Cell cycle . . . . .	20
2.1.2	Cell metabolism . . . . .	24
2.1.3	Cell mechanics . . . . .	32
2.1.4	Summary . . . . .	37
2.2	Nutrients and hypoxia . . . . .	38
2.2.1	Nutrient support <i>in vivo</i> and <i>in vitro</i> . . . . .	38
2.2.2	Hypoxia sources . . . . .	40
2.2.3	Microtumour structure and self-similarity . . . . .	41
2.2.4	Nutrient concentrations in blood and tissue . . . . .	44
2.2.5	Summary . . . . .	46
2.3	Diffusion solver . . . . .	47
2.3.1	Diffusion equation . . . . .	47
2.3.2	Solution schemes and steady-state approximation . . . . .	48
2.3.3	Cell density estimation for variable diffusion coefficient . . . . .	51
2.3.4	Moving boundary effects on tumour growth . . . . .	52
2.3.5	Summary . . . . .	55
2.4	Delaunay triangulations . . . . .	56
2.4.1	Representation of tissue in a Voronoi/Delaunay model . . . . .	56
2.4.2	Summary . . . . .	59
2.5	Radiation effects model . . . . .	60
2.5.1	Effects of ionising radiation on cells . . . . .	60
2.5.2	Damage kinetics and repair . . . . .	67
2.5.3	Particle irradiation . . . . .	70
2.5.4	Models for radiation response . . . . .	72
2.5.5	Fractionated radiation delivery . . . . .	73
2.5.6	Implemented radiation model . . . . .	76
2.5.7	Summary . . . . .	81
2.6	Chemotherapy and adjuvant therapies . . . . .	82
2.6.1	Anticancer drugs and synergy in chemoradiotherapy . . . . .	82
2.6.2	Hydroxyurea . . . . .	83

2.6.3	Drug distribution, pharmacodynamics and -kinetics	85
2.6.4	Summary	88
2.7	Observables	89
2.7.1	Tumour burden	89
2.7.2	Radiation survival and enhancement	89
2.7.3	Enhancement as true measure for sensitivity	90
2.7.4	Maximum total cycle length and relative cycle position	91
2.7.5	Synchronicity of cell populations	92
2.7.6	Integral enhancement	97
2.7.7	Summary	98
<b>3</b>	<b>Results</b>	<b>99</b>
3.1	Tumour spheroid growth	99
3.1.1	Tumour spheroid growth and histology	99
3.1.2	Cell cycle distribution during growth	103
3.1.3	Growth saturation	106
3.1.4	Cell flow and radial velocity	108
3.1.5	Cell shedding effects	111
3.2	Irradiation response	116
3.2.1	Tumour composition and radiosensitivity	116
3.2.2	Irradiation reaction	117
3.2.3	Dose-dependent dynamics of enhancement	121
3.2.4	The 4Rs of radiotherapy	124
3.2.5	Influences on the radiation response	129
3.2.6	Synchronicity and enhancement	138
3.2.7	Oxygen enhancement	141
3.2.8	Split-dose experiments	142
3.3	Fractionated irradiation	145
3.3.1	Maximal cell cycle effects during repeated delivery	145
3.3.2	Control dose and fast apoptosis effect	146
3.3.3	Simulation of clinical schedules	147
3.3.4	Optimal radiation delivery interval	151
3.3.5	Sterilisation dose as a function of fraction timing	152
3.3.6	Varying interval and dose rate	154
3.3.7	Triggered optimal delivery	158
3.3.8	Manual optimal scheduling	161
3.3.9	Automatic optimal enhancement-based scheduling	162
3.4	Hypoxia	167
3.4.1	Formation of a hypoxic cell population	167
3.4.2	Spatial and temporal dynamics of reoxygenation	168
3.4.3	Comparison to PET-results	172
3.5	Synergies in radiochemotherapy	174
3.5.1	Synchronisation using Hydroxyurea	174
3.5.2	Effect of release reaction factor $\rho$	176
3.5.3	Short application of HU	178
3.5.4	Combination of hydroxyurea and radiotherapy	178

3.5.5	Countering accelerated repopulation . . . . .	179
<b>4</b>	<b>Discussion</b>	<b>182</b>
4.1	Implication of main results . . . . .	182
4.1.1	Cell behaviour and tumour growth . . . . .	182
4.1.2	Irradiation response . . . . .	185
4.1.3	Fractionated irradiation . . . . .	189
4.1.4	Hypoxia . . . . .	192
4.1.5	Radiochemotherapy . . . . .	193
4.1.6	Particle irradiation . . . . .	194
4.2	Critical model review and expansion . . . . .	195
4.2.1	Cell behaviour and interaction . . . . .	196
4.2.2	Radiation model . . . . .	197
4.2.3	Cell metabolism . . . . .	198
4.2.4	Diffusion and drugs . . . . .	198
4.2.5	Voronoi . . . . .	198
4.2.6	Model type and mechanisms . . . . .	199
4.3	Further investigations . . . . .	200
4.3.1	Tumour control . . . . .	200
4.3.2	Effects of the immune system . . . . .	200
4.3.3	Influence of the circadian rhythm . . . . .	201
4.3.4	Cancer stem cells and selection . . . . .	201
4.3.5	High single-dose delivery . . . . .	202
	<b>Appendix</b>	<b>203</b>
4.4	Summary of the model and growth of sample spheroids . . . . .	203
4.5	Runtime of simulations . . . . .	204
4.6	Parameters . . . . .	205
4.7	Integrity tests of the diffusion solvers . . . . .	208
4.8	Further applications of the simulation framework . . . . .	209
4.9	Copyright terms / Urheberrechte . . . . .	214
4.10	Technical terms . . . . .	215
4.11	Cell lines . . . . .	216

# 1 Introduction

The deregulation of growth within a single cell is at the origin of the disease which is the main cause of death within developed countries worldwide. The significance of cancer is also reflected in the amount of research which has been performed on its causes and effects. Decades of investigations have produced vast amounts of data and uncovered countless mechanisms and regulations which are of importance for the development of cancer. Still, a “cure” for cancer remains to be found, but with increasing knowledge of the multifaceted and complex disease which cancer is, it becomes clearer that such a “universal” cure is highly unlikely to be developed.

While the goal of treatment is still the elimination of cancer, in many cases treatment has to resort to a management of the disease. A range of different therapeutic approaches are usually combined, in multimodal therapy in order to maximise the survival probability of patients. An understanding of how these different therapies can be efficiently combined is mandatory in order to maximise their effect.

Due to this complex optimisation problem, but also as a result of the inherent properties of the carcinogenic process and the growth of tumours, cancer has been also a prime target of mathematical and computational modelling. The wealth of data that has been obtained for different processes in cancer can be integrated within models in order to predict useful treatment approaches, or in order to investigate the interaction of different mechanisms.

As millions of patients receive cancer therapies each day, even small improvements in efficiency, which can be achieved as a result of according modelling can have a tremendous impact. Within the scope of this thesis such a model for the investigation of possible enhancing effects in radiotherapy is to be developed.

## 1.1 Cancer modelling

In general, models can offer a fully controllable mathematical or computational environment for the investigation of phenomena. This can be of great use if complex interactions within a system are to be disentangled and understood. If a model is sufficiently simple, all processes and interactions within it can be fully mapped. This is in sharp contrast to typical experimental settings, where the degree of control is usually drastically lower due to the immense complexity of cellular processes and interactions, which can be only restricted partially within each setting.

If a model can describe a range of phenomena using only a well-known set of processes and parameters in agreement with experimental observations, it can eventually reach predictive power. Accordingly predictions about unknown situations can be inferred from the model and used to guide the course of experimental investigation. In an ideal interaction, the results of further according experiments can be included into the model, which will in turn increase its predictive power. Thus a synergistic cycle between the model and according experiments can be established.

Hence models make a cost-efficient and fast investigation of different scenarios possible. A strong point is, that these investigations can also include unusual scenarios which cannot be easily, or not at all, realised in experimental settings.

Models must be build on a foundation of knowledge about the important processes of a system. As the complexity of models must be limited, usually a decision about important and negligible processes will have to be made. As cancer is a disease that is associated with many facets, care has to be taken to include all major mechanisms which will influence a specific reaction of interest within cancer models. In the example of the radiation response, this can include microscopic processes, such as the single cell response or local oxygenation, but also a macroscopic phenomena, such as the pressure distribution inside the tumour or global levels of acidity.

Consequently models should include as many mechanisms as necessary for an accurate description of the process of interest, but at the same time comprise as few mechanisms as possible. While this can be seen as a purely economic principle, it is necessary in order to preserve a predictive power within a model which will otherwise be too complex for realistic predictions.

The list of models which have been developed in order to study phenomena related to tumour growth and treatment is long enough in order to fill a whole thesis on its own. For this reason only an overview of some recent modelling approaches and methods of interest can be discussed in this introduction.

The monoclonal origin and the discrete nature of cancer makes the initial stages of its development highly suitable for modelling with agent-based approaches which use single cells as model basis. At the later stages of cancer growth, when typically billions of cells will be involved, continuous modelling approaches, which usually employ ordinary differential equations, have been quite successful in describing the characteristics of cancer growth and development.

An excellent range of reviews and overview papers is available for mathematical modelling of tumour growth [181], employed Monte Carlo techniques [65] and radiobiological models for tumour treatment [236].

As cancer is a phenomenon that is associated with a very high number of individual cells, continuum models based on ordinary or partial differential equations will be a type of standard model which is commonly employed in cancer research. While this seems contradictory in regards to the monoclonal origin and discrete nature of cancer, it can be justified, provided that the phenomena that should be studied will not be characterised by processes that rely on a small number of cells. Studies that compare continuous and discrete modelling approaches and identify suitable operational areas are numerous e.g [37] and [195].

Due to an increased complexity, discrete models, which contain a spatial representation, will frequently sacrifice spatial resolution or realism in order to minimize the required computing time or in order to simplify calculations. A common example is the use of stochastic models for cell populations which corresponds to an effective restriction of space to one dimension [226]. If such drastically simplified models can yield significant results will depend on the exact phenomena which are to be studied.

In general, it has been shown in numerous publications that if a realistic description of phenomena is of importance, which is especially true in models that are to be used for medical predictions, the use of three-dimensional modelling is of great importance [173]. A

## 1 Introduction

wide range of cellular processes has been demonstrated to be altered within three-dimensional culture systems when compared to classical quasi two-dimensional flask culture, as will be discussed later.

A straightforward computational approach to implement three-dimensional modelling is the use of a regular lattice, which can be used to discretise the simulation space [93]. This discrete spatial representation however does not correspond well to the lattice-free nature of tissue and thus will be usually unsuitable for the modelling of realistic interactions. Furthermore, spatial discretisation introduces the risk to yield artefacts of the underlying lattice in the results.

Radusweit et al. demonstrated that Voronoi/Delaunay-based model systems, as employed for example in [194], are able to avoid lattice artefacts and therefore are often superior to other spatial representations, especially when a highly realistic cell environment or complex interactions are to be modelled [173]. The nature of the Delaunay system allows for an efficient calculation of cell-cell interactions even for large systems. At the same time, the tissue representation can be based on polyhedral contact surfaces within the dual Voronoi tessellation. This will yield a representation of cells which is very similar to the exact organisation of cells in tissue.

A newly arising type of modelling is the so called hybrid multi-scale modelling, which aims to combine the advantages of discrete single-cell and continuous modelling. Within its approach the processes in the system will be categorized to be either suitable for agent-based or continuous modelling techniques and thus implemented accordingly. As two very different types of models are used to describe the same global processes, the coupling of the models is usually complex and requires sophisticated approaches in order to be solved. A comprehensive overview of different scales and techniques in multi-scale cancer modelling can be found in [57].

### 1.2 Experimental systems and data basis

Experimental data is obtained from specific model systems, which will place fixed limitations on the type of phenomena that can be studied. Systems can be as simple as cells of a defined lineage which grow as a monolayer in a culture flask, or as complex as an *in vivo* xenograft, in which cancer cells are implanted in laboratory animals in order to achieve the highest possible degree of realism.

The quasi two-dimensional culture of cells in flasks remains the de facto standard today. While flask culture is cheap and easy to perform, it can not capture major parts of the cell environment, such as concentration gradients or a realistic cell-cell contact. Depending on the question under consideration such simple systems can be sufficient, but in general a higher degree of realism is often needed. It has been shown that not only gradients of nutrients and oxygen can influence gene expression and reaction to drugs, but also that the amount of cell-cell contact can alter the way cells will respond to treatment. This cell contact effect has for example been demonstrated to be of importance in radiation resistance of tumours [164], [165]. Clearly these effects cannot be captured in monolayer experiments.

On the other end of the possible spectrum of available experimental methods are xenograft experiments. While xenografts cultures will most definitely comprise a highly realistic environment for the processes which are to be studied, they can suffer from a lack of control of

the according boundary conditions. A high variability in data from xenograft experiments is common, as results can drastically vary from animal to animal.

Consequently, while flask cultures present the experimenter with a problematic lack of mechanisms, *in vivo* xenograft cultures will most often pose the opposite problem of a wealth of entangled mechanisms, which complicate the interpretation of obtained results.

An experimental system for cell culture, which can act as an intermediary between simple monolayer culture and *in vivo* experiments is the multicellular tumour spheroid [99]. A cultivation of cells as self-adhering, three-dimensional aggregate will yield a realistic environment for tissue-like cell-cell contacts. As a result of the spheroidal shape and the associated limited diffusion, also tissue-like gradients of nutrients and other diffusing substances can develop inside the spheroid. Continued proliferation will lead to a growth of the aggregate until a macroscopic tumour nodule of up to 1 mm diameter is formed, which corresponds to an *in vivo* tumour in its initial stage. The spheroid will comprise distinct histological regions, including an outer viable rim, an intermediate layer of quiescent cells and an inner core of necrotic cells, which, in fully developed spheroids, will dissolve to form a hollow core (see figure 1.1). Spheroidal cultures can be used as model for metastatic nodules or, as discussed within this thesis, even for microregions in a self-similar macroscopic tumour. They can show complex responses to stimuli and it has been demonstrated, that they can be used to predict changes in tumours which occur as a result of multifractionated irradiation [200].

The basic spheroid culture of cells remains simple enough to allow an identification of most of the mechanisms which are of importance for its growth. The realisms of the spheroid cultures can be increased by adding further effects to its microenvironment, e.g. by the co-culture of different cell types in multicellular aggregates [119]. While this complicates interpretations, it allows at the same time a specific, controlled expansion of the tumour microenvironment which could not be obtained with other model systems. Another type of experimental system which can achieve a similar degree of realisms as multicellular tumour spheroids, is the use of three-dimensional co-culture models, which can also provide a highly realistic micro-environment for tumour cells [238].

As a consequence of their properties, multicellular tumour spheroid and co-culture models are of specific interest for experiments and modelling approaches alike. Tumour spheroids specifically have been demonstrated to be a valuable model for the *in vivo* radiation reaction of tumours [68]. As a consequence, a realistic *in silico* model of tumour irradiation effects might extend to the *in vivo* situation as well.

Recent advancements in cultivation techniques have made the use of spheroid cultures drastically simpler, so an increase in spheroid-derived data can be expected [230]. This can be of advantage, as a highly realistic testing of theoretical predictions in a synergistic feedback loop between theory and experiment can in principle be established.

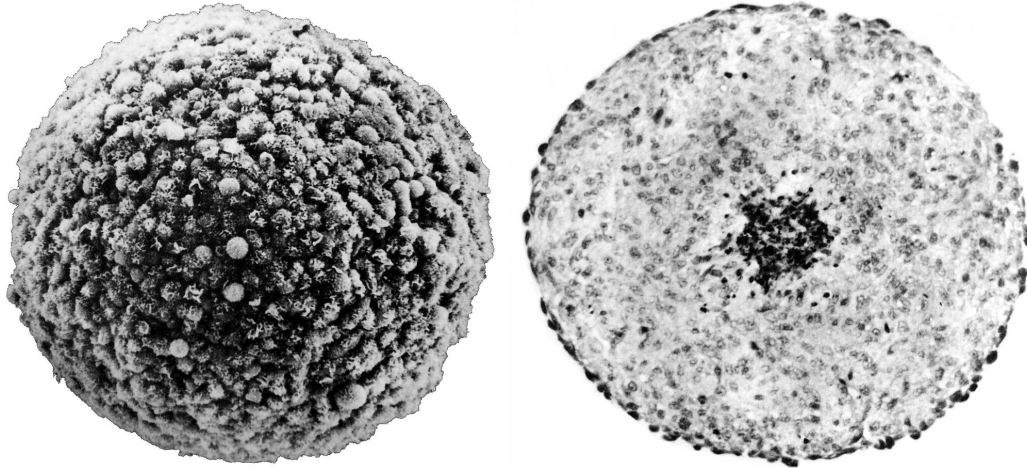


Figure 1.1: Multicellular tumour spheroids (MCTS) as growing aggregates of cells are a model system for tumour growth which is of special interest both for experimental studies and mathematical modelling. **(left)** MCTS after 15 days of growth from a small number of seeder cells with  $800\ \mu\text{m}$  radius which contains about  $8 \cdot 10^4$  cells. **(right)** Spheroid cross section showing central necrosis and viable rim of about  $200\ \mu\text{m}$ . Adapted from [86].

### 1.3 Clinical treatment planing and optimisation

A special interest in models of cancer growth and treatment reactions is given within a clinical setting. Treatment planing and optimisation both require the development of models which can describe the essential aspects of cancer development and the according available treatment techniques. Basic tumour control probability (TCP) models are routinely used in a clinical setting in order to predict the degree of control which can be achieved with a given treatment plan.

The inclusion of individual patient data from biopsies or other preferentially non-invasive monitoring methods will play an important role in the transition to personalised medicine and tailored treatment plans.

Especially in medical modelling it can accordingly be of advantage, to use models which can directly relate measurable parameters to predictions and vice versa, without the use of abstract representations. This allows for the direct inclusion of patient data and will furthermore facilitate the interaction between clinicians and modellers, as the model can be interpreted more intuitively.

The combination of multiple treatments is of high interest in medical modelling. With many model types a straightforward modelling of combined effects or even synergies between different therapeutic approaches is not possible, without a complete reformulation of the model. If the model is based on a realistic implementation of the involved processes and built in a object-based way, no reformulation of mechanisms is necessary in order to incorporate new phenomena into the model and describe possible synergies.

New measurement techniques of observables with high spatial and temporal precision continuously become available in a clinical setting and thus make treatment planing based on real-time data possible. At this point the computational efficiency of models becomes an important consideration, as real-time modelling requires typically either immense computational resources or very strong simplifications of the model.

## 1.4 Central questions

The central goal of this investigation is to describe the radiation reaction of a multicellular tumour spheroid as a model for the reaction of a macroscopic tumour under the effects of therapy.

For reasons discussed in the preceding section, the model which is to be developed within this thesis will follow an agent-based approach, which employs an abstraction of the cancer cell and its properties. An object-based implementation of the model will ensure the expandability and thus allow for an easy integration of new mechanisms. In order to achieve a realistic interaction of cells, a Voronoi/Delaunay-hybrid approach will be used for the spatial representation of the developing tumour spheroid.

A focus of the investigations will be on the dynamic cell cycle reaction, which is triggered in tumours in response to radiotherapy. A main question is, if and how a cell cycle response will be triggered, can be predicted and can be employed in order to enhance the outcome of radiotherapy.

An investigation of the effects of typical fractionated irradiation schedules is to be performed, especially in regards to the question if and how these therapeutic schedules can be optimised.

As radiation therapy is almost never applied as single treatment modality, the effect of adjuvant therapies, especially chemotherapy will be studied. Possible synergies in radiochemotherapy are of special interest.

The study of the spatio-temporal dynamics of hypoxia in tumours is of interest both for the treatment optimisation and for comparison with clinical measurements.

## 2 Model

Within this section an agent-based model for tumour growth and response to treatment is presented. The main focus of investigation is on radiotherapy and the according cell cycle effects. Parts of the model were developed for the Diploma thesis of the author (see [113]). Within the scope of this thesis the previous model has been largely extended and improved, so that only basic mechanisms which were already successfully tested (such as the general cell cycle model or the mode of cell interaction) remain unchanged.

The model consists of interacting cellular agents, which are spatially represented within a 3D-Delaunay triangulation and interact with a reaction-diffusion grid for soluble substances. The time evolution of the system is handled using synchronous updates with variable time intervals in which cells rearrange according to their interactions, update their cycle phase in response to internal and external triggers and consume nutrients from the diffusion grid.

### 2.1 Cell behaviour and its abstraction

The abstraction of the cell and its behaviour is a task of paramount importance in agent-based simulations. Most properties that a tumour will possess as a complex system emerge as a consequence of the single cell behaviour. In order to be a realistic representation of a cell, an agent must exhibit different features of real cells such as a cell cycle and its regulation, a metabolism, interaction and a response to damage which will be discussed in the following section. Many of these processes will actually be altered in cancerous cells when compared to benign cells. A good overview of common de-regulations and alterations which characterise the behaviour of cancerous cells is provided in [89]. Whenever a behaviour is characteristically deviating between cancerous and benign cells this will be discussed in the model. In regards to the possibility of modelling surrounding benign tissue in a tumour model, it is meaningful to be able to capture the behaviour of both cancerous and healthy cells in a realistic way.

While consequently the cell agent in the model is quite generic and thus can be fitted to represent a wide variety of different cell types and lines, simulations are by default performed with parameters which represent mouse mammary tumour cells of the EMT6 line (as for example described in [70] and [40]). This cell line was chosen as it is widely used in experiments and especially in studies of tumour spheroid growth.

#### 2.1.1 Cell cycle

##### Cycle phases and checkpoints

At the heart of the cells behaviour is the process of self-replication, which is normally tightly regulated within the cell cycle [110]. Cells will grow, replicate their DNA content and finally divide into two new cells. This seemingly simple process itself is extremely complicated in its regulatory structures, so a simplification is necessary to include this process in a tractable

model. Care has to be taken in order to feature all mechanisms which are necessary for realistic behaviour of the cell, while unnecessary complexity must be avoided.

The cell cycle of agents in this model follows a simple but realistic abstraction which was mainly published in [113] and [114] (an overview of which is visualised in figure 2.1).

Each cell agent will advance through distinct functional cycle phases characterised by cell growth (in G1 and G2 phase), DNA replication (S-phase) and division into two new cells (M-phase). For simplicity cells will continuously double their volume during the gap phases G1 and G2, so a volume conservation can be ensured when cells divide during cytokinesis (see also section 2.1.3 for more details on the cell size). Even though the real control of cell size is far more involved (see [231]), this wide-used approximation will yield reasonable results without the introduction of too many parameters.

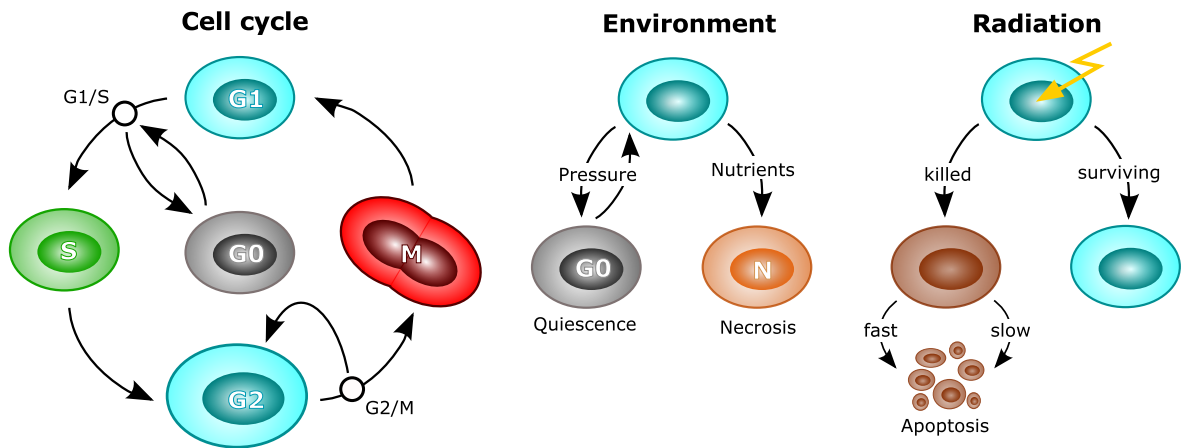


Figure 2.1: Overview of the inherent cell cycle of every agent, its response to environmental factors and a simplified radiation response. Black circles mark cycle checkpoints in the model. Details on the general cycle in section 2.1.1, on environmental response in section 2.1.2 and on radiation in section 2.5.

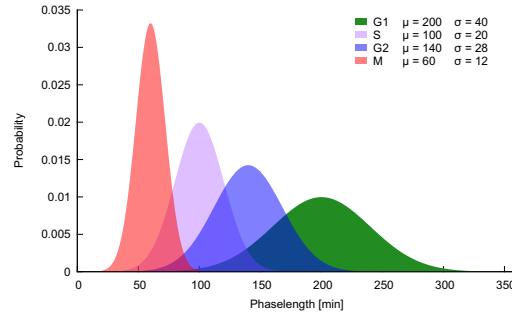
While cancerous cells will usually lose or circumvent a variety of mechanisms which normally regulate the cell cycle progression, at least parts of the normal regulatory responses are present also in cancerous cells [88].

Cells can enter and leave quiescence in response to high pressure or critical nutrient conditions at the G1/S checkpoint (which is also known as restriction point). If the critical conditions improve, cells re-enter the active cell cycle by passing the restriction point. This effect can lead to a synchronisation of cell cycle progression and is often also used to synchronise cell populations in experiments [152]. Even though this contact-inhibition effect is lost in some cell lines, most tumour cells retain a sensitivity to pressure and the possibility to become quiescent. An example of this are EMT6 tumour spheroids in the plateau phase of growth, which can consist of up to 90% cells in quiescence [70].

At the G2/M checkpoint cells will be halted if their DNA is damaged. This arrest in the G2-phase is subject to a chance of failure, so that, with a defined probability, cells can pass into mitosis even though their DNA is damaged. Usually the consequence of this faulty progression is either a fast cell death through mitotic catastrophe or cell death after a limited number of divisions.

If the cell passes the G2/M checkpoint it will commit to division in mitosis. The separation

Figure 2.2: The normal distribution of the cycle phase lengths used by each cell agent which is characterised by a mean value  $\mu$  and a relative width  $\sigma$ . A cutoff will be applied to the normal distribution usually at  $2\sigma$ .



of the mother cell into two daughter cells in cytokinesis is modelled following [113] by partially disabling the normal interaction between separating cells in order to ensure a smooth division.

Cell death in response to critical nutrient deprivation is possible at any time via necrosis and is discussed in more detail in section 2.1.2.

In response to irradiation, individual cells will die by apoptosis depending on their cell-cycle specific survival chance from the linear-quadratic model. Cell death in response to radiation is either via a direct commitment to fast apoptosis or by prolonged fixation at the G2/M checkpoint. Attempting cell division while DNA damage is present will lead to apoptosis as a result of mitotic catastrophe or other fatal errors. The damage response of cells is discussed in detail in section 2.5. A detailed review of cell cycle regulation, damage reactions and the associated checkpoints can be found in the review [189]. Even though the picture of discrete checkpoints is slightly outdated and was replaced by a picture of constant surveillance, we incorporate discrete checkpoints at the end of cycle phases for reasons of clarity and simplicity.

Cell death via necrosis or apoptosis will eventually lead to the removal of a cell from the system: either via a swelling of the cell followed by a violent rupture of the membrane in necrosis or via a “silent” dissolution of the cell into apoptotic bodies [49]. A major difference of both processes can be their immunogenic potential, which is high in necrosis and usually very low in apoptosis [225]. However this difference can only be observed in immunocompetent *in vivo* systems, which is a very rare experimental setting. Within the simulation, apoptosis and necrosis are distinguished and functionally different in their mechanical implementation. While a necrotic cell will slightly swell up before it shrinks, an apoptotic cell will just commit to shrinking. If a minimal size is reached after a characteristic time (see also section 4.6) both types of dead cells will be removed from the system.

### Cell cycle duration

The cell cycle phases are characterised by a typical length, which varies greatly between different cell types and cell lines as indicated in table 2.1. Quite often experiments will only measure doubling times for cell populations and not cycle times for single cells or even single cell cycle phases. A sample measurement of desynchronisation and the spread of the cell cycle time of initially synchronised V79 Chinese hamster cells can be found in [204] as shown in figure 2.3(a). Within this model a simple normal distribution of cell cycle phase lengths is assumed. This mechanism allows for an observation of cell cycle desynchronisation of initially synchronised populations and generally produces a reasonable cell cycle dynamic which is in agreement with experimental data (see figure 2.3).

Depending on the width of the normal distribution used to obtain cell cycle lengths, the

Cell line	G1	S	G2	M	Total
	[h]	[h]	[h]	[h]	[h]
EMT6/Ro	8	6	4.5	1	19.5
EMT6/UW	5.9	9.3	2.1	-	19.7
BT474	3.5	2	2.5	1	9
V79-285B	1.5	6	1.5	0.5-1	9.5-10
HeLa	7.6	7.3	0.8	0.5	16.2

Table 2.1: Example of cell cycle durations for different cell lines compiled from [70], [69], [121], [175], [205], and [126].

synchronous advancement of the cell cycle persists over long times within the population. Relatively low widths of about 15 percent will already lead to a broad distribution of cell cycle times and fast desynchronisation over 1 or 2 generations.

The fastest cycling mammalian cells in culture, crypt cells in the intestinal epithelium, have a cycle time as short as 9 to 10 hours while stem cells in resting mouse skin may have a cycle time of more than 200 hours. Most of this difference is due to the varying length of G1, the most variable phase of the cycle. M- and S-phase durations usually do not vary much. Cell cycle durations for *in vitro* cell cultures will also vary between monolayer, multilayer and spheroid cultures. Some of these effects, as for example reported in [227], are real alterations of the cell cycle length, while others are only apparent changes as a result of e.g. quiescent sub-populations. As only spheroid cultures are considered in the model, the cell cycle durations can be matched with typical experimentally determined durations for spheroid culture. A comprehensive overview of doubling times for 15 cell lines in monolayer and spheroid culture (as well as viable rim width and cell density) can be found in [69].

Even for a single cell line and its subcultures, significant deviations in reported cell cycle lengths can be observed, as for EMT6 cells: [121] determined cell cycle times by synchronised division of EMT6 cells from mitotic selection and found an average cycle time of 15 hours (G1: 6h, S: 5h, G2: 3h, M: 1h). [70] reports doubling times of 12.5 hours in monolayers and 15 resp. 17 hours for spheroid growth, [72] 21-25 hours doubling time within the first 3-4 days, [69] measured an initial doubling time of 24 hours for EMT6/Ro cells in spheroid culture (and only 9.5 hours for monolayer growth).

In many mathematical models of cell cycle progression, a gamma-distribution, or an Erlang distribution is used for cell cycle phase length (see e.g. [173]). This is most often only motivated by specific mathematical properties, as a gamma-distribution of cell cycle durations yields no advantage in the simulation. Instead shape and scale-parameters make the use of a gamma-distribution counter-intuitive, as there is no clear average duration to be defined in a convenient way. Although the mean is defined as  $k\theta$  adjusting a proper width for the distribution is not straightforward as with a normal distribution. This unnecessarily complicates the comparison of the distribution to experimentally measured data, which in almost all cases will be provided as mean and width. For a low width  $\sigma$  of e.g. 10 percent, the normal distribution closely resembles the gamma distribution, so that virtually no difference arises from using either of these distributions. As a consequence the simpler normal distribution

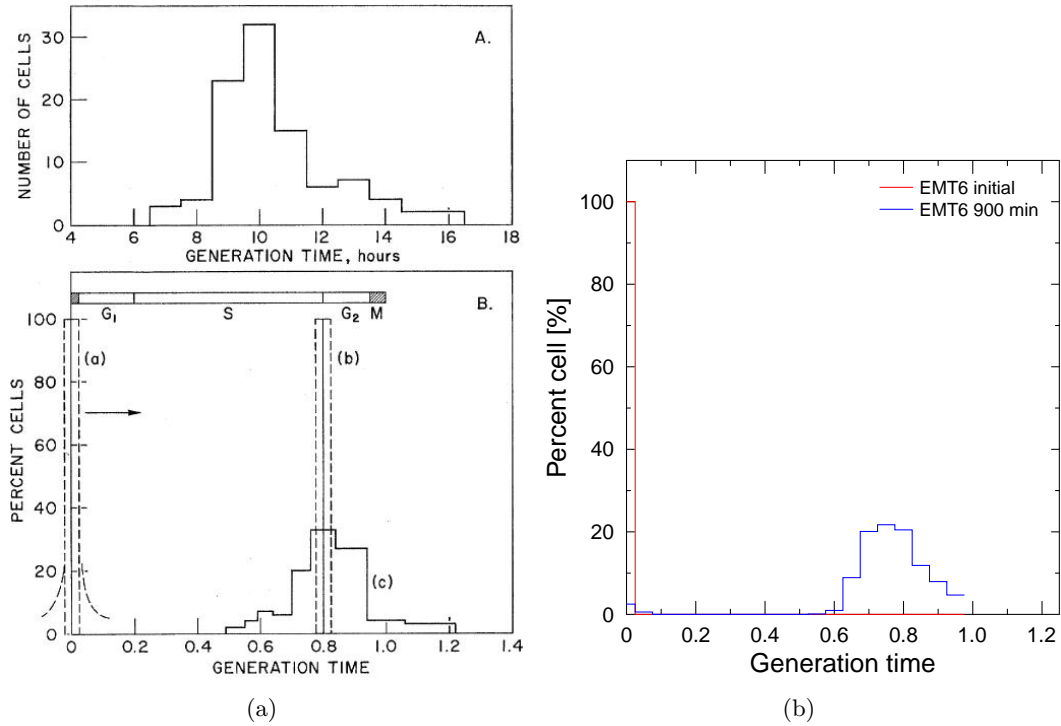


Figure 2.3: (a) Distribution of cycle durations (top) and the desynchronisation of initially synchronised V79 Chinese hamster lung cells (bottom) from [204]. (b) Sample of desynchronisation in the simulation using a relative  $\sigma = 0.2$  and a cutoff of 0.4. A cyclic measure of generation time is used, so that cells which completed a cycle will not advance to a generation time larger than 1 but instead restart at 0.

was chosen which also makes a comparison to experimental data easier.

## 2.1.2 Cell metabolism

### Basics of the cell energy generation

The initial stage of the cell metabolism is the breakdown of glucose to pyruvate in the process of glycolysis. This process is independent of oxygen and yields a net energy of 2 ATP. In glycolysis  $\text{NAD}^+$  is employed and reduced to NADH, so in order to continue the breakdown of glucose, a regeneration of  $\text{NAD}^+$  is necessary. If oxygen is available, the pyruvate and NADH will be processed by pyruvate decarboxylation, the citric acid cycle and eventually *oxidative phosphorylation* to generate 36 ATP molecules per glucose and oxidate NADH to  $\text{NAD}^+$  using  $\text{O}_2$ . This is the highly efficient standard cell metabolism, which overall for the clean combustion of glucose can be simplified to the reaction:



In the absence of oxygen, cells can use anaerobic mechanisms to regenerate  $\text{NAD}^+$ , albeit with greatly reduced efficiency (known as *anaerobic glycolysis*). This is done by lactic acid fermentation, which oxidates NADH to  $\text{NAD}^+$  using the pyruvate as proton acceptor eventu-

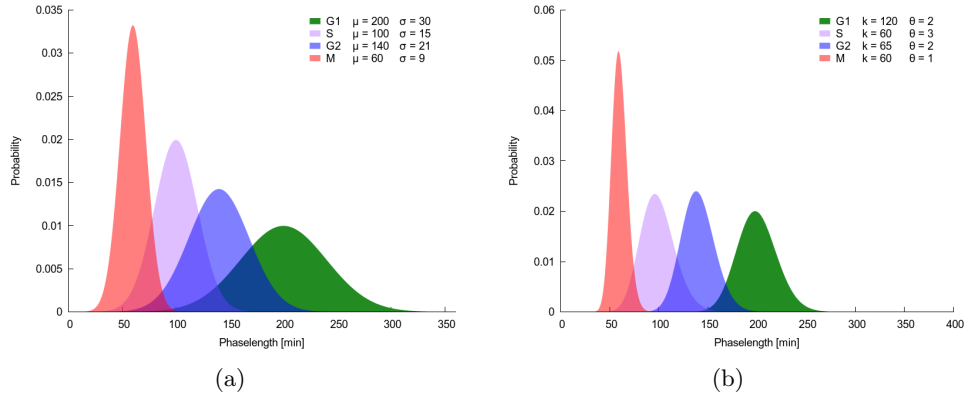


Figure 2.4: (a) Gauss-distribution with a width of 15 percent and (b) Gamma-distributed cell cycle lengths. Gamma mean values are given by  $k\theta$ .

ally converting it to lactate. As lactate will form lactic acid, this process will swiftly decrease the pH value within the cell or the tissue employing this fermentation. While this anaerobic mechanism allows for the continuous breakdown of glucose under anoxic conditions, it is highly inefficient when compared to the possible aerobic mechanisms for ATP generation. Again simplifying to an overall reaction yields:

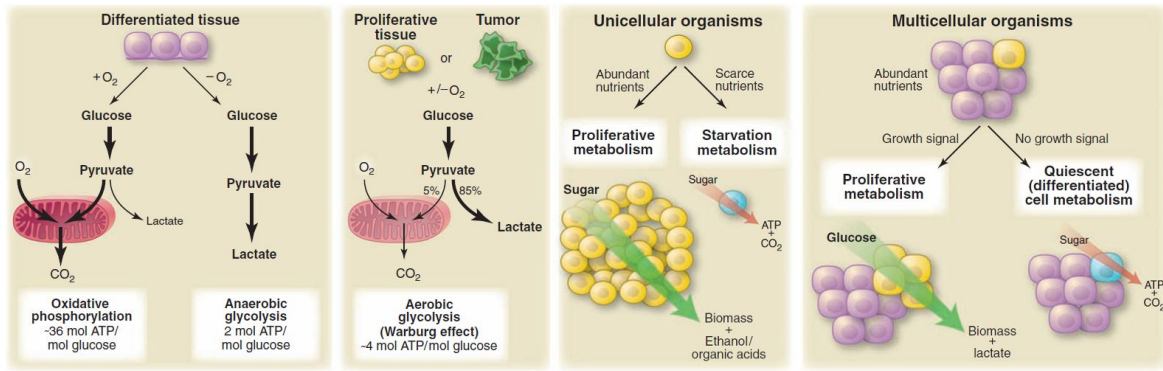
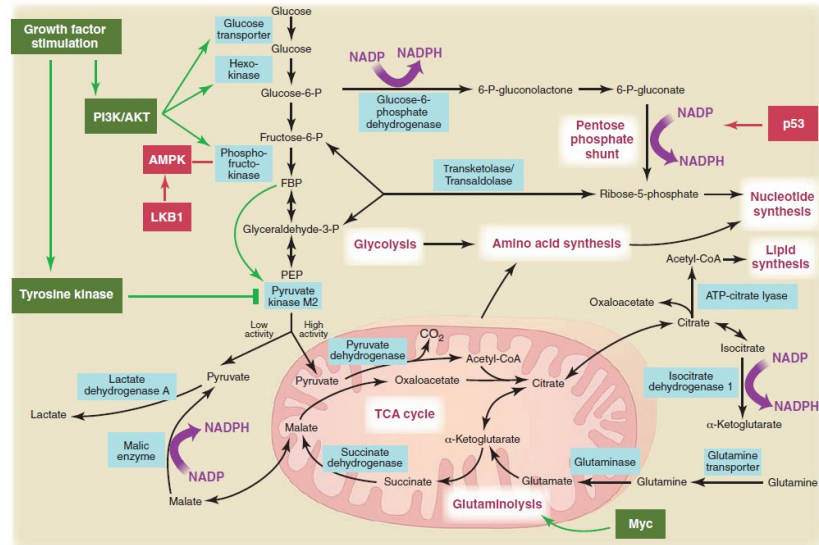


Figure 2.5: Metabolic modes of cells and their relation to growth regulation in multicellular organisms (adapted from [232]).

Within the lactic acid cycle of the liver, lactate will be converted to pyruvate and finally to glucose (therefore termed gluconeogenesis), reducing lactate levels throughout the blood. However within a limited region the use of the anaerobic metabolism is often limited by the pH-tolerance of the cells. For many tumour cell lines it is known that their ability to thrive even in very acidic environments is drastically enhanced even on the limited energy level that can be achieved by anaerobic glycolysis. This means that for these cells anaerobic glycolysis becomes vastly more attractive, as it will create an environment in which surrounding competing cells cannot proliferate or even survive, while the tumour cells themselves can

Figure 2.6: Detailed overview of the cancer metabolic pathways and key regulators from [232]. The enormous complexity of this system must be reduced in order to incorporate it in to a model.



thrive.

Tumour cells show an increased preference to perform a process similar to anaerobic glycolysis even when oxygen supply would allow the use of mitochondrial oxidative phosphorylation. This observation is commonly known as the Warburg effect or *aerobic glycolysis* (and is at the same time the loss of the Pasteur effect). A possible explanation is that the metabolism of tumour cells has been optimised to biomass production for cell replication and not for normal cell function, so that the use of glycolysis has been increased in favour of ATP production (see [232] for details). As long as nutrients are abundant, cancerous cells can afford to use an energetically “inefficient” metabolic pathway because it allows them to generate more net growth and thus have a significant proliferative advantage over benign cells (see also figure 2.5 for an overview of metabolic modes).

The key to this metabolic change seems to be HIF, which regulates the entry of pyruvate into the TCA cycle. In cancerous cells HIF is often not suppressed by oxygen and thus will increase glycolysis while preventing entry into the TCA cycle [111]. Attempts to influence this metabolic switch which is controlled by key oncogenes and tumour suppressor genes are a possible road to new cancer therapies, which could deny the tumour the chance to exhibit fast growth [134].

Furthermore an increased base level of autophagy is present in most cancer cells [117]. In this process cells will actively digest and recycle enzymes and even organelles (such as mitochondria). This effect is normally triggered only under nutrient deprivation and seems to convey further proliferative advantage to tumour cells. While autophagy and its regulation might prevent cancerous changes in benign tissue, it can have a beneficial effect on established tumour cells in buffering metabolic demands [44], [243].

The control of metabolic switches and pathways in tumours is achieved by a highly complex regulatory network as indicated in figure 2.6. In order to obtain a tractable model, a radically simplified cell metabolism, based on experimentally measured consumption rates has been assumed within this model. The measured rates will effectively contain most of the cellular metabolic phenomena discussed within this section. This simplification will be sufficient to describe both the growth dynamics of tumour spheroids and the oxygenation dynamics during therapy.

A high tolerance of the tumour cells to self-generated lactose-based acidity is assumed, so that the production of lactate will be of no further consequence within our simulation and is by default neglected. The effects of autophagy are assumed to be contained within the experimentally measured consumption rates and the observed reaction of cells to nutrient deprivation.

### Nutrient consumption

Measurements of single cell consumption rates (or rates at low cell-count) are error-prone and values found in the literature for EMT6-cells will vary more than twofold. Usually the parameters of cell consumption will not be critical, as no qualitative change is to be expected to arise from their variation. Therefore this simulation uses consumption rates which were compiled from multiple literature sources as presented in table 2.2, to obtain a reasonable consumption behaviour of the cells. If more accurate measurements become available for specific cell lines, these can be instantly absorbed into the simulation.

The ratio of glucose uptake to oxygen uptake is on average 2.6:1 for EMT6 cells, which contradicts the ratio of 1:6 which would be expected for purely aerobic cell respiration. This clearly shows that aerobic glycolysis is one of the major metabolic pathways used in EMT6 spheroids. Metabolic imaging in spheroids performed by [235] shows that the lactate concentration is already significant in smaller spheroids, while ATP production and glucose are coupled.

Freyer measured the oxygen and glucose consumption of exponentially growing EMT6 cells in bulk from the G1-phase on (see figure 5 in [70]) and found that the consumption rises linearly with the cell volume as the cells progress through the cycle. If this rise in consumption is only due to the volume increase along the cell cycle or due to a variation in the actual cell cycle phases could not be determined. Often further effects such as growth saturation due to quiescence are hidden in the measured consumption values.

While no reliable data for single cell cycle phases is available to the knowledge of the author, it would be reasonable that nutrient consumption is slightly increased during phases of high biosynthetic activity (such as during S phase) and lower during inactive phases such as quiescence. At least the variation of nutrient consumption between quiescent and active cells is of high interest for the simulation as synchronisation and activation of cells will cause a different profile of nutrient depletion, if a non-averaged consumption is implied.

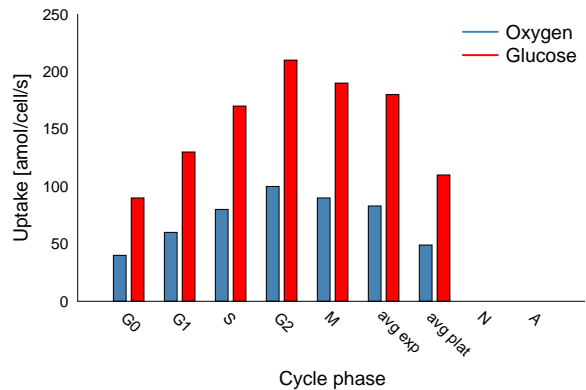
EMT6 cells in the plateau phase of growth (that is a majority of about 90% cells are quiescent) showed both smaller cell volumes and reduced rates of oxygen and glucose consumption (see table 2.2). These measurements of consumption in exponential growth phase and plateau phase allow an estimation of average uptake of active cycling cells compared to quiescent cells.

Following the available data, the consumption of cells has thus been divided into an average consumption for the active state and a quiescent state. No distinction has been made for single cycle phases, because of a lack of data and in order to avoid any unnecessary complication of the model. A twofold variation of glucose and oxygen uptake has been implemented. While this variation is higher as the ratio of consumption for exponential and plateau phase cells as measured in [70], it has to be taken into account that these measurements provide only average values for mixed populations, so that the real variation of consumption will be larger than the observed variation.

Table 2.2: Example of glucose and oxygen uptake measured for different cell lines.

Substance	Consumption [amol cell <sup>-1</sup> s <sup>-1</sup> ]	Remark
Glucose	180 ± 17	[70], EMT6/Ro spheroid (exponential)
C <sub>6</sub> H <sub>12</sub> O <sub>6</sub>	139 ± 9	[70], EMT6/Ro spheroid (plateau)
C <sub>6</sub> H <sub>12</sub> O <sub>6</sub>	153 ± 52	[241], EMT6/Ro spheroid
C <sub>6</sub> H <sub>12</sub> O <sub>6</sub>	90	[241], EMT6/Ro spheroid (r=500 μm)
C <sub>6</sub> H <sub>12</sub> O <sub>6</sub>	181 ± 36	[241], EMT6/Ro perfused
Oxygen	83 ± 5	[70], EMT6/Ro spheroid (exponential)
O <sub>2</sub>	48 ± 7	[70], EMT6/Ro spheroid (plateau)
O <sub>2</sub>	50	[68], EMT6/Ed spheroid
O <sub>2</sub>	45	[73], V79, spheroid initial phase
O <sub>2</sub>	15	[73], V79, spheroid plateau phase
O <sub>2</sub>	30	[68], V79-171b, spheroid
O <sub>2</sub>	100	[182], generic value

Figure 2.7: Consumption of oxygen and glucose for EMT6/Ro cells as listed in table 2.2 was used as a basis for the consumption in this simulation. Necrotic and apoptotic cells neither consume nor release nutrients. For reasons discussed in the text, by default only uptake of active and quiescent cells are distinguished, where either the average exponential consumption or the reduced value estimated for quiescent cells is used.



Larger reductions in specific consumptions have been confirmed in some cell lines. In [73] plateau phase cells had a fivefold lower rate of oxygen consumption than exponential cells, which was mainly attributed to the large quiescent cell population.

An average glucose consumption of 180 amol cell<sup>-1</sup> s<sup>-1</sup> glucose and 83 amol cell<sup>-1</sup> s<sup>-1</sup> oxygen is reasonable for active EMT6/Ro cells (see table 2.2). This value is obtained from exponentially growing spheroids, perfused spheroids or free cells. For spheroids in the plateau, phase consumption of glucose and oxygen is decreased to 57% and 77%. As spheroids in the plateau phase are dominated by quiescent cells [70] (but will still contain a small population of actively cycling cells), we can approximate a reduction of nutrient uptake that is associated with cell quiescence.

Necrotic or apoptotic cells will not consume nutrients. In the later case it would be also possible to model apoptotic cells as microscopic nutrient sources, as apoptotic bodies are recycled. As no quantitative data for this process is available it has been neglected.

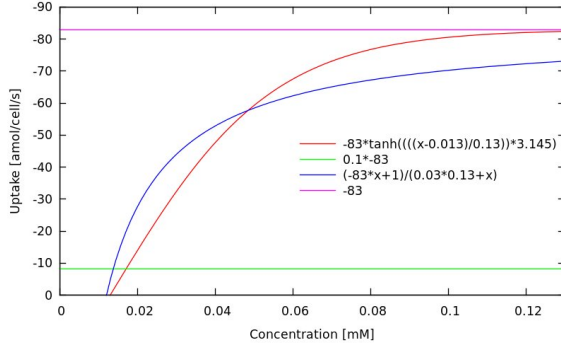


Figure 2.8: Concentration dependent uptake of oxygen using shifted  $\tanh()$  (red line) or Michaelis-Menten like kinetic (blue line). A baseline of uptake can be used (green line), if the absolute uptake rate is below a critical threshold, in order to ensure depletion of fast diffusing oxygen.

### Concentration-dependent uptake

In many biological systems, processes are concentration-dependent, such as in the typical example of enzyme kinetics. Sigmoidal functions are often used to model the functional dependencies. Other prominent examples which are employed for the description of kinetics are the Michaelis–Menten kinetics for enzymes and the Hill equation for the binding of ligands to macromolecules.

For nutrient uptake by cells, a concentration independence can generally be assumed, as the uptake is regulated by metabolic needs more than by environmental factors. However this concentration-independence of uptake rates is lost when the concentration becomes smaller than a critical value [203].

Following this logic it can be assumed that nutrient-uptake is not constant, but instead depends on the concentration of the nutrient itself. This dependency is often modelled using Michaelis-Menten kinetics, as defined by

$$Q(C(x,t)) = \frac{Q_{\max}C(x,t)}{C_h + C(x,t)}, \quad (2.3)$$

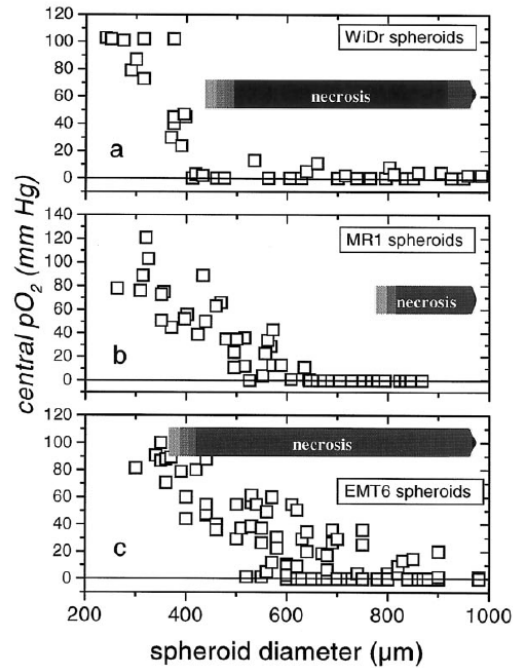
which relates uptake  $Q(C(x,t))$  and concentration  $C(x,t)$ , defined by a maximum uptake  $Q_{\max}$  and a concentration  $C_h$  at which the half maximum uptake is reached. Any other kind of function which relates uptake  $Q(C(x,t))$  and concentration  $C(x,t)$  can be used but typically it will be a sigmoidal or hyperbolic function, as the Hill-function or the tangens hyperbolicus.

In [182] a half-uptake concentration  $C_h$  of oxygen of  $8.3 \times 10^{-3} \text{ mol m}^{-3} = 0.0083 \text{ mM}$  is measured. This concentration is extremely low even for hypoxic areas, and thus suggests that concentration-dependent uptake will not be of major importance. The concentration-dependence of uptake has also been investigated in [70] with the result that, within common physiological concentrations, the uptake did not significantly depend on the concentration of the according nutrient.

Furthermore a variety of uptake kinetics has been tested for their effect on growth and treatment reactions in the model (see figure 2.8), but the effects have been found to be negligible. In order to reduce complexity and because of support for a concentration-independent nutrient uptake in the literature (see e.g. [70]), independent uptake rates have been used.

If nutrient depletion leads to cell death, the uptake rates become dependent on the concentration indirectly, corresponding to a step-function. Due to the discrete nature of the diffusion solver, another indirect dependency of uptake on concentration will develop. For very low nutrient concentrations cells will only consume the maximum available amount of

Figure 2.9: Onset of necrosis and oxygen concentration in various tumours from [157]. While in some tumour cell lines (WiDr) necrosis is observed simultaneously with anoxia, in others anoxia will develop before necrosis (MR1) or only after necrosis (EMT6). This suggests an individually different potential of tumour cell lines to cope with anoxia.



nutrient in the given time step (as otherwise small non-physical negative concentrations could develop). This corresponds to a reduction in the uptake rates at concentrations which are below a small threshold which is defined by the uptake rate and the time step of the diffusion solver.

### Nutrient deprivation and necrosis

Tumour cells show a higher tolerance to nutrient deprivation as they are adapted to hypovascular environments which provide insufficient nutrients [106]. Oxygen concentration can play a role in cell survival, even if the role is diminished by the capability of cells to deal with oxygen deprivation (see also [49]). Deprivation of oxygen will increase stress on the cells but especially tumour cells are able to withstand anoxia for prolonged periods of time. Survival of anoxic cells has been observed on a typical timescale of 1-3 days [157]. Further proof that cells can survive without oxygen but not without glucose over longer periods of time (1-2 days) can be found in [24].

Concerning the consequences of hypoxia it is concluded in [157], that hypoxia will neither necessarily induce quiescence nor cell death (see also figure 2.9). Consequently the assumption has been made in this model, that tumour cells can survive and grow even under anoxic conditions. Only complete deprivation of glucose will cause cells to starve and become necrotic.

[157] showed that quiescence is not a singular result of oxygen or other nutrient deprivation as it is already present in small spheroids. As a consequence, the main mechanism for induction of quiescence is pressure on a cell which will be discussed in section 2.1.3. If of interest, a critical oxygen or glucose concentration can deterministically lead to quiescence or increase the probability for quiescence. Both mechanisms have been implemented in the model but are by default not used in the simulation.

From a perspective of mathematical modelling, the growth data in [72] suggest that the

maximum tumour size and therefore the threshold for cell death by nutrient depletion can neither be accurately described by using glucose nor oxygen concentration alone. A possible solution is a product ansatz as derived in [194], where a critical product of glucose and oxygen concentration is evaluated to trigger necrosis:

$$C_{G1} * C_{O_2} < C_{crit} \quad (2.4)$$

However this solution suffers from a lack of biological motivation. From the metabolism previously discussed it is clear that especially tumour cells are able to survive even under anoxic conditions. While their growth rate might be slowed down due to the inefficient production of ATP and the large amount of waste produced, glycolysis can take place without the use of oxygen. Furthermore, if a critical product is used for triggering necrosis, no anoxic cells can be present in the tumour, as full oxygen depletion will immediately trigger necrosis. This limits the range in which a significant decrease in radiosensitivity through oxygen shortage can be observed in radiotherapy which might be unrealistic.

In order to allow a complete deprivation of oxygen, the trigger for necrosis can be changed to

$$C_{G1}(\alpha C_{G1} + C_{Ox}) < C_{crit} \quad (2.5)$$

using a critical concentration which is expressed as  $mMol^2$ . An alternative is the introduction of an anoxia-tolerance time, which can allow cells to remain viable under critically low oxygen conditions.

A simple biological solution is to make the necrosis depend only on a critical concentration of glucose

$$C_{G1} < C_{crit} \quad (2.6)$$

where  $C_{crit}$  is set to zero by default. This corresponds to the reasonable assumption that tumour cells can tolerate anoxic environments while being susceptible to a total deprivation of glucose. This can be modified by a starvation tolerance of cells, that is a limited period of time before cells in a glucose-free environment will become necrotic.

As we will see, the simple, biologically motivated dependence of survival on glucose concentration is sufficient to describe the tumour growth in most cases.

### Effects of hypoxia and anoxia

A lack of oxygen support will induce hypoxia in a cell which is discussed in detail in [233] and [36]. Per definition a cell is typically considered to be hypoxic if it is exposed to an oxygen concentration of  $< 2.5mmHg pO_2$ . Radioresistance effects are well-established at this level of oxygen. Depending on the linear energy transfer (LET) of the applied radiation, the critical concentration at which strong dose-reducing effects are observed decreases (see also section 2.5.1 for a detailed discussion of oxygen enhancement effects).

Apart from a direct dose-reducing effect during radiotherapy, hypoxia leads to a number of further changes in the cell. Changes in the proteome will affect cell behaviour such as to induce quiescence (arrest at the G1/S-checkpoint), lower the level of observed proliferation, increase heat-shock protein 70 which leads to damage resistance, increase the base level of

enzymes involved in damage repair. Further effects have a genetic nature, as critical oxygen concentrations can lead to higher mutation rates, selection for resistant populations, loss of Apoptosis through p53. An increased tendency for invasion has been observed in hypoxic tumours [17], [207].

Above 5%pO<sub>2</sub> no effects of a reduced oxygen concentration are observed in a cell, while below the OER raises depending on the LET of the applied radiation. Below 2.5%pO<sub>2</sub> a cell is typically considered to be clinically hypoxic, below 1% the probability of the cell to become quiescent rises significantly, at 0%pO<sub>2</sub> a cell is highly likely to go into quiescence with an increased probability for apoptosis. Some sources report a half-life of anoxic cells of 4-10 days [229].

Furthermore hypoxia will often lead to acidosis by increased anaerobic glycolysis. The production of lactic acid and the upregulation in carbonic anhydrase will lead to an acidification of the tissue and an increase in pCO<sub>2</sub>. Effectively an increase in CO<sub>2</sub>-concentration will also increase the respiratory coefficient in hypoxic tumours [233].

Hypoxic conditions will also trigger the upregulation of MMPs for breakdown of the ECM and often stimulate motility in tumour cells which is one possible explanation for the increased invasive tendencies associated with hypoxia [102].

Within the scope of this thesis, cells are considered to be hypoxic if exposed to an oxygen concentration below 10 mm Hg pO<sub>2</sub> in accordance to common literature values (see table 2.5).

### 2.1.3 Cell mechanics

#### Cell-cell interaction

Basic assumption of the model is that a free cell can be approximated as an adhesive, elastic sphere which will form contact surfaces if brought into contact with other cells. While a cell will try to assume a spherical shape to minimise the energy, adhesion between cell membranes can pull interacting cells together. A matching model for cell interaction is based on investigations on the applicability of the Johnson-Kendall-Roberts model [109] on living cells, which is a combination of the purely repulsive Hertz model [129] and an adhesive contribution. [46] showed that the cell cytoskeleton can provide an elastic structure of low deformability to which the JKR theory can be applied. Following the approach described in [193] and [113], an approximation for the JKR interaction between cells in the model is applied. This yields an interaction force  $\mathbf{F}_{ij}^{\text{JKR}}(\mathbf{x}_i, \mathbf{x}_j)$  between two cells  $i$  and  $j$  which is defined by

$$\mathbf{F}_{ij}^{\text{JKR}}(\mathbf{x}_i, \mathbf{x}_j) \approx \{E_{ij}^* \sqrt{r_{ij}^*} h_{ij}^{3/2} - \sqrt{6\pi\sigma_{ij} E_{ij}^* r_{ij}^{*3/2} h_{ij}^{3/2}}\} \hat{\mathbf{e}}_{ij} \quad (2.7)$$

is in dependence of the cell interpenetration depth  $h_{ij}$  and uses the surface energy  $\sigma$ , the effective elasticity  $E_{ij}^*$ , and the effective radius  $r_{ij}^*$

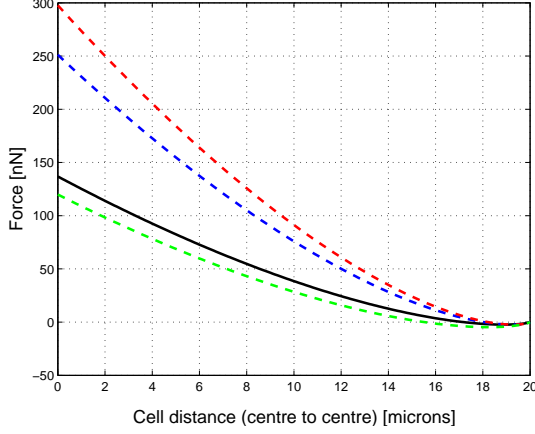


Figure 2.10: Analytical solution of the JKR force in nN for cells of  $10 \mu\text{m}$  size and the parameter set typically used within this thesis (black line,  $\nu = 0.5$ ,  $E = 1 \text{nN}/\mu\text{m}^{-2}$ ,  $\sigma = 0.1 \text{nN}/\mu\text{m}^{-1}$ ). Blue line  $\nu = 0.75$ , red  $E = 2 \text{nN}/\mu\text{m}^{-2}$ , and green  $\sigma = 0.2 \text{nN}/\mu\text{m}^{-1}$ .

$$\frac{1}{E_{ij}^*} = \frac{3}{4} \left[ \frac{1 - \nu_i^2}{E_i} + \frac{1 - \nu_j^2}{E_j} \right] \quad (2.8)$$

$$\frac{1}{r_{ij}^*} = \frac{1}{r_i} + \frac{1}{r_j} \quad (2.9)$$

$$h_{ij} = r_i + r_j - \|\mathbf{x}_j - \mathbf{x}_i\|. \quad (2.10)$$

Thus cells will be subject to an overall attractive force  $\mathbf{F}_{ij}^{\text{JKR}}(\mathbf{x}_i, \mathbf{x}_j)$  if brought into contact which will always be directed according to the plane normal of the cell-cell contact surface defined by  $\hat{\mathbf{e}}_{ij} = \frac{\mathbf{x}_j - \mathbf{x}_i}{\|\mathbf{x}_j - \mathbf{x}_i\|}$ . The JKR force becomes repulsive if a critical cell-cell distance is undercut. At an overlapping equilibrium distance, the resulting force between the cells will be zero as adhesive and repulsive contributions to equation 2.7 are equal. For large, unphysiological overlaps the JKR force is strongly repulsive and no force is defined if the distance between the cells is larger than the added radii (see also figure 2.10).

As the definition of the JKR contact surface provided in [109] cannot be transformed into a load-displacement relationship as provided in equation 2.7 without ambiguities, an approximation of the force has been used which is described in full detail in [195] and which is valid in the parameter regime under investigation.

A significant advantage of the JKR model is that interaction of cells can be based on experimentally accessible parameters. Mechanical parameters of cells have been the target of a large number of investigations using techniques such as atomic force microscopy or optical tweezers (see [248], [50], and [101]). Parameters provided by these experiments can be directly used within the JKR interaction model.

Thus cells in the simulation will be spherical if isolated, but otherwise form a three-dimensional polyhedral structure comprised of contact surfaces between neighbouring cells (see also section 2.4 for details).

Differential adhesion between cells can either be realised by using different JKR-parameters for each cell population (as for example done in the simulation of cell demixing in [113]), or by the inclusion of adhesion molecules. Assuming different concentrations of cellular adhesion molecule (CAM) receptors  $c^{\text{rec}}$  and ligands  $c^{\text{lig}}$  on the cell contact surface  $A_{ij}$ , we can use the adhesion energy per bond  $\epsilon^{\text{adh}}$  to include the CAM-adhesion:

$$F_{ij}^{\text{adh}} = A_{ij} \epsilon^{\text{adh}} \frac{1}{2} (c_i^{\text{rec}} c_j^{\text{lig}} + c_i^{\text{lig}} c_j^{\text{rec}}) \quad (2.11)$$

Adhesion molecule expression is altered by a multitude of processes, including cell irradiation. Furthermore it has been shown that the concentration of adhesion molecules will affect cell behaviour (or vice versa) including cell-cell and cell-matrix contact, invasion, angiogenesis and metastasis [10]. In cancer therapy, adhesion molecules are of interest for their possible use in targeted therapy against upregulated adhesion molecules.

Furthermore, the contact model and the use of Voronoi-surfaces allows specific modelling of features such as gap junctions between cells in a straightforward manner which can be of great interest in regards to drug and radiation resistance [164].

### Equation of motion

Cells in a tissue will usually be embedded into the extracellular matrix (ECM) using their adhesion molecules. While in an *in vitro* system such as multicellular tumour spheroids an ECM is usually not present, also cell-cell adhesion will effectively provide a medium of high viscosity for cell movement.

For determination of their movement, cells in the simulation will integrate all forces which are acting on them. This includes the JKR interaction force with each neighbour in contact  $\mathbf{F}^{\text{JKR}}$ , forces resulting from the binding of CAMs  $\mathbf{F}^{\text{CAM}}$ , active cell movement  $\mathbf{F}^{\text{act}}$  (if cells are motile) and may include further components based on cell pressure  $\mathbf{F}^{\text{pre}}$  and drag forces  $\mathbf{F}^{\text{drag}}$ .

Following [55] and [194], a velocity decay using Stokes friction is assumed for cells, which is defined by

$$v(t) = v_0 \exp \left\{ -\frac{6\pi\eta r}{m} t \right\}. \quad (2.12)$$

For a sample parametrisation of radius  $r = 5\mu\text{m}$ , initial velocity  $v_0 = 1\mu\text{m s}^{-1}$  and viscosity  $\eta = 10^{-2}\text{P}$  equation 2.12 will yield a stopping distance of only  $\frac{mv_0}{6\pi\eta r} \approx 10^{-11}\text{m} = 0.01\text{nm}$ . As the viscosity of tissue will be drastically higher than water, it is safe to assume an instant decay of velocity and thus use an over-damped approach to solve the cell's equation of motion, neglecting accelerations:

$$\ddot{\mathbf{x}}(t) \approx 0 \quad (2.13)$$

Summation of all force components, inclusion of velocity-dependent Stokes friction  $\gamma\dot{\mathbf{x}}(t)$  and application of the over-damped approach yields the cell's equation of motion

$$\dot{\mathbf{x}}_i(t) = \frac{1}{\gamma} \{ \mathbf{F}_i^{\text{act}}(t) + \sum_{j \in \mathcal{N}} \{ \mathbf{F}_{ij}^{\text{JKR}}(\mathbf{x}_i(t), \mathbf{x}_j(t)) + \mathbf{F}_{ij}^{\text{CAM}}(\mathbf{x}_i(t), \mathbf{x}_j(t)) \} \}. \quad (2.14)$$

which is integrated using a simple forward Euler algorithm. Even if this integration scheme is of first order, its use is reasonable for small simulation time steps. It is preferred to more

complex integration schemes like Runge-Kutta as no intermediate points are necessary, which would make a frequent re-computation of the triangulation necessary. If higher precision of the integrator is needed, instead of the calculation of intermediary points, the integration time step for the Euler algorithm can be diminished.

A global adaptive time step  $\Delta t_{\text{adapt}}$  following [113] is used for integration

$$\Delta t_{\text{adapt}} = \frac{\Delta x_{\text{max}}}{v_{\text{max}}} \quad (2.15)$$

which is based on the maximum cell velocity  $v_{\text{max}}$  and will ensure that no cell moves further than a defined fraction of a typical cell size  $x_{\text{max}}$  in each integration step. A local adaptive step size algorithm based on an adiabatic approach as described in [113] will be used to treat the low amount of relatively fast cells in the simulation independent of the global adaptive time step.

Explicit cell-matrix interaction is neglected as it is contained within the over-damped approach. Furthermore within an *in vitro* setting usually no extracellular matrix will be present, even if tumours can develop a filament network on their surface [190]. If cells are embedded in an agar-gel or in tissue, the effects of the environment can be indirectly included via adaptation of the friction coefficient. In specific cases the friction coefficient can be position-dependent, as is the case of glioma growth, where cells show different motility within white and grey matter [222]. Support for space-dependence of the friction coefficient has been implemented and tested, however for the case of *in vitro* spheroid growth in a nutrient solution a homogeneous friction coefficient is used by default.

### Cell size estimation

An estimation of the cell size can be produced using data from [70] and [158]. Even though the growth in the number of viable cells is slowing down over time, the diameter is increasing constantly. This is, because a large fraction of the diameter is generated by the necrotic core of the spheroid as can be seen in figure 3.4(a).

In the initial growth phase, no necrotic core is present, that is the full volume of the spheroid is taken up by viable cells. About 15000 cells aggregate to a spheroid of 400  $\mu\text{m}$  after 8 days of growth.

This will yield an average cell radius of

$$r_{\text{cell}} = \sqrt[3]{\frac{r_{\text{tumour}}^3}{N}} \quad (2.16)$$

$$= \sqrt[3]{\frac{200^3}{15000}} \quad (2.17)$$

$$= 8.11 \mu\text{m} \quad (2.18)$$

assuming that imperfect packing and overlap of spheres will cancel each other out.

Taking data from [70], a spheroid grown for 16 days will contain about 200000 viable cells in an outer shell of 250  $\mu\text{m}$  thickness while at a diameter of 1000  $\mu\text{m}$ .

Therefore the average cell radius can be estimated to be:

## 2 Model

Cell	Initial size (begin $G_1$ ) [ $\mu\text{m}$ ]	Final size (end $G_2$ ) [ $\mu\text{m}$ ]	JKR equilibrium distance [ $\mu\text{m}$ ]
EMT6	7.94	10.0	13.28
BT474	7.5	9.5	12.32
small cell	4.76	6.0	7.32
large cell	15.87	20.0	28.6

Table 2.3: Example values for cell radii and the resulting cell equilibrium distance for cells of  $G_1$ -radius in the JKR model (parameters for JKR interaction are  $\nu = 0.5$ ,  $E = 1 \text{ nN}/\mu\text{m}^{-2}$ ,  $\sigma = 0.1 \text{ nN } \mu\text{m}^{-1}$ ). Size values for cells have been compiled from [70] and [216].

$$r_{\text{cell}} = \sqrt[3]{\frac{r_{\text{tumour}}^3 - r_{\text{necro}}^3}{N}} \quad (2.19)$$

$$= \sqrt[3]{\frac{500^3 - 250^3}{200000}} \quad (2.20)$$

$$= 8.17 \mu\text{m} \quad (2.21)$$

From [70] figure 4 the average radius of the cell can be directly estimated. As it is stated that cells dissociated from the spheroid at  $150 \mu\text{m}$  spheroid diameter had a volume of approx.  $3000/10^{-9} \text{ cm}^3$  which corresponds to  $3 * 10^6 \mu\text{m}^3$  this corresponds to a radius of about  $8.9 \mu\text{m}$  (correcting the error in [70] which would lead to a radius of  $89 \mu\text{m}$ , which is obviously unphysiological). At a spheroid diameter of  $1000 \mu\text{m}$  the average cell volume decreased to  $2 * 10^6 \mu\text{m}^3$  or a radius of  $7.9 \mu\text{m}$ .

Assuming a volume doubling of the cell from the start of  $G_1$  to the end of  $G_2$  phase, this matches with the cell sizes of minimal  $7.94$  and maximal  $10.0 \mu\text{m}$ .

Nevertheless the size of cells seems to be extracted correctly, as starting from  $10$  cells a radius of about  $75 \mu\text{m}$  will be reached once the cells divided to a number of  $500$ . This corresponds to the reported diameter of  $150 \mu\text{m}$  for spheroids containing  $500$  cells in [72].

### Pressure and quiescence

Solid stress is able to halt the advancement of cells through the cycle as was shown in agar gels of different concentration by [97]. These qualitative results were refined by [43], where EMT6 spheroids have been exposed to different levels of micro-environmental mechanical stress (from  $0-60 \text{ mmHg}$  which is equivalent to  $0-8000 \text{ Pa}$  with conversion  $1 \text{ Pa (Pascal)} = 0.00750061683 \text{ Torr (mmHg)}$ ). High levels of mechanical stress lead to suppression of cell proliferation and to increased apoptosis levels. However no critical pressure threshold for the inhibition of growth of a single cell has been measured.

Therefore most computational approaches incorporate this contact inhibition by assigning a critical volume fraction  $\Delta V/V_0$  which will lead to the onset of or release from quiescence as in [76]. If  $V_0$  is always the free cell volume for a cell at the current position in the cell cycle this is largely independent of the general cell size. Another possible mechanism for quiescence triggering can be implemented by making contact inhibition dependent on the number of cell

neighbours which have established contact to the cell. If this value exerts a critical threshold, cells enter quiescence.

As an alternative, the pressure on the cell contact surfaces (spherical intersection resp. Voronoi faces) can be summed up mechanically to get the total pressure on a cell, which is defined by

$$P_i^{\text{total}} = \sum_{j \in \mathcal{N}} P_{ij} = \sum_{j \in \mathcal{N}} \frac{|\mathbf{F}_{ij} \cdot \mathbf{n}_{ij}|}{A_{ij}} \quad (2.22)$$

where  $P_{ij}$  denotes the pressure imposed on cell  $i$  by its neighbour  $j$ ,  $\mathbf{F}_{ij}$  the force between them,  $\mathbf{n}_{ij}$  the normal vector from  $i$  to  $j$  and  $A_{ij}$  the Voronoi contact surface.

Cells will thus enter quiescence once subject to a pressure above a critical threshold as was investigated in [194] and [114]. This has the advantage of being directly comparable to experimental values.

#### 2.1.4 Summary

##### Summary 1 (Cell behaviour)

- Cell agents advance through discrete cell cycle phases with normal distributed lengths corresponding to experimental measurements
- Quiescence is induced by high pressure on a cell (optionally also by locally critical nutrient levels)
- Cells become necrotic upon total deprivation of glucose
- Nutrient uptake of cells is uniform throughout the active cycle phases and decreased for quiescent cells as measured for cell populations *in vitro*
- High tolerance of cells to hypoxia/anoxia and acidity is assumed
- Cells interact with neighbours in contact using the JKR-interaction model
- Equation of motion is derived using the over-damped approach and integrated using the Euler algorithm with adaptive step size

## 2.2 Nutrients and hypoxia

### 2.2.1 Nutrient support in vivo and in vitro

As discussed within section 2.1.2, cells within a tumour depend on the supply of oxygen and nutrients in order to survive and thrive. *In vivo* this supply is delivered by adjacent blood vessels, while in an *in vitro* setting a nutrient solution will perform this task.

The lowest scale of blood flow *in vivo* is through capillaries, which are small tubes of endothelial cells about 10  $\mu\text{m}$  in diameter. A detailed investigation of the capillary network can be found in [124, 125] and later works. As general conclusion Krogh deduces, that a typical capillary density will be around 1500 capillaries per  $\text{mm}^2$ , strongly depending on the amount of nutrients consumed by the tissue (e.g. up to three times this value in muscle tissue). Nutrients enter the tissue from the capillaries via diffusion and waste products will be removed in the same way.

Since cells consume oxygen and nutrients (and proliferating tumour cells do this at an increased rate), the distance through which a metabolic active substance can diffuse through a living tissue is limited. Depending on the concentration, the efficient diffusion coefficient of the tissue and the uptake rate of the cells, a typical distance for oxygen diffusion through tissue is in the range of 100-300  $\mu\text{m}$  [233] or [153].

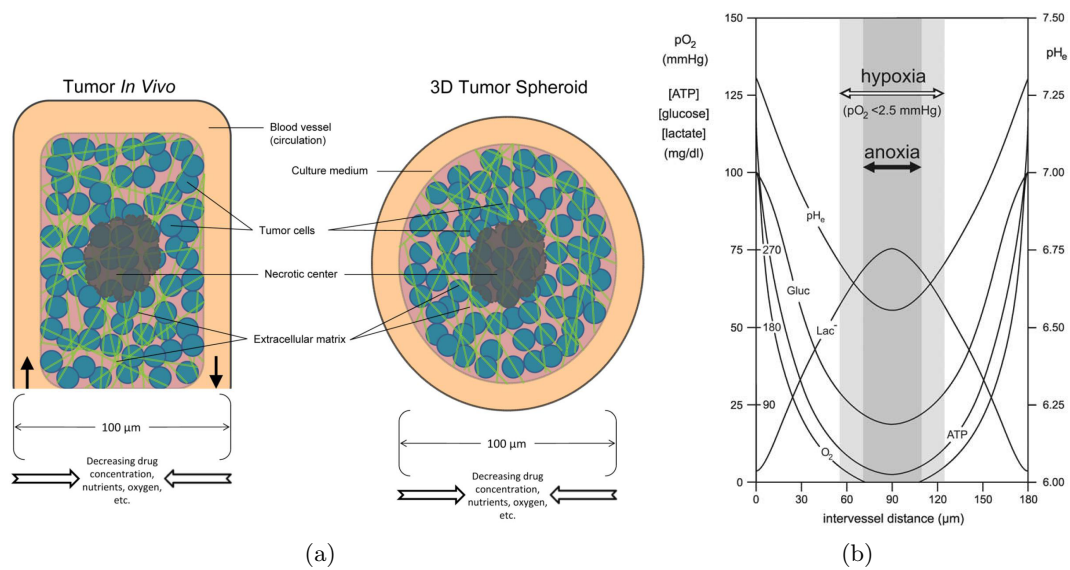


Figure 2.11: (a) Comparison of microstructure and functional regions between a microscopic tumour volume and a tumour spheroid from [168]. (b) Typical diffusion range of oxygen and glucose in breathing tissue and concentration of related substances in dependence of vessel-distance from [233].

In order for a tissue to stay supplied by nutrients this requires the maximum distance from every healthy cell to the next capillary to be below the shortest diffusion range of all required substances. EMT6 tumours have been reported to show a blood vessel density (investigated via CD31-staining) of about  $0.14 \frac{\text{vessels}}{\mu\text{m}^2}$  with a distance of hypoxic regions from the nearest blood vessel of about 100  $\mu\text{m}$  [170]. The local oxygen tension  $\text{pO}_2$  will have a classical V-shaped profile in between capillaries, with a central hypoxic or even anoxic region as shown

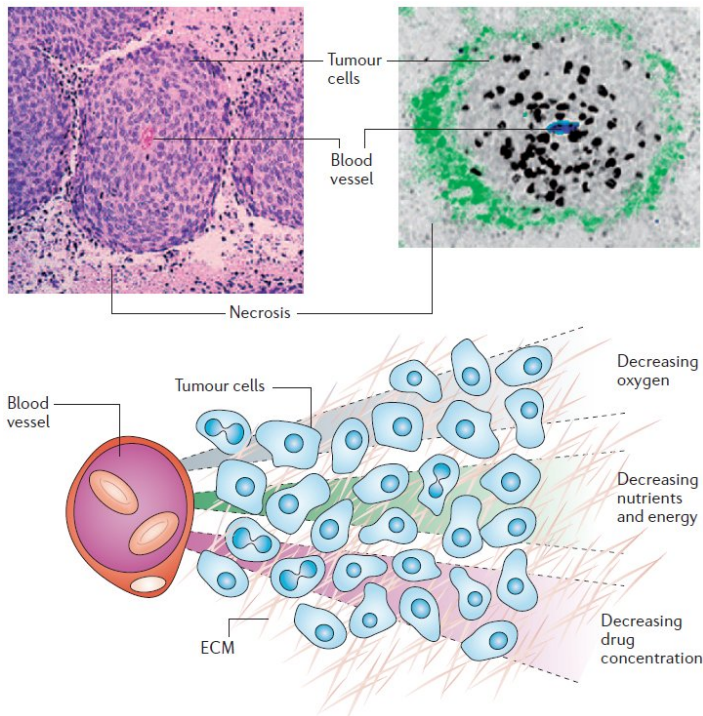


Figure 2.12: Xervix and colon cancer xenografts which show blood vessels and surrounding tumour cells. The number of proliferating cells (labelled black with bromodeoxyuridine) is higher close to the capillary. Top right picture shows hypoxic regions as green using a pimonidazole-staining and endothelial cells as blue. From [153].

by [98]. Local  $pO_2$  will also influence the metabolism as discussed in section 2.1.2 whereas a decrease in pH value is not always coupled with low oxygen concentration.

### Vascular network and angiogenesis

Fully grown, vascularised solid tumours will on average consist of about 60% tumour cells, 35% interstitium and 5% vasculature [128]. If the level of vascular support is insufficient for the local demand and a region of cells becomes hypoxic, it can try to induce new capillary growth by secreting angiogenic growth factors (e.g. FGF, VEGF). These will trigger vessel growth via the receptors present on endothelial cells. While this process is normally only required during development of an organism and later on during healing of wounds, it is of vital importance for tumour cells in order to support their pathological growth (see also [36] for this topic and [35] on possible exploitations for treatment).

The capacity of vascular growth is very high with sprouts growing up to several mm per day. Recently it has also been shown that glioblastoma can generate their own pool of endothelial cells which might serve in the formation of new blood vessels and thus facilitate blood support and metastasis [176], [237], [13].

Counteracting this efficient angiogenesis is the fact that the microvasculature in tumours is distorted and inefficient due to the unregulated nature of its growth [233],[128]. Figure 2.13 provides a direct visual comparison of healthy vasculature with the distorted tumour-vasculature of the same tissue type. Common problems include for example disturbed perfusion, lacking vascular hierarchy and arterial-venous shunts as discussed in [157].

An increased permeability of the endothelial lining of dysfunctional blood vessels will allow for an increased influx of fluids into the interstitial space. This will lead to an increase in pressure, thus inducing a high-pressure environment and limiting the influx in drug-diffusion [36]. It has been shown by [233] that interstitial tissue fluid in tumours can exhibit a pressure of up to 20mmHg which corresponds to approx. 2500Pa. A detailed examination of

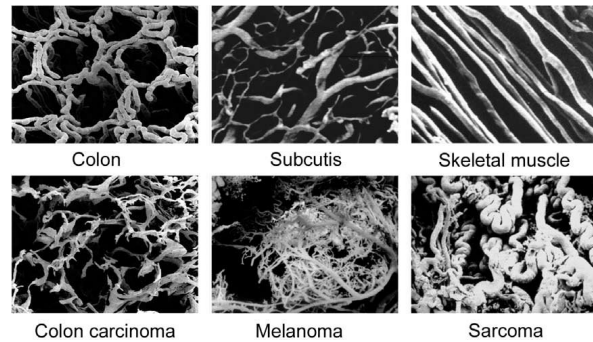


Figure 2.13: A comparison of the vasculature in benign tissues and the according cancerous tissues shows the inefficient organisation of vessels in tumours. Adapted from [233].

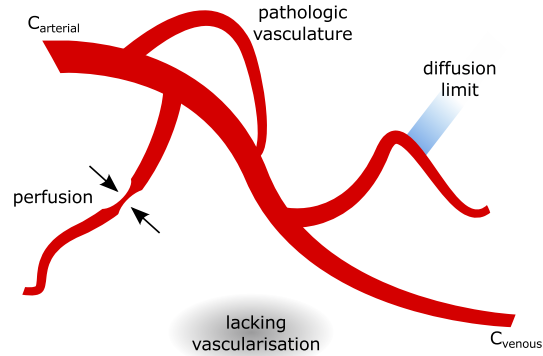


Figure 2.14: Illustration of common sources of hypoxia in tumours.

interstitial fluid pressure in tumours can be found in [137].

This high pressure inside the tumour can lead to the blocking of vessels and will thus induce transient hypoxia [84]. It can also be involved in the formation of quiescent subpopulations as discussed in section 2.1.3.

## 2.2.2 Hypoxia sources

Multiple sources of hypoxia within tumours can be identified as listed in table 2.4 and illustrated in figure 2.14.

On a global scale, a gradient of oxygen concentration from an arterial concentration  $C_{\text{arterial}}$  to a venous concentration  $C_{\text{venous}}$  can be the cause of lacking oxygen and nutrient support (see also table 2.5). The presence of large hypoxic areas will thus depend on the position of the tumour relative to major arteries. The maximum support that can be obtained in a specific part of a major tumour will thus be space-dependent and not uniform. However the spatial scale for this phenomenon is larger than the typical scale modelled within the simulation. Also, the temporal scale of changes in these macroscopic gradients will be weeks or months.

A macroscopic decrease of oxygen tension in tumours over the distance of a millimetre or more has been observed [138]. In a model this can be included on a small scale using different boundary concentrations on the faces of the diffusion solver cube (see section 2.3).

On a smaller spatial scale, local regions which are not supplied by capillaries because of lacking vascularisation will be hypoxic. Even if new vessels are formed, there is a chance that they will be in a pathological state, so the nutrient supply generated is limited. A typical timescale of days-weeks can be assumed for these processes.

Temporary occlusions of vessels, which are thought to arise and vanish “randomly” ([sic] [84]) will lead to further lack of support in small volumina (if capillaries are blocked) or

Spatial scale	Timescale	Basis	Mechanism
Micro	chronic	diffusion	limited diffusion range of substances in breathing tissue will lead to viable rims around capillaries
Macro	acute	perfusion	obstruction of capillaries through increased pressure will lead to transient hypoxia
Macro	chronic	vascularisation	insufficient and pathological vascularisation of tumour will lead to hypoxic areas
Macro	chronic	tumour site	location of tumour relative to main arteries will determine macroscopic nutrient concentration

Table 2.4: Different effects that induce and influence hypoxia and insufficient nutrient-supply in tumours.

larger areas (if arterioles are blocked) [36]. This *acute hypoxia* could also lead to macroscopic variations in oxygen concentration which are visible in PET-scans. A likely deterministic source of these obstructions is the high interstitial pressure within the tumour tissue or high pressure generated by excessive tumour growth. Thus irradiation of the tumour or other treatments which actively kill cells can induce changes in this perfusion block.

On a microscopic scale, the diffusion-limit of substances in an active tissue will be the defining feature. The diffusion range can change within minutes in response to cell killing and density changes which are a result of treatment.

Figure 2.15(b) illustrates both examples of chronic, diffusion based hypoxia and acute, perfusion based hypoxia. In the top right figure all areas which are further than a maximum distance from a capillary are identified as hypoxic using a red staining. The bottom right picture uses the labelling of blood vessels with two separate dyes (blue and green) at two time points with 20 minutes difference. Cells around the blood vessel highlighted with an arrow are marked in the first staining, but not by the second staining 20 minutes later, indicating a strong change in perfusion associated with acute hypoxia.

Measurement of hypoxia *in vitro* and *in vivo* commonly employs polarographic needles as discussed in [179] and [138] or uses advanced immunohistochemical staining methods like in [185].

### 2.2.3 Microtumour structure and self-similarity

Summing up the effects, it can be concluded that a macroscopic tumour volume in the vascularised stage will be permeated by a network of capillaries which leads to a good, but not optimal, support of the expanding tumour mass. Due to the defects in the vasculature and the inherent lack of nutrient support for the tumour growth, hypoxic and necrotic areas will form (one textbook example of this diffusion limitation *in vivo* is the growth of tumour cords in bronchial carcinoma).

A large tumour will thus be comprised of many subvolumes within the capillary network with each composed of viable, hypoxic and necrotic cells with rising distance from the nearest capillary as illustrated in figure 2.17. This microstructure should be a universal feature of every solid tumour and is of great interest for modelling.

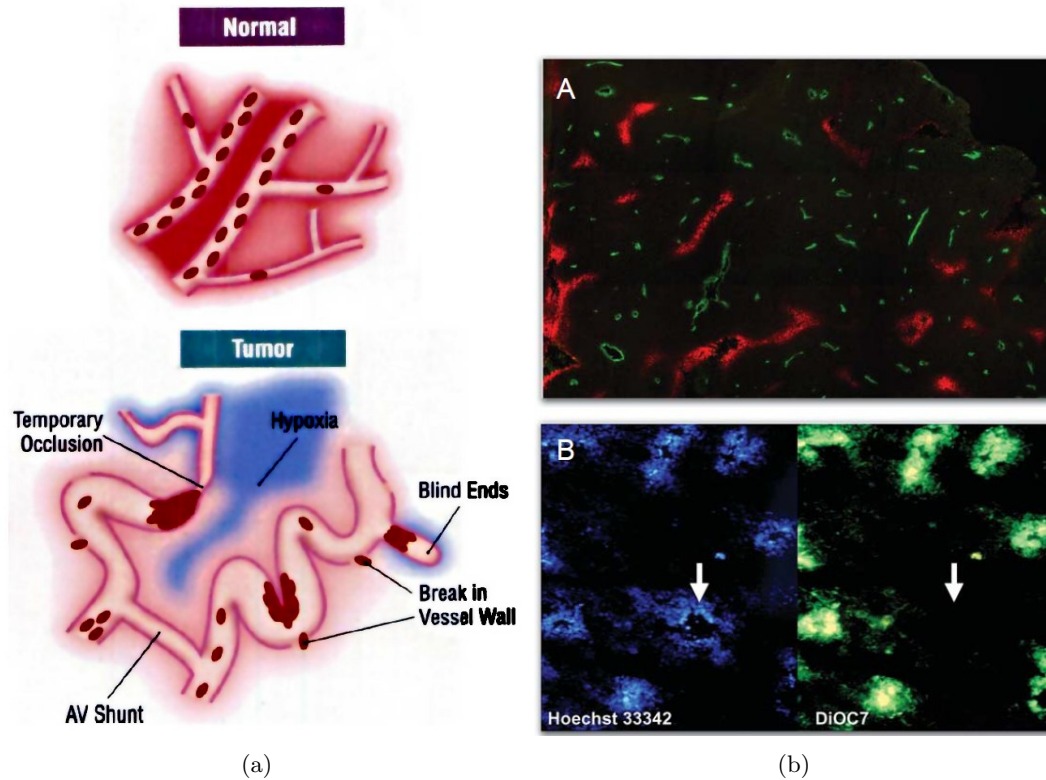


Figure 2.15: (a) Features of pathogenic nutrient support in tumour vasculature from [36]. (b) Visualisation of chronic hypoxia (top, vessels in green, hypoxic tumour cells in red) and acute hypoxia (bottom, blue and green visualise cells near vessel with a time separation of 20min) from [35].

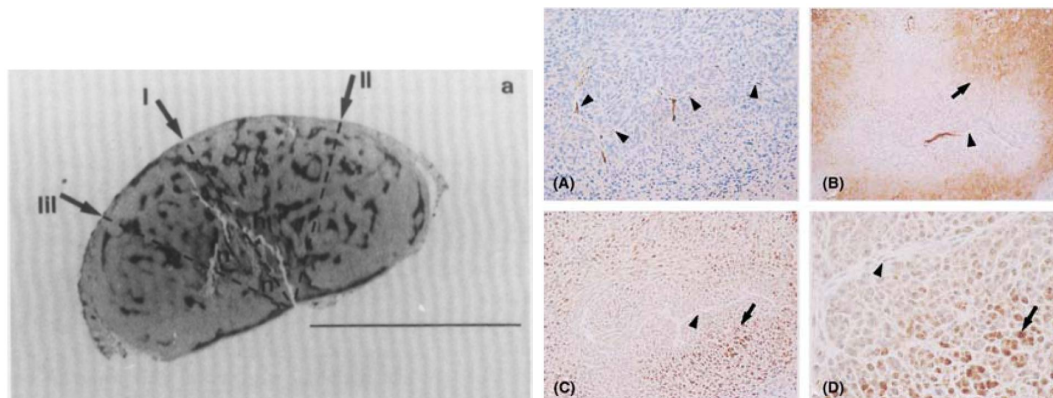


Figure 2.16: (left panel) Staining of hypoxia in a melanoma xenograft tumour. The regular structure of hypoxic regions is immediately visible. N indicates necrosis. Dotted lines visualise path of polarographic needles used for oxygen-tension measurements. From [138]. (right panel) Hypoxic regions near a capillary in a glioma (LN229) from [112]. (a) Factor VIII antigen staining of vessel (arrowhead in subfigures). (b) Pimonidazole-staining highlights hypoxic areas which are in 10-15 cell layers distance from the vessel. (c-d) Hif1 $\alpha$  nuclear staining and magnification.

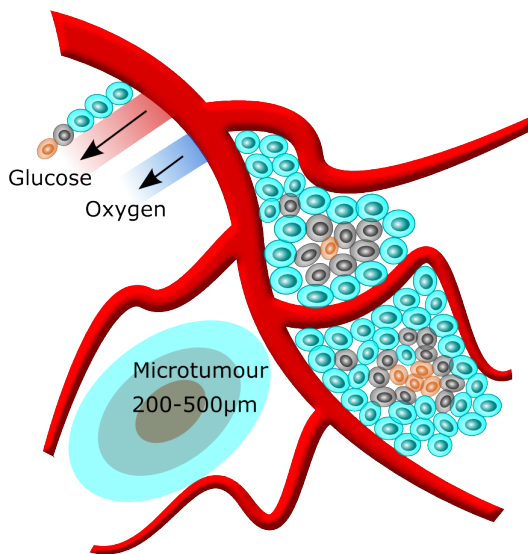


Figure 2.17: Nutrient support of tissue is provided by capillaries. In breathing tissue glucose and oxygen will have a limited diffusion range into tissue (DR). Within a healthy tissue the typical inter capillary distance (ICD) will be lower than the diffusion range of these substances. For malignant tissue growth this is no longer true, as the tissue will expand with only limited blood vessel formation. A microtumour can expand until its growth is slowed by the lack of nutrients and the onset of necrosis in its centre. Either local reseeding or vascularisation of the tumour will lead to a macroscopic tumour which will be comprised of countless microtumour regions.

Only necrotic parts (which are inactive) can exist beyond the reach of nutrient supply. Thus the viable, active responsive parts must be allocated within a region of 100-300  $\mu\text{m}$  close to the capillaries. However all of these active areas which make up the macroscopic system of a tumour over multiple centimetres are also present within the microscopic system of a tumour spheroid.

Thus if the microtumour is modelled in full detail, the observed response to treatment should be transferable to a macroscopic tumour volume, provided that no macroscopic mechanisms interfere with the outcome.

For the case of hypoxia this can be understood in the following way: One major factor determining the reoxygenation of a tumour after irradiation is the increased diffusion range of nutrients due to tissue damage and reduced nutrient uptake by dead cells. As this is diffusion-driven in the limit of a breathing tissue it is clearly a microscopic process, so it must be modelled on a microscopic scale. As this process takes place in every subvolume of the tumour, so the predicted response to irradiation is also applicable to a macroscopic system. In the case of reoxygenation it is known that there are also macroscopic factors influencing the oxygen concentration, such as the transient occlusion of vessels or the tumour position relative to the major arteries. Some of these macroscopic factors can be traced back to microscopic sources again, as is the case of vessel occlusion, which as pressure related phenomenon is connected to the microscopic pressure release due to dead cells. Others might be beyond the scope of a microscopic analysis, as for example the macroscopic position of the tumour relative to major arteries.

As long as it is clear which phenomena can be directly transferred from a microscopic to macroscopic level (e.g. the diffusion-limit), which phenomena can be indirectly inferred (e.g. vessel freeing due to pressure release) and which cannot be taken into account (macroscopic position), predictions can be transferred from the microsystem to the larger system of a real tumour.

Stained cutsections from various tumours from [170] which are shown in figure 2.18 confirm the macroscopic composition of tumours out of repeating microscopic regions.

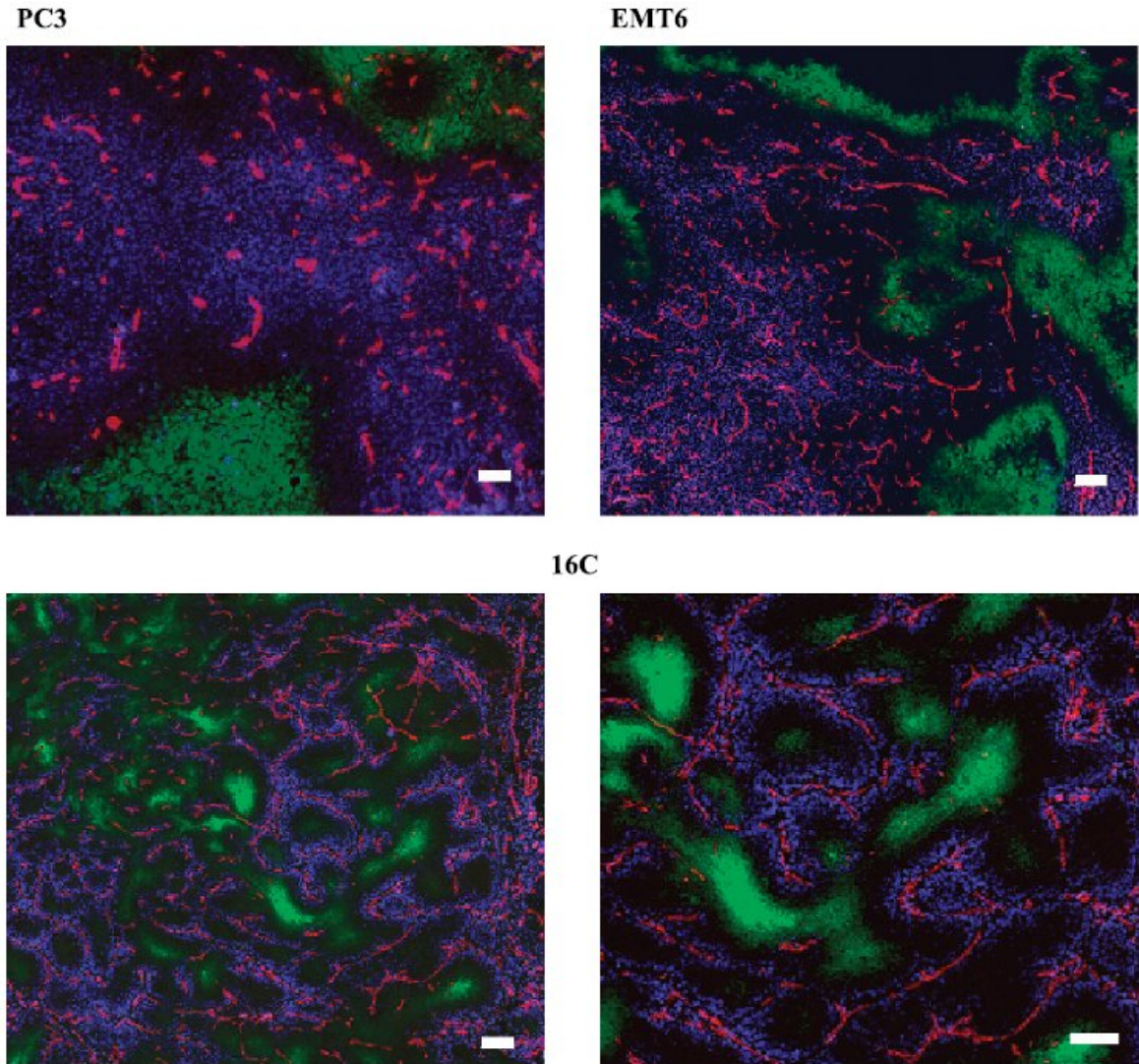


Figure 2.18: Cutsections from PC-3, EMT6 and 16C tumours with staining for blood vessels (red), hypoxia (green) and doxorubicin distribution (blue) illustrate the self-repeating composition of macroscopic tumours. Scale bar is 100  $\mu\text{m}$ . From [170].

### 2.2.4 Nutrient concentrations in blood and tissue

In order to simulate the tumour microbehaviour inside our system, the nutrient concentration has to be adapted to the typical concentration found in human capillary blood or in the according *in vitro* experiment. Solubility of substances will also be of importance when the transport of drugs in cancer therapy is to be modelled [132].

Within the simulation, consumption of cells will be measured in  $\text{amol/s}$  and the concentration of substances on the diffusion grid will be given in  $\text{mM}$ .

#### Oxygen concentration

Oxygen solubility in water or blood depends strongly on factors such as temperature, pH and pressure [39]. Normally, a large fraction of oxygen molecules in the blood is bound to hemoglobin which drastically increases the carrying capacity of blood [202]. However a small

fraction will be dissolved in plasma or, in an *in vitro* setting, within a nutrient solution.

Generally the amount of gas that is dissolved in a liquid is predicted well by Henry's law

$$c = \frac{p}{k_H} \quad (2.23)$$

where  $p$  is the according partial pressure of the gas,  $k_H$  the solubility and  $c$  the concentration. As the solubility is subject to great variations, often the partial pressure  $p$  of the gaseous solute is used directly instead of the actually solved concentration  $c$  [80].

For an *in vitro* nutrient solution, [72] measured the amount of solved oxygen at 37°C and obtained 0.28 mM when equilibrated with 20% pO<sub>2</sub> and 0.07 mM when the gas phase was 5% oxygen (according to the method of Robinson and Cooper [179]).

The local concentration of oxygen within a tissue is determined by a multitude of factors. A general idea of the oxygen concentration can be obtained by the oxygen cascade, which describes the transfer of oxygen from inhaled air to blood.

At atmospheric pressure of 760 mmHg, oxygen will have a partial pressure in accordance to its amount within normal air of 21%. This yields a normal partial pressure of  $760 \cdot 0.21 = 159$  mmHg. Due to the humidification of air during ingestion, this partial pressure will decrease by the saturated vapour pressure of 47 mmHg to  $(760 - 47) \cdot 0.21 = 149$  mmHg. Finally due to different mechanisms, the partial pressure of oxygen will be decreased by the concentration of oxygen in outflowing blood (about 40 mmHg) and the respiratory quotient (about 0.8) to  $149 - (40/0.8) = 100$  mmHg. This value can act as a general idea of the pO<sub>2</sub> in systemic capillary blood. For the solved oxygen concentration, this estimation leads to about 100 mmHg or 0.137 mM of solved O<sub>2</sub> in capillary blood.

This value will of course decrease towards the venous end of capillaries, as nutrients and oxygen have been exchanged with the supported tissue and consumed by cells. Within tissue this concentration will drop to an average value of 40 mmHg or 5.5% pO<sub>2</sub> while in tumour tissue the average concentration is even lower with an average of 7 mmHg or 1% pO<sub>2</sub>. Also the temporal variations in oxygen concentration within tissue can be quite pronounced: variations from 2 to 16 mmHg in less than 1 hour have been observed in 9L-xenografts in rats [38].

An overview of typical values of oxygen concentration in benign and cancerous tissues can be found in [7].

Thus a tissue like oxygen concentration in the spheroid can be obtained by setting the partial oxygen pressure of the surrounding medium to 95 mmHg which corresponds to  $(95/159) \cdot 0.2188$  mM = 0.1313 mM solved oxygen molecules. For *in vitro* settings such as in [73], the according concentration needs to be calculated if not provided directly.

### Glucose concentration

The glucose level in human blood is regulated by homeostatic mechanisms to be about 5 mM or 100 mg/dL. Typical natural variations are in the range of 3.6 and 5.8 mM (64.8 and 104.4 mg/dL), while the maximum postprandial in nondiabetic persons should be less than 10 mM or 180 mg/dL. <sup>1</sup>

As the molecular weight of glucose C<sub>6</sub>H<sub>12</sub>O<sub>6</sub> is about 180 g/mol, a conversion between the common measurement of mg/dL and mmol/l can be achieved simply with a factor of 18.

<sup>1</sup>source is <http://www.nlm.nih.gov/medlineplus/ency/article/003438.htm>

Oxygen [%]	[mm Hg]	Solved O <sub>2</sub> [mmol/l]	Remark
21	159	0.28±0.012	normal air, 37°C, culture medium [73]
21	159	0.2188	normal air, 35°C, clear H <sub>2</sub> O
21	159	0.176	normal air, 35°C, sea H <sub>2</sub> O
13	100	0.137	arterial blood [53]
5.3	40	0.055	venous blood [53]
5	38	0.07	culture medium [73]
4	30	0.0412	avg. normal tissue [98]
2	15	0.0206	early tumour [98]
1.3	10	0.0135	hypoxia threshold [91]
0.5	3.8	0.0052	half-life of OER effect [86]

Table 2.5: Overview of typical oxygen pressures and solved oxygen in water.

In most *in vitro* experiments of tumour growth, well defined glucose concentrations are used within the nutrient solution. However they sometimes extend into the non-physiological regime such as in [73], where a glucose concentration of 16.5 mM is used in the solution.

### 2.2.5 Summary

#### Summary 2 (*Nutrient support and hypoxia*)

- *Tumours suffer from a lack of nutrient support as their growth exceeds the capacity of the local supply*
- *Hypoxic cells can stimulate the formation of new blood vessels in order to increase tumour support*
- *Vasculature inside the tumour is disturbed both temporarily (perfusion) and permanently (pathological state)*
- *Overall, a tumour will consist of small, diffusion-limited microregions which together form a repeating macroscopic structure*
- *Tumour spheroids will show the same concentration gradients of nutrients which can be found *in vivo**
- *Four hypoxia types could be distinguished which vary on a spatial and temporal scale*
- *Supporting capillary blood will on average carry about 0.137 mM pO<sub>2</sub> and 5 mM glucose*

## 2.3 Diffusion solver

Diffusion is a process of paramount importance in biological systems. The passive distribution of nutrients on a small scale is just one example of the vital importance of this process. Diffusion is also of great interest for the use in mathematical biology in an abstract way, describing the spread of population or diseases. Accordingly the solution of the diffusion equation is one of the standard problems approached by computational biologists.

Even if the solution of diffusion problems can be considered a standard-problem, it must be noted that most available implementations resort to the solution of the simplest possible problem. Such a diffusion solver will typically handle only cubic geometries while assuming a constant diffusion coefficient and will not allow for the inclusion of diffusion obstacles or unusual boundary shapes. However these requirements can be of great importance for diffusion in biologically relevant systems.

Within this investigation, a diffusion solver was developed based on the algorithms in [169] and implementations in [194] and [21]. The solver is able to incorporate a wide range of biological phenomena which are of importance for tumour growth, as will be discussed in the following sections.

### 2.3.1 Diffusion equation

The basis of our investigation is the normal one dimensional diffusion equation, which relates a temporal concentration change to a spatial concentration change:

$$\frac{\partial C(x, t)}{\partial t} = \frac{\partial DC(x, t)}{\partial x^2} \quad (2.24)$$

An all too common assumption is a constant diffusion coefficient  $D$  within the whole system, which allows the simplification of equation 2.24 by removing  $D$  from the differentiation:

$$\frac{\partial C(x, t)}{\partial t} = D \frac{\partial^2 C(x, t)}{\partial x^2}. \quad (2.25)$$

However, within biological systems, the assumption of a constant diffusion coefficient is rarely justified. In fact a spatial and temporal variability of  $D$  should be assumed, which prevents the simplifying step that led to 2.25. Assuming a spatial and temporal variable diffusion coefficient will yield a slightly more involved version of 2.24:

$$\frac{\partial C(x, t)}{\partial t} = \frac{\partial}{\partial x} \left( D(x, t) \frac{\partial C(x, t)}{\partial x} \right) \quad (2.26)$$

Another common observation in biological systems is the localised production or consumption of the diffusing substance. This can be included via a reaction rate  $Q(x, t)$ , which will again have a spatial and temporal dependency in biological systems. Inclusion of this additive term is straightforward and will yield the complete diffusion equation:

$$\frac{\partial C(x,t)}{\partial t} = \frac{\partial}{\partial x} \left( D(x,t) \frac{\partial C(x,t)}{\partial x} \right) + Q(x,t) \quad (2.27)$$

For the steady-state case defined by

$$\frac{\partial C(x,t)}{\partial t} = \frac{\partial}{\partial x} \left( D(x,t) \frac{\partial C(x,t)}{\partial x} \right) + Q(x,t) \approx 0 \quad (2.28)$$

a simple Poisson problem is obtained

$$\frac{\partial}{\partial x} \left( D(x) \frac{\partial C(x)}{\partial x} \right) = -Q(x). \quad (2.29)$$

Both types of equations can be efficiently solved by methods discussed in the following section.

### 2.3.2 Solution schemes and steady-state approximation

After temporal

$$\frac{\partial C_I}{\partial t} \rightarrow \frac{C_I^{n+1} - C_I^n}{\Delta t} \quad (2.30)$$

and spatial discretisation

$$\begin{aligned} \frac{\partial^2 C_{i,j,k}}{\partial x^2} &= + \frac{(D_{i+1,j,k} - D_{i-1,j,k})(C_{i+1,j,k} - C_{i-1,j,k})}{4\Delta x^2} + D_{i,j,k} \frac{C_{i+1,j,k} - 2C_{i,j,k} + C_{i-1,j,k}}{\Delta x^2} \\ &+ \frac{(D_{i,j+1,k} - D_{i,j-1,k})(C_{i,j+1,k} - C_{i,j-1,k})}{4\Delta y^2} + D_{i,j,k} \frac{C_{i,j+1,k} - 2C_{i,j,k} + C_{i,j-1,k}}{\Delta y^2} \\ &+ \frac{(D_{i,j,k+1} - D_{i,j,k-1})(C_{i,j,k+1} - C_{i,j,k-1})}{4\Delta z^2} + D_{i,j,k} \frac{C_{i,j,k+1} - 2C_{i,j,k} + C_{i,j,k-1}}{\Delta z^2} \\ &+ Q_{i,j,k} \end{aligned} \quad (2.31)$$

into a finite difference form, equations 2.27 and 2.29 can be simplified using the linear operator  $\mathcal{L}$  which thus contains the information on geometry and diffusion properties of the system

$$\frac{C_I^{n+1} - C_I^n}{\Delta t} = \mathcal{L}C_I + Q_I(t) \quad (2.32)$$

$$\mathcal{L}C_I = -Q_I. \quad (2.33)$$

Following the classical solution schemes and algorithms described in [169], which have been implemented in [194] and [114], different solvers for the three-dimensional version of equation 2.27 and its steady-state form 2.29 have been developed and used within the simulation.

As the most basic finite difference method, the FTCS scheme (Forward-Time Central-Space) was used for debugging within the limits of its stability condition [169]. It is simply obtained by reordering and solution of equation 2.32 to:

$$C_I^{n+1} = \{1 + \Delta t \mathcal{L}^n\} C_I^n + \Delta t Q_I^n. \quad (2.34)$$

Using the implicit Euler method (BTCS) defined by

$$\{1 - \Delta t \mathcal{L}^{n+1}\} C_I^{n+1} = C_I^n + \Delta t Q_I^{n+1}, \quad (2.35)$$

an average over both methods can be performed to obtain the Crank–Nicolson method [54], which is an unconditionally stable scheme (in the free diffusion case) and defined by

$$\left\{1 - \frac{\Delta t}{2} \mathcal{L}^{n+1}\right\} u_I^{n+1} = \left\{1 + \frac{\Delta t}{2} \mathcal{L}^n\right\} u_I^n + \frac{\Delta t}{2} (Q_I^n + Q_I^{n+1}). \quad (2.36)$$

A faster solution of the full diffusion system in three dimensions can be achieved by operator splitting methods, which follow a general scheme

$$\mathcal{L} = \mathcal{L}_x + \mathcal{L}_y + \mathcal{L}_z. \quad (2.37)$$

As the most prominent operator splitting scheme, the alternating direction implicit method (ADI) of Douglas and Gunn was implemented [61]. Within each temporal substep of the splitting method, a single dimension is treated implicitly, whereas the other dimensions are treated explicitly, as illustrated in the example from [169]:

$$\begin{aligned} \left\{1 - \frac{\Delta t}{3} \mathcal{L}_x^{n+1/3}\right\} u_{i,j,k}^{n+1/3} &= \left\{1 + \frac{\Delta t}{3} \mathcal{L}_y^n + \frac{\Delta t}{3} \mathcal{L}_z^n\right\} u_{i,j,k}^n, \\ \left\{1 - \frac{\Delta t}{3} \mathcal{L}_y^{n+2/3}\right\} u_{i,j,k}^{n+2/3} &= \left\{1 + \frac{\Delta t}{3} \mathcal{L}_x^{n+1/3} + \frac{\Delta t}{3} \mathcal{L}_z^{n+1/3}\right\} u_{i,j,k}^{n+1/3}, \\ \left\{1 - \frac{\Delta t}{3} \mathcal{L}_z^{n+1}\right\} u_{i,j,k}^{n+3/3} &= \left\{1 + \frac{\Delta t}{3} \mathcal{L}_x^{n+2/3} + \frac{\Delta t}{3} \mathcal{L}_y^{n+2/3}\right\} u_{i,j,k}^{n+2/3} \end{aligned} \quad (2.38)$$

While in two dimensions the method preserves unconditional stability, in three dimensions the updating scheme will be conditionally stable if

$$D\Delta t / \Delta x^2 \geq 1/2 \quad (2.39)$$

depending on the step size in time  $\Delta t$  and space  $\Delta x$ .

The diffusion of glucose and oxygen is orders of magnitude faster than other processes in the tumour system, namely typical random cell motilities and expansion of the tumour mass as result of proliferation. For the slowest diffusing substance of glucose in dense tissue with a diffusion coefficient of  $D = 105 \mu\text{m}^2/\text{s}$  and an update time step of  $\Delta t = 600 \text{ s}$ , the associated diffusion length is defined by

$$L = \sqrt{6D\Delta t} \quad (2.40)$$

## 2 Model

and will be approximately 600  $\mu\text{m}$ , which is more than the largest spheroid radius modelled within the simulation.

Consequently, the concentration of nutrients was by default updated in time steps of  $\Delta t = 600\text{ s}$  in a pseudo-steady-state approximation [239, 194]. The corresponding steady-state equation 2.29 was solved using the iterative biconjugate gradient method provided in routine `linbcg` in [169].

As cells are freely positioned in a lattice-free Delaunay-triangulation, a standard tri-linear interpolation is used to obtain local concentrations at cell positions and to distribute reaction rates onto the discrete diffusion nodes.

To ensure stability and numerical accuracy of the employed solvers, a number of test problems have been solved and compared to their analytical solution if available. Figure 2.19 shows the result of a diffusion test-problem, in which a point-source is located in the middle of two half-spaces, which show a different diffusion coefficient. For this problem a full comparison to an analytical solution is possible [193].

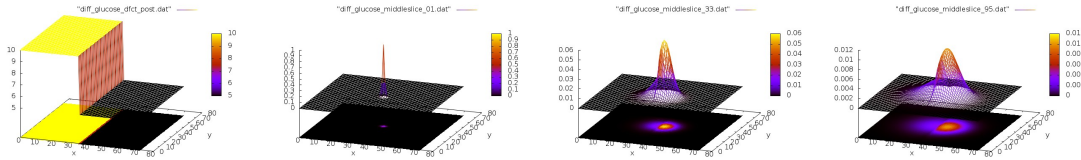


Figure 2.19: Solution for the time evolution of a point source when the diffusion constant differs in between the two half-spaces as indicated in the leftmost panel.

For a simplified system of variable diffusion coefficients and local rates defined by

$$D(z) = D_0 + \alpha z^2 \quad (2.41)$$

$$Q(z) = Q_0 + Q_0 3 \frac{\alpha}{D_0} z^2 \quad (2.42)$$

an analytical solution can be derived following [193], which is given by

$$C(z) = C_0 - \frac{Q_0}{2D_0} z^2 + \frac{C_L - C_0 + \frac{Q_0}{2D_0} L_z^2}{\arctan\left(\sqrt{\frac{\alpha}{D_0}} L_z\right)} \arctan\left(\sqrt{\frac{\alpha}{D_0}} z\right), \quad (2.43)$$

or in a simplified form for vanishing rates  $Q(x) = 0$ :

$$C(z) = C_0 - + \frac{C_L - C_0}{\arctan\left(\sqrt{\frac{\alpha}{D_0}} L_z\right)} \arctan\left(\sqrt{\frac{\alpha}{D_0}} z\right). \quad (2.44)$$

Figure 2.20 illustrates the development of the concentration and its correspondence to the analytical solution of the problem for zero rates (variable diffusion coefficient problem only). A perfect agreement between the analytical solution of the problem and numerical solution is found within reasonable accuracy limits.

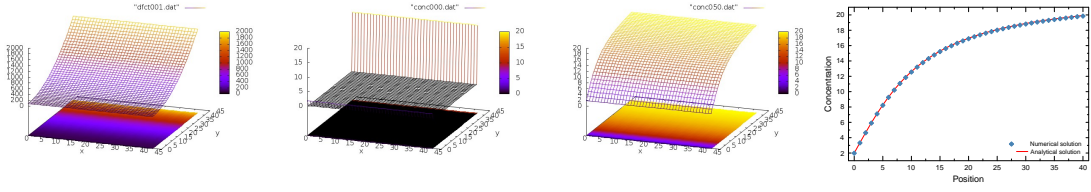


Figure 2.20: Varying diffusion coefficient combined with mixed boundary conditions will lead to a stable solution that can be obtained analytically for comparison. Left to right: diffusion coefficient, initial concentration, steady concentration after evolution, comparison of numerical and analytical solution.

A range of further tests was performed to ensure the stability and accuracy of the solution solvers (see appendix section 4.7 on page 208).

### 2.3.3 Cell density estimation for variable diffusion coefficient

The diffusion coefficient within the system is space-dependent and will vary linearly between the experimentally obtained diffusion coefficients of the substances in water  $D_{\text{water}}$  and tissue  $D_{\text{tissue}}$ :

$$D(x, t) = D_{\text{tissue}} + (D_{\text{water}} - D_{\text{tissue}}) \frac{\varrho(x, t)}{d_{\text{max}}} \quad (2.45)$$

In order to vary the diffusion coefficient between its extremal values, the maximum density of cells which corresponds to a dense packing in a tissue  $d_{\text{max}}$  has to be provided. A naive estimation of a maximum object density can be obtained by

$$d_{\text{max}} = V_{\text{vol}}/V_{\text{cell}} \quad (2.46)$$

where  $V_{\text{vol}}$  is the volume of a diffusion node and  $V_{\text{cell}}$  the volume of a cell.

This estimation will however only be of limited use, as two counteracting effects are important for the packing of cells. The first effect is that the packing of spheres in a volume will be imperfect. Thus a lower maximum density of cells per volume is obtained. This has to be taken into account via a correction factor  $p > 1$ , which will effectively increase the cell volume and thus reduce the maximum density. Irregular packing of spheres will typically not exceed a density of about 64% even under pressure [209] so we can estimate  $p$  to be approximately 2 for a non-pressurised packing.

If the objects under consideration are spherical, a second effect will be the intersection volume, which cells will be sharing. Using the JKR-interaction model, a large part of the cell volume will be filled up virtually by overlap with other cells. Of course in nature no actual overlap or intersection will be observed, but there will be a contact surface formed. However, when estimating the density in a numerical system, the overlap will be of importance. The volume defect due to intersection  $i$  of a cell of volume  $V_{\text{cell}}$  can be estimated by

$$i = \frac{V_{\text{cell}} - \sum_{NN} V_i}{V_{\text{cell}}} \quad (2.47)$$

## 2 Model

where  $V_i$  is the intersection volume with a neighbour. This estimation neglects overlaps of the intersection volume of different neighbours within a single cell, which is valid as long as the radii are much larger than the interpenetration depths. For densely packed cells and JKR interaction  $i$  will be as low as 0.15.

In order to get a suitable estimation of the maximum cell density, we can employ both corrections to the simple estimate

$$d_{\text{cor}} = V_{\text{vol}}/V_{\text{cell}} \cdot p \cdot i \quad (2.48)$$

For a value of  $p \cdot i = 0.5$  the predictions of the cell density correspond well with the measured cell density in the simulation. An example of the density-dependent diffusion coefficient for a test tumour is provided in figure 2.22(b).

### 2.3.4 Moving boundary effects on tumour growth

Within the typical scenario for spheroid growth, a compact mass of cells is freely floating in a nutrient solution. If the consumption of the spheroid is negligible when compared to the total amount of substance in the reservoir, the concentration of nutrients outside the spheroid will be constant. Within the nutrient solution that surrounds the spheroid, substances will not be limited to transport via diffusion but convection takes place and is probably the dominating effect (apart from macroscopic stirring of the nutrient solution).

Therefore it is reasonable to assume that the concentration outside the cell mass should be kept constant at all times. This of course implies that in an according experiment, the nutrient solution is exchanged within reasonable intervals, as is the case for all non-starvation experiments. If no exchange is performed, the concentration of nutrients will globally decrease over time.

In any case, the concentration on diffusion nodes outside the spheroid which do not contain any cells within their sub-volume should be kept constant. If the information about the cell distribution is available, as in the density-dependent diffusion coefficient approach, a simple solution to the problem is to update the position of the system boundary depending on the position of cells in the system. If a diffusion node is not marked as containing cells, it will be treated as belonging to the boundary. As the solution becomes trivial within the boundary region, this can also speed up the computation by a factor equal to the ratio of the volume which contains cells (roughly spherical) to the total diffusion volume (usually cubic).

It is important to take the stirring of the medium and the according moving boundary region into account, as otherwise the tumour will only receive a sub-boundary concentration of substances within the simulation as substances first need to diffuse from the system boundary to the tumour through the assumed “unstirred” culture medium.

### Moving boundary and hollow simulation objects

If an updated moving boundary is employed as described previously, then this can result in problems if hollow objects are contained within the diffusion volume. In the case of a tumour spheroid, a central necrosis will lead to a hollow spheroid of cells, whose central volume is just filled by necrotic debris of cells. Thus the effective cell density in the centre is zero, so the diffusion coefficient can be as high as in water. However this would cause the function which

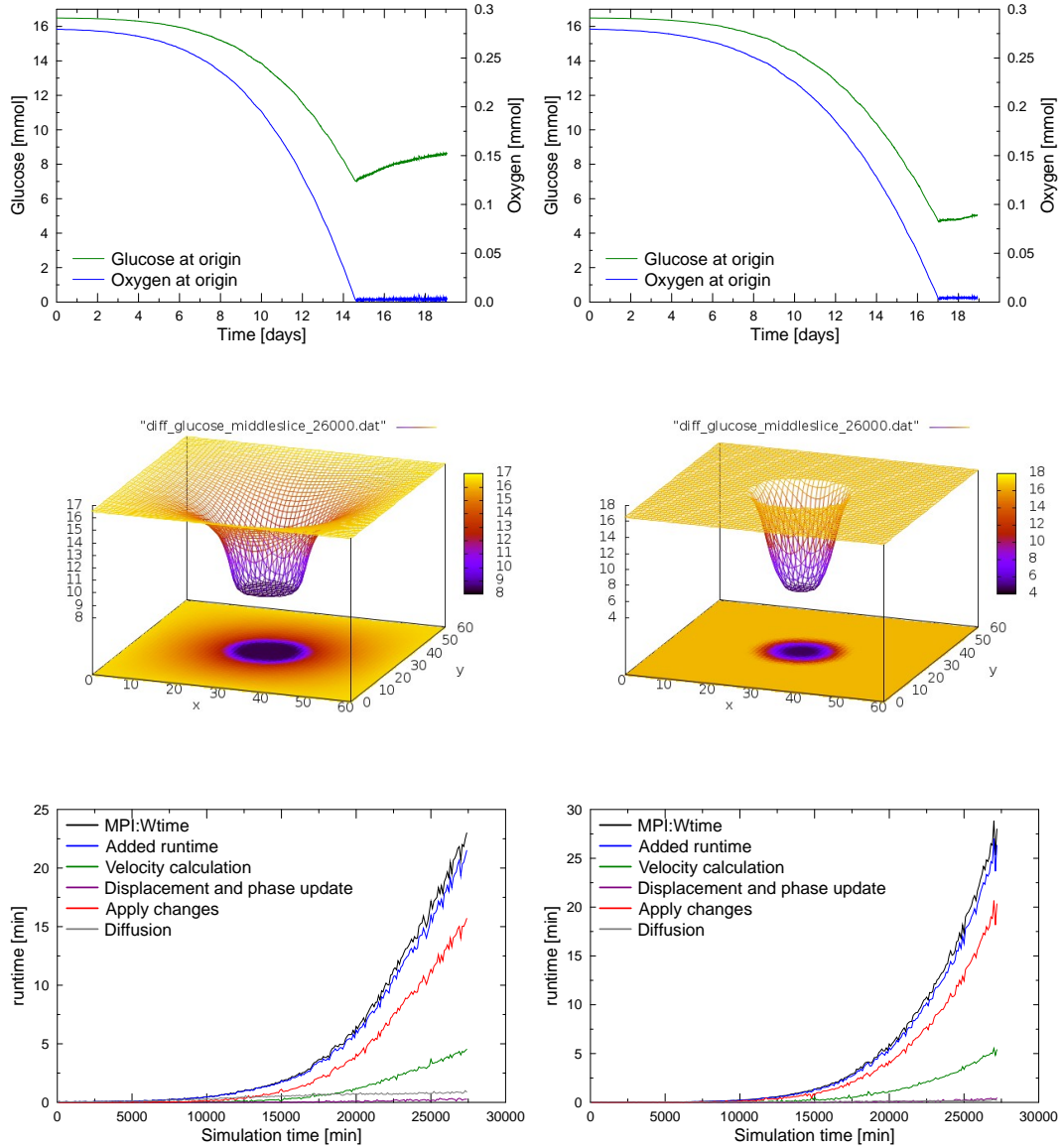


Figure 2.21: Example of glucose and oxygen diffusion in a test tumour system which contains a growing central tumour spheroid. Concentration of glucose and oxygen will decrease until local depletion or cell death limits the local consumption (in this test case upon depletion of oxygen). Neglecting a moving boundary as in the left column will lead to an unrealistic concentration decrease outside the tumour volume and an earlier depletion. Runtime for the solution of diffusion is greatly decreased by the moving boundary approach, while the total simulation runtime is increased due to the larger size of the tumour.

## 2 Model

updates the boundary depending on the local density to treat this central hollow volume as a boundary, even if this effect is unphysiological.

In order to prevent this, the diffusion solver includes a function, which will dynamically mark a growing central region around the origin of the solver, which cannot become marked as boundary. The function `mark_hollow_core_for_moving_boundary( radius )` will flag all diffusion nodes that lie within the radius as being unsuitable for a boundary. These flags are taken into account by the `update_boundary_by_objects()`-function when redistributing the boundary. An illustration of this mechanism from a diffusion test system that includes a hollow tumour spheroid can be found in figure 2.22.

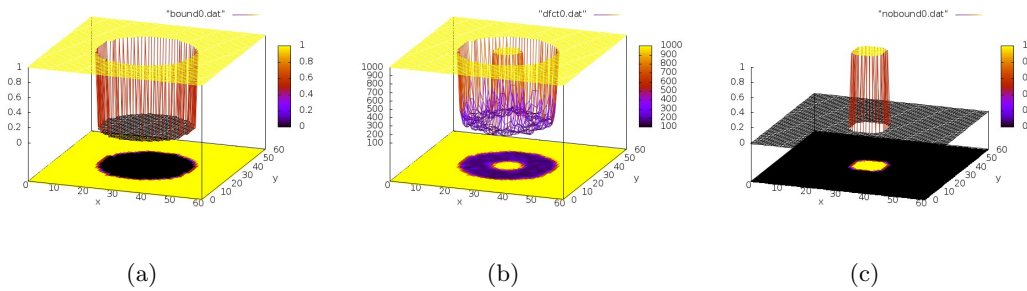


Figure 2.22: Z-central slice through the diffusion system depicting the position of Dirichlet boundary nodes in (a), the local diffusion coefficient (inversely proportional to the cell density) in (b) and the field which marks nodes which cannot become boundary by update in the central hollow volume of the object in subfigure (c). See also figure 2.21 for the according test run.

This simple approach, which can be generalised to arbitrary geometries, ensures that only an outer cell-free volume can be made boundary as long as a sufficient radius (e.g. the maximum radius of the necrotic core at that time) is passed to the function.

### 2.3.5 Summary

#### Summary 3 (*Diffusion solver*)

- Cells are able to consume nutrients from a reaction-diffusion grid with defined boundary values that match experimental conditions
- The reaction diffusion equation is numerically solved in a finite difference form using by default the Crank Nicholson scheme
- A pseudo-steady-state approximation can be applied to recalculate the steady-state of diffusion in fixed time steps
- The diffusion solver supports a local cell-density dependent diffusion coefficient
- A moving boundary approach is used in order to keep track of the expanding tumour spheroid while the rest of the diffusion system is treated as boundary
- Inner necrotic, hollow parts of the spheroid will show an increased diffusion coefficient, but cannot become marked as boundary

## 2.4 Tumour spheroids and tissue simulation using Delaunay triangulations

### 2.4.1 Representation of tissue in a Voronoi/Delaunay model

In order to model tumour growth, a spatial representation of cells and tissue must be realised. The most basic task that a spatial representation should be able to fulfil is to provide a neighbourhood-relation for interaction of objects which are in contact. A collision-detection for cell movement is closely related to this task. As a more complex demand, a representation framework should yield a realistic object shape and according contact surfaces between interacting objects. While very simple lattice-based approaches can fulfil some of the demands, their discrete nature remains unrealistic, as cell movement will always be a continuous phenomenon. A naive n-to-n approach for interaction is prohibitive because of its scaling behaviour, as soon as larger systems are to be studied. While for the problem of collision-detection a variety of methods has been developed (see figure 2.23), the only method which perfectly matches all demands formulated before is the representation of cells within a Voronoi/Delaunay hybrid model.

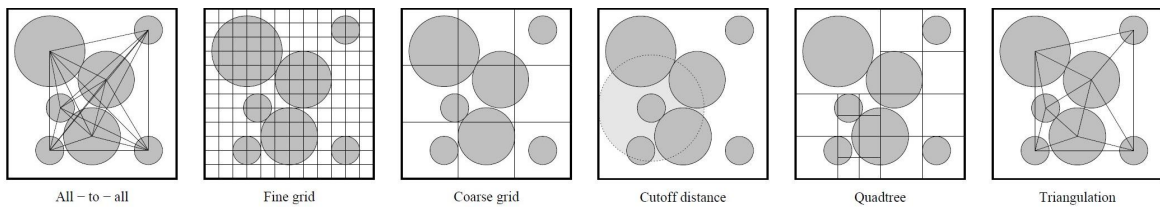


Figure 2.23: Overview of typical methods which can be used for collision-detection within the spatial representation of simulation agents. Adapted from [67].

The use of Delaunay/Voronoi hybrid models for the representation of tissue *in silico* has consequently become a well established tool in agent-based simulations within recent years. As the complexity of spatial tessellations is well beyond the scope of this thesis, only a brief idea of the concept is provided here, introducing the necessary terms and concepts. A wealth of detailed fundamental information on spatial tessellations can be found in [4] and in [162]. The Delaunay Object Dynamics code employed within this thesis is based on an algorithm for parallel computation of kinetic and dynamic regular triangulations as developed in [23]. It supports local updates of the triangulation in response to the movement of vertices or the insertion and deletion of vertices. Efficient parallel algorithms have made it possible to manage dynamic triangulations which contain  $\mathcal{O}(6)$  vertices and more (see [48], [67], [23]).

A Voronoi tessellation in three dimensions can be mathematically defined, following [21], by using a number of points  $\mathbf{v} \in \mathcal{S}$  as generators. The subdivision of space into regions  $C_n$  fulfilling

$$\bigcup_n C_n = \mathbb{R}^3 \quad \text{with} \quad C_n = \{ \mathbf{x} \in \mathbb{R}^3 : \|\mathbf{x} - \mathbf{v}_n\| < \|\mathbf{x} - \mathbf{v}_m\| \quad \forall m \neq n \} \quad (2.49)$$

will be called a Voronoi tessellation, where  $C_n$  denotes the Voronoi cells which will be 4-simplices in the three-dimensional case. In solid state physics the Voronoi tessellation

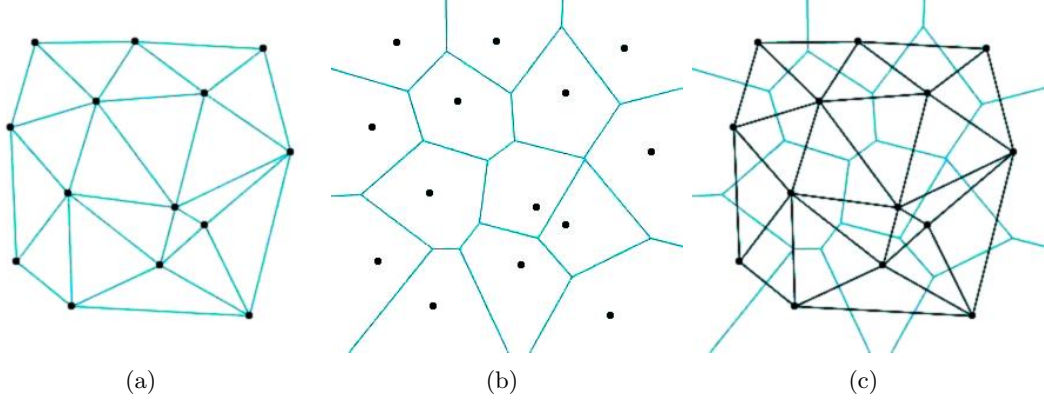


Figure 2.24: **(a)** A Delaunay triangulation from a random set of generators  $\mathbf{v}_n$  compared to the Voronoi tessellation of the point set **(b)**. The composition of both images illustrates the dual nature of the graphs **(c)**.

is well known as partition of space into Wigner-Seitz cells and its geometric construction is quite intuitive by bisection of connections between the points of a set (as visualised in figure 2.24(b)).

The generators  $\mathbf{v} \in \mathcal{S}$  of the tessellation can be associated with a weight  $w$ , as for example in the case of cellular agents with a defined cell radius. When the distance  $\|\mathbf{x} - \mathbf{v}_m\|$  in equation 2.49 is replaced by a power distance

$$\rho(U, V) = \|\mathbf{u} - \mathbf{v}\|^2 - w_u - w_v, \quad (2.50)$$

a generalised, weighted Voronoi tessellation, also referred to as power diagram, can be computed as subdivision of space into disjunct regions  $C_n$ , such that

$$C_n = \{\mathbf{x} \in \mathbb{R}^3 : \|\mathbf{x} - \mathbf{v}_n\| - w_n < \|\mathbf{x} - \mathbf{v}_m\| - w_m \forall m \neq n\} \quad (2.51)$$

$$= \{\mathbf{x} \in \mathbb{R}^3 : \rho(X, V_n) < \rho(X, V_m) \text{ with } X = (\mathbf{x}, 0) \forall m \neq n\}. \quad (2.52)$$

The dual graph of the weighted Voronoi tessellation is the regular Delaunay triangulation. It can also be defined directly via the empty orthosphere criterion (see [21]).

A restriction in regards to the position of the generators is the assumption of affine independence known as general position. Thus this implies that no two points are identical, no three points are collinear, no four points are coplanar and no five points are co(ortho)spherical. This restriction is generally of low importance for the simulation of cells in a tissue, but it must be kept in mind when simulating quasi-2D arrangements such as monolayer cultures.

Within this model, cells are spatially represented as vertices in a three-dimensional power-weighted Delaunay triangulation. While the triangulation efficiently provides the cell neighbourhood relations, the Voronoi tessellation of the system represents the cell shape. Free cells are assumed to be of spherical shape, while aggregated cells or cells in a tissue form polyhedral contact surfaces. This natural arrangement of cells can be perfectly described using a Voronoi tessellation and its dual graph the Delaunay triangulation as visualised in

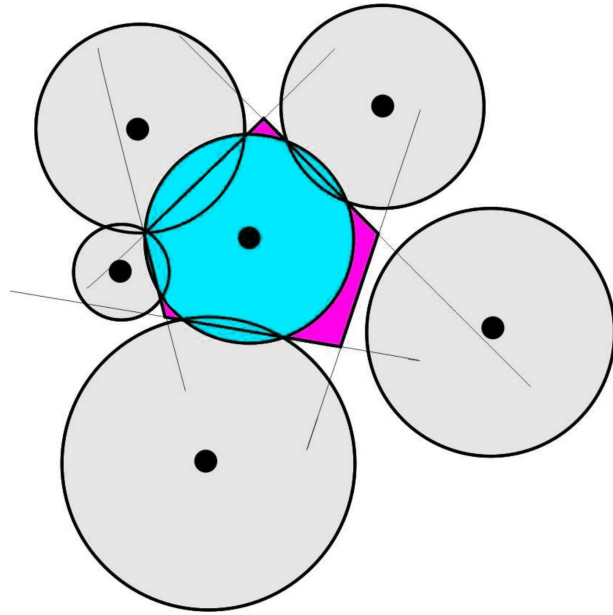


Figure 2.25: Two-dimensional illustration of a weighted Voronoi tessellation in which vertices are associated with a weight  $w$ . The Voronoi cell of the cyan cell is the magenta-coloured polygon. Adapted from [20].

figure 2.26(a). Not all cells which are connected within the Delaunay triangulation are actually in contact as can be seen for the central and bottom right disc in figure 2.25. If cells are connected within the triangulation an additional check for interpenetration of the spheres must be performed. In the case that cells are not in contact, the Voronoi cell is reduced to the real spherical section on this face of the cell agent.

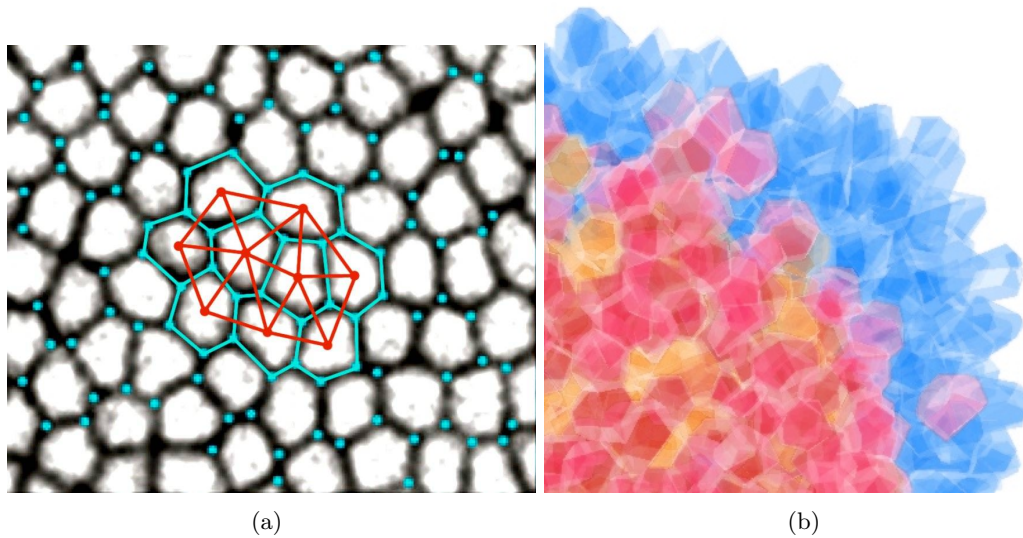


Figure 2.26: **(a)** Polyhedral arrangement of cells in a tissue overlaid with an illustration of a Voronoi tessellation and Delaunay triangulation. **(b)** Rendering of a quarter-section from a tumour spheroid in its Voronoi-cell representation as used in this model. The three-dimensional, polyhedral structure of the tissue in 3D is visible. On the surface of the spheroid, Voronoi cells will be bound by artificial vertices (not shown).

Thus a power-weighted Delaunay triangulation can provide a lattice-free localisation of cellular agents, collision detection for cell interaction and movement and size representation

of objects. Through the dual graph of the Voronoi tessellation at the same time cell volumes and contact surface areas are available.

The employed framework for object representation within kinetic and dynamic regular triangulation is a flexible tool and has been applied to a variety of other problems (see [194], [21]). A range of further problems that have been studied using the simulation framework developed within this thesis is provided in the appendix, section 4.8 on page 209.

### 2.4.2 Summary

#### Summary 4 (*Delaunay object dynamics*)

- *Cell agents are represented as weighted vertices in a three-dimensional, regular Delaunay triangulation*
- *Cell shape is polyhedral in a weighted Voronoi tessellation as dual graph of the Delaunay triangulation*
- *For dynamics the triangulation is locally updated after vertex movement, weight-changes, insertion, or deletion*
- *Neighbourship relation of cells is obtained from the Delaunay triangulation with an additional interaction-check*
- *Cell volume and contact surfaces can be calculated from the Voronoi tessellation*

## 2.5 Radiation effects model

In order to describe the tumour reaction to a complex regimen of fractionated irradiation, a simple but realistic model for cell survival and the reaction to radiation must be implemented. Within the following section the effects of ionising radiation as used in radiotherapy are discussed and their relevance to the simulation is classified.

Radiation sensitivity varies strongly with the cell cycle phase [206], a phenomenon which can be perfectly modelled using agent-based techniques. Another strong variation of radiosensitivity is observed for quiescent cells [142] and for hypoxic cells. All of the above effects will be present in an *in vivo* tumour, but can also be evaluated in a multicellular tumour spheroid as demonstrated in [68]. A comprehensive overview of principles and techniques employed in radiation therapy, which is far beyond the scope of this introduction, can be found in [29, 51, 64].

### 2.5.1 Effects of ionising radiation on cells

Ionising radiation has been employed for over 8 decades in the cure of cancer and other illnesses, however the full scope of effects which convey damage to the cell is still not understood today. Connell and Hellman provide a comprehensive overview of developments from the initial discovery of the damaging effects, over first successes with fractionation of radiation delivery, up to modern microarray techniques for radiation-induced alterations in gene expression and the use of hadrons in particle therapy [51].

The physical basis of the interactions between ionising radiation of different types (predominantly  $\gamma$ -radiation, but also light and “heavy” ions in a radio-biological sense) and molecules such as DNA components at microscopic scales, is a main area of research connected to cancer therapy and an extremely wide field in itself as discussed in [221] or [171].

At the basis of biological action is the effect of ionising radiation on cell components. While after the discovery of the DNA it seemed obvious that this vital blueprint is the main target of radiation damage, it has become clear that a highly complex regulatory network is at the heart of the cell’s reaction to irradiation and that the DNA is not the only target of radiation damage. An extremely simplified overview of some of the cellular stimuli, pathways and responses which are important in the cell’s reaction is visualised in figure 2.27 and discussed in [51]. Generally radiation-induced damage in the cell is reported by specific damage sensors and thus triggers a response which usually can be categorised either as DNA repair, transcriptional change, damage checkpoint or cell death [189].

A central role in the damage response is played by cell cycle checkpoints as discussed in detail in [189]. A cascade of signals pathways will be triggered that delay or halt the cell cycle progression of cells which are affected by radiation (as previously discussed in section 2.1.1). Although the specific name “DNA checkpoint” which is commonly used implies a discrete point in time when the integrity of DNA is examined, the sensing of DNA damage and according actions are more of a continuous nature. Repair of DNA damage as well as apoptosis induction remains largely independent of the cell cycle progression, even though many processes will be coupled through key proteins [189].

If the exact nature of the cell response is left aside, the coarsest and most important relationship is the one between applied radiation dose and observed cell survival as endpoint as shown in figure 2.29. Usually only a clonogenic survival is measured as the ability of cells

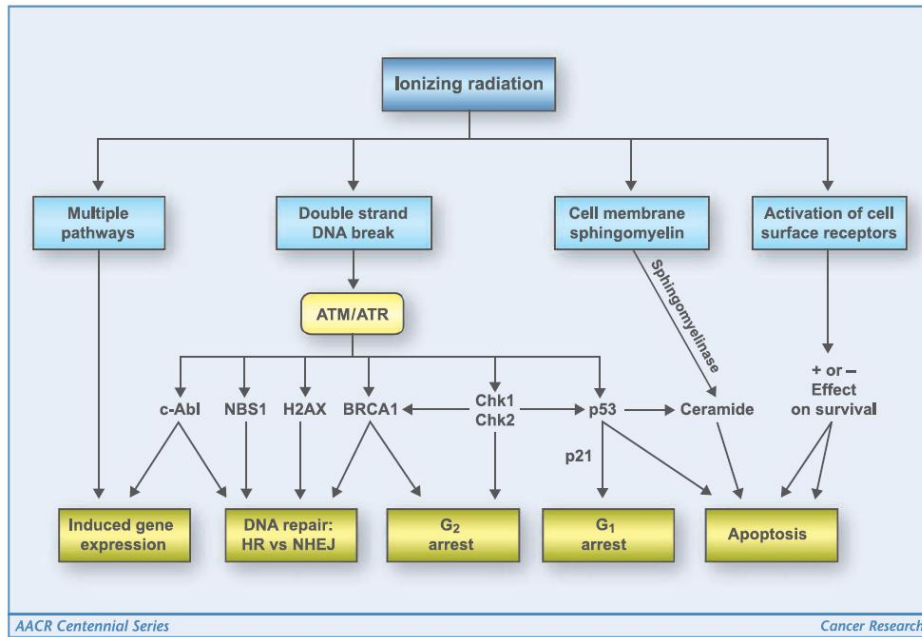


Figure 2.27: The cellular pathways involved in radiation damage as illustrated in [51].

to form new proliferating colonies after irradiation, but also single-cell survival probabilities can be determined experimentally. The measurement and prediction of exact levels of cell survival is of paramount importance for the treatment planning in a clinical setting, where radiotherapy should ensure that cancerous cells are fully sterilised, while benign cells are affected as little as possible.

### Cell cycle dependence

One of the main determinants of cell survival is the current cell cycle phase which is (sometimes also termed cell age) [84]. Depending on the localisation of DNA in the different cycle phases, the availability of repair mechanisms for radiation induced damage is limited [189]. If the DNA is distributed loosely in the nucleus in G1-phase as a single copy, only non-homologous end joining (NHEJ) is available for repair (or if blocked microhomology-mediated end joining (MMEJ)). At the same time, the probability for clustered DNA lesions in response to irradiation is lowered. If a second DNA strand is present, more effective mechanisms of repair such as homologous recombination (HR) become available. However, on the other hand, too close condensation of the DNA, as in M-phase, will increase the chance of radiation inducing severe clustered lesions.

As a result of this mechanism, the cell survival in response to radiation exposure will continuously vary with cell age as shown in figure 2.28. The actual degree of variation will vary between cells of different type, cell lines or even among subcultures of the same cell lines as is visible for the HeLa cells in the figure.

In our model the fact of the different availability of repair mechanisms and the subsequent difference in survival is reflected by using experimentally determined survival curves for the individual cell cycle phase (see figure 2.37(a)). Thus the cell cycle distribution of the tumour will strongly influence the radiation response as will be discussed later.

## 2 Model

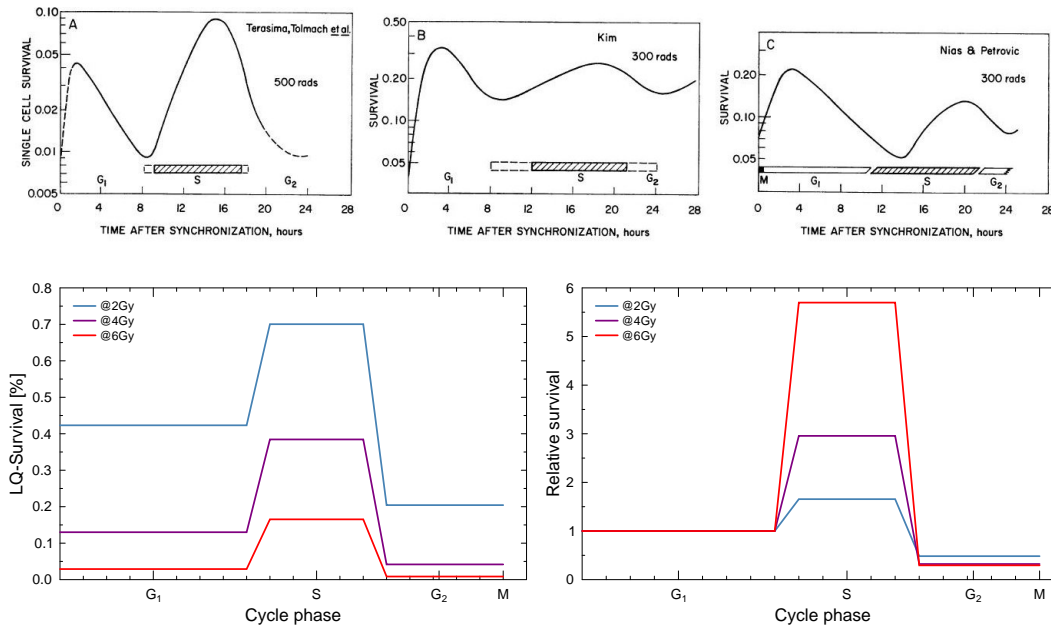


Figure 2.28: **(top row)** Cell age-dependent survival of synchronised HeLa cells in different experiments from [204]. **(bottom row)** The radiosurvival of V79 cells at different doses of  $\gamma$ -radiation discriminated by cell cycle phase and the relative survival in relation to the  $G_1$ -survival probability as used in the model. Based on measurements from [204].

A factor which strongly influences the triggered effects is the linear energy transfer (LET) of the applied radiation, defined as the energy deposited in a tissue per length and usually measured in units of  $\text{keV}/\mu\text{m}$ . While radiation of low LET such as  $\gamma$ -radiation ( $\approx 2 \text{ keV}/\mu\text{m}$ ) or carbon-ions in the entry channel ( $18 \text{ keV}/\mu\text{m}$  in the plateau region) will show a high dependency on cell cycle effects, it is decreased for radiation of high LET as for example carbon-ions in the extended Bragg peak region ( $60 \text{ keV}/\mu\text{m}$ ) [213].

### Quiescence effects on radiosensitivity

Quiescent cell populations will form in tumours in response to pressure or nutrient deprivation as previously discussed in section 2.1.1. Their survival probability in response to radiation can however not be measured in a standardised colony forming assay which made measurements of quiescent cell survival unavailable. Using an indirect measure by micronucleus frequency and BrdU staining, it has been shown that the non-cycling but viable cells in  $G_0$  exhibit an increased radiation resistance [144]. Their repair of potentially lethal damage is enhanced and they will usually be subject to a lower degree of oxygenation. All of these factors intermix and lead to an increased survival of quiescent cells after irradiation. This remaining quiescent population can refill the tumour once they are activated [143].

Control of the quiescent subpopulation is therefore of great interest for overall tumour control. There is strong evidence that the RBE of heavy ion (or high-LET) radiation is relatively higher for quiescent cells [146]. While they will still show an enhanced radioresistance, high-LET radiation is more suitable to also kill quiescent cell populations.

In a model this fact can be included by using an adapted survival probability for quiescent cells, which is increased in comparison to the baseline  $G_1$  LQ-survival, in the simplest case

by a constant factor. A more realistic approach scales the effective dose which is received by  $G_0$  cells (see figure 2.29). Judging from the micronucleus frequency in the total tumour cell populations versus the quiescent population only (see [146]), an effective dose reduction factor ranging from about 1.1 for high-LET radiation to 1.7 for low-LET radiation is proposed in [145].

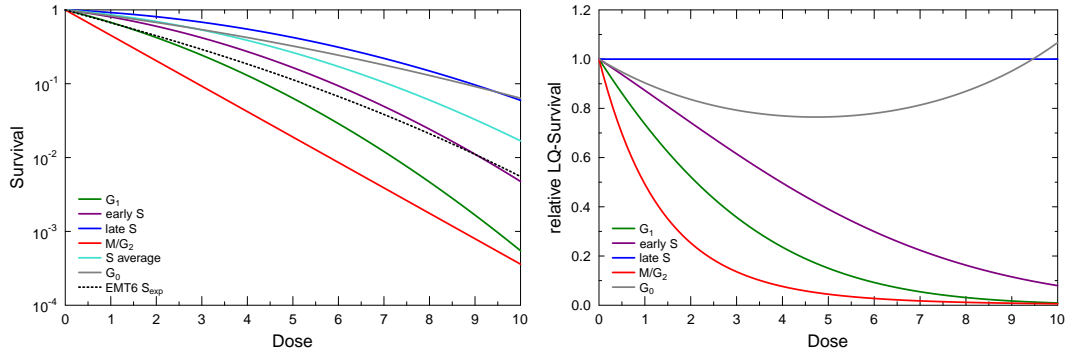


Figure 2.29: Radio-survival of V79 cells in response to X-rays. The second plot shows the survival relative to the most resistant phase (late S). Even at a dose of 2Gy the possible gain (difference in survival between late S and M/G2) is strong, while it saturates above 4Gy.  $G_0$ -survival curve assumes a resistance factor of 2 in this case, so that cells effectively receive a halved dose. Note that the effect of radiation resistance of quiescent cells thus increases in strength with dose.

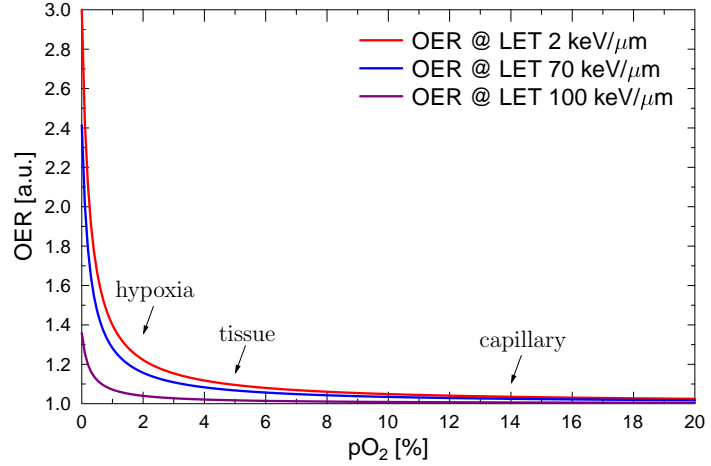
This will drastically alter and even dominate the overall radiosensitivity of the system, as in larger tumours a high fraction of quiescent cells (up to 60 percent) will be present. Therefore the effective cell cycle length of  $G_0$  is very long and the observed survival will be drastically different from the expected survival for an exponentially growing cell population.

### Oxygen enhancement

**Oxygen effects** The concentration of oxygen inside a tumour is of paramount importance for the efficiency of therapeutic approaches. Tissue in hypoxia, that is with a critically low oxygen concentration, will be very resistant to conventional radiation therapy and to a wide range of drugs. In order to incorporate this effects into the simulation, we model the oxygen concentration inside the tumour spheroid applying the same approach as for the glucose concentration as discussed in section 2.3. Cells which are subject to a critically low concentration of oxygen enter a hypoxic state. This can change their metabolism to anaerobic glycolysis thereby reducing the pH value in their vicinity and will affect their reaction to radiation.

As shown in [84] the radiosensitivity of cells decreases with oxygen tension. However this effect is only observable at low oxygen tension below a partial oxygen pressure of about 30 mmHg. For a partial pressure above this threshold the so called oxygen enhancement ratio (OER) will be unchanged, even when cells are subject to higher than normal concentrations of oxygen (e.g. pure  $O_2$  at 760 mmHg). Below the critical threshold the radiosensitivity increases until it reaches a maximum if the system is void of oxygen. The OER is defined as the ratio of doses needed to achieve a certain survival in cells either in normoxic conditions  $D_{\text{normoxic}}$  or under hypoxic conditions  $D_{\text{hypoxic}}$ :

Figure 2.30: Oxygen enhancement ratio in dependence of oxygen pressure for radiation of different LET in a parametrisation from [199] as in equation 2.54. X-rays will typically achieve a LET of 2 keV/μm, while within a spread-out Bragg peak in HI-irradiation an average LET of around 70 keV/μm will be typical.



$$\text{OER}(pO_2) = \frac{D_{\text{hypoxic}}}{D_{\text{normoxic}}} \Big|_{\text{same effect}} = \frac{m \cdot pO_2 + H}{pO_2 + H} \quad (2.53)$$

Equation 2.53 already implies a dependency which is defined by the maximum OER effect  $m$  and the  $pO_2$  at half effect  $H$ .

The oxygen enhancement is also present in irradiation with non-conventional radiation such as heavy ions, as it depends on LET. As LET is not constant across the heavy ion region of dose deposition, the problem of oxygen enhancement becomes especially challenging in heavy ion treatment planning.

The oxygen enhancement ratio in radiation damage will be calculated depending on the local oxygen concentration using the following parametric formulation from [199]:

$$\text{OER}(L, pO_2) = \frac{B(Am + L^3)/(A + L^3) + pO_2}{B + pO_2} \quad (2.54)$$

The typical LET  $L$  for heavy ion irradiation will be 70 keV/μm within a spread out Bragg peak using the further parameters  $A = 8.27 \cdot 10^5$ ,  $B = 0.25$ , and  $M = 3.0$ . A plot of the function is presented in figure 2.30.

The magnitude of the cell cycle phase dependent radioresistance (CCR) and oxygen enhancement effects (OER) are compared in figure 2.31. In x-ray irradiation the potential gain or loss from cell cycle effects is larger than the effects of hypoxia. With an increase in LET this ratio will vary.

The maximum OER of X-rays (250 kV) in V79 spheroid cells was measured to be 2.8, for carbon-ions in the plateau-region 2.7 and for the extended Bragg peak region 1.4. The according LETs of the radiation are 1.7 keV/μm, 18 keV/μm and 60 keV/μm [213].

**Irradiation and hypoxia** As a radiation dose is applied, a multitude of effects, some of which are described in detail below and in table 2.6, are triggered which will induce severe changes in the microscopic and macroscopic distribution of oxygen.

As cells are killed, the relative consumption per volume is decreased at the same time as the diffusion of substances to the tissue is facilitated. The result is a increased maximum

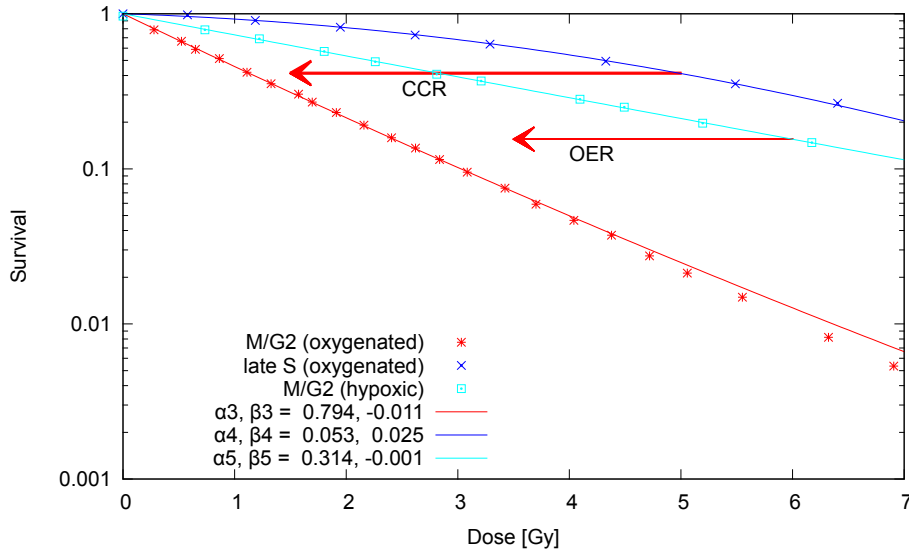


Figure 2.31: Comparison of the effects of oxygen enhancement ratio (OER) and the variation of radiosensitivity with the cell cycle phase (CCR) for Chinese hamster cells in response to x-ray radiation [84].

diffusion range for substances, which can lead to a reactivation of previously dormant areas, which are now sufficiently supplied with nutrients and oxygen. As a consequence, this will increase the local consumption, so the final increase in diffusion range will be limited.

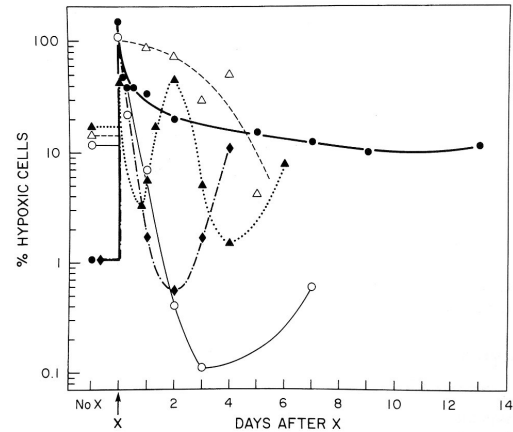
On the macroscopic scale, the shrinkage of the tumour volume will lead to a pressure release possibly clearing previously obstructed vessels. Radio-killing of epithelial cells will on the other hand limit this effect as it will negatively affect the blood supply. Inflammation processes might have an effect in both directions, blocking vessels but also leading to an increased circulation.

Thus the reoxygenation response of *in vivo* tumours to irradiation will be extremely involved as illustrated in figure 2.32. Tumour spheroids provide a system of limited complexity in which parts of the response that are present in an *in vivo* system can be studied and understood. As for adapted boundary concentrations of nutrients and oxygen, the structure of

Mechanism	Effect
Cell death	reduced consumption per volume
Reactivation of survivors	increased consumption per volume
Cell dissolution	increase in diffusion coefficient
Pressure release	release of transient vessel occlusion
Temporal vessel damage	inflammation and increased flow
Permanent vessel damage	death of epithelial cells
Inflammation	change on macroscopic pressure and blood circulation

Table 2.6: Possible effects of irradiation on blood supply and oxygenation.

Figure 2.32: Hypoxic fraction of cells in response to x-ray irradiation in five transplanted *in vivo* tumours. Reoxygenation dynamics are extremely involved and vary from tumour to tumour. Adapted from [86].



the developing tumour spheroid is equal to the proposed microstructure within macroscopic tumours, the model can be used to predict the irradiation reaction and reoxygenation of macroscopic tumours to a certain degree.

**Oxygenation and PET scanning** In order to assess the oxygenation status of tumours before and during treatment, positron emission tomography (PET) is typically employed [123]. Spatially the PET-signal resolution is  $5 \mu\text{m}$  cubed with a varying time resolution often as low as once per 5 days. Significantly smaller scanning intervals are possible but usually scans are just repeated every few days in order to decide if the treatment conditions changed, thus requiring adjustment of the treatment plan.

In order to have a valid interpretation of the PET-data, the dynamics of tissue reoxygenation have to be investigated and understood. If the critical timescale of reoxygenation is not known, then PET-scans at the wrong time might over- or underestimate the real oxygen concentration, which can have dire consequences when designing a treatment plan in respect to oxygen enhancement.

The dynamics of reoxygenation are not trivial, as a multitude of factors will play a role in determining the oxygen concentration in the tissue after treatment. Irradiation will disturb the maximum diffusion length of nutrients within the respiring tissue by killing cells, reactivating dormant cells, effectively changing the diffusivity of the tissue and the tissue organisation. These effects will lead to a complex reaction that cannot be easily predicted without the use of a spatially resolved agent-based model.

As a comparison to the PET-signal, the integral oxygen amount in the diffusion system can be used, so that its relative change will correspond to the relative change in the PET-signal after treatment. Absolute values can be obtained only if the tumour volume is taken into account and not the whole diffusion system.

Another observable is the amount of hypoxic cells in the tumour. Experimental measurements report a typical relative amount to be approximately 15% [84]. In response to treatment the hypoxic fraction will drastically rise, then behave differently by tumour type (from oscillations to rapid drops) while typically returning to the baseline level after some days as indicated in figure 2.32.

### Environment and differentiation effects

Cells will show a different range of behaviours when in contact with other cells or when organised in a tissue. This modulation is also the case in radiotherapy as has been reported e.g. in [227] for the radiation response of cell mono-, multilayer and spheroids. One of the advantages of spheroid cultures is the presence of a, albeit limited, microenvironment and extensive cell-cell contacts which makes them a suitable model system to study realistic radiation reactions including the so termed contact effects of radio-resistance [68].

Realistic variations in radiosensitivity within tumours can be well modelled using multicellular tumour spheroids [157] as “spheroids mirror the radiosensitivity of differentiated tumors *in vivo* more closely than conventional cell cultures”. By experimental manipulation of cell interactions Stevenson and Lange could demonstrate that the extracellular matrix and the cytoskeleton are important modulators of radiosensitivity [220]. Adhesion molecule expression is also altered by radiation which has effects on cell behaviour as cell-cell and cell-matrix contact, invasion, angiogenesis and metastasis [10]. These alterations can also be used in targeted therapy against upregulated adhesion molecules.

Korff and Augustin [119] showed that the integration of endothelial cells in multicellular spheroids effectively prevents apoptosis and induces differentiation. Cell organization can also influence the type of radiation-induced cell death: while MG-63 monolayer cells undergo mitotic catastrophe, spheroid cells die of apoptosis [105].

Furthermore, as a form of cell differentiation, senescence is of interest, as senescent cells can effectively be considered as clonogenically dead. Thus every cell which is driven into terminal differentiation by radiation damage is removed from the tumour burden. Usually radiation will only induce senescence in damaged cells over the course of multiple generations. However, as a long-term effect this is of interest for the outcome of the therapy. Recently, the induction of premature senescence in two human fibroblast cell lines was investigated by Zahnreich et al. who demonstrated that irradiation with a high, fractionated X-ray dose can result in an increase of chromosomal aberrations and earlier senescence [247].

The bystander effect is another interesting phenomenon of the tumour microenvironment in which cells that have not been directly affected by radiation suffer damage or are killed after radiation has been applied in their vicinity [85]. It can either act via soluble chemo- and cytokines or signalling between cells in contact at gap junctions [212].

### 2.5.2 Damage kinetics and repair

As previously discussed in section 2.5.1, cells have a variety of potent mechanisms at hand in order to repair damage to their DNA as also discussed in great detail in [189]. The kinetics of DNA damage are of special interest, if radiation is not applied in a single dose, but fractionated into multiple smaller doses.

Damage to the cell DNA is often characterised either as lethal damage (LD), sublethal damage (SLD) or potentially lethal damage (PLD) with the associated repair capabilities of the cell termed as SLD-repair (SLDR) or PLD-repair (PLDR). Lethal damage can usually not be repaired and thus will lead to the clonogenical death of the cell. The repair of SLD can be demonstrated by split-dose irradiation. If a total dose is split into two fractions, the resulting total survival is higher, indicating that SLD was repaired between the delivery of the fractions. An estimate for the typical timescale of sublethal damage repair in CHO cells

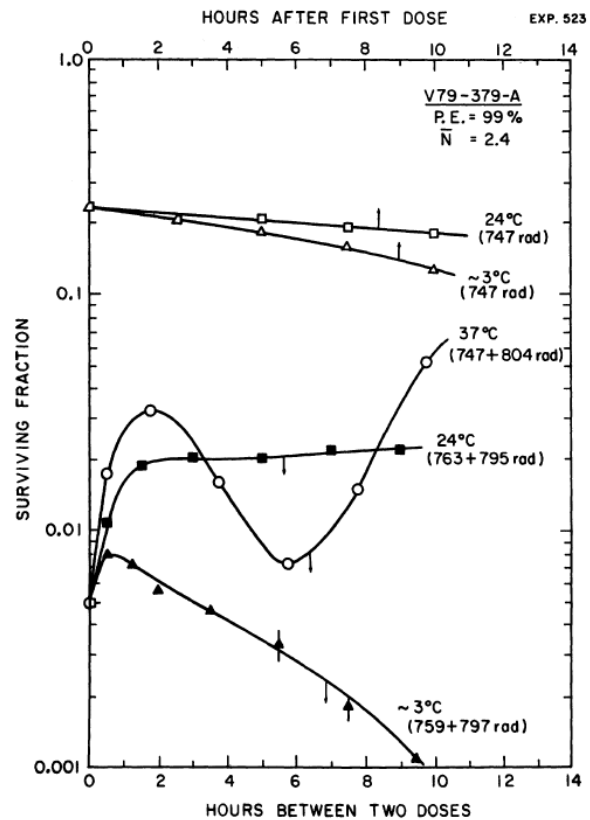


Figure 2.33: Survival of V79 cells of subline 379-A in response to one dose of radiation or the same total dose split in two fractions. Sublethal damage repair and cell cycle dynamics are present at 37°C, while at 24°C no cycle dynamics occur anymore. At 3°C also damage repair is inhibited. From [66].

can be found in [66]. In this split-dose experiment the survival of cells to two fractions of 8 Gy x-rays will be dominated by the cell cycle effects as discussed in section 2.5.1. Cooling of the cell population to 24°C after the first dose will prohibit any cell cycle progression while still allowing for repair. The sublethal damage repair is almost completely achieved in a time window of two hours post irradiation. When cells are sufficiently cooled down in the experiment SLDR-mechanisms will also be strongly affected.

PLD is any kind of damage which can, in principle, be repaired, but only if conditions are favourable. Repair can require arrest at a cycle checkpoint, a specific cycle phase (e.g. S-phase) or total arrest of the cell cycle as in quiescent cells. As tumour cells often lack central cell cycle control mechanisms, PLD can be repairable for healthy cells but not for cancerous cells. While PLDR can alter survival for irradiation with x-rays, neutron or even HI-irradiation will usually not allow a large fraction of potential damage repair [175]. Thus it is a mechanism which is most important for very fast fractionated irradiation with  $\gamma$ -irradiation. The capacity of quiescent cells for PLDR is higher than that of active cells, which is one of the reasons for the increased radio-resistance of quiescent cells [146]. Consequently PLDR can be increased by adverse growth conditions, which keep cells fixated in quiescence.

The half-life  $T_{1/2}$  for damage repair is estimated to be around 1-2 hours (as shown in figure 3.47(a)). It is thus more rapid than common cell cycle effects [175]. However different repair mechanisms can exhibit individual half-lives.

DNA damage can be visualised and quantified using H2AX which is one of the genes which encodes histone H2A. In the presence of DNA Double-strand breaks (DSB) H2AX becomes phosphorylated to  $\gamma$ H2AX, which can be marked by a fluorescent antibody. As the number of developing  $\gamma$ H2AX fluorescence foci is almost correlated one-to-one with the number of

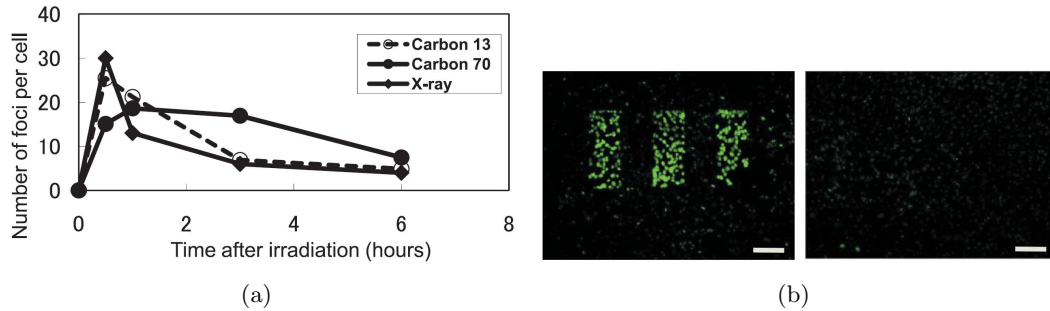


Figure 2.34: (a) Kinetics of DNA damage measured via the formation of  $\gamma$ H2AX-foci in human cells from [87]. (b)  $\gamma$ H2AX-antibody staining of double-strand breaks in V79 cells in response to microbeam irradiation fixed 1 h and 12 h post irradiation adapted from [212].

DSBs even quantitative measurements are possible [212]. Especially in x-ray radiation a fast formation of  $\gamma$ H2AX-foci is observed, but the kinetics show a very fast clearing of DNA damage within 3 hours [87]. For particle radiation, especially at a higher LET an increased persistence of  $\gamma$ H2AX-foci can be observed (see also figure 2.34(a)).

In microbeam experiments with a 5.35 keV pencil beam and doses between 2 and 10 Gy [212] it was shown that the majority of the DNA damage has been repaired within 12 hours after irradiation. Small amounts of damage may persist longer, however it remained unclear if this is due to unsuccessful repair or bystander damage at a later point in time than irradiation (see figure 2.34(b)).

Quantitative assessment of DNA damage using  $\gamma$ H2AX was even demonstrated *in vivo* recently by Conelissen et al., opening up the possibility to monitor damage to DNA during treatment in the future [52].

Within a simulation it is safe to model fractionate therapy regimens, as long as the minimal time in between fractions is higher than the typical timescale of sublethal damage repair. If time intervals below this threshold are chosen without correction to the irradiation model, the survival chances of cells will usually be overestimated. This is because the two events will be handled independently, which results in a higher total survival, even though in reality there would be an enhancing effect of cell killing resulting from the lack of sublethal damage repair. An upper safety margin of 6 hours is typical for sublethal damage repair, even though the majority of damage will already be repaired within 2 hours [51].

### Apoptosis, necrosis, LET and radioresistance

Depending upon the cell line under consideration, the sensitivity and reaction of cells to irradiation may change drastically. While EMT6 mouse tumour cells show nearly no apoptosis in response to irradiation, HX142 human neuroblastoma cells die almost exclusively via apoptosis [84]. The blockage of the apoptotic pathway as in EMT6 cells is associated with a high radioresistance, as cells will not react via the “healthy” induction of apoptosis in response to radiation damage. Induction of apoptosis or necrosis in response to irradiation damage will also largely depend on the LET of the applied irradiation. In general, high-LET radiation will lead to an increase in apoptosis relative to necrosis independent of the p53 status of the cell line under consideration [87].

### Dose-rate effects

As the survival curve is composed of an initial shallow shoulder and a later steeper part, splitting a given dose in two fractions will effectively repeat the initial shoulder two times. The resulting overall survival will be higher than if the full dose would have been applied in one fraction. With protracted treatment time the possibility for sublethal damage repair increases as discussed in the previous section. If the dose-rate is lowered accordingly it will lead to increased survival up to the maximum repairable sublethal damage.

For further reduced dose-rates, cells will amass in the radiosensitive G2 phase, which will effectively increase cell killing again. This effect is known as the inverse dose-rate effect [86].

For even further (extremely) decreased dose-rates the division of cells becomes an increasingly important factor which limits the effectiveness of the irradiation.

Coming from a high dose rate this means that by lowering the dose-rate the overall killing will first drastically decrease, then rise again and then decrease further. Details on this effect can be found in [84].

Usually it is preferable to deliver a high dose in a short amount of time, that is with a high dose-rate (e.g. 1Gy/min). If the dose-rate is decreased, cells might be able to repair sub-lethal damage before receiving additional hits, thus escaping apoptotic mechanisms. The cell survival will usually increase drastically if the dose rate is lowered to extreme values (e.g. 0.1Gy/h). In some cell lines an inverse dose-rate effect can be observed, as continuous low-rate irradiation leads to the induction of a G2 block. Due to the cell sensitivity in G2 the amount of damage in some cell lines can be as high as for a high dose-rate even if the actual dose-rate is very low. HeLa cells are known to show this behaviour [84].

Within the scope of this thesis, only high dose-rate irradiation will be considered as it is almost exclusively applied in external radiotherapy. As the standard damage model does not include sublethal damage, the effects of repair are neglected. Effectively when using the term dose-rate in this thesis we will most of the time refer to the amount of radiation per time interval in a context of a prolonged irradiation schedule (such as 2Gy/24h).

### 2.5.3 Particle irradiation

In recent years the use of charged particles in radiotherapy has become a promising new mode of therapy. Due to the different physical properties of photons and charged particles the effects of both radiation types on cells are different. Comprehensive reviews of the according developments and the state of the art of particle therapy can be found in [64] and [87]. Technical developments in delivery of heavy-ions are described in [154]. A summation of typical treatment times, fraction schemes and experience with heavy-ion therapy can be found in [163].

Charged particles moving through matter interact with atomic electrons in the material. These interactions can lead to excitation or ionisation-events in the atoms. The energy loss of a charged particle per distance travelled has been described by Bethe in 1930 [19] as

$$-\frac{dE}{dx} = \frac{4\pi}{m_e c^2} \cdot \frac{nZ^2}{\beta^2} \cdot \left(\frac{e^2}{4\pi\epsilon_0}\right)^2 \cdot \left[ \ln\left(\frac{2m_e c^2 \beta^2}{I \cdot (1 - \beta^2)}\right) - \beta^2 \right] \quad (2.55)$$

with  $\beta = v/c$ ,  $v$  the velocity of the particle,  $E$  the energy of the particle,  $x$  the penetration

depths,  $c$  the speed of light,  $Ze$  the particle charge,  $e$  the electron charge,  $m_e$  the resting mass of the electron,  $n$  the electron density of the target,  $I$  the mean excitation potential of the target, and  $\varepsilon_0$  the permittivity of free space.

As a result of the interaction described by equation 2.55, charged particles will show a beneficial depth-dose profile. While a large fraction of the dose in conventional photon-therapy will be deposited in the entry channels, a majority of energy deposition for charged particles is found near the end of their penetration, in the so called Bragg peak (see figure 2.35).

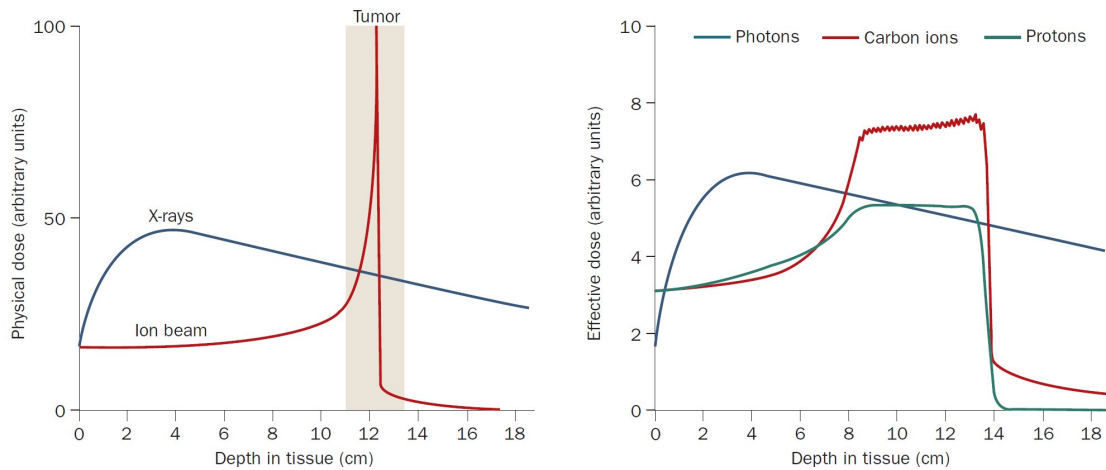


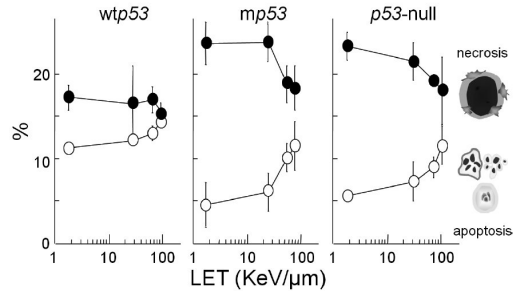
Figure 2.35: Depth-deposition profile of charged particles in comparison to X-rays (left panel) and effective dose as a result of a spread-out Bragg peak used for radiation delivery. Adapted from [64].

About two thirds of the dissipated energy is transformed into kinetic energy of  $\delta$ -electrons [221]. These then produce secondary and tertiary ionisation processes around the ion track. The energy spectrum of the emitted  $\delta$ -electrons determines the diameter and the local dose inside the track. This cascade is the main reason for the great difference in biological effect when comparing e.g. photons and ions in radiation treatment [120].

Within the entry channel (plateau region) particle radiation will have a high energy and an associated low LET. In terms of survival curves, particles yield similar results to x-rays within this region. This implies a high OER of about 3 and a high cell cycle dependence [64]. At the Bragg peak a high LET of particle irradiation will lead to a lower OER and lower cell cycle dependence. As a large part of damage is caused by direct energy transfer, the dependence on tissue oxygenation is lower in particle radiation with high LET.

In reality some of these effects are limited, as an extended Bragg peak (spread-out Bragg peak SOBP) is generated by superposition of multiple Bragg peaks in order to treat macroscopic target volumes. This is a result from extremely small fractions with different energy and thus different penetration depths which can be delivered in a 3D scanning concept [154]. The LET within this extended Bragg peak will vary greatly. This variation goes from low LET in the frontal part of the target volume, which is always subject to an “entry-channel” low-LET dose when slices behind it are targeted, to a high LET in the close-to-distant part of the target, as the slices close to the end are mainly only irradiated using high energy (and thus high LET) beams. Only fragmentation of particles will also decrease the average LET in this final slices to a certain degree. So while the dose can be equally distributed in the

Figure 2.36: Induction of necrosis or apoptosis varies with LET of radiation. At high LET, similar levels of apoptosis are reached in wild-type p53 cells (wtp53) as in mutant and p53 and p53-null cells. From [87].



extended Bragg peak, the composition of particles which carry this dose and thus the RBE and the LET vary considerably.

With this varying LET in the extended Bragg peak, heavy ion irradiation also becomes subject to topics such as oxygen enhancement ratios (OER) and cell cycle dependent radiosensitivity (CCR), even though it is a common assumption that these phenomena do not play an important role in heavy ion irradiation.

Apart from the physical radiation effects microarray analysis or specific methods like the gene expression analysis method called HiCEP (high coverage expression profiling) showed that gene-expression in cells changes differently in response to X-rays or particle radiation [87].

Furthermore it has been shown that high-LET radiation will trigger preferentially apoptosis but not necrosis regardless of p53 status [223] (see also figure 2.36).

## 2.5.4 Models for radiation response

Over the prolonged use of radiation in therapeutical settings, a variety of models have been developed to describe and predict the irradiation reaction of cells. An overview of damage models can be found in [9] and [236]. The most widely-used model (especially clinically) which is employed to fit the survival of cells in response to irradiation is the so called linear-quadratic (LQ) model

$$S = e^{-(\alpha D + \beta D^2)} \quad (2.56)$$

which describes the amount of survival  $S$  after a radiation dose  $D$  depending on two cell specific parameters  $\alpha$  and  $\beta$ . Underlying the model is the assumption of a linear and quadratic response to irradiation which is characterised by the parameters  $\alpha$  and  $\beta$ , which describe the amount of cells killed by a single action of radiation (e.g. by a lethal DSB) and the amount of cells which are killed by a cooperative action (e.g. of two sublethal damage sites which together cannot be repaired anymore).

Numerous extensions of the LQ model have been developed over the years. These include models that strive to incorporate effects such as repair and repopulation phenomenologically [228] as well as redistribution [83] and reoxygenation [33]. Nanodosimetry-based variations of the linear-quadratic model have been developed especially for mixed-LET radiations [45].

The Repairable-conditionally repairable damage model (RCR) is another example of a damage model. It is based on dual Poisson processes [135] and has been also used for an analytical description of cell survival depending on LET [240]. Especially in the region of very high LET, specific models have been developed. One of these is the Local Effect Model

(LEM), which has been applied within treatment planning at GSI, and combines charged particle track structure and conventional photon radiation reaction of cells [197].

However it has been noted that the linear-quadratic model and most other common radiobiological models result in similar predictions of time-dose relationships [34].

Propositions for the increased inclusion of sub-cellular and molecular responses in new models have been frequent as in [31] where a “more general systems biological approach to radiation therapy and treatment” is anticipated or [236] where a bottom up approach is followed. Also on the basis of multiscale approaches radiation damage models are developed which try to link radiation action on small scales (such as the interaction of  $\delta$ -electrons with DNA) to a macroscopic output as the overall probability of DNA damage [208].

However for numerous reasons the linear-quadratic model remains the standard for clinical predictions, as it has an unrivaled applicability and usefulness. As Brenner states in [32]: “(1) it is a mechanistic, biologically based model; (2) it has sufficiently few parameters to be practical; (3) most other mechanistic models of cell killing predict the same fractionation dependencies as does the LQ model; (4) it has well-documented predictive properties for fractionation/dose-rate effects in the laboratory; and (5) it is reasonably well validated, experimentally and theoretically, up to about 10 Gy/fraction and would be reasonable for use up to about 18 Gy per fraction”.

Especially the biological basis and the simplicity are of importance for a radiation model which is to be included in a larger simulation framework. Furthermore, most of the effects that are thought to be included phenomenologically in extensions of the LQ-model can be directly implemented within the simulation, as for example the redistribution of cells or reoxygenation of the system. Thus the introduction of new parameters in the radiation damage model can be avoided.

The linear-quadratic model can be easily extended to yield a survival which is specific for a distinct cell-cycle distribution in a tumour, by using cell-cycle phase dependent  $\alpha_p$  and  $\beta_p$  values:

$$S_p = e^{-(\alpha_p D + \beta_p D^2)} \quad (2.57)$$

Oxygen enhancement and also the effects of quiescent cells can be directly included as discussed in section 2.5.1. Within this simulation, the LQ model is thus a reasonable approach which can be based on experimental measurements.

Criticism in applying the LQ model especially in the high-dose regime of radiosurgery is discussed in [118], however, the applicability in extreme ranges has been positively discussed in [32]. In the low and very high dose regimes, the validity of the LQ-model becomes limited as discussed in [30], however for doses studied within this thesis it is safely applicable.

### 2.5.5 Fractionated radiation delivery

Not only the total dose of radiation which is applied to a tumour is of importance, also the time pattern of radiation delivery will greatly alter the outcome [83]. Spatial and temporal dynamics are triggered inside the tumour by each radiation dose which lead to a number of effects that influence the overall radio-sensitivity. Withers described a number of these dynamic effects which have been termed the *4Rs* of radiotherapy and which form the basis

of fractionated treatment regimens until today [245, 86]. These effects are:

**Repair** Assuming that repair pathways are most often impaired in malignant cells, a fractionation of the dose with at least 6 hours inter-fraction time will give affected healthy cells the possibility to repair SLD and PLD as discussed in section 2.5.2.

**Redistribution** Describes the fact that cells will redistribute in the cell cycle phases in response to irradiation. A main mechanism is the cell cycle phase specific radiosensitivity as discussed in section 2.5.1. Cells which had a low chance of being affected by a fraction, e.g. because they were in S-phase during irradiation, will eventually move on in the cell cycle and enter radio-sensitive phases, where they can be treated. Another part of redistribution is the reactivation of quiescent cells, which will drastically alter the overall cell cycle distribution.

**Reoxygenation** The effects that a radiation dose will have on the oxygenation status of a tumour as discussed in sections 2.2.2 and 2.5.1 are subsummed under the 3rd *R*. Fractionation of treatment can allow for reoxygenation as temporary occlusions in the vasculature are lifted or previously chronic areas are supported because of cell killing.

**Repopulation** Tumours will often react with accelerated repopulation to radiotherapy. Both benign and cancerous tissue will show an increase in growth fraction and a decrease in doubling times. Typically this phenomenon is only considered to be important after 4-5 weeks of treatment (depending also on the early- or late-responding characteristics of the tissue). However also a fast increase in doubling times can be observed.

In recent years a fifth *R* is frequently added - namely “Radiosensitivity” - to feature the intrinsic radiosensitivity or radioresistance of specific cell types. The typical clinical fractionated treatment schedule which evolved in response to description of the 4*Rs* will deliver fractions of approximately 2 Gy every 24h until an integral dose of about 60 Gy has been delivered.

For the development of fractionation plans the individual characteristics of tissues have to be taken into account. One of the characteristics is the discrimination of early and late responding tissues. Early responding tissues usually exhibit a high  $\alpha/\beta$  value in the LQ-model, which makes their radiation response linear (examples of early responding tissues include the testis and small bowel). Late responding tissues in contrast have a low  $\alpha/\beta$  value and thus show a more curved shape of dose-survival curves (e.g. spinal cord, skin or kidney). The concept of early and late responding tissues is discussed in more detail in [86]. When comparing isoeffects curves (total dose needed for effect over dose per fraction applied), late responding tissues usually show steeper curves than early responding tissues [86]. So, for late responding tissues, a treatment with higher single doses (e.g. hypofractionation) is of usually very effective as a much lower integral dose is needed for the same overall effect.

Depending on these and other characteristics of tissue, a wide range of treatment schedules has been developed and are employed clinically or investigated in clinical trials. The number of publications on studies of both established and new fractionation schedules is extremely high. A range of experimental investigations of different schedules which are of interest for the investigation within this thesis can be found in [75, 103, 5, 246, 160, 28].

Treatment protocols differ greatly with respect to how an integral dose to the tumour  $D_I$  is delivered over time [160]. Typically, schedules can be categorized into one of these classes:

**Conventional** standard clinical schedule; the total dose  $D_i$  fractionated typically into fractions of approximately 2 Gy per 24 h; often therapy is paused during the weekend

**Hyperfractionation** integral dose is sub-divided into a larger number of smaller fractions

**Hypofractionation** a fewer number of fractions with a higher dose each is applied

**Accelerated** fractions are delivery in shorter time-intervals leading to an overall shorter treatment time

**Concomitant boost** an additional boost-dose of radiation is applied, either within temporal or spatial confines, to the tumour

**Split course** a longer treatment pause is included in the schedule which typically lasts for several days

Each of the general schedules can be considered to be especially effective in a given therapeutic situation. While hyperfractionated schedules are suitable to treat a late-responding tissue, an accelerated schedule can be of great use in order to overcome regrowth in a fast dividing tumour.

Hypofractionated treatments will produce increased rates of late effects (when their dose is adjusted to give equal acute effects to conventionally fractionated treatments), while hyperfractionated treatments show lower rates of late effects. This is reasonable as the high dose per time in hypofractionation will allow relatively low repair in surrounding benign tissue. While this increases chances for secondary malignancies it can be of great use in palliative treatment, when secondary cancer is of lower importance than simple survival due to a reduction of the tumour burden.

Hyperfractionation trials such as the one performed by the European Cooperative Group (EORTC 22791) in the 1990s showed an increase in local tumour control from 40 to 59% which also resulted in an improved 5-year survival. At the same time, the side effects of the treatment did not increase. The dose-response relationship is characterised by a slightly higher surviving fraction among late-responding tissues at lower doses and a significantly lower survival at high doses compared to early responding (tumour) tissues [28].

Accelerated treatment delivers the same dose in a shorter amount of time, giving multiple fractions of the same dose per day. Especially in the case of multiple doses a day (e.g. three+), it has been shown that this type of fractionation will drastically increase late effects as bystander tissue is not able to repair sustained damage before the next fraction is applied. In trials (EORTC 22851) it was shown that while local tumour control was increased this did not translate into a survival advantage. However, acute and late effects were increased, thus rendering this treatment only useful for very special cases where it must be used to overcome rapid accelerated repopulation of a fast-growing tumour.

A number of very specific treatment schedules exist, one very prominent member of this class being the CHART (Continuous Hyperfractionated Accelerated Radiation Therapy) schedule which applies 36 fractions over 12 days, with 3 fractions a day at an interval of 6 hours and a dose per fraction of 1.4 to 1.5 Gy to a total dose of 50 to 54 Gy . CHART was able to achieve an increase in local tumour control in clinical studies [192]. It counteracted the repopulation of the tumour by a short time in between fractions and also the overall growth due to the relatively short time of the total protocol (12 days). Acute effects were increased, but late effects stayed acceptable because of low integral treatment dose.

## 2 Model

The actual design of protocols is a very involved process, as a high number of coupled effects such as regrowth, reoxygenation, accelerated population, early and late response of tissues, chance of secondary malignancies et cetera have to be carefully weighted as discussed in [86].

### 2.5.6 Implemented radiation model

As discussed in the previous section, only a minimal irradiation damage model has been implemented in order to keep the simulation as simple as possible. Cell cycle redistribution, repopulation and reoxygenation as main effects of interest are included (compare to the 4Rs in the previous section), other effects of irradiation have been neglected. As the radiation model under consideration is only one part of the class-based simulation it can be easily expanded or exchanged at any time if necessary.

The cell radiation response is based on cycle phase specific single cell survival parameters  $\alpha_p$  and  $\beta_p$  for Chinese hamster cells (V79 line). They were measured for irradiation with 250 kV X-rays at a dose rate of 1.1 Gy/min in [206] and [204] (see figure 2.37(a)). Alternatively, LQ survival parameters from heavy ion irradiation of CHO cells with carbon ion at 11 MeV energy can be used [198]. For the later case, no dependence on the cell cycle phase is available and therefore the heavy ion irradiation is only modelled in specific cases. A sample of available datasets for cell survival is provided in table 2.7.

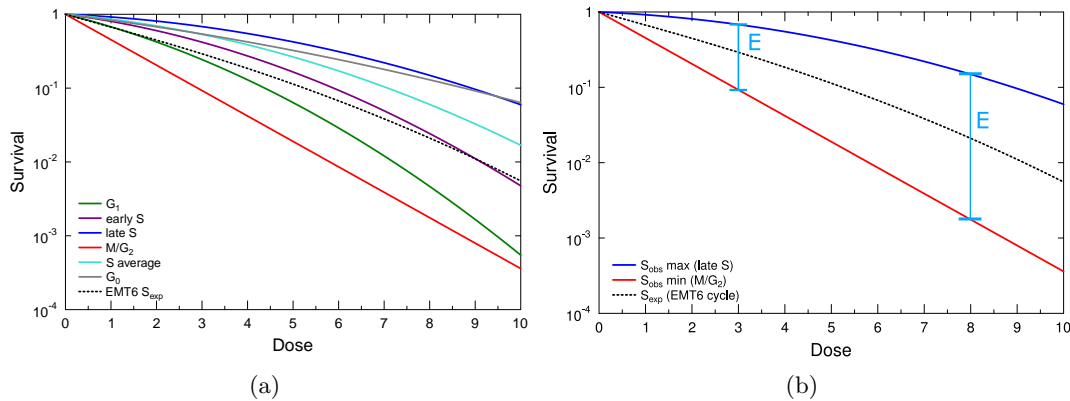


Figure 2.37: Cell cycle based survival including the average S-phase survival used in the simulation, survival of resistant quiescent cells (modelled as  $G_1$ -survival at reduced dose with resistance factor between 1 and 2), and the expected survival  $S_{exp}$  for the weighted cell cycle times from EMT6 cells used for calculation of the enhancement  $E$ . At higher doses the variation of the enhancement  $E$  is larger as can be seen by comparing relative survival probabilities.  $\alpha_{G1} = 0.351$   $\beta_{G1} = 0.04$ ,  $\alpha_{eS} = 0.185$   $\beta_{eS} = 0.035$ ,  $\alpha_{lS} = 0.062$   $\beta_{lS} = 0.022$ ,  $\alpha_{M/G2} = 0.793$   $\beta_{M/G2} = 0$  for V79 Chinese hamster cells [204], quiescence resistance according to [142].

In order to modify the cell survival by the oxygen enhancement ratio, the effective dose applied to each cell will be scaled by the OER before calculation of the according survival probability. Thus, hypoxic cells will experience a survival which corresponds to a reduced radiation dose due to their radioresistance.

As discussed in the previous sections, cell cycle effects (CCR) and OER are of the same order of magnitude in x-ray radiation and for other radiation types with low LET. Cyclic

Cells	Type	Radiation	Remark	Source
AG1522	monolayer	$\gamma$ , C (9.8 MeV)	no cell age	[247]
A549	suspension	$\gamma$	no cell age, split-dose	[148]
MCF7	suspension	$\gamma$	no cell age, split-dose	[148]
CHO	suspension	C (11 MeV)	no cell age	[198]
V79	monolayer	C (11 MeV)	cell age	[204]
V79	spheroid	C	no cell age	[213]
SCC VII	<i>in vivo</i>	$\gamma$ (C60), C 290 MeV	quiescent	[146]
EMT-6	<i>in vivo</i>	$\gamma$ (300kV)	chemoradiotherapy	[174]

Table 2.7: Selection of publications which contain cell survival data for the linear-quadratic model, which can be used for the simulation.

responses are thus as important as the oxygen effect in dose modification [204].

The increased radioresistance of quiescent cells follows measurements by [142]. Quiescent cells will thus exhibit an increased resistance to radiation damage by reduction of the effective dose they receive. By default a factor of 1.5 is used to scale the dose which corresponds to measurements in [142, 145] (see figure 2.37(a)). The tumour will thus show an altered response to irradiation which depends on the current cell cycle distribution and the size of the quiescent sub-population.

Repair-dynamics are not modelled directly within the simulation. As discussed in section 2.5.2 the majority of sublethal damage repair will happen on a timescale of under 2 hours which is shorter than the shortest investigated treatment interval in our scheduling tests (see [87] for DNA damage kinetics obtained by  $\gamma$ H2AX foci measurement). Thus a cell which initially would have suffered damage but subsequently has been able to repair this damage is considered to be clonogenic and healthy at all times in our model. As we will see, this does not affect the correspondence of the observed cell cycle response to experimental measurements. The focus of the investigation is on the macroscopic dynamics of the tumour and not on single-cell repair kinetics.

If a dose of radiation is applied in the simulation, usually a homogeneous distribution of the radiation will be assumed. However, targeting of subregions within the tumour is possible at arbitrary precision. Examples of targeting include selection of only the outer layer for irradiation or an effective splitting of the tumour by high-dose irradiation of a central cut-plane. Also if particle irradiation is modelled, the assumption is that irradiation within the spread-out Bragg peak of heavy ions will on average distribute an isotropic dose everywhere in the system, as the maximum observed system size is 1.5 mm. Local variations in LET or dose effects can be integrated into the model.

Overall, the single cell survival probability  $S(p, pO_2, q)$  from the LQ-model will finally depend on cell phase  $p$ , local oxygenation  $pO_2$  and cell quiescence status  $q$ . Cells within an affected volume of the tumour will subsequently draw a random probability to determine their fate which will mark them either as surviving cell or dying cell.

Once committed to the death path, a cell can be killed immediately via a fast mecha-

nism (with a given probability called “apoptotic chance”  $AC$ ) or a slow mechanism (inverse probability  $1 - AC$ ) as indicated in figure 2.38. The fast mechanism correspond to direct commitment of the cell to apoptosis in response to heavy DNA damage (e.g. clustered lesions) which cannot be repaired and is sufficient to trigger an apoptotic reaction (lethal damage). The slow mechanism corresponds to severe DNA damage and thus a prolonged inability to pass the G2/M checkpoint (potentially lethal damage which could not be repaired). It is eventually followed by mitotic catastrophe or any other event which will lead to a delayed apoptosis. The latter mechanism will lead to the pile-up of cells in the  $G_2$ -phase after irradiation. Repair of sublethal and potentially lethal damage is not modelled explicitly as it will be contained in the obtained LQ cell survival probability.

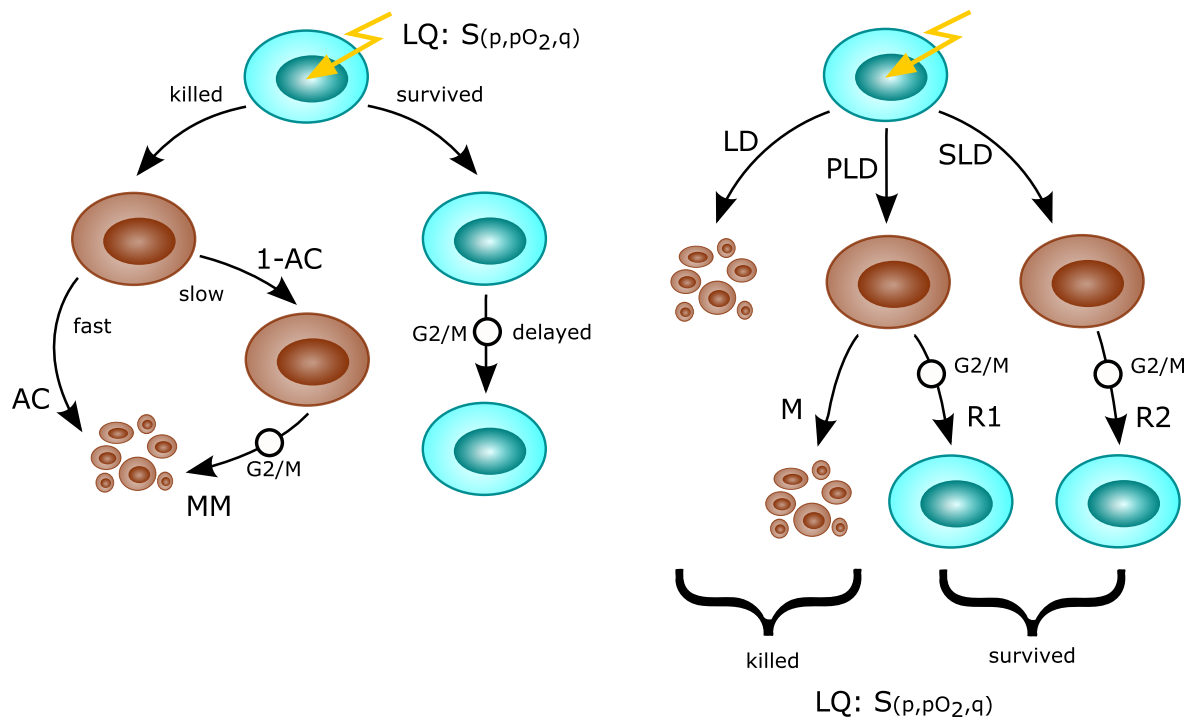


Figure 2.38: Illustration of the irradiation response model which is used in the simulation by default (**left**) and an alternative probability-based model which has been implemented (**right**). The default model uses the linear-quadratic cell survival as input and will only require two parameters (apoptotic chance  $AC$  and mitotic mismatch chance  $MM$ ) to reproduce experimentally measured cell cycle reactions to irradiation. Alternative models will usually require a significantly higher number of parameters for damage and repair kinetics and the resulting total survival and killing must be in agreement with the survival predictions of the LQ-model.

A fraction of cells which have been marked as “surviving” according to their survival probability can be delayed at the G2/M checkpoint in order to simulate cell cycle delay as a result of repair of sub-lethal damage. However this is not done by default, as it is not necessary in order to match the cell cycle dynamics after irradiation to experimental measurements and would introduce further parameters.

Radiobiologically, no distinction is made between apoptosis and necrosis except for an altered clearing time for the dissolution of cells in the model. The main difference would be the immunogenicity of the cell death modes, however immune effects will not be present

within an *in vitro* spheroid model. Apoptosis remains the exclusive mode of cell death for radiation-affected cells, while necrosis is exclusive to nutrient-induced death, which allows for an easy separation of the two mechanisms in the results. A mixed mode of radiation-induced death which uses apoptosis or necrosis in dependence of the radiation LET as shown in figure 2.36 can be introduced but will not lead to significant changes of the radiation response in absence of further mechanisms which depend on cell death as bystander killing or immune effects.

The radiation quality is included explicitly by the survival probability  $S(p, pO_2, q)$  or respectively  $S(pO_2, q)$  for HI-irradiation as no cell-cycle dependence is defined. Also the oxygen enhancement ratio will vary depending on the radiation type. Furthermore the radiation quality will influence the branching of fast and slow cell death.

This radiation model has the advantage, that it uses an experimentally verified survival probability as starting point and describes the according dynamics with only 2 parameters in use (AC and MM) and an optional delay of surviving cells (which is not used by default). It can be further simplified to a simple kill/survive model by omitting the discrimination between fast and slow death, which will yield results which are still in good agreement with experimental measurements.

Other radiation models have been implemented and tested, one example of a repair-mechanism, probability-based model is visualised in figure 2.38. Being based on different types of damage such a model will require significantly more parameters, as the exact amount of lethal, sub-lethal and potentially lethal damage caused by radiation, the repair rates  $R$  of the according damage type and chances for misrepair  $M$ . While this allows for a more precise description of the radiation quality in terms of damage types, a precise determination of the according rates on the basis of the currently available measurements seems infeasible. As this type of model does not use the LQ-survival as input in a top-down approach, the results of the model in terms of overall survival and overall cell killing will eventually have to correspond to the predicted survival from the LQ-model.

The minimal model of radiation damage effects will be sufficient to reproduce the radiation response in accordance with experimental measurements. A range of reactions will furthermore not depend directly on the radiation damage model but on other mechanisms, such as the reactivation of quiescent cells or the redistribution of cells in the cycle phases. Thus a simplified approach is suitable to be used in the investigations.

Mechanism	Implemented	Used by default	Sources
Cell cycle redistribution	yes	yes	[204],[245]
Reoxygenation	yes	yes	[245]
Reactivation	yes	yes	[245]
Oxygen enhancement	yes	yes	[86]
Quiescent resistance	yes	yes	[142]
Adhesion expression	yes	no	[10]
Repair of light damage	no	no	[189]
Vascular changes	no	no	[131]
Bystander effect	yes	no	[96]
Immune activation	no	no	[58]
Motility changes	yes	no	[12]
Lactate and radioprotectors	no	no	[100]

Table 2.8: Overview of possible effects of radiation on tumours, their implementation in the model, and according literature sources.

### 2.5.7 Summary

#### Summary 5 (*Radiation model*)

- Ionising radiation can kill cells or limit their clonogenicity by induction of DNA damage, changes in their gene expression
- Cells show a cell cycle phase specific radiosensitivity mainly as the availability of repair mechanisms and the localisation of DNA changes
- Hypoxia will limit damage to cells and thus increase their survival probability (OER)
- Quiescent cells will show an increased radioresistance
- Further effect include bystander damage, microenvironment and adhesion effects
- The radiation model uses cell-age/cell-cycle phase dependent LQ-survival values from experimental measurements [204]
- Quiescent resistance and oxygen enhancement and included in the survival probability
- Damage repair is neglected as its timescale is lower than typical fractionation times in the model
- Minimal damage dynamics are included via a branching between fast commitment of killed cells to apoptosis with probability  $AC$  or slow cell death by mitotic mismatching with the inverse probability
- For  $AC=1$  a minimal LQ-based kill/survive model is obtained

## 2.6 Chemotherapy and adjuvant therapies

Radiation is almost never applied as stand-alone therapy, but is combined with a surgical resection or chemotherapy as a multimodal therapy. The shrinkage of a tumour mass before application of radiotherapy is considered to be of paramount importance in order to reduce the necessary dose for treatment and increase therapeutic outcome. In neoadjuvant chemotherapy (preoperative treatment), an initial chemotherapy is administered in order to shrink the primary tumour before local therapy using surgery or radiotherapy. An adjuvant therapy can also be applied after or concurrently during irradiation regimens and surgical treatments in order to employ multiple anti-cancer effects at the same time or minimize the chances of a recurrence. The question of a synergistic combination of chemo- and radiotherapy either as induction chemotherapy and concurrent chemoradiotherapy has received a lot of attention in recent years. An overview of clinical trials which studied different forms of induction chemotherapy and concurrent chemoradiotherapy is given in [234].

In the case of adjuvant chemotherapy, numerous synergies between drugs and radiation have been investigated both experimentally and clinically e.g. for hydroxyurea versus misonidazole [218], temozolomide and radiotherapy [3, 177] or tirapazamine, cisplatin, and radiation [178]. Almost all studies confirm the benefits of chemoradiotherapy in terms of an increased locoregional control and median survival. However, to the knowledge of the author, no modelling approaches have been undertaken to understand the dynamical interplay between chemotherapies and tumour spheroids in respect to the cell cycle kinetics. Such a model can predict optimal combinations of radio- and chemotherapy for further experimental investigation.

### 2.6.1 Anticancer drugs and synergy in chemoradiotherapy

Modern anticancer drugs use a wide range of mechanisms whose introduction is far beyond the scope of this work. Figure 2.39 provides a basic overview of different classes of chemotherapeutics. A common classification is achieved by the mechanisms of interaction between the drug and the cancer cells. Many drugs will only affect cells in certain phases of the cell cycle as is indicated in the figure. As a consequence, administration of these drugs will often lead to a synchronisation of cells [149]. This can be of great interest for a combination with other treatments.

Non-specific drugs such as alkylating agents will affect all dividing cells alike, exploiting the fact that most tumour-cells are fast-dividing. The drawback is immediately evident: not only can slowly-dividing tumour cells (such as cancer stem cells) escape the mechanism of

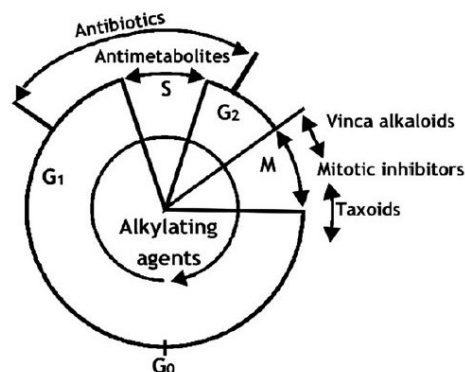


Figure 2.39: An overview of the cycle points at which different anticancer drug types will act on the cell from [1].

action but also benign but fast-dividing cells such as hair-follicles or the intestinal linings will be severely affected. Antimetabolite compounds are a class of drugs which act only on cells in a specific cycle phase. Their main mechanism of action is an inhibition of normal DNA synthesis using analogues to the normal building blocks of DNA which will be incorporated by cells in the synthesis phase. However, they will show the same drawback as alkylating agents. Many drugs can also act as radiosensitizers, that is they effectively increase the sensitivity of cells to radiation damage, either as their main effect or as an additional action. Prominent examples of this type of anticancer drugs are 5-fluorouracil and cisplatin. Cytostatic drugs, which effectively halt the cell cycle progression of cells via a range of different mechanisms are another frequently used type of drug. They can be used in order to slow down or halt the growth of tumours at least for a limited time before any resistance can develop. A more modern and highly specific approach is offered by targeted therapies which make use of specific mechanisms (e.g. antibody-principle) that are mainly or exclusively observed in cancer cells of a certain type. This enables targeted therapies to either design drugs which mainly or even exclusively affect cancer cells, or release a coupled drug compound only in the presence of cancer cells. While many drugs are only effective in the presence of normal oxygen concentrations, some drugs are metabolised and activated only in hypoxic regions. These hypoxic cytotoxins are therefore very interesting for a use in adjuvant treatment, since they can target cells specifically in hypoxic regions where other approaches are often strongly diminished in their effectiveness due to resistance.

With the use of chemotherapeutic compounds, a high degree of control over the cell cycle progression can be achieved. Depending on the type of drug which is administered cells can be halted at specific checkpoints during their cycle as demonstrated in [186]. In combination with radiotherapy, these mechanisms can be used to prepare tumours into a sensitive state or counteract unwanted dynamic reactions which are triggered by radiotherapy.

Many widely used chemotherapeutica like Doxorubicin or Mitomycin C have been shown to work strongly synergistically with radiotherapy. A comprehensive list of known synergies between drugs and radiation is provided in [84].

### 2.6.2 Hydroxyurea

Hydroxycarbamide (also hydroxyurea or HU) is one example of drugs which are noted to show only low synergy with radiation. Nevertheless, the effects of hydroxyurea make it extremely interesting for a combination with radiotherapy, provided the cell kinetics which are triggered by its administration can be predicted.

Hydroxyurea's main mechanism of action is its effectiveness as an inhibitor of DNA synthesis, which makes it a selective toxic drug for cells in S-phase. A second effect is the inhibition of cell cycle advancement from G1 phase to synthesis phase. If applied with a sufficiently high concentration, HU will thus kill the majority of cells in S-phase and gather all cells at the G1/S checkpoint in a synchronous state (as shown in figure 2.41). When hydroxyurea is removed from the system it will release cells from the G1/S-block and permit cell cycle progression in the population (see also figure 2.40). Because of these properties HU is often used experimentally in order to synchronise cell populations in preparation for following investigations. A more detailed description of hydroxyurea's effects including its synergy with radiation can be found in [205] or [86].

Hydroxycarbamide has a high distribution and availability throughout the body as reported

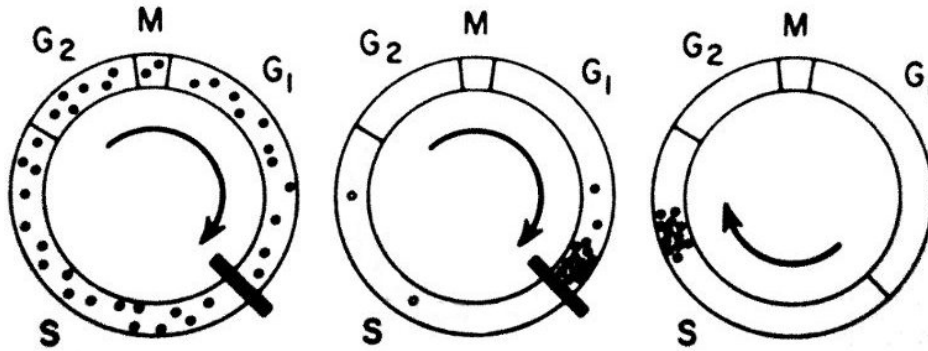
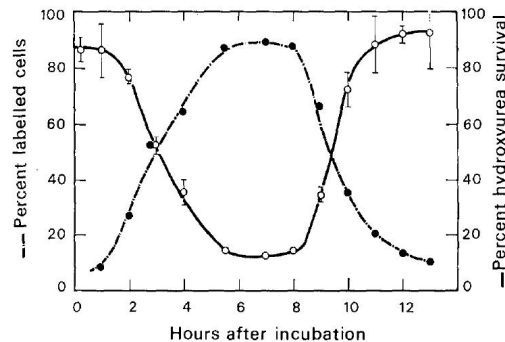


Figure 2.40: Illustration of the main mechanisms of action for hydroxyurea (HU) adapted from [84]. After administration HU will kill cells in S-phase and prohibit progression from G1 to S-phase for other cells. If HU is removed from the system a synchronous population is released from the block.

Figure 2.41: Percent of V79 cells labelled by autoradiography (in synthesis phase) and according cell survival in response to 1mM hydroxyurea for at least two hours. Radiosensitivity and chemosensitivity are exactly opposed which makes a combination of both treatments interesting. Adapted from [25].



in [211]. It was shown that upon administration of 80 mg/kg within two hours a serum concentration of 2 mM will be reached within 2 h which remains above 1 mM for 4 h and 0.5 mM for 8 h [14]. Hydroxyurea can furthermore penetrate the blood-brain barrier, which increases its potential use in radiotherapy of brain tumours. As a drug it is commonly employed in the treatment of neoplasia, myeloproliferative disorders, sickle-cell disease and AIDS. In combination with radiotherapy, it is employed in regimens such as TFHX (taxanes, 5-fluorouracil, hydroxyurea, x-ray) for which a significant survival advantage for patients has been observed in clinical trials [90]. Other uses of HU in chemoradiotherapy have been the target of recent investigations as for example [217], [166] and [42]. Even if all clinical studies showed benefits from radiochemo, one of the conclusions is a lack of understanding of the exact interplay between drug and radiation. Stehman concludes that the “...optimal dose and schedule of hydroxyurea is unknown.” [218] To the knowledge of the author, there exists no detailed *in vivo* study of the cell kinetic effects which are triggered by HU-application. This makes it especially interesting to investigate the effects in a simulation, as the combination of hydroxyurea and radiotherapy appear highly beneficial as indicated in figure 2.41.

Within the agent-based model, the effects of hydroxyurea can be implemented in a straightforward manner (see also figure 2.42): if the local concentration of HU is above a threshold, it will instantly kill any cell agent which is currently in synthesis phase via induction of apoptosis. This corresponds to the cell’s reaction to the failed synthesis of DNA as a result of hydroxyurea. Furthermore a cell agent will not be able to pass the G1/S checkpoint while a sufficient concentration of HU is present. It can be arrested indefinitely at the G1/S check-

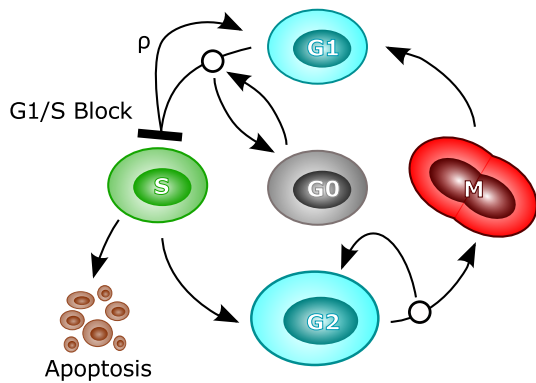


Figure 2.42: The effects of hydroxyurea within the agent-based model. A dose of HU will kill cells in S-phase by induction of apoptosis. Progression of cells into the S-phase will be blocked for as long as the drug is present. Cells which would reach the S-phase will draw a new G1-phase length from the normal distribution scaled with a factor  $\rho$  which allows for fast or slow reaction to HU-removal.

point in this manner. Thus cells are effectively synchronised at the G1/S checkpoint if HU is applied for a sufficiently long time.

Release of hydroxyurea, that is a drop in concentration below its threshold of action, will consequently release the block of cells and allow for a synchronised progression of cell agents through the cycle. The responsiveness of cell agents to changes in the concentration of HU can be influenced by the time-interval for being halted at the G1/S checkpoint. Cells will draw a modified G1-phase length for being halted at the checkpoint. This phase length can be altered by the scaling factor  $\rho$  to arbitrary small values, allowing for everything from an instantaneous reaction of cells to a spread-out response over the duration of a whole G1-phase length or even more. By default it is assumed that cells can respond to a release at the G1/S checkpoint quite fast. A scaling factor of  $\rho = 0.1$  is used to obtain a new reduced G1-phase length whenever blocked cells would advance past the G1/S checkpoint. Thus cell agents can, on average, respond to a change in hydroxyurea within 48 min.

### 2.6.3 Drug distribution, pharmacodynamics and -kinetics

A significant problem in chemotherapeutic approaches is the delivery of drugs to the tumour cells. Many therapeutic approaches rely on the administration of soluble drugs. In the best case the drug can be part of a targeted therapy and thus be released only in the tumour volume as a result of a tumour-specific marker mechanism. The worst case scenario is the systemic administration of a huge dose of the drug in order to achieve a sufficient concentration in the tumour volume. While in this case effects will be visible throughout the whole body they might be strongest in the desired region of interest.

Concentration gradients of nutrients, oxygen and drugs arise locally as a consequence of limited diffusion from blood vessels through a heterogenous microenvironment [170]. While molecular mechanisms of drug resistance have been studied in detail, the effects of the tumour microenvironment have been widely neglected. The predominant use of monolayer cultures in experiments which lack all effects of a microenvironment has led to a lack of knowledge when effects of this environment are concerned as was stated in [153].

Drug penetration and transportation in tumour tissue itself requires sophisticated modelling as discussed in [153], [132] and [108]. A complete model would need to consider the global availability of the drug (its pharmacodynamics), local supply to the region of interest, extravasation and flux through the tissue or interstitial spaces and the detailed consumption of the drug by the local cells as indicated in figure 2.43.

## 2 Model

Extravasation of drugs from a vessel can occur by diffusion and convection. The flux  $J$  of a drug through a vessel wall has been described by Jain [107] using the equation

$$J = \kappa S dC + L_p S (1 - \sigma) [dp - \sigma d\pi] C_p \quad (2.58)$$

Thus a multitude of parameters need to be known in order to accurately describe the extravasation, including the vascular permeability  $\kappa$ , the vessel surface area  $S$ , the concentration difference between plasma to interstitial space  $dC$ , hydraulic conductivity of the vessel wall  $L_p$ , the pressure difference between vascular and interstitial space  $dp$ , the osmotic reflection coefficient  $\sigma$ , and the osmotic pressure difference  $d\pi$ .

Once extravasated into the interstitial matrix of a tissue, the flow will be determined by a mixture of diffusion and convection, which can be described by

$$\frac{\partial C}{\partial t} + v \nabla C = D \nabla^2 C + R \quad (2.59)$$

with concentration  $C$ , the pressure-dependent interstitial fluid velocity  $v$ , diffusion coefficient  $D$ , and reaction term  $R$  which described binding and degradation of the drug [108]. As the fluid pressure tends to equilibrate inside the tumour, the convection component will only be of importance in the outer layer of the tumour.

While in the specific case of hydroxyurea some parameters for the pharmacokinetics and pharmacodynamics are available in the literature [211], it is obvious that a complex model for the drug distribution would introduce a wide range of uncertain parameters to the model. Thus the development of a fully-detailed model for the HU concentration in a compact tissue is beyond the scope of this thesis.

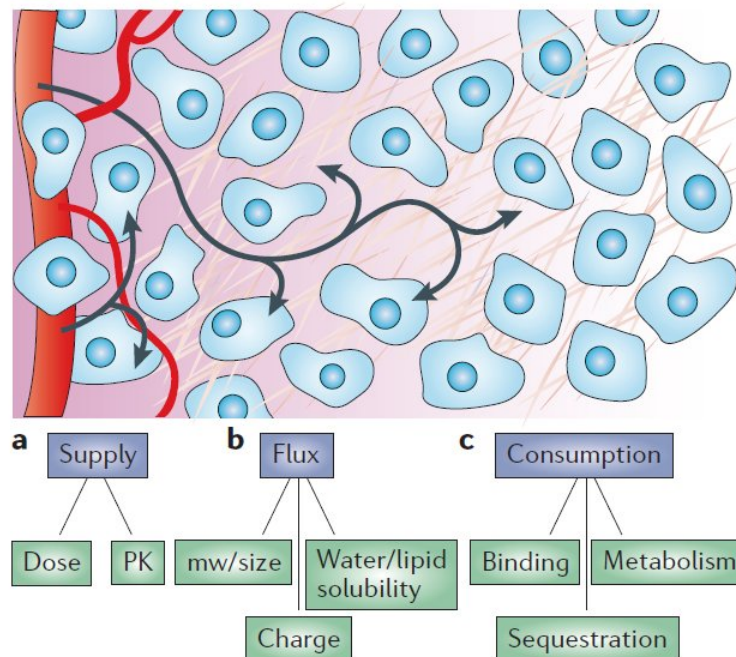


Figure 2.43: An overview of important phenomena for drug availability in tumour tissue from [153].

For the *in vitro* experiments under consideration within this thesis, drugs will be usually mixed into the nutrient medium which sustains the cell growth. Thus in the case of a growing cell spheroid, the drug has to diffuse into the tumour volume in order to have an effect. This mechanism can either be modelled directly using a diffusion grid or a dedicated pharmacokinetics approach.

Assuming an infinite reservoir of the drug in the medium, fast diffusion, and a constant metabolic degradation/consumption of the drug in the tissue, the distribution inside the tumour can also be approximated using a steady-state approach. Thus, for a spherically symmetric tumour, the concentration of the drug will depend on the concentration in the medium  $C_o$  and on the radial distance  $|r|$  from the tumour boundary via an effective decay constant. This decay constant  $\eta$  depends on the local drug penetration/diffusion, degradation and metabolism and will usually not be available.

For modelling of *in vitro* experiments such as flask or spheroid culture a drastic simplification of the drug availability throughout the system can be used.

One assumption in regards to the drug distribution is that the drug compounds are sufficiently small in order to diffuse efficiently into the tumour, or at least into the viable regions.

Availability of the drug will be constant in the nutrient solution which surrounds a tumour spheroid. A natural assumption is a concentration gradient of the drug from the boundary to the centre of the spheroid, e.g. following an inverse-square law. By adjusting the concentration of drug in the medium, so that within viable regions it will always be above the threshold dose required for drug action, a constant effect of the drug can be achieved throughout the tumour. The tissue depths at which a threshold concentration of the drug must be exceeded is quite low in tumour spheroids with about 300  $\mu\text{m}$  to 400  $\mu\text{m}$ .

## 2.6.4 Summary

### Summary 6 (*Adjuvant therapies and drugs*)

- A combination of radiotherapy and chemotherapy as multimodal treatment of cancer is today's standard
- Induction- or concurrent chemotherapy are both used in combination with radiotherapy
- Hydroxyurea (HU) is a chemotherapeutic drug which is part of established clinical treatment plans (e.g. TFHX)
- HU selectively kills S-phase cells and prohibits cycle progression past the G1/S checkpoint which can be directly implemented as effects in the agent-based model
- A drug concentration above the action-threshold can be achieved in the whole tumour by choosing a sufficient concentration in the medium (high-dose approximation)
- *In vitro* HU is cleared from the system fast via medium change and washing with PBS, this corresponds to an instantaneous removal of the drug in the simulation
- Cell agent ability to react to a release of the hydroxyurea-initiated G1/S-block is determined by a scaling factor  $\rho$  which acts on the G1-phase length used as restriction time

## 2.7 Observables

Some observables which will be used within the investigation are self-explanatory or have been derived from typical experimental measurements. This includes the observables of mitotic index (MI, the fraction of mitotic cells among viables), the labeling index (LI, fraction of S-phase cells often labelled by autoradiography) or the potential doubling time ( $t_{\text{pot}}$ ) of the tumour. Further observables have been defined to be used in assessment of the tumour treatment response.

### 2.7.1 Tumour burden

In order to compare the success of treatment schedules, the observable of **tumour burden** is introduced. It is defined as integral of the total viable cell number  $C(t)$  over the time of interest  $T$ :

$$\text{AUC} = \int_T C(t) dt. \quad (2.60)$$

This measure allows for a straightforward comparison between the strength of tumour growth. If the time window for integration is restricted to the time of treatment during fractionated irradiation, the ratio of two AUCs for different schedules can be used to point out the increase or decrease in therapeutic effectiveness. A reasonable unit for the AUC within this thesis is  $10^6$  cell day.

### 2.7.2 Radiation survival and enhancement

In order to assess the level of survival and possible loss and gain in efficiency due to cell cycle variations, different observables are introduced.

The most simple measurable is the **observed survival**  $S_{\text{obs}}$  of a tumour in response to a mock irradiation at the moment of interest. The impact of a dose of radiation is measured without subsequent application of the according changes to the tumour system. Relating the amount of surviving cells  $c_{\text{viable}}$  to the amount of killed cells  $c_{\text{killed}}$  yields the observed survival:

$$S_{\text{obs}} = \frac{c_{\text{viable}}}{c_{\text{killed}}} \quad (2.61)$$

This measure gives a reliable expression of how efficient a radiation dose would be at a given time in the current tumour state. The observed survival will be determined by the current fraction of cells in each cycle phase weighted by the dose and cycle-phase dependent survival probability for each phase.

In order to obtain a relative measure of enhancement, the observed survival  $S_{\text{obs}}$  can be related to a baseline-level of expected survival  $S_{\text{exp}}$ , which would be typically associated with the irradiation of a tumour with the given dose.

The **expected survival**  $S_{\text{exp}}$  is defined as the average of the survival probabilities of the active cell cycle phases. Each cell cycle specific survival probability from the LQ-model  $S_p$  is thus weighted with the relative average duration of the according phase  $\tau_p$ :

$$S_{\text{exp}} = \sum_{p=[G_1, S, G_2, M]} S_p \tau_p \quad (2.62)$$

This expected survival reflects the typical survival of an exponentially growing tumour without quiescent sub-population and with uniform distribution of the cells proportional to the cycle phase-lengths (as will be the case for unsynchronised growth).

The ratio of observed and expected survival is defined as **enhancement**  $E$ :

$$E = \frac{S_{\text{exp}}}{S_{\text{obs}}} \quad (2.63)$$

If fewer cells survive a radiation dose at the current time than expected, the enhancement  $E$  will be greater than 1, while an enhancement below 1 will indicate that fewer cells are killed than would be expected on average. Thus  $E$  is a measure of enhancement dependent on the current state of the tumour.

While the measure of the observed survival does include quiescent cells, the phase length-dependent average of expected survival cannot, since no typical phase length is associated with quiescence. Furthermore an explicit survival probability cannot be defined for the quiescent cells directly, as standard colony forming assays cannot be applied. However, estimates using micronucleus frequencies are available, which show that the radioresistance of quiescent cells is increased (see also section 2.5.1). As this has been incorporated into the model, the presence of a quiescent population will lead to an increase in observed survival, while the expected survival for the tumour remains constant. Thus the rise of a quiescent population will lead to a decline in the enhancement  $E$ , as would be expected for such a measure.

It is expected that the enhancement  $E$  decreases during the formation of a large tumour spheroid and will be increased in response to irradiation. If raised to a level of 1 this means that the resistance effect of a quiescent population has been removed (or that some synchronising effect increased the sensitivity). Measures greater than 1 indicate that the tumour was brought into an especially sensitive state.

### 2.7.3 Enhancement as true measure for sensitivity

The spread between survival of radioresistant S-phase cells and sensitive M-phase cells grows larger with increased dose (at least for reasonable fraction sizes of up to 10 Gy) as seen in figure 2.37(b). Therefore, at higher doses, the cell cycle distribution can lead both to a larger enhancement of radiosensitivity or a strong decrease in radiation efficiency, increasing the possible variation width of the observable  $E$ .

$S_{\text{exp}}$  is calculated by weighting the cell cycle specific survival with the relative EMT6 cell cycle durations (G1: 0.41, S: 0.31, G2: 0.23, M: 0.05).

Even if the level of survival is different at different dose levels, the enhancement will still reflect the deviation in radiosensitivity that the tumour shows when compared to an exponentially growing tumour with uniform cell cycle phase distribution when irradiated with the given dose.

### 2.7.4 Maximum total cycle length and relative cycle position

The maximum cell cycle length is the result of drawing single cell phase lengths from Gaussian distributions. It will be given by the sum of normally distributed random variables according to:

$$\begin{aligned} X &\sim N(\mu_X, \sigma_X^2) \\ Y &\sim N(\mu_Y, \sigma_Y^2) \\ Z &\sim N(\mu_X + \mu_Y, \sigma_X^2 + \sigma_Y^2) \end{aligned} \quad (2.64)$$

Since a cutoff distance  $c$ , defined relative to the mean  $\mu$ , is used, a maximum cell cycle time  $T_{\max}$  can be defined as a sum of the single maximum cell cycle phase times  $\tau_p^{\max}$ :

$$\begin{aligned} \tau_p^{\max} &= \mu_p + c\mu_p \\ T_{\max} &= \sum_p \tau_p^{\max} \end{aligned} \quad (2.65)$$

$T_{\max}$  will be the absolute maximum of active cell cycle duration within the simulation. The total cell cycle duration however can be arbitrarily long, as cells can stay in quiescence for arbitrary periods of time.

Each cell will draw *individual* cell cycle durations at its generation to determine the length of its current cycle. A maximum cell cycle time for the individual cell  $T_i$  can be obtained as a sum of its individual phase-lengths. The current active cell cycle time  $t_i$  is given by the time which was spent in the active cycle phases (not advancing if a cell is quiescent). Thus a relative progression through the cell cycle  $\phi$ , also called **phase-angle**, can be defined for every cell as

$$\phi_i = \frac{t_i}{T_i}. \quad (2.66)$$

Figure 2.44 illustrates the relationship between  $T_{\max}$ ,  $T_i$  and  $t_i$ . For an equilibrated system each cell cycle phase will contain an amount of cells  $c_p$  which will correspond to its relative length in the total cycle  $T_{\max}$ .

The measure  $\phi$  can be used to compare the relative progression through the cell cycle among different cells.

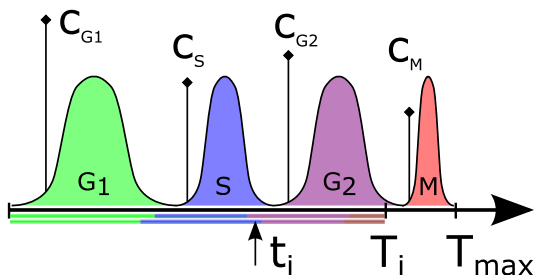


Figure 2.44: Duration of individual cell cycle phases are random Gaussian variables with a defined cutoff, so an absolute maximum active cell cycle time of  $T_{\max}$  is globally defined. Each cell will have an individual maximum cell cycle time  $T_i$  and a current active cell cycle time  $t_i$ , so that a relative progression through the cell cycle can be defined as  $\phi_i \in [0, 1)$ . However if two cells show the same relative progression, they can still be in different functional cell cycle phases as indicated by the coloured bars.

### 2.7.5 Synchronicity of cell populations

Biologically, the amount of observables which can be used to identify the synchronicity status of a population is limited [152]. While synchronisation of cell populations is often used within experiments and can be achieved in a number of ways (see [56], [63]), the actual level of synchronicity is almost never analysed quantitatively. Sinclair describes in [204] that the “true age [of cells] is difficult to describe”, as it is “obviously determined by its biochemical state at a given instant”. Still this biochemical state cannot be assessed with a precision that would allow a unified definition of single cell age or synchronicity.

A definition based on the functional cell cycle phase (or more precisely, the amount of DNA found in each cell) is possible by flow cytometry (FCM) using DNA-staining e.g. with propidium iodide (PI). Fluorescence-levels in each cell will correspond to the amount of DNA and thus allow a discrimination between cells with single DNA content ( $G_0, G_1$ ), mixed ( $S$ ) and double content ( $G_2, M$ ). This can only provide a coarse estimation of the cell cycle distribution but does not describe how synchronous these cells are within their phases.

Fluorescence-activated cell sorting (FACS) would also allow an investigation of the level of Cyclin-Dependent Kinases (CDKs) in cells, which in turn can be used to assign a distinct cell cycle position to cells. This method is more advanced, since it would be able to discriminate not only between group of phases but can possibly yield a continuous estimation of the cell position. However, to the knowledge of the author, such a method is not usually employed within experimental settings.

The precise determination of the synchronicity of cell populations is of great interest, especially in the collective development of cell cycle dependent radiosensitivity or when cell cycle specific treatments are to be planned. A measure for synchronicity can be constructed following different approaches which were developed in this thesis, a selection of which is presented in this section.

All approaches will exclude dead cells (currently undergoing apoptosis or necrosis) from the measurement, while they are safe to include quiescent cells. Since cells will enter  $G_0$  always after completion of  $G_1$ , the active cycle position  $\phi$  of these cells will be kept fixed at the position where they entered quiescence as long as the cells stay inactive. This can be a major contributor to synchronisation if a large number of cells are committed to quiescence.

#### Based on discrete cycle phases

The naive functional approach for an observable of synchronisation is to take into account the distinct cell cycle phases of each cell. Using integer phase values from 0 (quiescent) to 4 (mitotic) the standard deviation of the cell cycle population can be calculated. The cyclic nature of the distribution needs to be taken into consideration so that e.g. the distance between mitotic phase (4) and  $G_1$  (1) is 1 and not 3.

This definition will be functional and close to biology in the sense that cells are not considered to be distinguishable by the relative position within a single cell cycle phase but just by the functional cycle phase alone. A further simplification can be achieved by not distinguishing all cycle phases but just between the grouped phases of  $G_0 + G_1$ ,  $S$  and  $G_2 + M$  (that is by DNA content). However, this approach can show artefacts because of the different mean length of the cell cycle phases.

### Based on relative phase distribution

Synchronicity can be defined based on the relative amount of cells in a specific cycle phase  $c_i$ ,

$$\varphi = \sum_i \left(\frac{c_i}{C}\right)^2 \quad (2.67)$$

where  $C$  is the total number of cells. The sum can either include all viable cell cycle phases or only active cycle phases.

However, this measure does not take into account the circular nature of the cell cycle and thus is not really suitable for measuring synchronicity of a cell population.

### Based on cell cycle time difference

The minimum distance of all cells in a population with respect to their active cell cycle time can be used to define the synchronicity as

$$S_d = \frac{1}{n} \sum_i \sum_{j \neq i} d(i, j) \quad (2.68)$$

The distance  $d()$  between the cell cycle times  $i$  and  $j$  is defined as the minimum distance taking into consideration the circular nature of the cell cycle phases, that is:

$$\begin{aligned} d_1(i, j) &= |j - i| \\ d_2(i, j) &= \max - |j - i| \\ d_c(i, j) &= \min(d_1(i, j), d_2(i, j)) \end{aligned} \quad (2.69)$$

$\max$  is the average maximum cell cycle time (so the sum over all average active cell cycle phase durations, ignoring the width of the normal distribution). Due to the Gaussian distribution of the cell cycle phase lengths, the active cycle lengths of cells may exceed  $\max$ . This happens in about 3% of the cells with an average of 10% excess above  $\max$ . Either the maximum cell cycle length needs to be increased by a factor which reflects a typical excess resulting from the Gaussian phase lengths or the excessive active cell cycle times will be cut to  $\max$  when calculating the synchronicity.

The resulting value of  $S_d$  can be mapped onto the interval  $[0, 1]$  so that 1 corresponds to full synchronicity (all cells have the same active cell cycle time) and 0 corresponds to full desynchronisation:

$$O_d = 1 - \left(\frac{S_d}{\max/2}\right) \quad (2.70)$$

However the measure of orderedness  $O_d$  will report a full desynchronisation of the population even if the active cell cycle times are distributed as two distinct peaks with a distance of  $\max/2$ . This is obviously not a suitable choice for measuring the true synchronicity.

**Based on relative cell cycle progress**

Using the cell phase-angle  $\phi$  the standard deviation can be used as a measure of the total synchronicity of a population with size  $N$ :

$$\sigma = \sqrt{\frac{1}{N} \sum_{i=1}^N d(\phi_i, \bar{\phi})^2} \quad (2.71)$$

Since the cell cycle is a closed loop, the distance measure  $d(x, y)$  in the standard deviation needs to be adapted to identify the shortest distance between two relative positions, so that a cell with  $\phi_i = 0.1$  and  $\phi_j = 0.9$  will have a distance of 0.2 instead of 0.8. This can be achieved by again using the definition for a circular distance  $d_c$  (see also figure 2.45):

$$\begin{aligned} d_1(\phi_i, \phi_j) &= |\phi_j - \phi_i| \\ d_2(\phi_i, \phi_j) &= 1 - |\phi_j - \phi_i| \\ d_c(\phi_i, \phi_j) &= \min(d_1(\phi_i, \phi_j), d_2(\phi_i, \phi_j)) \end{aligned} \quad (2.72)$$

When using the synchronicity definition via the standard deviation of the relative cell cycle position  $\phi$ , the fact that cells will have different relative durations of each distinct cycle phase will be ignored. In terms of the individual total cycle length  $T_i$ ,  $\phi_i$  will always be in  $[0, 1]$ .

Normalisation of the resulting standard deviation would be required in order to map the synchronisation to  $[0, 1]$  where 1 should represent a fully synchronised system (all cells have the same  $\phi$ ) and 0 a maximally desynchronised system (uniform distribution up to the maximum total cell cycle length). However, if no binning is applied to discretise the number of states that  $\phi$  can be in, the calculation of a normalisation factor (that is, the maximal standard deviation of the system if cells are uniformly distributed within  $[0, T_i]$ ) becomes involved.

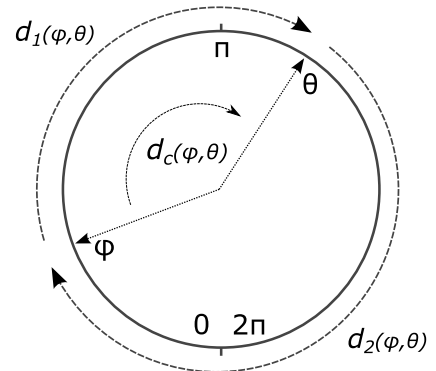


Figure 2.45: The circular distance of the cell cycle phase angle of different cells can be used to define the synchronicity of cell populations. Cells with a similar relative cell cycle progression (which can be mapped to  $[0, 2\pi)$  as in the example) will have a small circular distance  $d_c$ , which is the minimal distance between both cell cycle states.

It has to be noted that even though the relative cell cycle progress of each cell will be in the interval  $[0, 1)$  (or  $[0, 2\pi)$ ), the relative fraction of functional cell cycle phases within this interval will be different for each individual cell. That means that while two cells might have exactly the same relative cell cycle progression in terms of phase-angles  $\theta_i = \theta_j = \pi$  functionally cell  $i$  might still be in S-phase, while cell  $j$  already progressed to  $G_2$ -phase.

### Circular variance of phase-angles

We can calculate the angle of the circular cell cycle progression  $i$  by mapping the phase-angle  $\phi_i$  according to

$$\theta_i = \phi_i \cdot 2\pi. \quad (2.73)$$

The circular sample of cell phase-angles  $\theta_i$  can be used to calculate the circular sample variance and circular sample standard deviation which are defined by

$$\overline{\text{Var}(z)} = 1 - \bar{R} \quad (2.74)$$

$$\bar{S}(z) = \sqrt{\ln(1/\bar{R}^2)} = \sqrt{-2 \ln(\bar{R})} \quad (2.75)$$

and will take values from  $[0, 1]$  resp.  $[0, \infty]$ .

$\bar{R}$  is the length of the sample mean resultant vector of the cell population  $N$  which can be obtained by:

$$\bar{R} = \sqrt{\bar{C}^2 + \bar{S}^2} \quad (2.76)$$

$$\bar{C} = \frac{1}{N} \sum_{n=1}^N \cos(\theta_n) \text{ and } \bar{S} = \frac{1}{N} \sum_{n=1}^N \sin(\theta_n) \quad (2.77)$$

This yields an expression for the circular sample variance  $\overline{\text{Var}}$  that is dependent on the relative cell cycle angle  $\theta_n$

$$\overline{\text{Var}(\theta_n)} = 1 - \sqrt{\left(\frac{1}{N-1} \sum_{n=1}^N \cos(\theta_n)\right)^2 + \left(\frac{1}{N-1} \sum_{n=1}^N \sin(\theta_n)\right)^2} \quad (2.78)$$

which can be used as measure of synchronisation within the cell population. Additionally, the probably biased sample variance was transformed to an unbiased sample variance by applying Bessel's correction in equation 2.78, even though the sample size will be large enough during standard runs to avoid a bias of the variance.

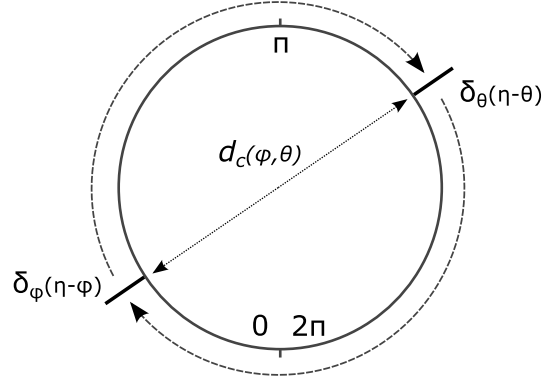
If "apparent synchronisation" is present, which would be caused by symmetric cell cycle distributions, this can be identified by using the skewness of the population (3rd moment). In extreme cases even the 4th moment of kurtosis must be taken into account, however, for biological distributions this is not to be expected.

Again, this definition of synchronisation is limited in its usefulness as can be demonstrated by assuming that the cells are distributed in two distinct delta-distributed peaks with an angular difference of  $180^\circ$  (see figure 2.46). The mean will be undefined and the variance is maximal, even though the total population is fairly synchronised in two populations.

### Based on Shannon entropy

A reasonable approach to measure the synchronicity of a cell population is by calculation of the Shannon entropy of the system. The circularity of the problem is of no concern in this formulation. For a discrete system of  $N$  states, the entropy can be simply calculated using

Figure 2.46: The circular variance will be maximal for a distribution of the angles in two distinct delta peaks with a distance of 180 degree (or  $\pi$ ) since the mean resultant vector  $|R|$  is zero. However this configuration would represent a cell population of medium synchronicity, so the variance measure fails for this type of distributions.



the probability mass function  $p(x)$  of the total population  $X$

$$H(X) = \sum_{i=1}^N p(x_i) \log_2 \left( \frac{1}{p(x_i)} \right) = - \sum_{i=1}^N p(x_i) \log_2 (p(x_i)) \quad (2.79)$$

with the assumption that

$$\lim_{p \rightarrow 0^+} p \log p = 0 \quad (2.80)$$

which can be confirmed using l'Hôpital's rule. In the case of our cell system, the probability mass function (pmf) can either be the binned distribution of cell phase-angles  $\phi$  from  $[0, 1)$  or the distribution of discrete physiological cell phases which are represented by an integer value (G1: 1, G2: 2, S: 3, M: 4).

The pmf can be approximated by using the number of cells in each bin or cycle phase  $x$   $c_x$  and the total number of cells  $C$ :

$$p(x) = \frac{c_x}{C} \quad (2.81)$$

Furthermore, a typical entropy for the system can be defined by estimating the average population in each cell cycle phase either by the observed normal cell count or by the relative length of each phase in comparison to the total cell cycle length. This typical entropy can be used to compute the deviation of the cell population from the normal state.

In order to rid the entropy calculation of the artefact of different cell phase lengths, the population of each phase can be rescaled by the according phase length and the subsequent probability mass function normalised by the total.

Alternatively, the entropy can be calculated for a probability mass function of the binned cell phase-angles  $\phi$ . Assuming a uniform distribution among  $N$  bins defined by the pmf  $p(x) = 1/N$  the Shannon entropy  $H$  will show a maximum of

$$H_{\max}(X) = \sum_{i=1}^N p(x) \log_2 \left( \frac{1}{p(x)} \right) \quad (2.82)$$

$$= N \frac{1}{N} \log_2(N) \quad (2.83)$$

$$= \log_2(N) \quad (2.84)$$

Within our simulation the population will never reach the maximum level of entropy, as

cells will count as two independent bodies upon the initiation of cytokinesis at the start of M-phase. Thus the amount of cells undergoing mitosis at any point will be twice the amount which would normally be expected by the phase length of mitosis. This can be corrected by modification of the pmf in a way that only half the mitotic cells are counted  $p(m) = \frac{1}{2} \frac{c_m}{C}$ . However, the error from this contribution is very small, as only a small number of cells is in mitosis at the same time.

The maximum of the entropy  $H_{\max}$  can be used for the definition of the normalised **orderedness**  $O(X) \in [0, 1]$  of the system  $X$  as

$$O(X) = \frac{H_{\max}(X) - H(X)}{H_{\max}(X)} \quad (2.85)$$

where  $X$  will be time-dependent as  $X(t)$ .

For a more complex discussion of the entropy of circular random vectors see [155] or [224]. Within the scope of this thesis, the Shannon entropy as synchronicity measurement will yield meaningful results for all possible cell distributions and is therefore used as default observable.

### 2.7.6 Integral enhancement

In order to assess the overall efficiency of a treatment plan, the integral enhancement can be used, which is defined similar to the tumour burden, as the area under the curve of the enhancement  $E$ , integrated over the time of interest  $T$ :

$$IE = \int_T E(t) dt. \quad (2.86)$$

Usually  $T$  will be the time window of the treatment. A baseline enhancement of 1 integrated over the treatment duration can be subtracted from  $IE$  in order to yield only the differences to the ideal exponentially growing tumour system. Thus a positive integral would correspond to a tumour which was, on average, in a more sensitive state than an exponentially growing tumour while a negative integral indicates a tumour that was, on average, in a resistant state.

### 2.7.7 Summary

#### Summary 7 (*Observables*)

- Tumour burden AUC is defined as area under the curve of viable cells
- Radiosensitivity enhancement  $E$  is defined as the ratio of cells which would be killed by a given dose to cells that would be expected to be killed as a result of the normal cycle distribution of the cell line
- $\phi$  as the cell phase-angle is defined as the relative active progression of a cell through its individual total cycle time
- Cell cycle synchronicity is quantified using following measures:
  - $\varphi$  squared sum of the relative cell phase distribution  $\sum(\frac{c_p}{C})^2$
  - $S_d$  minimum distance of active cell cycle time
  - $\sigma$  standard deviation based on phase-angle  $\phi$
  - $\text{Var}(\theta_n)$  circular variance of phase-angles (0-2 $\pi$ )
  - $H_x$  Shannon entropy
  - $O_x$  Orderedness via Shannon entropy
- The Shannon entropy  $H_x$  and orderedness  $O_x$  employ either  $n$  bins over all active cell phase-angles (subscript  $x = n$ ),  $n$  bins over all viable cells (including quiescent  $x = nq$ ), cell grouping by detectable DNA ( $x = DNA$ )
- Integral enhancement  $IE$  is defined as area under the curve of the radiosensitivity enhancement  $E$

## 3 Results

The following chapter contains results of tumour spheroid growth simulations, reaction to radiation and chemotherapy, and irradiation using fractionation schemes, which were performed with the model summarised in section 4.4 using default parameters as listed in section 4.6.

As the spheroid growth characteristics are not the main target of the investigation, only a short validation of the growth is performed in order to ensure that the model yields realistic growth dynamics for the simulation of treatment approaches. Some growth effects which are of potential interest in conjunction with therapeutic approaches such as cell flow and cell shedding for the tumour are investigated more closely.

The main focus of investigation rests on the irradiation reaction and possible enhancement effects as well as the predictions of the effect of fractionated irradiation. Development and treatment response of hypoxia in tumours is studied as one of the main resistance factors in radio- and chemotherapy. Finally possible synergies in radiochemotherapy are analysed.

### 3.1 Tumour spheroid growth

#### 3.1.1 Tumour spheroid growth and histology

When a low number of seeder cells is embedded into a culture medium they will start to proliferate and, depending on the cell line and culture conditions, adhere to themselves, eventually forming a tumour spheroid. Growth curves vary extremely between different cell lines and environmental conditions. It has been shown in [114] and [194] that various growth dynamics can be realistically described with an agent-based model of the type which is used in this thesis. A comparison to the growth of *in vitro* spheroids can be used to test if the model can realistically describe the growth dynamics.

For the validation of the growth model according *in vitro* growth, studies with EMT6/Ro cells from [72] have been selected. Within the experiments spheroids are seeded with an uncontrolled low number of cells, so that spheroids comprise of about 500 cells after 4 days of cultivation, when first measurements are performed. Error bars are not provided by [72] but can be assumed to be large because of the biological nature of the system and because data points represent individual values from two different experiments each measuring 50 spheroids (combined into one dataset for comparison within this thesis).

Figure 3.1 shows the results of tumour growth runs in the simulation which employ similar nutrient boundary conditions as the experiments of [72]. A corresponding tumour growth can be either obtained by starting the spheroid growth with 500 seeder cells at day 4 or by using an initial sum of about 10-20 cells.

The initial growth observed in the agent-based model will be exponential, as is visualised by the exponential growth fit  $10 \cdot 2^{t/t_d}$  with a doubling time  $t_d$  of 1170 min. After about 4 days of growth, the effects of pressure-induced quiescence become visible as the growth falls below the exponential line. As quiescence is exclusively induced by pressure, and thus

### 3 Results

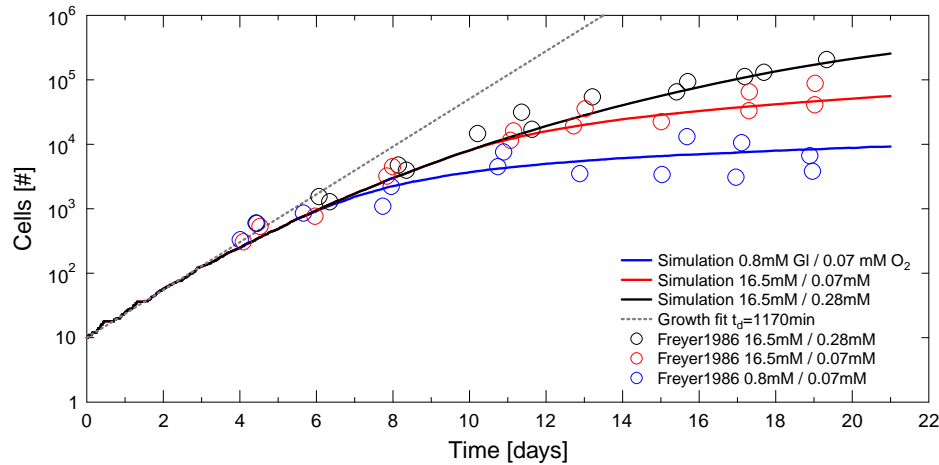


Figure 3.1: Comparison of *in silico* EMT6 tumour spheroid growth under different nutrient conditions within the simulation to *in vivo* growth curves from [72].

largely independent of the nutrient conditions, the initial decline in growth can be observed in all runs. At day 6 and day 10 the growth curves for sub-optimal nutrient conditions deviate from the curve of growth at high glucose and high oxygen. These mark the points in time at which a necrotic core is formed inside the according tumours in response to nutrient depletion. In the case of high nutrients conditions, necrosis is observed after day 15. Necrosis will drastically decrease the growth of the spheroid.

While the total cell count of the spheroid offers some information on the growth, Freyer and Sutherland conclude that it “is a crude measure, since it gives no indication of the internal composition of the spheroids.” [72]. However, an agent-based model allows the investigation of the cell population at arbitrary precision, so that the exact composition of the tumour can be analysed.

In the plateau phase of growth, the tumour will be dominated by a quiescent population of cells for the case of high nutrient availability (figure 3.2(a)). A moderate amount of quiescent cells can be observed for medium availability (figure 3.2(b)) while quiescence is almost absent after the onset of necrosis for low nutrient availability (figure 3.2(c)). Low nutrient conditions in [72] with 0.8 mM glucose and 0.07 mM oxygen are well below typical nutrient concentrations which are encountered *in vivo* as listed in table 2.5 and in section 2.2.4. At the vascular interface of tissue concentrations of 5 mM glucose and 0.135 mM oxygen are expected. The according physiological conditions will be used later in order to tune the growth of the tumour spheroid to the dynamics of an *in vivo* tumour nodule.

Figures 3.3 and 3.4 show central cutsections of tumour spheroids *in silico* and in comparison to *in vitro* results. After initial seeding with a low cell number, the spheroid quickly grows in size. A substantial number of cells will become quiescent especially in the central region of the tumour which is associated with high pressure. Once nutrients are fully depleted in the central region, cells become necrotic. Within this regions cells will swell up, eventually rupture and dissolve as they are committing to necrosis. As this dissolution of cells will remove mass from the centre, it is associated with a decrease in pressure on the inner part of the viable cells. Even in cells of the same line the onset size at which necrosis appears will vary considerably. Müller-Klieser thus suggests a statistical process for necrosis or at least a

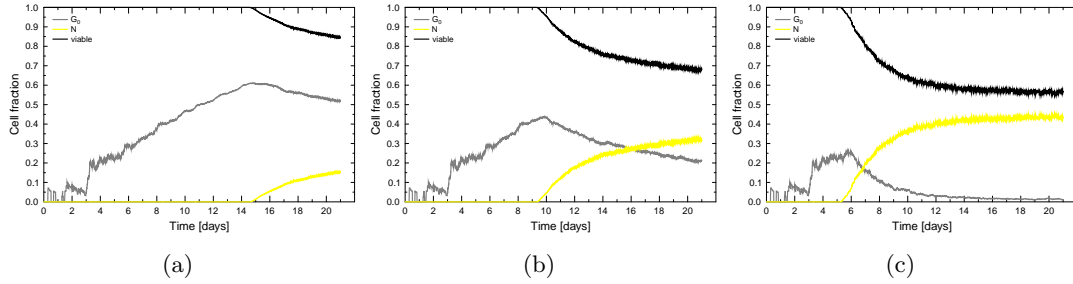


Figure 3.2: Relative amount of viable cells, quiescent cells and necrotic cells in tumour spheroid cultured under nutrient conditions of (a) 16.5 mM glucose, 0.28 mM oxygen, (b) 16.5 mM glucose, 0.07 mM oxygen, and (c) 0.8 mM glucose, 0.07 mM oxygen as in [72] and shown in figure 3.1. Growth will be limited by different mechanisms as discussed in the text.

process which is not fully determined by the diffusion geometry of the system [157]. In the simulation this can be included via a random component in the triggering of necrosis, which is evaluated with an increasing necrosis probability for decreasing nutrient availability.

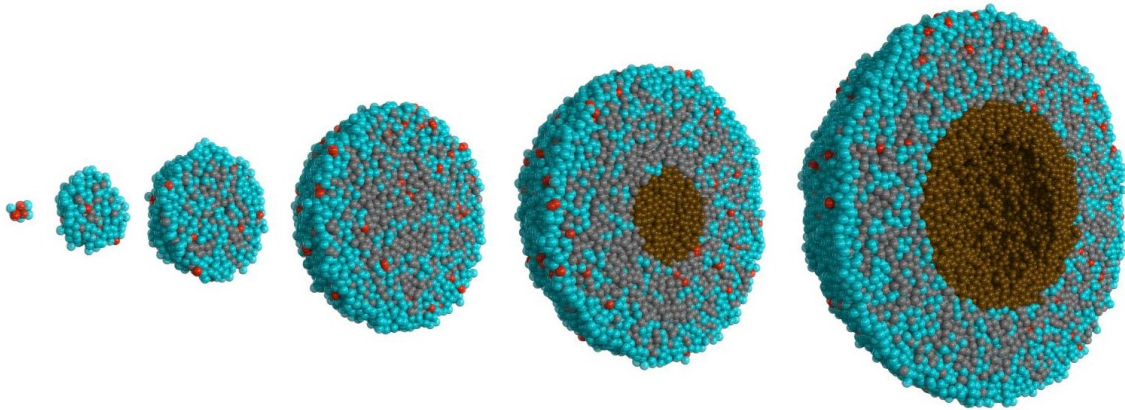


Figure 3.3: Central cutsection at days 1, 5, 7, 10, 12, and 14 after seeding. Active cells stained in turquoise (G1, S, G2), cells currently undergoing cytokinesis (M-phase) in red, quiescent cells in grey, necrotic cells in brown. Cells are visualised as spheres for visibility but are handled as polyhedra in the Delaunay/Voronoi system.

After necrotic cells dissolve, the tumour will be a hollow sphere with an expanding shell of viable cells. This viable rim has a typical thickness which depends on the nutrient consumption of cells and the external concentration of nutrients.

[69] reports the viable rim thickness in 15 cell lines grown as spheroids to be in the range of 85  $\mu\text{m}$  for CHO-XRS hamster fibroblasts up to 257  $\mu\text{m}$  for MCC26 mouse colon carcinoma cells. This immense variation mainly reflects the difference in cell metabolism, tolerance to nutrient deprivation and growth suppression by necrosis from cell line to cell line. Initial doubling times in spheroids also showed a variation from 16 to 64 hours.

Within the simulation a viable rim of about 190  $\mu\text{m}$  is observed, which is well in agreement with experimental observations for EMT6 spheroids. During spheroid growth, the thickness of the viable rim will stay constant, while the necrotic radius grows constantly with the total

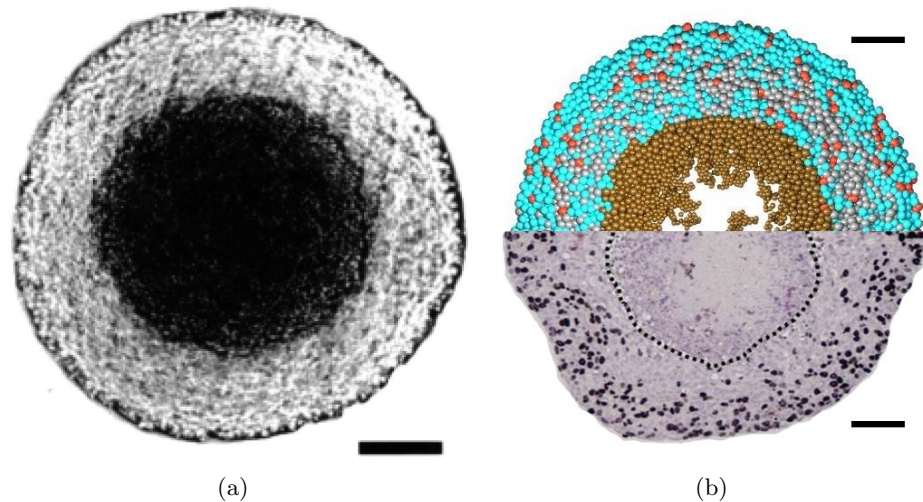


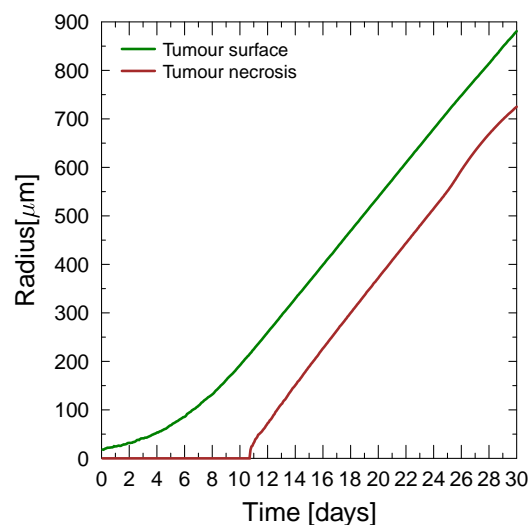
Figure 3.4: (a) Unstained equatorial cryosection of 10  $\mu\text{m}$  thickness through a WiDr human colon adenocarcinoma spheroid as visualized by a phase contrast microscope (bar size 250  $\mu\text{m}$ ). From [158]. The central necrotic area takes up about half the diameter of the spheroid. (b) Direct morphological comparison of an BT474 spheroid *in vitro* (autoradiography by incubation with  $^3\text{H}$ -TdR from [172]) and central cutslice of an *in silico* tumour spheroid. Bar size 100  $\mu\text{m}$ .

spheroid radius as indicated in figure 3.5.

The maximum rim thickness observed *in vitro* is about 250  $\mu\text{m}$  while at high glucose and oxygen concentration a rim thickness of only 100  $\mu\text{m}$  is reported in [72]. A paradox effect in rim thickness is reported, as the viable rim thickness decreases slightly for higher concentration: at fixed oxygen concentration the rim is thickest for 1.7 mM of glucose and becomes thinner for 0.8 mM as well as for physiological concentration at 5.5 mM or high glucose at 16.5 mM. Furthermore the thickness of viable rim is only weakly dependent on oxygen concentration as discussed in [72].

For the viable rim of spheroids, Müller-Klieser proposes a subdivision into three distinct regions: A viable, actively dividing outer rim, a quiescent normoxic interlayer, and a quiescent

Figure 3.5: A viable rim of cells will form in a tumour spheroid as diffusing nutrients are depleted with increasing distance from the spheroid boundary. The width of the viable rim will stay constant while the total radius increases.



hypoxic layer in the centre close to the necrotic core [157]. This layering can be confirmed in the simulation, however as quiescence is not dependent on oxygen concentration by default, the quiescent interlayer will develop as a result of high cell-cell pressure.

As the onset of necrosis is only correlated with lack of oxygen (but not fully caused by anoxia!) three types of tumours can be identified, depending on the timing of necrosis and anoxia (figure 2.9). In the case of tumours which are composed of anoxia tolerant cells, oxygen concentrations of around 0 mmHg can be observed where cells are still viable maintaining relatively high levels of ATP [157]. The glucose level at early necrotic sites is still as high as 0.17 mM with a lactate level of 0.05 mM. These levels do not comprise a hostile environment which will form only during later stages of the growth.

In summary, it is concluded that cell death in tumour spheroids is not a simple phenomenon which can be attributed to a single mechanism. Anoxia will not necessarily cause necrosis while necrosis does not necessarily imply anoxia. In some cases it seems to be the case that the developing central necrosis is the secondary result of stress-induced apoptotic events which have the highest rate of incidence closer to the tumour centre [172].

### 3.1.2 Cell cycle distribution during growth

If the exact cell cycle distribution is to be obtained, experimental approaches are limited. A typical measure that can be obtained as estimation of the cell cycle distribution is the ratio of cells in G0/G1-, S- and G2/M-phase. Discrimination of cells will be performed by sorting in accordance to each cell's DNA content.

Figure 3.6 show the detailed development of the cell cycle distribution within a growing tumour spheroid under nutrient conditions which correspond to *in vivo* concentrations as discussed in section 2.2.4. A complete depletion of oxygen is allowed, so that glucose will be the necrosis-inducing factor upon depletion.

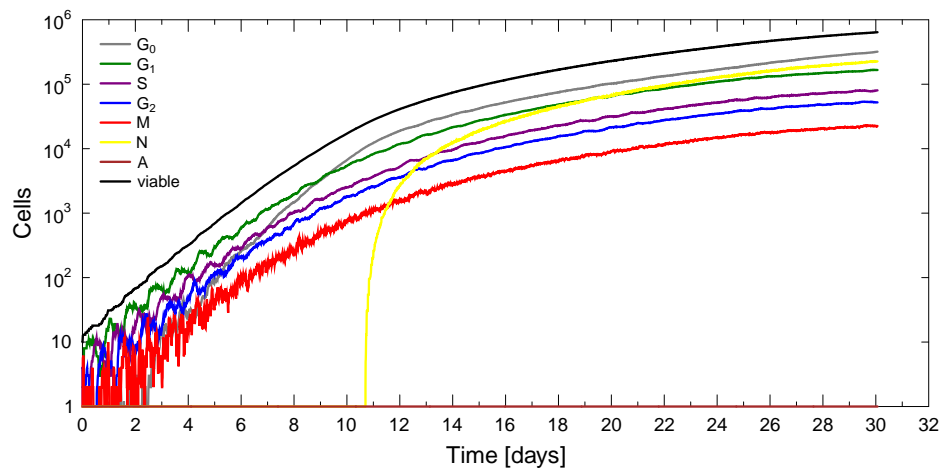


Figure 3.6: Development of the cell cycle phase distribution in an EMT6 tumour spheroid grown from 10 seeder cells under nutrient conditions similar to typical *in vivo* concentrations of 5 mM  $C_6H_{12}O_6$  and 0.13 mM  $O_2$ .

An initially synchronised progression of the cell cycle can be observed which is due to the seeding of the system with a low number of cells. As a result of the normal distribution of cell cycle times, this synchronisation is quickly lost. Furthermore, quiescence of cells followed

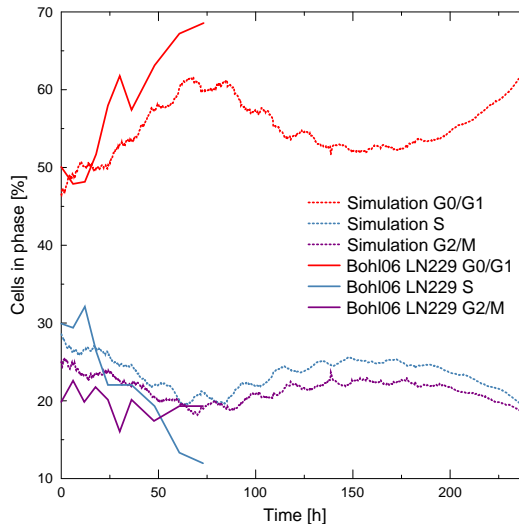


Figure 3.7: Initial development of the cell cycle distribution in a LN229 monolayer *in vitro* from [27] and in an *in silico* spheroid model of EMT6 cells within the simulation.

by reactivation upon local pressure release will contribute to the desynchronisation of the population.

A pronounced quiescent population is established by contact inhibition which will dominate the tumour spheroid about 8 days after seeding. This quiescent population will be of great interest for therapeutic approaches, as it represents a pool of dormant cells which can be reactivated by any treatment which alters the conditions inside the tumour. A large quiescent fraction therefore corresponds to the potential for a very fast regrowth in response to cytotoxic drugs or radiotherapy.

With a loss in synchronisation, the cell cycle distribution will be determined by the relative duration of the cell cycle phases (from longest to shortest G1, S, G2, and M) and reach a steady state after about 12 days of growth.

Figure 3.7 shows the development of the cell cycle distribution for a monolayer culture of LN229 cells *in vitro* and for a spheroid of EMT6 cells *in silico*. Measurements within the monolayer culture are continued for 3 days, while the spheroid can be followed for an arbitrarily long time. Within the spheroid and the monolayer culture, the rise in the G0/G1 fraction is associated with the onset of quiescence in the interlayer between boundary cells and core or respectively in overpopulated region. A transient drop in quiescent cells in the spheroid corresponds to the loss of quiescent cells as a central necrosis develops. Finally the fraction of quiescent cells will increase again as the interlayer has stabilised. A high steady level of the plateau growth phase is only reached after about 12 days.

Even though the systems of 2D monolayer and 3D spheroid culture are different, the overall composition of the systems with respect to the cell cycle distribution is comparable at least during the initial stages of growth. This will also be confirmed by the similar irradiation reaction discussed in section 3.2.2.

[70] report that exponentially growing EMT6 spheroids contain 35,50,15% of G0/G1,S,G2/M cells whereas the amount of G0/G1 cells in the plateau-phase of growth was  $> 90\%$ . Cells in the plateau-phase showed both smaller cell volumes and reduced rates of oxygen and glucose consumption as included in the current model. For exponentially growing EMT6/Ro spheroids in spinner culture, Wehrle et al. report a cycle distribution of G0/G1 50+-5%, S 33+-%, G2/M 17+-5% [241].

An overview of cell cycle distributions for tumour cells in exponential and plateau phase

of growth is provided in figure 3.8.

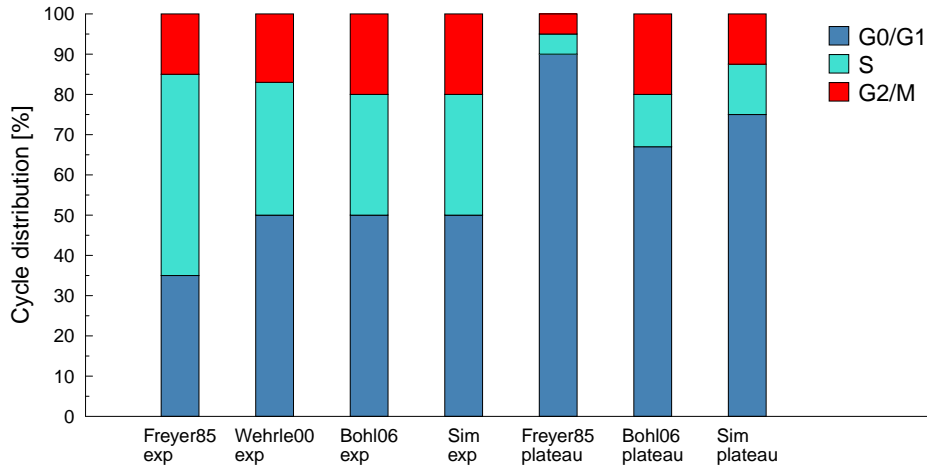


Figure 3.8: The cell cycle distribution for the initial exponential growth phase and the final plateau phase measured in different *in vitro* experiments [70], [241], [27] compared to *in silico* results (Sim) of the default setup of tumour growth within the model as shown in figure 3.6.

For both the cell cycle distribution during the initial exponential growth phase and during the plateau phase, a good agreement exists between data from the simulation and from experimental sources.

### Cell cycle histogram

In order to visualise the distribution of cells in the cell cycle phases or their progress through their individual cell cycle, a cycle histogram can be used as shown in figure 3.9. For this histogram the phase-angle  $\phi$  of all viable cells will be binned into 20 bins of equal width. After normalisation the results can be plotted to visualise the distribution of cell progress through the cycle phases.

Initially, cells in the example are uniformly distributed throughout the active cycle phases with the exception of M-phase, which has not been filled in order to leave a “marker gap” in the histogram. This initial “M-phase-depression” will move through the cycle histogram to be lost after a few hours due to natural variations in the cycle length. The cell cycle phases indicated at the bottom are an illustration of the average cell phase length. In reality, the individual cycle lengths are determined by normal distributions and thus will overlap.

After advancing for a given time, the cycle histogram will show a peak at an average phase-angle which will correspond to the  $G_1/S$ -transition. This marks the pile-up of quiescent cells in the system. The cell cycle distribution can be significantly altered by irradiation, as will be discussed in more detail in the following sections.

However, if a small test-dose of radiation is applied, the pre- and post-irradiation histograms can be compared. This reveals a slight change in the relative cell cycle distribution as a result of the differences in radiosensitivity between the different cycle phases.

In response to irradiation, the quiescence peak will decline as cells are reactivated, as discussed later. A pile-up of cells at the  $G_2/M$ -checkpoint can occur as a result of DNA-damaged cells which will be arrested at the DNA-integrity checkpoint.

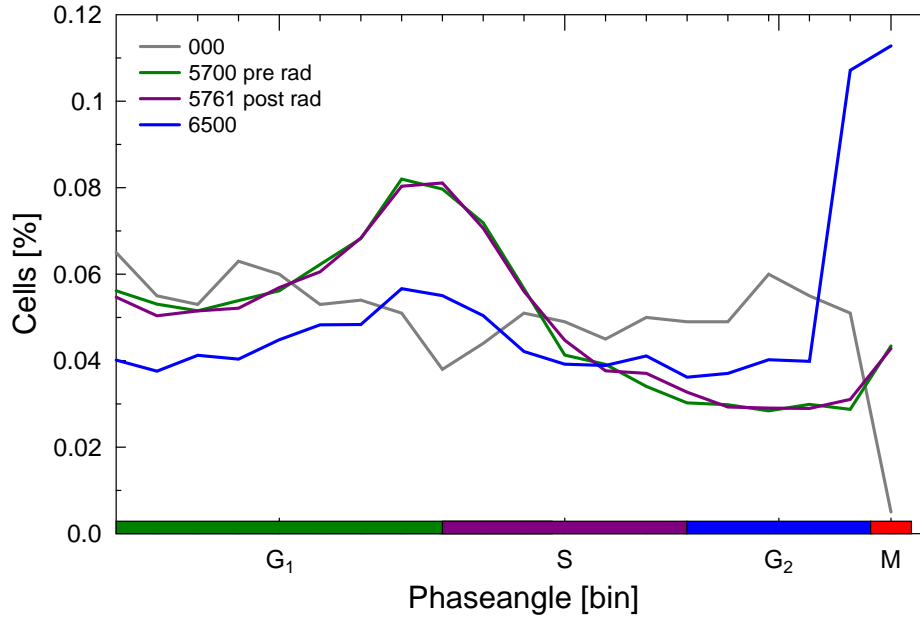


Figure 3.9: The cell cycle histogram of the phase-angle  $\theta$  in 20 bins at different points in time in response to irradiation with 8 Gy. The initial distribution will be uniform through the phases  $G_1, S, G_2$ , while  $M$  will be not populated (approximate average population per bin 0.05). After a few hours the "M-depression" will move to the early  $G_1$ -phase, while the number of very early  $G_1$ -cells increases through mitosis. Later on a pile-up at the  $G_1/M$ -checkpoint can be seen.

### 3.1.3 Growth saturation

A full saturation of tumour spheroid growth is not observed within the typical simulation time of 3 weeks of untreated growth under physiological boundary conditions. In a low nutrient environment of 0.8 mM  $C_6H_{12}O_6$  and 0.07 mM  $O_2$  corresponding to [72], the spheroid will reach a saturated state within 20 days even without further saturating mechanisms such as cell shedding as shown in figure 3.1.

One of the main reasons for the lack of growth saturation under high nutrient conditions is that no growth inhibiting factors are modelled. Usually necrotic cells will release toxic substances that act as growth and viability inhibitors. This will suppress proliferation for viable cells in the inner shell and add an increased tendency to commit to necrosis or apoptosis, which will drive the tumour into saturation [72]. Furthermore, cell shedding from the surface of spheroid is typically observed in experiments at a significant rate. This cell shedding is thus proportional to the tumour boundary surface and will further reduce the growth but is not accounted for in the simulations by default [130].

Spontaneous apoptosis is another mechanism which is observed in multicellular aggregates. Cells will commit to apoptosis in response to environmental stress which they are exposed to (low nutrients, high pressure, viability inhibiting solubles). This results in a typical baseline level of apoptosis which increases with tumour depths and contributes to growth saturation [213].

Release of growth and viability inhibiting factors can be simulated in a bystander damage approach or on an additional diffusion grid for waste substances. Shedding of surface cells

has been implemented via the identification of boundary cells by using a loss rate for random cell removal (see section 3.1.5). Mechanisms for a stress-dependent apoptosis in response to prolonged quiescence, critical nutrients or a high amount of neighbouring necrotic cells have also been implemented and tested.

While growth-saturating mechanisms have been implemented and studied (see following sections), they are basically irrelevant for the main investigative scope of this thesis. Tumour spheroids will show a typical histology and cell cycle composition which is close to a steady state long before growth saturation is reached. Thus a radiation response can be modelled independent of growth saturation. Furthermore, during a therapeutic regimen, spheroids will be far from a growth-saturated state as they are shrinking and actively re-proliferating at a high rate, which makes the inclusion of saturation mechanisms in the model unnecessary for the study of radiation reactions.

Most experimental investigations of spheroid growth will not observe a full saturation of growth, but only a deceleration of growth as in [72]. However, the experimental investigation and modelling of the according mechanism is of interest as “growth saturation in spheroids is analogous to the situation of a nonvascularised tumour or metastatic nodule *in vivo*” [69]. Therefore, any understanding of the induction and regulation of growth saturation could be of use for cancer therapy.

#### Increased cell-cell adhesion

Higher adhesion alone will not lead to a full growth saturation in the model. When the surface energy-term in the JKR interaction model is increased from  $\sigma = 0.1$  to a value of 0.5, the tumour radius will increase significantly slower, as can be seen in figure 3.10. However, the increased cell-cell adhesion will not lead to the fill-up of the hollow tumour core which would be necessary in order to arrive at a steady flow-equilibrium of proliferation in the viable rim and necrosis at the central viability-boundary.

Functionally, the tumours behave similarly for higher or lower cell adhesion, with almost identical cell cycle distributions. Also the timings for onset of quiescence and necrosis are similar.

In the absence of an artificial radial force, cells will form an expanding viable shell. With increasing time this shell will expand as proliferating cells show an positive radial velocity component, as investigated in section 3.1.4. While cells in the inner part of the shell will show an inward flux, the integral inwards flux is lower than the outwards flux. Thus the expansion of the spheroid (shell) is continued. *In vitro* a limiting factor could be the environmental pressure on the spheroid.

#### External pressure on boundary cells

Within tissue, a tumour will be subject to external pressure exerted by the surrounding microenvironment. This effect can be included in the simulation by affecting cells on the surface of the spheroid with a small force which is directed inwards from the surface. As a spherical growth is observed in the tumour without any exterior forces, it is safe to assume that the external force will point towards the centre of the tumour spheroid at every point, that is towards the origin of the simulation system. Otherwise a local surface normal can be constructed using the Delaunay neighbours of the cell in multiple tiers if necessary.

### 3 Results

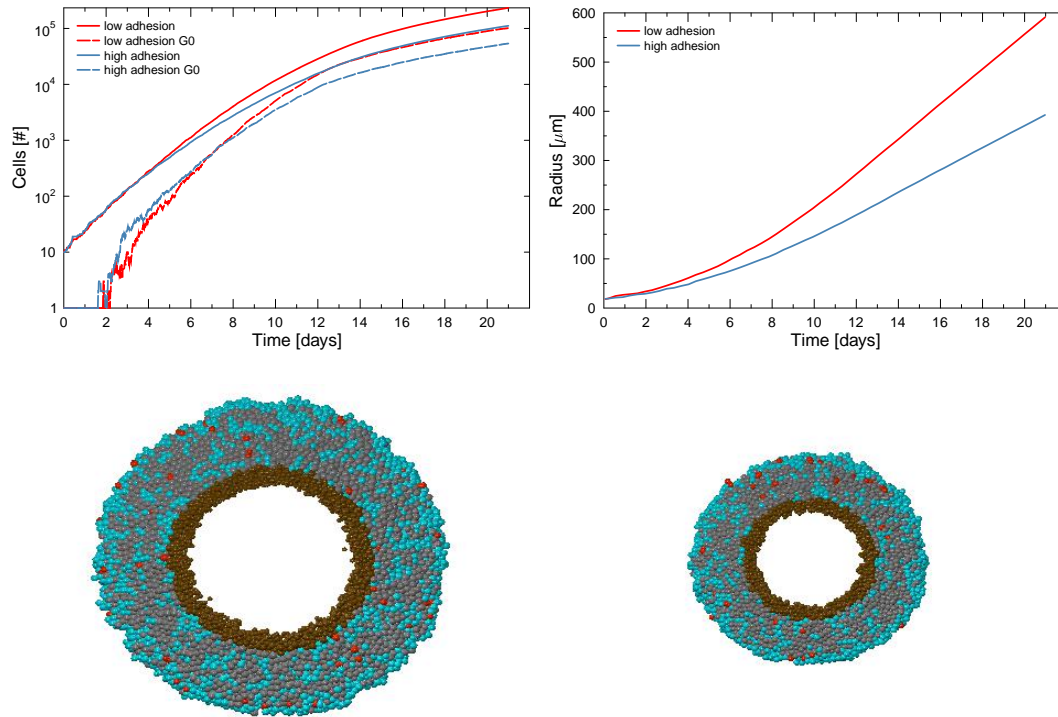


Figure 3.10: Tumour growth using normal JKR-interaction and JKR-interaction with increased surface energy of  $\sigma = 0.5$  instead of  $\sigma = 0.1$ . Lower row shows a central cross-section of both tumours at 16.6 days of growth with same scaling.

As can be seen in figure 3.11 the external pressure has an extreme effect on the growth of the tumour. The magnitude of 4 nN is well within the range of physiological forces as discussed in section 2.1.3. An increasing fraction of cells will enter pressure-induced quiescence in response to the boundary force until a majority of cells will be in quiescent state due to their pressure sensitivity at higher boundary pressures. Even relatively small forces of 4 nN induce an effective restriction of proliferation to the outer free surface layer of cells. In boundary-pressure free growth under high nutrient conditions, about 65% will be in quiescence. This fraction will slightly decrease in response to a necrosis-induced freeing of space. A moderate boundary force of 1 nN will raise this fraction to 70% and delay the onset of necrosis about 2 days in response to an overall lower growth. When the boundary force is increased to 4 nN about 80% of cells will be quiescent and no necrosis will be observable within the time of interest.

While this growth-inhibiting effect is potent, many cancerous cell lines will possibly avoid it by a decreased sensitivity to high pressure. Actually, *in vitro*, the central necrosis should lead to an influx of water which might produce an osmotic pressure on the internal boundary cells due to the influx of water into the hollow core. This pressure gradient would lead to a force which counterbalances the pressure from surrounding tissue.

#### 3.1.4 Cell flow and radial velocity

When the cell motion inside the spheroid is visualised, a constant stream of cells can be observed flowing inwards from the central region of the viable rim into the necrotic core.

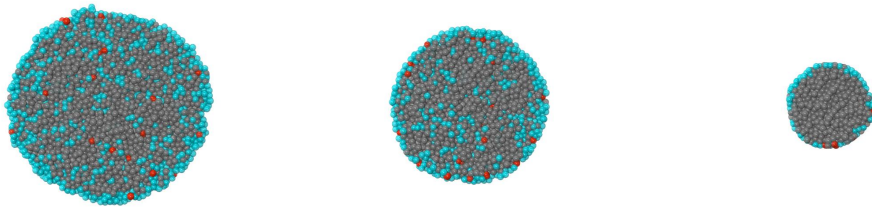
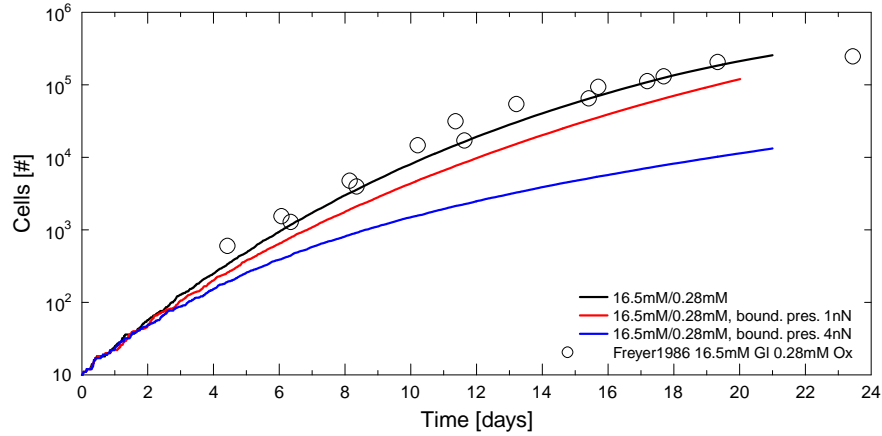


Figure 3.11: Overall growth curves for tumour growth in accordance to data from [72] compared to the growth under the effect of a central force on tumour surface cells of either 1nN or 4nN. According cutsection through spheroids after about 14 days of growths from 10 seeder cells below. An increasing amount of quiescence is visible in the cutsections.

This radial movement of cells can also be studied quantitatively: Cells within the simulation are binned according to their radial distance from the spheroid centre. Within each bin  $N$ , the velocity component of each cell in the radial direction is summed up and normalised by the number of cells in the bin to yield a final net average radial velocity  $\chi$ . The radial velocity component of each cell is obtained by calculation of the scalar product between the cell's velocity vector  $\mathbf{v}_i$  and the normalised vector towards the spheroid centre at the cell's positions  $\hat{\mathbf{r}}_i$ :

$$\chi = \sum_{i \in N} \mathbf{v}_i \cdot \hat{\mathbf{r}}_i \quad (3.1)$$

The average radial velocity for different times in spheroid growth is shown in figure 3.12. While during the initial growth of the spheroid the average radial velocity will be positive for all radial shells, as the spheroid expands and cells are pushed outside, this profile changes after the onset of necrosis. Due to the dissolution of cells in the centre of the spheroid, a strong inwards flux can be observed. Cells which are within the inner third of the viable rim are pushed inwards as a result of proliferation in the viable layer. In the outer region of the viable rim an outwards average velocity remains in effect.

Adhesion to necrotic cells can increase the inwards flux by effectively pulling cells into the necrotic centre of the spheroid. This effect would be altered if necrotic cells lose their

### 3 Results

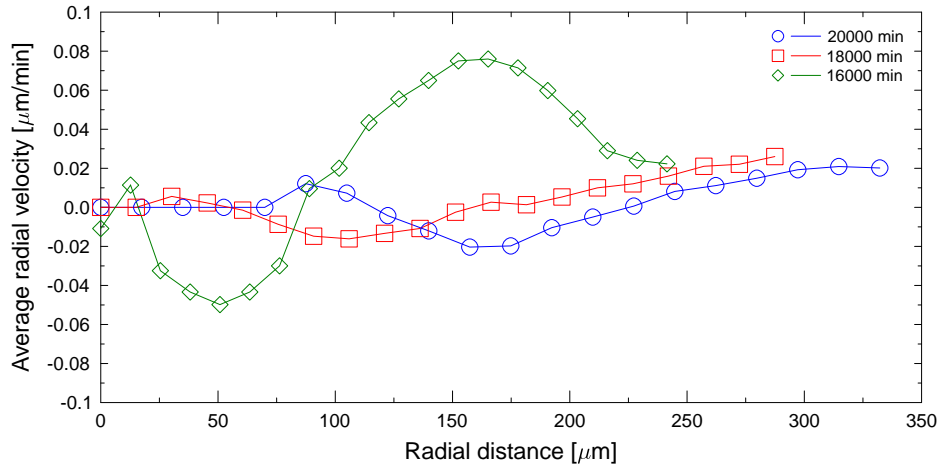


Figure 3.12: The average radial cell velocity profile of a centrally necrotic tumour at different points in time. A necrotic core formed at 10.5 days of growth and immediately led to a two-phased velocity profile with an inner cell flux to the tumour centre.

adhesivity. This is a reasonable assumption that could be tested. Another alteration could come from a change in the model of necrosis: as implemented at the moment, necrotic cells in the model swell up to an increased size over the associated phase length of necrosis to be eventually removed from the simulation. This increase in size could decrease the inwards flux of cells by actively pushing them out of the necrotic volume. This would be an adverse effect to growth saturation.

The average radial velocity profile of the tumour will also show interesting changes in response to irradiation. Figure 3.13 visualises the velocity profile in a fully grown tumour spheroid which is subject to an irradiation dose of 4 Gy on day 14 after seeding.

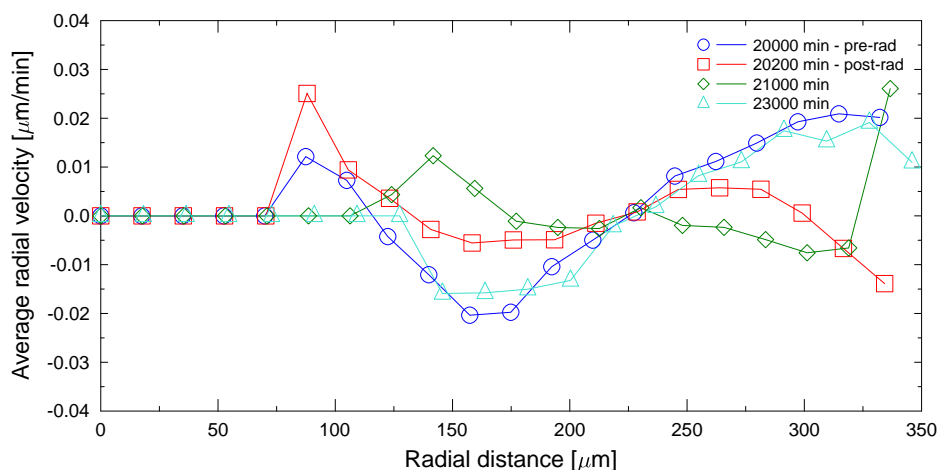


Figure 3.13: The average radial cell velocity profile of a centrally necrotic tumour at different points in time pre- and post-irradiation.

The central necrotic area is void of cell flow with an average velocity of 0. While pre-irradiation the same velocity profile as for the un-irradiated tumour is present, an increased average outwards velocity can be observed in the inner part of the shell, while an aver-

age inwards velocity is in effect at the surface. This effect is triggered by the apoptosis of radiation-killed cells, which is associated with a shrinkage in cell volume. As adhesion of apoptosis cells is kept unaltered, this will lead to a pull inwards into the viable cell layer both at the surface of the spheroid and at the boundary to the necrotic core. An according small counter-velocity can be found in the intermediate region, with a slight outwards movement in outer central region and an inwards velocity in the inner central region of the spheroid shell.

About 16 hours after the application of the radiation dose, apoptotic cells are dissolved and re-proliferation of cells will lead to a high outwards velocity on the surface of the spheroid. Approximately 2 days after irradiation the tumour radial velocity distribution has equilibrated back to the undisturbed state.

### 3.1.5 Cell shedding effects

A major contributor to growth saturation of EMT6 tumour spheroids *in vivo* is the shedding of cells from the surface of the tumour. Cells which lose contact to the spheroid are lost in the reservoir of nutrients and will eventually be removed from the system with each medium exchange.

The rate of cell shedding for EMT6/Ro spheroids is reported to be 218 cells/mm<sup>2</sup>h and comprised up to 1.5% of the total spheroid cell content per hour in the experiments of Landry et al. [130]. Freyer and Sutherland reported shedding rates for EMT6 spheroids between 175 and 280 cells/mm<sup>2</sup>h with a mean of 221 cells/mm<sup>2</sup>h [72]. It is stated that the shedding rate appeared to be independent of tumour diameter. Furthermore, no correlation between shedding and the culture condition was found.

Within the simulation, the shedding of cells from the surface has been tested in compliance with the experiments in [130]. Surface cells of the tumour are identified by a connection to an artificial bounding vertex in the Delaunay triangulation. An average surface area of the spheroid is calculated by using the averaged radius of all boundary cells. According to the surface area and the time-step, a matching cell shedding count is calculated and the cells are subsequently removed from the spheroid either instantly by deletion of the cell or by induction of apoptosis (this has the advantage that it yields a high potential to visualise cell loss while having minimal impact on the spheroid growth). A shedding rate  $\sigma$  of approximately 200 cells/mm<sup>2</sup>h is assumed as default in agreement with [72].

Cell shedding from the surface of EMT6/Ro spheroids is reported to be associated with a decrease in cell-cell attachment during mitosis. Cells which are obtained from the culture medium *in vitro* were largely synchronised and about 95% of cells shed were mitotic during their release [130]. Accordingly, shedding can be restricted to mitotic cells on the spheroid surface in the simulation (see also figure 3.14). Alternatively, a preferential shedding of mitotic cells, where further random cells can be shed to fulfil the shedding requirements, can be implemented. The default is a random shedding of surface cells determined by a defined shedding rate.

A sample of tumour growth under the effect of surface cell shedding is shown in figure 3.15. A large initial aggregate of 1000 cells is subject to a shedding rate of 200 cells/mm<sup>2</sup>h. The steady increase in surface area which is associated with the spheroid growth leads to a rising shedding rate over time. Between days 3 and 5 the relative amount of total cells shed to viable cells in the tumour is highest. It will decrease for continued tumour growth. As the surface to volume ratio of the spheroid is sufficient, it will steadily grow in size.

### 3 Results

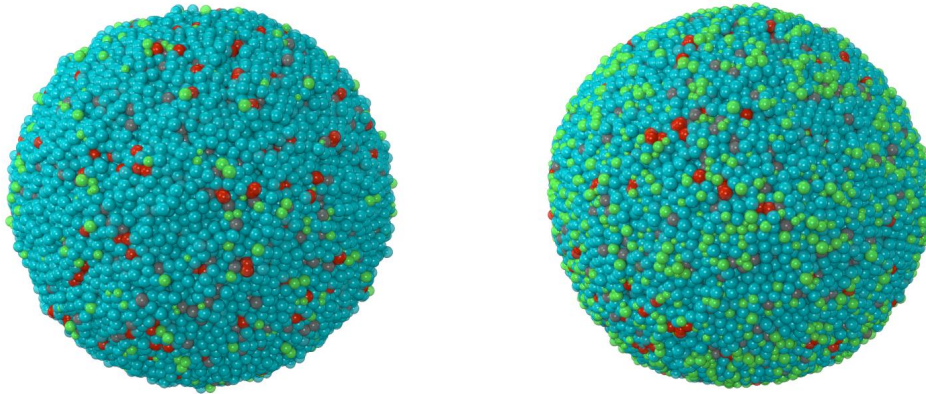


Figure 3.14: Shedding from the tumour boundary modelled via apoptosis in a visualisation. Shedding can be restricted to mitotic surface cells only, so that the amount of mitotic surface cells will limit the rate (as implemented in the left image).

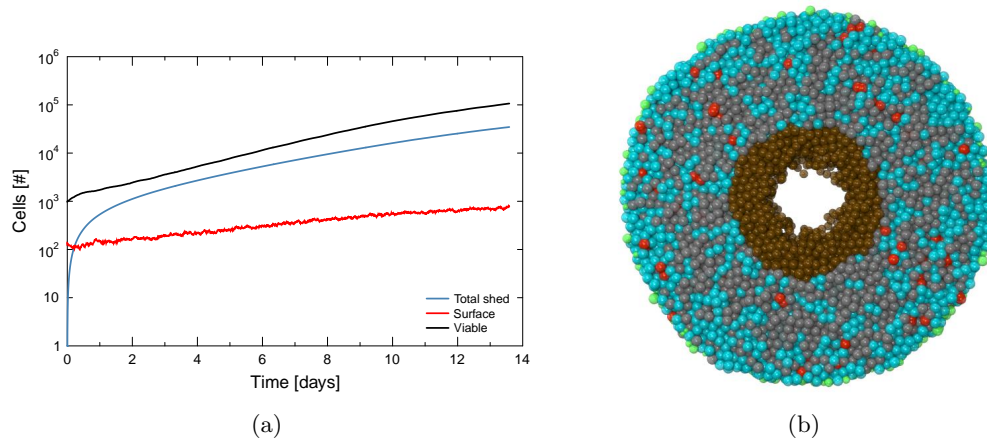


Figure 3.15: (a) Shedding from a tumour spheroid seeded with 1000 cells for a shedding rate of 200 cells/mm<sup>2</sup>h. (b) Visualisation of the according tumour histology in a central cutslice and shedding from the tumour surface (green cells).

If the shedding rate is assumed to be independent of the spheroid size, cell shedding will effectively prohibit the formation of spheroids if the initial seed cell count is too low or the shedding rate is too high. This can be seen in the overview of tumour growth scenarios for different amounts of initial seeder cells and shedding rates  $\sigma$  which is provided in figure 3.16. Obviously, for very small spheroids the shedding rate must be lower than reported. Otherwise aggregation of cells into large spheroids would not be possible due to a constant loss of cells from the surface, which eventually leads to a complete dissolution of the spheroid.

If the shedding is restricted to mitotic surface cells, then for small tumours the rate of shedding can temporarily exceed the amount of mitotic cells on the surface which are available for shedding. As the shedding rate will be integrated in small time-steps in order to yield a total count of cells that should be shed, this can lead to a temporary "shedding-debt" of the tumour, which is decreased and can be totally compensated for with time, as more surface cells enter mitosis. An example of the limiting influence of mitotic shedding is shown

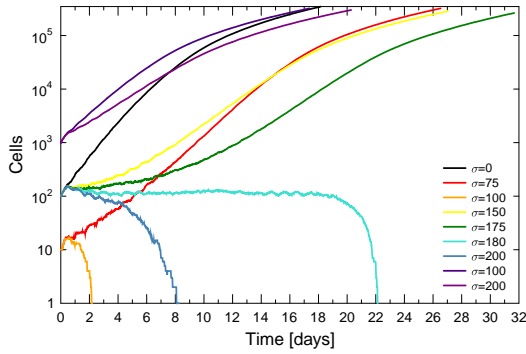


Figure 3.16: Results of tumour growth for different initial sizes of the aggregate and shedding rates  $\sigma$ .

in figure 3.18. Variation of the shedding rate  $\sigma$  from 100 to 200 cells/mm<sup>2</sup>h will have a significant limiting effect on growth. However, if shedding is restricted to mitotic surface cells, the restriction acts as a limiting factor of shedding, so that, independent of the rate to be achieved, a lower actual rate of shedding is in effect. The developing "shedding debt" will be higher in the case of the higher planned shedding rate of 200 cells/mm<sup>2</sup>h.

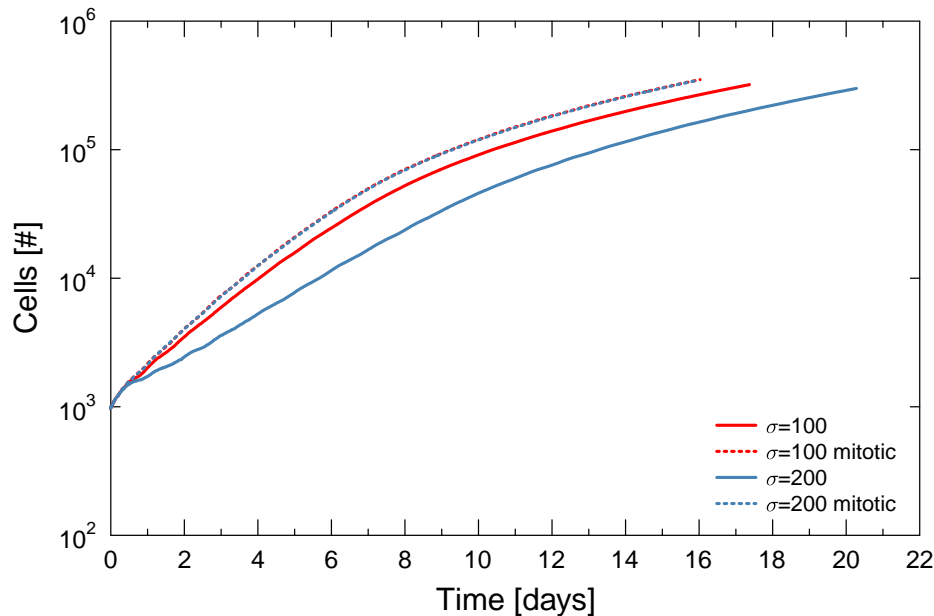


Figure 3.17: Variation of the shedding rate  $\sigma$  for tumour spheroids grown from 1000 initial seeder cells. The maximum amount of shedding is bound by the availability of mitotic surface cells.

This restriction further confirms that in EMT6 tumour spheroids the rate of shedding must not be independent of size and cannot be limited to only mitotic surface cells.

A further interesting observation is the fact that tumour spheroid growth depends critically on the rate of shedding. As shown in figure 3.18, the fate of the tumour growth is determined by the amount of cell loss from its surface. Below a critical rate of approximately  $\sigma=178$  cells/mm<sup>2</sup>h the tumour will dissolve as a consequence of shedding. If  $\sigma$  is lower than the critical rate, the spheroid will grow until reaching saturation.

Small perturbations of the rate will result in stochastic effects that either lead to full development of a tumour spheroid or a complete dissolution of the spheroid as a result of

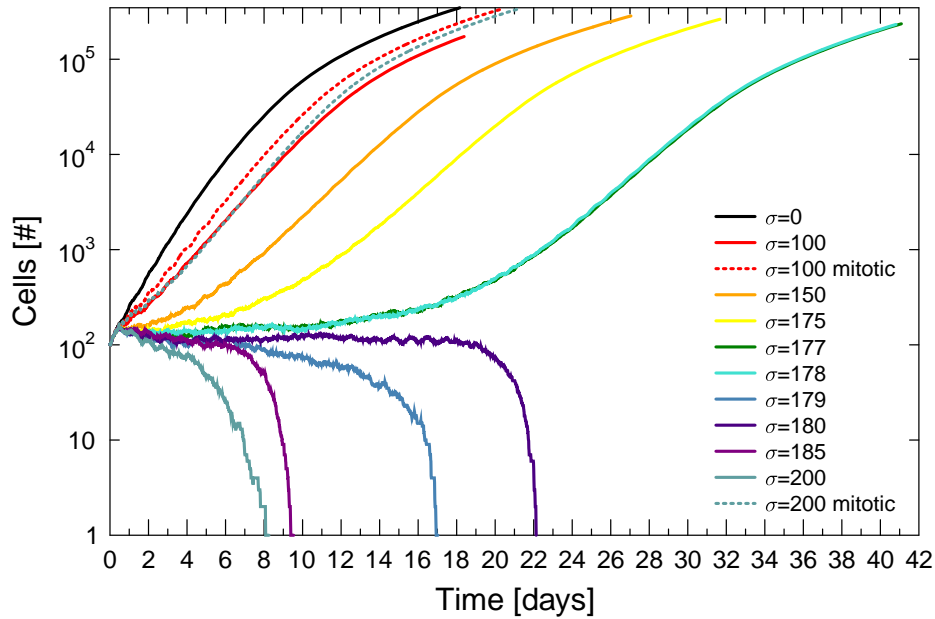


Figure 3.18: Variation of the shedding rate  $\sigma$  for tumour spheroids grown from 100 initial seeder cells will reveal a critical dependence of tumour growth on shedding. Very low variations of the shedding rate can switch between a growing or dissolving state when close to the critical shedding rate of about  $\sigma=175$  cells/mm<sup>2</sup>h.

shedding. This critical behaviour is of great interest as it implies that the fate of a tumour spheroid is determined by its rate of cell loss. If this rate can be influenced, a dissolution of small tumour nodules can be initiated.

When shedding effects are modelled, oscillations of the total cell number and the tumour radius can be observed in some cases. This is a result of the partially synchronised cell cycle progression and the associated synchronous cytokinesis, which will increase the tumour radius as cells are pushed outwards by mitotic neighbours. An increase in radius will yield an according increase in surface area and thus an increased shedding. When the radius has sufficiently decreased, losses due to shedding are lower than the proliferation of cells again, leading to an increase in tumour cell count and radius and so forth. Surface shedding will result in a more compact tumour as a fraction of surface cells will be continuously stripped from the tumour boundary.

A constant rate of shedding should be sufficient to limit the growth of tumour spheroids. In principle, the surface to volume ratio would become favourable for growth over shedding with increasing tumour radius. However, as a necrotic core is present and the growth is restricted to a viable shell of cells, the surface to volume ratio will drastically increase once necrosis develops. Examples of the surface to volume ratio  $\Omega$  of tumour spheroids grown without shedding or with a shedding rate  $\sigma$  of 175 cells/mm<sup>2</sup>h are presented in figure 3.19. In both cases, an initial decrease of  $\Omega$  can be observed as a result of the tumour volume growth. If shedding is present, as in figure 3.19(b), then a limited initial increase in  $\Omega$  can be observed as a result of a shedding-associated decrease of the tumour radius. However, if the cell number of the spheroid is high enough, this process will be turned into a decrease of  $\Omega$  as proliferation expands the tumour. The initial decrease in  $\Omega$  will speed up proliferation, as shedding effects are relatively decreased. However,  $\Omega$  will drastically increase as soon as a

necrotic core develops inside the spheroid and proliferation is limited to a viable shell volume.

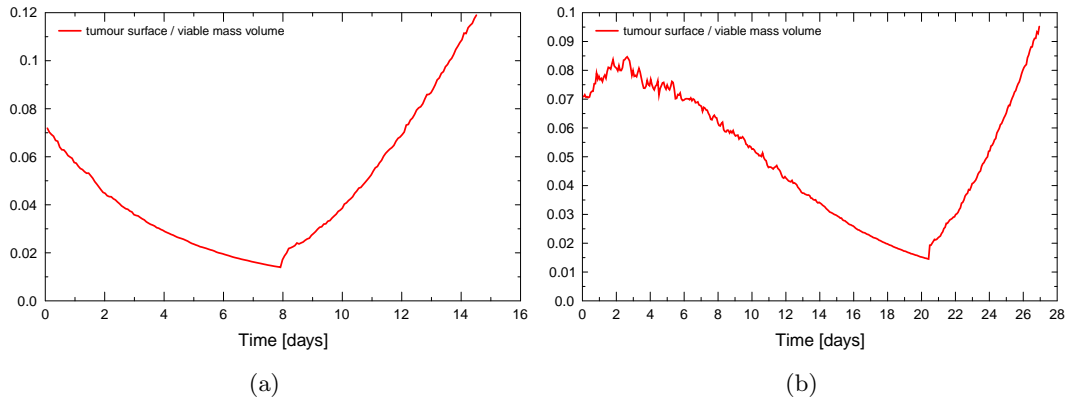


Figure 3.19: Development of the surface to volume ratio  $\Omega$  during growth of a tumour spheroid either without shedding **(a)** or with a shedding rate of  $\sigma=175$  cells/mm<sup>2</sup>h **(b)**. Initial tumour aggregate consists of 100 cells.

If only mitotic cells are subject to shedding, the amount of observed shedding cannot, at most times, match the amount suggested by the shedding rate. This opens up the possibility of modelling possible influences on cell shedding: if every mitotic cell on the tumour surface will be subject to a chance of being shed, a probabilistic representation of cell shedding can be developed and compared to experimentally observed rates. Furthermore, this shedding mechanism will lead to a variation in the shedding which depends on the tumour state, as should also be observed *in vitro*. A dose of hydroxyurea, for example, should almost completely inhibit cell shedding as no cells can enter mitosis while the drug is present. As cell shedding is a possible mechanism at the heart of the metastatic process of local and body-wide tumour reseeding, according modelling could prove insightful.

## 3.2 Irradiation response

### 3.2.1 Tumour composition and radiosensitivity

When irradiating a complex tumour system, the exact composition of the system in terms of the number of cells in defined cell cycle phases can make a great difference to the survival probabilities. During the growth of a tumour spheroid, a large quiescent population can form as discussed in section 3.1.2. Another difference in cell cycle distribution can arise as result of the properties of the cell lines which is to be irradiated, as the typical cell cycle phase durations can show large variations between different cell types and even between subcultures of a single cell line. While some cells will exhibit a very long S-phase, which is associated with a high radioresistance, other cell lines remain the longest in G2-phase, resulting in an overall low radioresistance.

The expected survival curves for different tumour compositions can be predicted by calculation of the total survival out of individual phase-dependent survival values, weighted by the ratio of cells in this phase (defined either by phase lengths or by relative amounts). Figure 3.20 shows an overview of the expected survival curves for tumours of different relative composition as detailed in table 3.1.

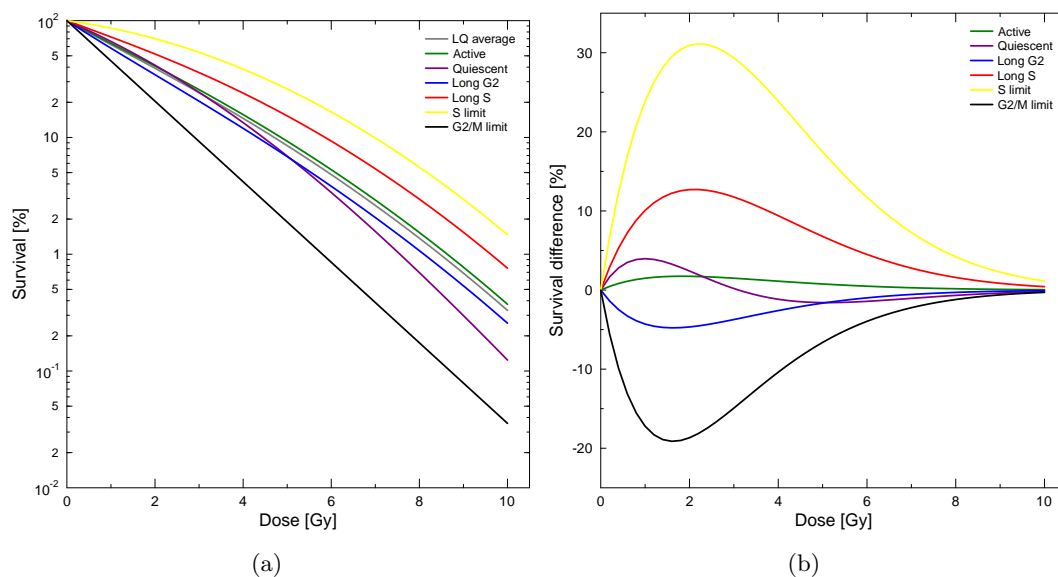


Figure 3.20: **(a)** Effect of the tumour composition as in table 3.1 on the expected overall survival. **(b)** Difference in absolute survival of the corresponding tumours when compared to the average LQ-survival.

Especially at lower, clinically relevant, doses the tumour composition will significantly alter the radiation response. The maximum survival difference of more than 30% is observed in the region of 2 Gy, which is the standard clinical fraction size. This emphasises that the cell cycle distribution can have a drastic effect in radiotherapy which can either be positive for treatment or negative, if neglected.

The spread between survival of radioresistant S-phase cells and sensitive M-phase cells grows larger with increased dose (at least for reasonable fraction sizes of up to 10Gy) as illustrated in figure 3.20(a). Therefore, at higher doses the cell cycle distribution can lead

Phase length distribution (G0, G1, S, G2, M) [min]	Tumour phenotype
(75, 10, 5, 9, 1)	Quiescent
(15, 30, 25, 24, 15)	Active
(15, 15, 50, 15, 5)	S-phase dominated
(15, 15, 15, 50, 5)	Long G2-phase
(0, 0, 100, 0, 0)	Extreme resistance
(0, 0, 0, 50, 50)	Extreme sensitivity

Table 3.1: Different tumour phenotypes and matching exemplary cell cycle distributions. In figure 3.20 the resulting survival-curves are presented which differ as a result of the varying  $\alpha$  and  $\beta$  values associated with each cycle phase.

both to a larger enhancement of radiosensitivity or a strong decrease in radiation efficiency, increasing the possible variation of the observable  $E$  (see also figure 2.37(b) in section 2.5.6).

Survival relationships for according heterogeneous cell populations are of high interest for the prediction of therapeutic outcomes and have been studied in a number of publications e.g. [83] and [95] as will be discussed later in comparison to results of the simulation.

### 3.2.2 Irradiation reaction

Application of a dose of radiation to a tumour spheroid will induce a variety of dynamical reactions, which are to be described in the following section. Figure 3.21 provides an overview of corresponding changes in cell cycle distribution, orderedness and enhancement, as well as a visualisation of the cell cycle changes in an EMT6 tumour spheroid which is subject to 4 Gy of X-ray radiation. The spheroid was grown from 10 seeder cells under physiological nutrient conditions in accordance with the standard parameter set used for simulation of irradiation reactions as provided in section 4.6.

After an initial exponential growth phase and the subsequent deceleration of growth as a consequence of quiescence and necrosis, the spheroid will have a diameter of about 800  $\mu\text{m}$  when irradiation is applied at day 14. As is visible in the visualisation and the cell cycle distribution, the spheroid will have developed the typical histology of a tumour nodule, so that a natural radiation response can be studied. Cell cycle progression is largely desynchronised and the formation of a large quiescent population will decrease the radiosensitivity due to the resistance of quiescent cells.

A radiation dose of 4 Gy will damage and kill about 80% of the cells in the spheroid and thus induce a strong dynamic reaction. The relative distribution of cells in the cycle phases will change according to their radiosensitivity. As a majority of cells is committing to apoptosis, as visualised in figure 3.21(c), the pressure inside the spheroid will decrease, leading to a large-scale reactivation of previously quiescent cells. Nutrient limitations that previously lead to the development of a necrotic core will be lifted, so that, for a brief period, the spheroid is void of necrotic cells. Due to fast regrowth, the spheroid will return to a steady state within a few days and reform its typical histology and cell cycle distribution.

### 3 Results

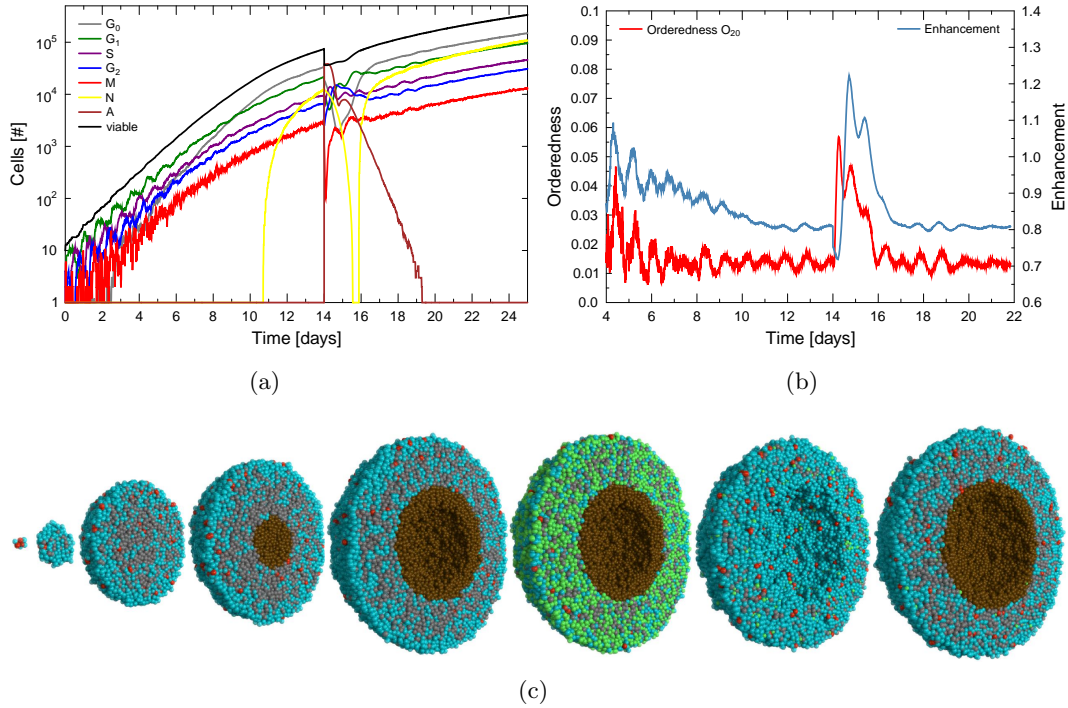


Figure 3.21: **(a)** Cell phase distribution during growth of a tumour spheroid and in response to irradiation with 4Gy. The corresponding development of orderedness and radiosensitivity are shown in **(b)**. **(c)** A visualisation of a laterally cut tumour spheroid during different phases of growth and irradiation. An initial small number of seeding cells will form a solid tumour spheroid, where cells in high-density regions go into quiescence. Nutrient deprivation and dissolution of necrotic cells lead to a hollow core. After irradiation with 4Gy, a majority of cells will be apoptotic, however a reactivation of quiescent cells is the result, which leads to a fast regrowth and to the re-establishment of a necrotic core.

Orderedness and enhancement will initially fluctuate due to the low number of seeder cells, but will soon reach a steady state. Irradiation disturbs this steady state and leads to an increase in orderedness and the formation of a discrete peak in radiation sensitivity.

Comparison of the theoretical cell cycle reaction to irradiation with an experimental result can be used to verify the model or to tune the reaction to a specific cell line. In [27] LN229 cells in monolayer flask culture are exposed to 2Gy of X-ray radiation and afterwards the percentage of cells in G0/G1-, S- and G2/M-phase is tracked in time. Naive comparison of the simulation results to the experimental data in figure 3.22 shows that the basic response of cells to irradiation can be faithfully reproduced with the radiation damage model of the simulation. The fast S-phase response matches the experimental one even without adaptation of parameters.

If a high number of cells are subject to a slow damage response, as in figure 3.22(b), the G2-arrest is too prolonged in the simulation to match the experimental data. This also explains the shift of the G0/G1 population as it substantially delays cells from entering mitosis and then to fill up the compartment of cells in G1.

G2 accumulation after irradiation of V79 cells with 9.4Gy rises from 10 to 40% after 5 hours and diminishes to 25% after 10 hours [74]. The results from [27] for LN229 cells are in contradiction to this, as for a comparable dose of 8Gy (to 9.4Gy at high dose rate in [74])

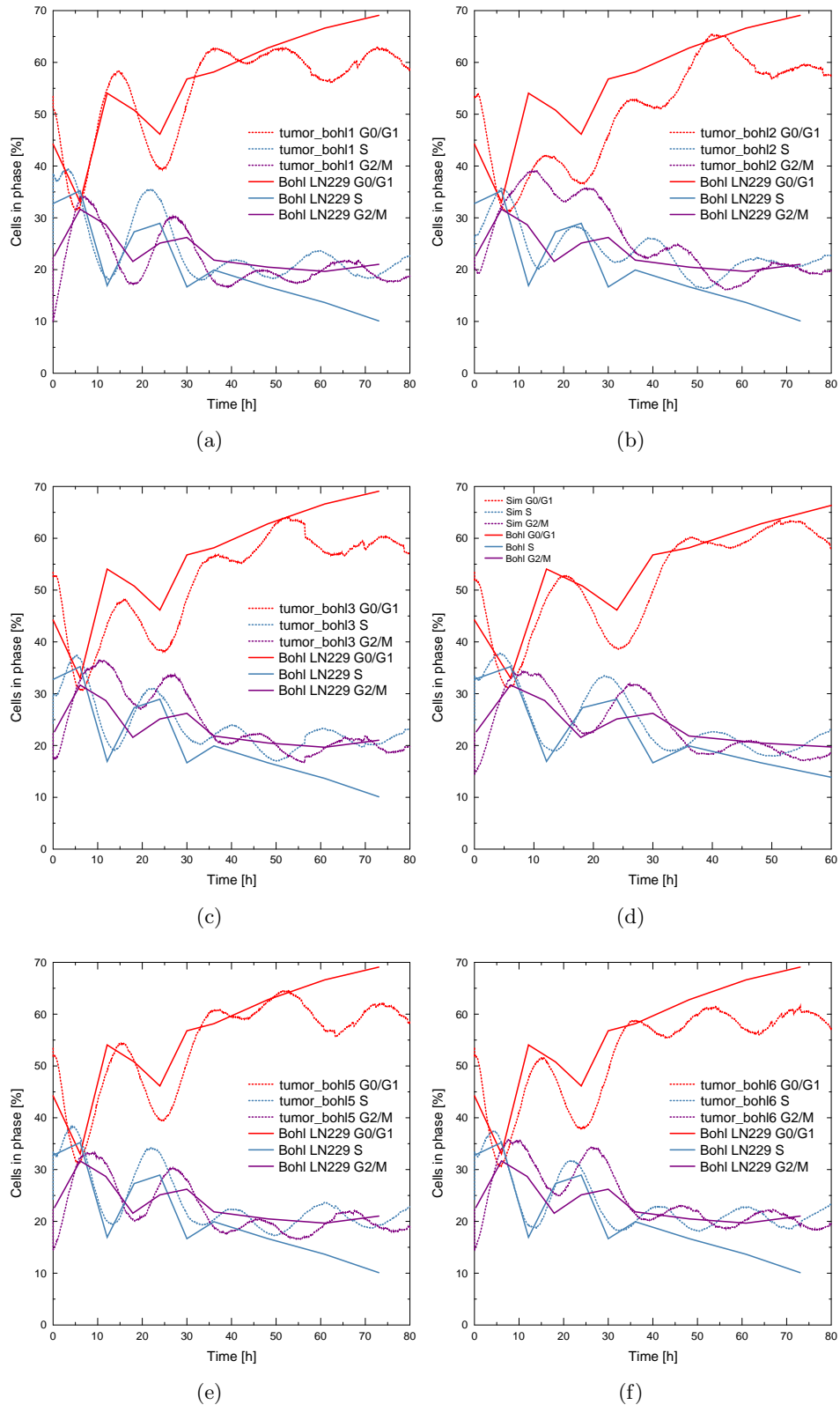
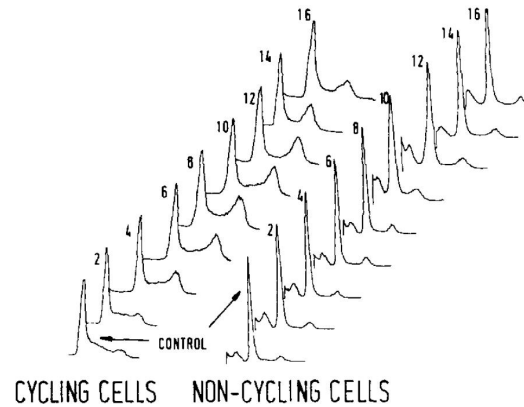


Figure 3.22: **(a-f)** Cell cycle reaction of LN229 cells in flask culture (from [27]) and the matching reaction of EMT6 cells in simulation to 2Gy of X-ray radiation in response to different damage dynamic parameters: **(a)** apoptotic chance (AC) 1.0 **(b)** apoptotic chance (AC) 0.3, mitotic miss chance (MM) 0.3 **(c)** AC 0.6, MM 0.3 **(d)** AC 0.8, MM 0.3 **(e)** AC 0.8, MM 0.6 **(f)** AC 0.8, MM 0.1

Figure 3.23: DNA distribution of V79 spheroid cells after 3.2 Gy of X-rays. Response is different for cells in the outer, active layer of the spheroid, where a G2/M block can be observed, than in the inner layer of non-cycling cells. From [136].



a maximum of 65% is reached about 10 hours post-irradiation. This variation reflects the differences in repair capability and branching which can be drastic from cell line to cell line.

From comparison of the used irradiation model to the experimental data from [27], it seems feasible to simplify the irradiation model to a pure kill/survival model. Even though the runs shown in figures 3.22(d) and 3.22(e), which use the mechanism of G2/M arrest and eventual mitotic catastrophe, can approximate the experimental results slightly better, figure 3.22(a), in which the irradiation model is pure survival or apoptotic death, still yields a reasonable approximation of the cell cycle dynamics even without a mechanism which would allow a slow damage response of the cells. Thus the irradiation model can be drastically simplified to be fully derived from the parameters of the LQ model.

Figure 3.23 shows the radiation response of V79 spheroid cells to 3.2 Gy of X-rays as DNA content over time. Within the outer layer of cycling cells a transient increase of cells in G2-phase can be observed in response to irradiation. A peak in G2-cells is reached approximately 8 hours post-radiation and will decrease within 16 hours post-radiation. This is in correspondence to the cell cycle dynamics that are observed within the model for standard parameters.

Within the extended Bragg peak of heavy-ion irradiation, the damage dynamics are often altered as shown in figure 3.24. A more prolonged G2/M block is formed, which persists for 48 hours as would correspond to a stronger impact of the slow damage pathway in this model as illustrated in figure 3.22(b). However, the temporal resolution of measurements by Staab et al. is too low in order to resolve any underlying dynamics in detail. It is possible that an oscillatory response of the cell cycle distribution will not be noticed if measurements are performed with a temporal resolution of only 24 hours. As illustrated in figure 3.22, the radiation reaction will often be oscillating with phase lengths which roughly correspond to the average time needed to complete the cell cycle. Thus, if the temporal resolution is too low, interpolation of data points can suggest that a G2/M block is in effect, while the cell population is actually low on G2 cells.

If measurements are obtained for use in treatment planing, care has to be taken to use a measurement frequency which is well adapted to the characteristic time which determines the process, namely the typical cell cycle time. This observation is in loose analogy to the Nyquist–Shannon sampling theorem.

Overall, the chosen model for radiation damage can reproduce the radiation response of cancer cells and tumours as measured *in vitro*. It can be tuned to yield dynamics which correspond to specific radiation types or cell lines. For investigations within the scope of

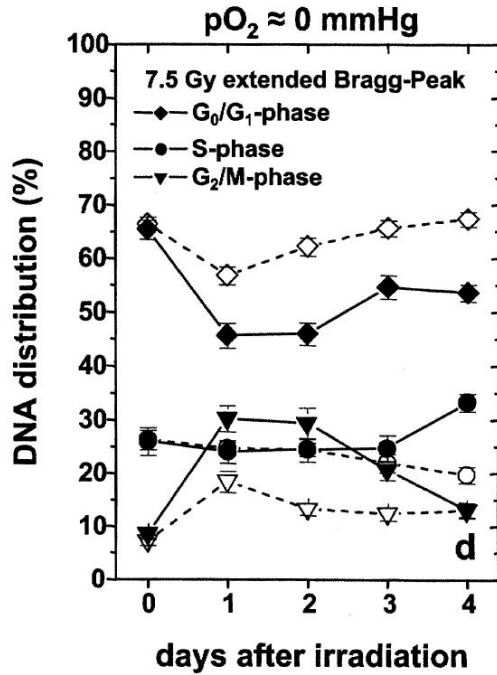


Figure 3.24: Cell cycle distribution of V79 spheroids after irradiation with 7.5 Gy in the extended Bragg peak of carbon ions. From [213].

this thesis, a tuning to the reaction as shown in figure 3.22 was chosen with  $AC=0.8$  and  $MM=0.3$ . This features a relatively high degree of fast apoptosis which is combined with a smaller slow damage response. As both response pathways are used, the model is thus able to yield a generalised response, which should uncover universal effects that are present in all kinds of cancer cells and tumours.

### 3.2.3 Dose-dependent dynamics of enhancement

The radiation response of the tumour will change depending on the irradiation dose. Figure 3.25 shows a detailed study of the enhancement development in response to different doses of radiation in a range from 1 Gy to 8 Gy.

The possible overall enhancement attainable is dose-dependent, as the relative variation of radiosensitivity will increase with dose as shown in figure 2.37(b). As a large subpopulation of radioresistant quiescent cells develops in the tumour, the enhancement will decrease to a steady minimum level previous to irradiation. The resistance effect is relative to the dose as discussed in section 2.5.1, so that the enhancement will show a stronger reduction for large doses.

Upon irradiation an immediate decrease in enhancement is a result of the applied dose. This is a consequence of the cell cycle dependent radiosensitivity. Radiation will selectively kill cells in sensitive phases, so that the remaining population has lower radiosensitivity on average (see also figures 3.29 and 3.30).

As discussed in section 3.2.2, a drop in pressure and an according reactivation of quiescent cells is a result of irradiation. The re-entry of quiescent cells into the cycle will be the basis of a prolonged dynamics response within the tumour. On average, the radiosensitivity of the tumour increases as cells leave quiescence, and their increased radio-resistance is lifted. Furthermore, the re-entry into the cycle will be largely synchronised at the G1/S checkpoint. Thus, a synchronous progression of cells into S-phase can be observed, as shown in figure 3.26.

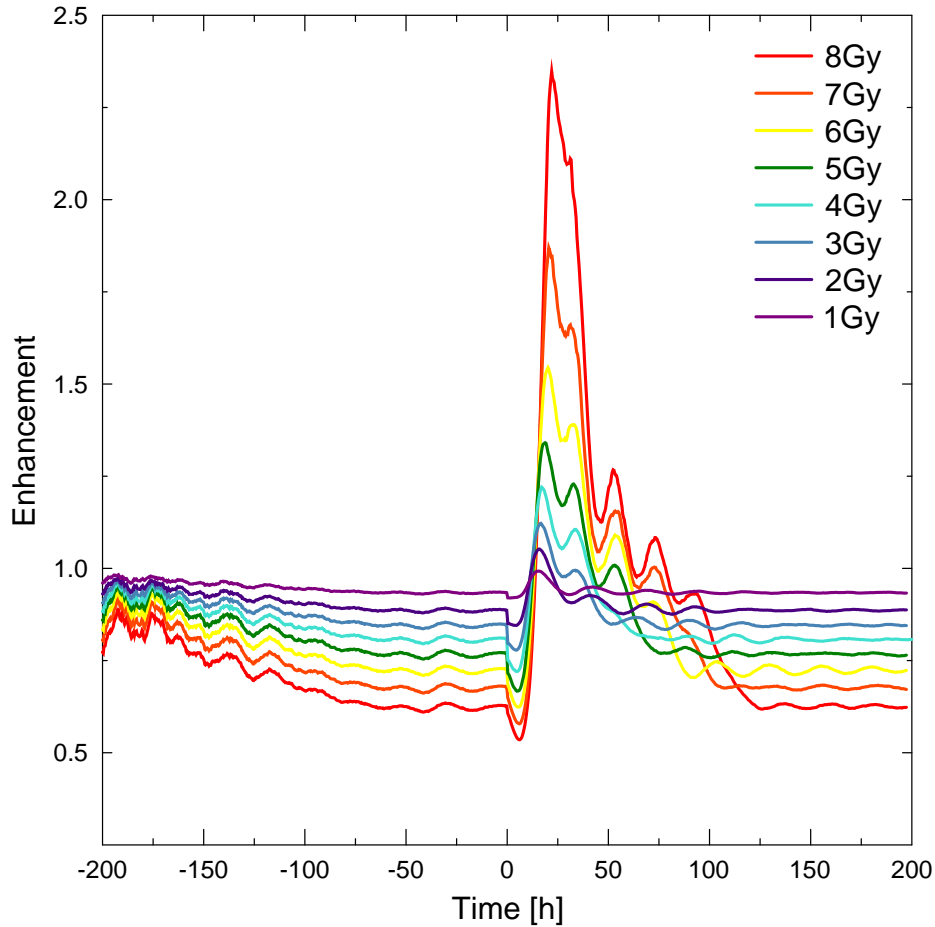


Figure 3.25: Dose-dependent effect of a single administration of radiation applied at 0h on the sensitivity of the tumour. After irradiation, an initial period of increased radioresistance is followed by transient maxima in radiosensitivity which are suitable for targeting by radiotherapy. Oscillations of enhancement are dampened by the entry of cells into quiescence after regrowth and by the normal distribution of cell cycle phase lengths. Also compare to figure 3.45(a) for the effects of enhanced quiescence resistance with  $QRF=2$ .

The peak of cells in S-phase will coincide with the post-radiation minimum in enhancement as visible in figure 3.25. As the cell cycle progression continues, a synchronous advancement of cells into the radiosensitive G2-phase will follow. Blocking of damaged cells at the G2/M checkpoint will lead to a further increase of G2-phase cells and to the transient interchange of the ratio of cells in G1-phase to G2-phase as shown in figure 3.26 and as discussed in [114]. As a result, the increase in G2-phase cells will lead to a sudden drastic increase in the average radiosensitivity of the tumour which is visible as a strong peak in the enhancement reaction.

A transient, two-peaked enhancement reaction to irradiation is observed, followed by synchronised cell cycle progression, which will lead to a period of fluctuating sensitivity. Peaks in the enhancement will occur in correlation to the typical overall cell cycle time of the cells which are subjected to irradiation as illustrated in figure 3.27. In the case of EMT6 cells, as used in the simulation, this implies a timing of about 1170 minutes.

As the cell cycle progression is subject to phase lengths drawn from a normal distribution, the radiation-induced synchronisation will decrease with time. Furthermore, a wave of pro-

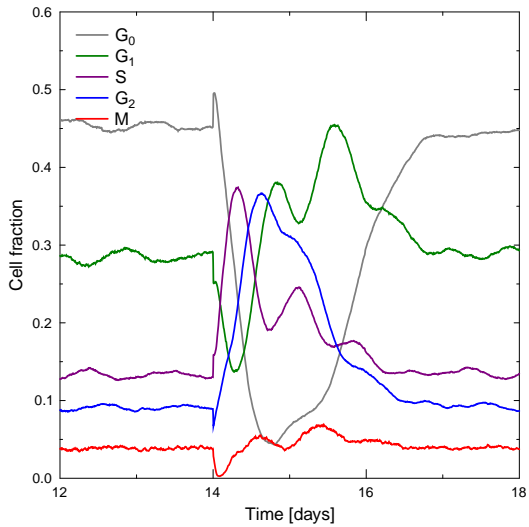


Figure 3.26: Change in the relative fraction of viable cells in response to irradiation with 4 Gy X-rays at day 14. Radiation will trigger an immediate redistribution based on radiosensitivity and a strong following redistribution based mainly on the re-cycling of quiescent cells.

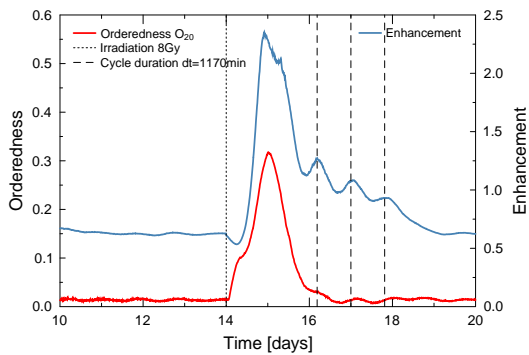


Figure 3.27: Detail of enhancement development and orderedness in response to 8 Gy of radiation. A cyclic development of enhancement is observed, which follows the average cell cycle length of the tumour cells.

liferation, visible as a spike in the mitotic fraction in figure 3.26, will lead to an increase in tumour pressure and thus to the re-establishment of a large quiescent population within 2 days post-radiation. This quiescence significantly contributes to the fast re-development of a baseline-enhancement at pre-radiation levels.

The dampening of the induced oscillation of the cell cycle progression and the according enhancement, will be largely determined by the threshold of cells for induction of quiescence, as will be investigated in the following sections.

The characteristic timing of the enhancement peaks will be largely independent from the applied dose. While a small variation with applied dose can be observed for the first peak, which will be analysed in the following sections, the timing of the follow-up peaks remains constant.

Overall, the dose-enhancement response curve predicts windows of opportunity in which the tumour shows an increased sensitivity to radiation. At the same time, regions of lower enhancement exist which are prohibitive for an administration of radiation. While a fully grown tumour will initially be only half as sensitive to a dose of 8Gy as a comparable tumour in exponential growth phase, after irradiation its sensitivity will increase by a factor of up to 2.5. One goal in treatment planing can be to design a radiation delivery schedule which has been optimised to use these recurring periods of transient sensitivity increase and avoid dose delivery during times of decreased sensitivity as will be discussed in section 3.3.

Similar oscillatory responses to radiation as observed within the simulation have been also predicted by other models, e.g. by Hahnfeldt and Hlatky [83] and observed in experiments

### 3 Results

and termed as protracted-exposure-sensitisation [244]. A ringing of the radiosensitivity in response to split dose-irradiation (as will also be discussed in section 3.2.8) can be observed purely as a result of cycle-phase dependent survival in an age-structured model of cell populations as described in [83].

While the oscillatory responses described by Hahnfeldt are purely a result of the different assumed cell cycle dependent sensitivity (similar to the one used within this model as discussed in section 2.5.1), a similar, albeit more complex, response can be observed within the spatially and temporally more realistic representation used within this investigation.

The comparable case to the predictions of Hahnfeldt and Hlatky shown in figure 3.28 is the drastically simplified model of a tumour spheroid which does not show any quiescence or nutrient-induced inhomogeneities, nor any complex radiation response as oxygen enhancement or the like (and thus corresponds to a purely mathematical compartment model for a cycling cell population). Indeed, the responses as shown in figure 3.28 correspond qualitatively to the enhancement dynamics for a tumour reaction in the absence of quiescence as for example shown in figure 3.36.

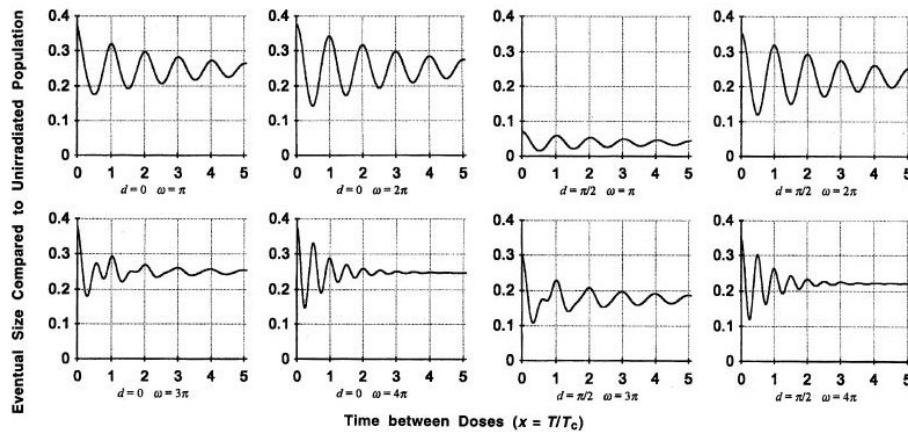


Figure 3.28: Predicted radiosensitivity response of a cell population within a compartment model of cycling cells, which are subject to radiation killing that depends on different cell-age/cell-cycle radiosensitivity functions. Survival is expressed as the relative reduction in population size by a split-dose of radiation which is applied at different times. An oscillatory enhancement response is predicted. Compare also the enhancement dynamics e.g. in figure 3.36. Adapted from [83].

#### 3.2.4 The 4Rs of radiotherapy

As discussed within section 2.5.5, irradiation will trigger responses within a tumour which have been described as the 4Rs of radiotherapy and which form the basis of fractionated irradiation [245, 86]. Apart from the fourth R of repair, all responses can be observed and studied within the model, as will be discussed within the following section. The fifth R of inherent radiosensitivity is included via the measured cell cycle-dependent radiosensitivity which is used as the basis of the response [215].

### Redistribution and Resynchronisation

The strong redistribution and resynchronisation response which is triggered in a tumour by radiation was, to some degree, analysed in section 3.2.2. In summary, a range of different synchronisation sources will contribute to the total amount of synchronisation that is observed. The three main contributors to resynchronisation will be:

- Direct redistribution due to radiation killing
- Amassment of cells at the G2/M checkpoint
- Reactivation of quiescent cells

Upon irradiation, the ratio of cells in sensitive phases to cells in insensitive phases of the cell cycle will change drastically. Figure 3.29 shows cell cycle histograms pre- and post radiation. A slight radiation-induced shift of the histogram can be observed when the cell phase-angle of all non-dead cells is analysed. However, this will include a large proportion of cells which are marked as DNA-damaged and thus will eventually commit to apoptosis at the G2/M checkpoint.

If only non-dead, non-damaged cells are plotted in the histogram, the magnitude of the cell cycle redistribution becomes visible. As the post-radiation data is obtained 1 hour after irradiation, the amount of reactivated quiescent cells which already contribute to the amassment of cells in S-phase is limited. The re-activation of quiescent cells will take a longer time, as is visible in figure 3.26.

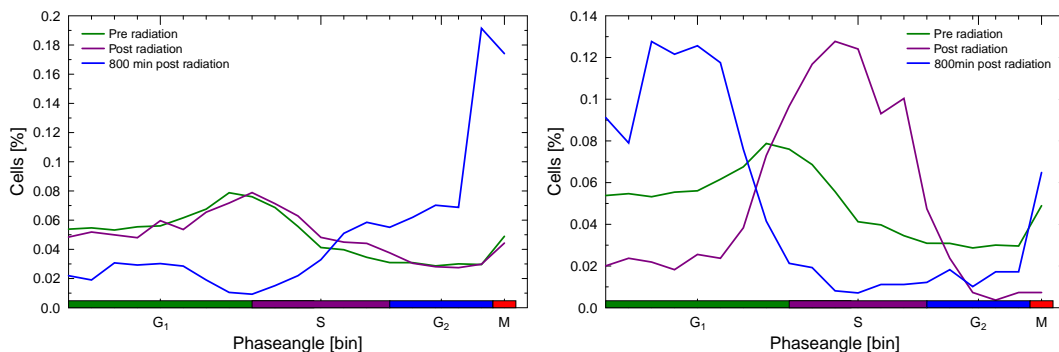
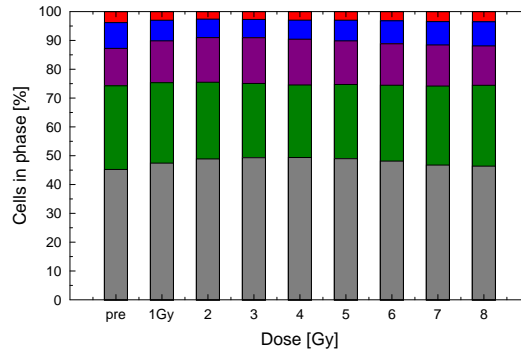


Figure 3.29: Cycle histograms in which *non-dead* cells only or *non-dead, non-damaged* cells reveal the direct redistribution of cells in response to irradiation. Pre-radiation and post-radiation data is obtained directly before and 1 hour after administration of radiation.

A strong accumulation of cells at the G2/M checkpoint is visible in the histogram of non-dead cells. This accumulation is in agreement with experimental observations. Lücke-Huhle et al. report an amassment of 61% of cells in G2/M phase, within 8 hours of irradiation with 8 Gy. This corresponds to observations within the simulation [136]. As is visible in figure 3.26, the G2-block of cells will be completely released within a period of 24 hours, which corresponds to experimental observations [201].

For non-damaged cells, the survival-synchronisation in S-phase will progress into a peak of cells in M-phase and G1-phase within 800 minutes.

Figure 3.30: The immediate effect of a radiation dose on the cell cycle distribution as described in figure 3.31.



A detailed dose-response investigation for runs with a single dose of irradiation between 1 and 8 Gy is provided in figures 3.31 and 3.30. As figure 3.31 demonstrates, the immediate redistribution effects based on the different cycle phase radiosensitivity are minor when compared to the effects that the dynamics of DNA-damaged cells will induce. The direct effects reflect the different relative distances between the survival curves of cells in a specific phase at a given dose as shown in figure 2.37(a).

Even if drastic differences in survival are present (the ratio of most resistant to most sensitive phase survival ranges from 2 at 1 Gy to 32 at 8 Gy), these are not necessarily reflected in a drastic form on the level of the cell killing. This is especially true at high doses, where a large relative survival difference between cell phases (5,5% in S-phase to 0,2% in G2/M-phase) will still lead to an almost uniform killing of cells in all phases: the absolute probability for cell killing (100% - survival) ranges accordingly from 94,5% in S- to 99,8% in G2/M-phase. This effect will limit the direct effect of cell cycle redistribution.

Accordingly, the direct cell cycle redistribution effect is rather small with an absolute change of 10% in cell cycle distribution for a typical therapeutic dose-range of 1-2Gy. The maximum redistribution occurs at 4Gy and reaches a total of about 15% (change in relative cell cycle distribution between pre- and first post-radiation state). This finding is illustrated in figure 3.30.

The later redistribution effects, which are triggered by irradiation and develop within hours post-radiation, are very strong and depend to a high degree on the dose that has been applied. They are illustrated in figure 3.31. The main contribution stems from the reactivation of previously quiescent cells at the restriction point. With increasing dose, an increasing fraction of cells will be blocked at the G2/M checkpoint. At the same time the clearing of cells inside the tumour will reduce the size of the quiescent sub-population proportionally to the applied dose. While a dose of 2Gy will already drastically reduce the size of the quiescent population, doses of 4Gy and higher lead to a temporary full clearing of quiescent cells.

A further source of resynchronisation could be a synchronous re-activation of cells which are quiescent in response to a critical oxygen level associated with hypoxia. As discussed in section 2.1.2, experimental evidence suggests that cells will have an increased probability of entering quiescence for decreasing local oxygen concentration  $pO_2$ . Since quiescence entry in the model is restricted to high pressure in contact-inhibition only, this possible source of synchronisation is not included.

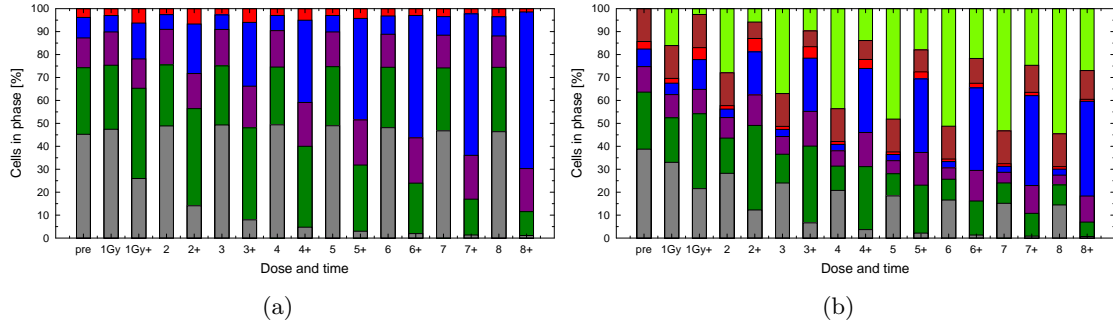


Figure 3.31: Cell cycle redistribution triggered by different levels of irradiation in the dose-study runs of 1Gy-8Gy. Left bar shows the cell cycle distribution immediately before application of a dose (pre), following bars depict the distribution immediately after the dose (20160 minutes plus - labelled by the according dose) and later after irradiation (21180 minutes plus - labelled with according dose and a “+”). Figure (a) shows the relative percentage of viable cells while figure (b) takes into account also dead cells. For better visual comparison the immediate effects are also shown in figure 3.30.

### Repopulation

In response to a dose of radiation, a reactivation of the previously dormant tumour can be observed in the model. Re-entry of non-proliferating, quiescent cells into the cycle, as discussed in the previous section, will eventually lead to a wave of cell division. While the tumour was in a plateau-phase of growth, or even reached a growth saturation prior to irradiation, after administration of a dose a majority of surviving cells will be actively dividing again.

This effect is experimentally and clinically known as accelerated repopulation. It is often observed as a drastic reduction in potential doubling time of the tumour. Sham and Durand report for the irradiation response of V79 spheroids that “potential doubling time decreased steadily from the early part of treatment, remaining of short duration until the spheroids almost attained the pre-treatment number of clonogenic cells” [200]. This observation will be confirmed when the response of spheroids to fractionated irradiation is studied in section 3.3.

For single irradiation, the doubling time of the spheroid will also show a characteristic change as shown in figure 3.32(a).

While the potential doubling time  $T_{pot}$  in case of EMT6 cells corresponds to the average cell cycle length of 1170 minutes, the actual doubling time  $T_d$  can be estimated by scaling of the potential doubling time by the fraction of cells which are available for proliferation (non-quiescent and non-necrotic). As apoptosis is only connected to radiation-death, apoptotic cells are not considered when the doubling time is calculated.

Irradiation will first induce a short increase in doubling time, which is associated with an increase in quiescent cells as an immediate effect of their increased radioresistance. Within hours after irradiation the doubling time will drop drastically, until it almost reaches the initial doubling time, which is equal to the potential doubling time for an initial exponential cell population.

A fast repopulation of the tumour is the result of the decrease in doubling time, as shown in figure 3.32(b). Prior to irradiation, the tumour spheroid grows at a reduced rate, visible as low slope from day 12 to 14. After irradiation has been applied, the overall number of viable

### 3 Results

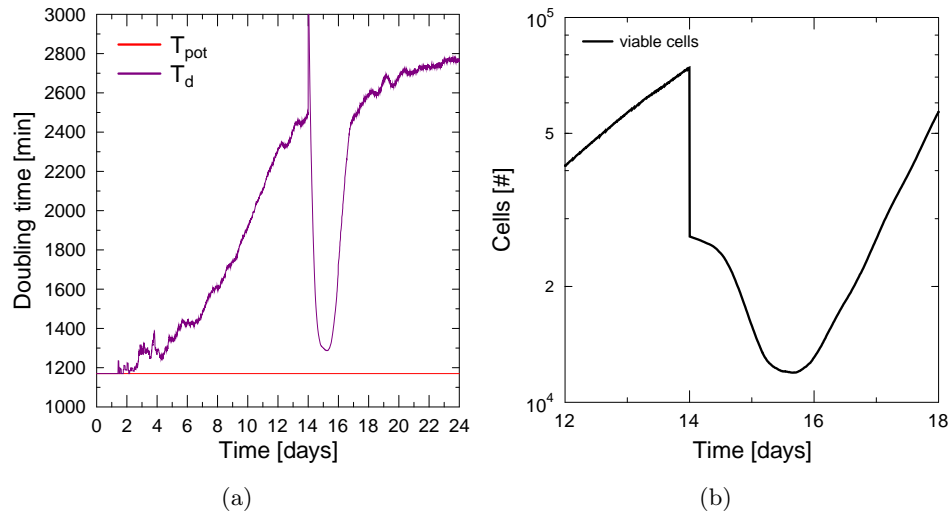


Figure 3.32: **(a)** Potential doubling time  $T_{pot}$  and actual doubling time  $T_d$  of a tumour spheroid during growth and after irradiation with 4 Gy. **(b)** Accelerated repopulation in response to a dose of 8 Gy.

cells within the spheroid will drastically decline, however, after about 2 days the spheroid starts to re-proliferate with a very high slope which is identical to the initial growth in the exponential phase.

Accelerated repopulation will be also marked by a high S-phase fraction and a high mitotic index, as can be seen in figure 3.26. This makes it interesting as target of chemotherapeutic approaches, which trigger cells in synthesis phase as discussed in section 3.5.

#### Reoxygenation

As reoxygenation is of special interest, the change in the oxygen distribution of the tumour and the response to irradiation is discussed separately in sections 3.2.7 and 3.4.

### 3.2.5 Influences on the radiation response

In order to assess the universality of the radiation reactions that were described in the previous section, an investigation of critical parameters in the model for their influence on the tumour response is performed within the following section.

#### Radiation damage dynamics and sensitivity increase

The observed timing and shape of the radiosensitivity enhancement depend on the branching between fast and slow damage in the radiation model. As discussed in section 2.5.6, cells are either instantly killed via a quick process of apoptosis in response to severe damage (fast damage response), or they are marked as damaged and halted at the G2/M checkpoint until they die in delayed apoptosis or mitotic catastrophe due to checkpoint failures (slow damage response).

Consequently, if the ratio between fast (with probability  $AC$ ) and slow death ( $1-AC$ ) is varied, this has an effect on the observed sensitivity dynamics. Figure 3.33 shows enhancement and cell cycle distributions for runs with a variation of the standard radiation parameters in use.

As extreme cases, a radiation response which relies strongly on a slow pathway via the G2/M block ( $AC=0.3$ ,  $MM=0.1$ ) and a very fast radiation response exclusively via the fast apoptosis pathway ( $AC=1$ ) are chosen. A run with a mixture of both pathways ( $AC=0.66$ ,  $MM=0.3$ ) is used as comparison.

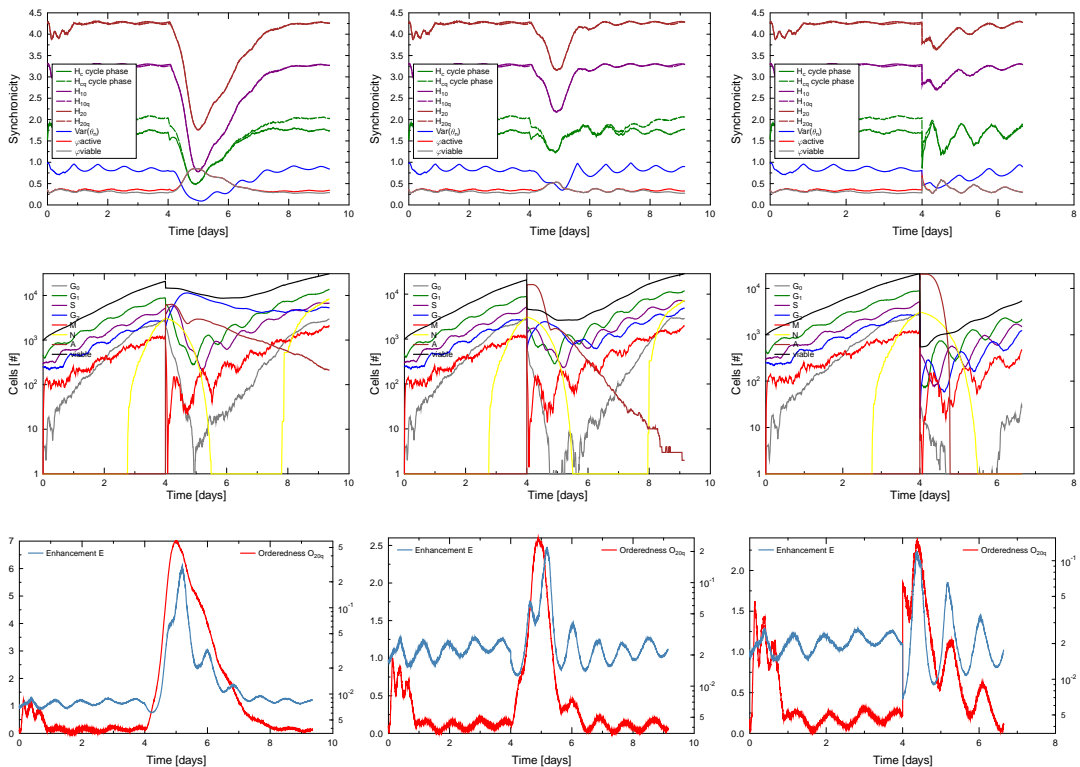
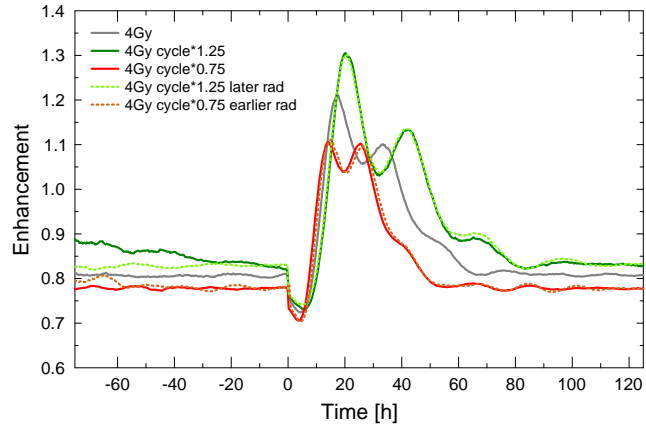


Figure 3.33: Comparison of irradiation using low level of fast apoptosis ( $AC=0.3$ ,  $MM=0.1$ ), intermediate levels (middle column) ( $AC=0.8$ ,  $MM=0.3$ ) and exclusively fast apoptosis (right column) ( $AC=1$ ) in terms of synchronisation and enhancement.

Figure 3.34: Dependence of radiation reaction to 4 Gy at day 14 on the overall average cell cycle time. Total cycle time has been scale up or down by a factor of 0.75 or 1.25 respectively. Additionally, radiation has been performed at day 17 for a larger tumour spheroid.



If a strong emphasis is on the slow damage response pathway a sustained block of cells at the G2/M checkpoint is induced, which is visible as strong decrease in the systems entropy measures. The block of cells in G2 is associated with a high enhancement. A low amount of fast apoptosis will not induce a lasting pressure release in the tumour. While transiently the quiescent population is cleared in the test run, almost immediately after clearance a new population of quiescent cells forms. Synchronisation and the associated enhancement are quickly lost. The enhancement peak shows a slight tow-peaked structure, where the side peak is a result of direct redistribution of cells according to their radiosensitivity and the later main peak a result of foremost quiescent cells which have progressed to G2 phase.

In the case of exclusive cell death via fast apoptosis a sharp change in the observables is the result. A strong initial increase in orderedness is the result of a high amount of re-distribution of cell according to their radiosensitivity. This increase is slightly separated from the following increase in orderedness which will be mainly a result of a synchronous filling of G1 due to cells which reach mitosis phase. The high level of direct redistribution of cells will also lead to an earlier onset of the enhancement peak (as will be also discussed in section 3.2.5). Accordingly also a shift from a double-peaked structure of the first enhancement peak to a single peak is the result. A persistent oscillatory response in the sensitivity enhancement is triggered which is a result of the synchronous advancement of cells in the cycle. The desynchronising effects of quiescence are suppressed for a longer time by the high amount of dissolving apoptotic cells which lead to a decrease of pressure in the spheroid.

If a mixed radiation model is used a balance between fast and slow mechanisms will increase the double-peak structure of the enhancement. All previously discussed mechanisms of re-distribution can be observed. A substantially lower amount of G2-blocked cells will result in a lower enhancement.

It is clear that resynchronisation of the tumour cell population is present independent of the damage mechanisms being fast or slow.

### Variation of average cell phase lengths

As described previously in section 3.2.2, the average duration of the cell cycle phases is connected to the response of the tumour system. Therefore, a variation of the dose-enhancement curve is expected if the average cell cycle times are varied.

A dose-enhancement response to cell cycle times for which the average duration of the cycle phases was altered is shown in figure 3.34.

A change of the typical cell cycle times by a factor of 1.25 and 0.75 will lead to a predictable shift of the enhancement curve. The first enhancement peak is shifted by a factor of 1.16 or 0.82 in response to the corresponding variation of cycle time. The second peak will be shifted by 1.25 and 0.76. This shows that the time position of the second peak exactly reflects the shift of cell cycle times. While the magnitude of the first enhancement peak varies by about 8 percent up or down in response to an increase/decrease in cycle time, the magnitude of the second enhancement peak (and following peaks) remains almost unchanged.

The dampening of the response decreases with an increase in cycle time. Thus a lower cycle time will permit the faster re-formation of the pre-radiation tumour cycle distribution with a high level of quiescence (compare also figure 3.36). For a lower cell cycle duration the progression of cells will be so fast that a full formation of the first enhancement peak is limited by a peak of cells which already enter synthesis phase and thus lower the overall resistance. Accordingly, for a longer cycle duration, the first enhancement peak can develop to a slightly higher magnitude when compared to the reference run.

Furthermore, an alteration of the cell cycle times will lead to a drastically faster or slower overall tumour growth. In order to verify that the cell cycle duration effects are not influenced by the size of the tumour, additional runs have been performed. Within these the tumour was grown to a matching cell number with the 4Gy reference-run before application of irradiation. In the case of reduced cell cycle time (faster growth), this meant that irradiation had to be applied earlier, while in the case of increased cycle time the reverse effect is present.

The different growth speeds are visible in figure 3.34 as the initial variation of growth-retardation and establishment of a quiescent population, both of which influence the enhancement accordingly. However, after radiation has been administered, the enhancement response is not altered for the runs in which radiation has been applied earlier or later to match the reference tumour size.

This implies that, as long as the tumour developed all functional regions, the quality of the enhancement response is not affected if the radiation is applied earlier or later. The variation of the enhancement response depending on the tumour size and moment of irradiation will also be investigated in more detail in section 3.2.5.

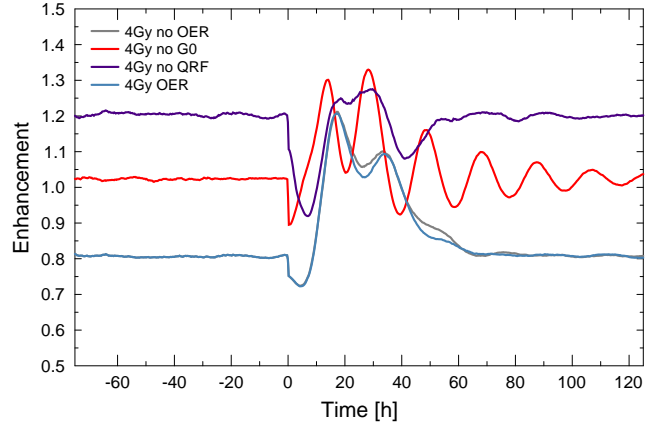
### **Absence of quiescence**

As concluded previously, the induction of quiescence will have a strong influence on the radiation response as a main mechanism of re-synchronisation in response to radiation. However, within cancerous cells, the entry into quiescence might be impaired due to a very high tolerance to environmental stress such as nutrient deprivation or pressure (e.g. the loss of contact inhibition). In order to examine the consequences of a loss of quiescence, simulations were performed in which the mechanisms of quiescence for cells was disabled.

When comparing the reference run for response to irradiation with 4 Gy in figure 3.35 with the run without quiescence (4Gy no G0), a time difference in the enhancement peaks can be observed. While the first peak is shifted by 200min the second peak will be shifted 305min. This can be explained by comparison of the importance of direct cell cycle redistribution versus re-entry from quiescence in both runs: while the run without quiescence shows a strong direct increase in the relative amount of resistant S-phase cells in response to irradiation, the main mechanism of redistribution for the reference run is re-entry of quiescent cells into the cycle. Therefore, the time difference for a majority of cells to reach G2 and establish an

### 3 Results

Figure 3.35: Dependence of radiation reaction to 4 Gy at day 14 on different mechanisms, showing the response for a system without quiescence (no G0), quiescence resistance factor of 1 (no QRF), and oxygen enhancement ratio (OER). By default all runs use a QRF of 1.5 if not stated otherwise. Details of the cell cycle distribution for the runs are provided in figure 3.36.



enhancement peak is half the average duration of S-phase, which will therefore lead to an approximate shift of 180 minutes.

Due to the persistent return of quiescent cells into the cycle over 12h (see figure 3.36) the second enhancement peak in the reference run will be shifted even further relative to the second peak in the quiescence-free run.

The absolute peak position in a quiescence-free case can be approximated by  $\frac{1}{2}\tau_{G1} + \tau_S + \tau_{G2} = 870min$ , as the majority of cells will still be in  $G_1$ -phase after irradiation. Due to the relative high number of S-phase cells directly after irradiation, the maximum will be reached slightly earlier, as these cells only need to advance through S- and  $G_2$ -phase in order to increase the enhancement.

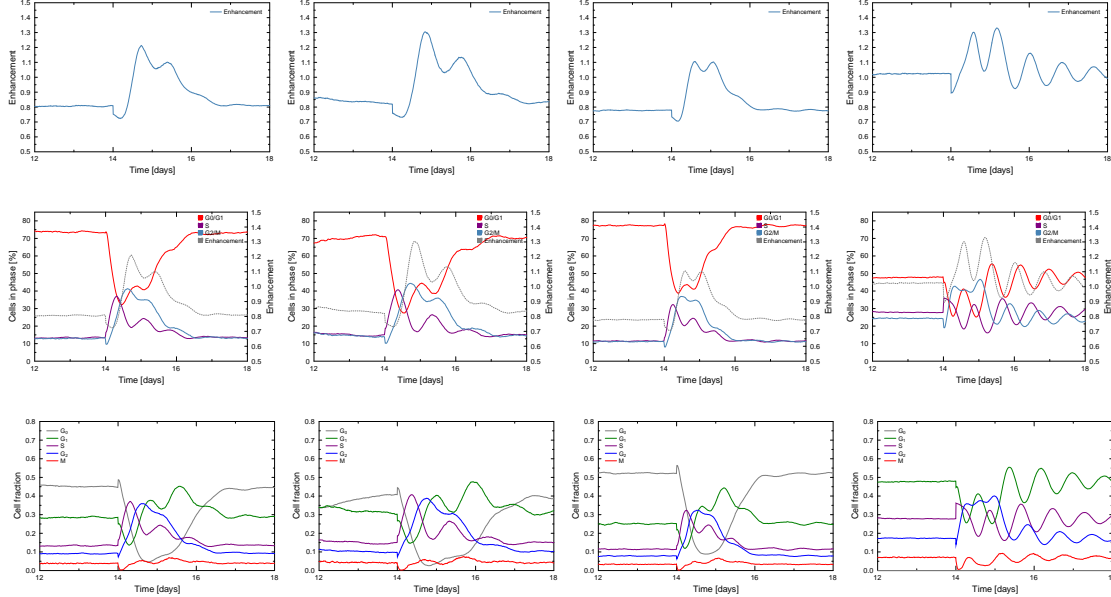


Figure 3.36: Relative cell cycle distribution after irradiation with 4 Gy at day 14. Left column shows a run with standard parameters (4Gy in figures 3.34 and 3.35), columns 2 and 3 with scaled cell cycle times by factor 1.25 and 0.75, column 4 shows response if no quiescence is allowed.

### Quiescence pressure threshold and enhancement

Since the effects of quiescence on the enhancement response are strong, a more detailed investigation of the dependence of the radiation reaction on the induction of quiescence was performed. A change to the critical pressure threshold  $P_{\text{crit}}$  for induction of quiescence will affect the radioresponse of the tumour as shown in figure 3.37.

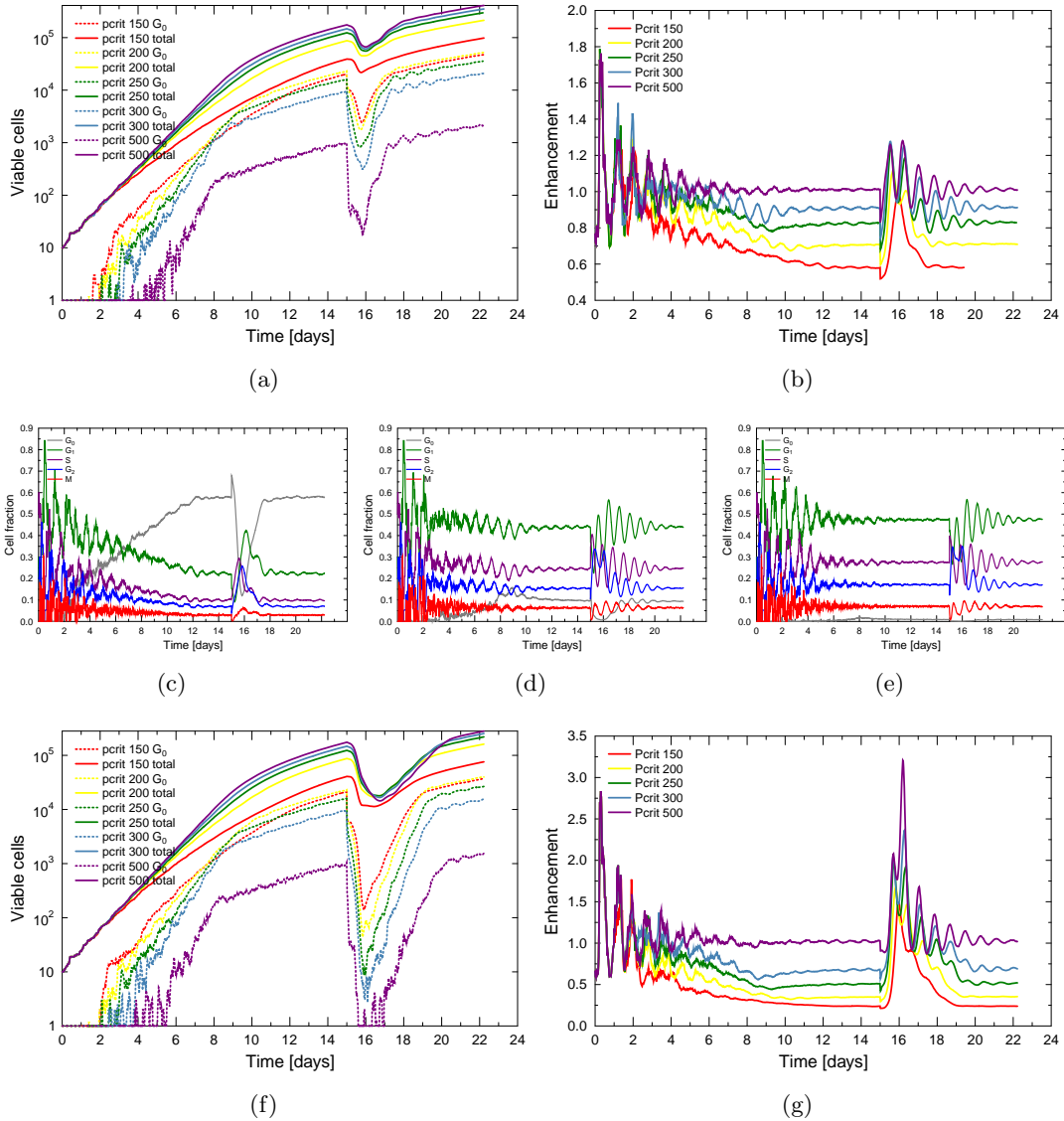


Figure 3.37: **(a-b)** Reactions of a tumour system to a radiation dose of 4 Gy, for different threshold pressures and for the induction of quiescence  $P_{\text{crit}}$ . Quiescence resistance factor is 2. **(c-e)** Relative cell phase distribution of the systems with quiescence pressure thresholds of 150, 300, and 500 Pa. **(f-g)** Tumour reaction to a dose of 8 Gy with varied quiescence threshold.

If a lower threshold is used, a larger quiescent population will develop during the spheroid growth. The resulting reaction to radiation will be relatively short-lived, as the critical pressure needed to re-enter quiescence is quickly built up again and the triggered synchronous oscillation of the cell cycle is accordingly dampened. For low values of  $P_{\text{crit}}=150$  Pa, only

### 3 Results

one distinguishable enhancement peak will thus develop. This peak is almost completely determined by the mechanism of re-entry of quiescent cells into the cycle. As a result, it will occur later than a peak which relies on the direct redistribution of cells as it can be observed for very high pressure thresholds (e.g.  $P_{\text{crit}}=500$  Pa) in which the size of the quiescent subpopulation is drastically decreased (compare figure 3.37(a)).

A higher threshold will lead to a lower quiescent population and an oscillating radioreponse. As all quiescent cells are effectively removed from the tumour by reduction of pressure, the development of sensitivity will just depend on the collective cell cycle progression which is triggered by direct redistribution.

The level of quiescence will shift the importance of radiosensitivity development between the quiescence re-entry and cycle redistribution effects. At the extremes of ubiquitous quiescence, only the re-entry will be the determinant mechanism, while for a lack of quiescence, only direct redistribution will be in effect. A continuous variation of the critical pressure threshold for quiescence will yield a continuous change in the enhancement dynamics. However, the change will be more drastic in the region of critical pressure which corresponds to the typical level which is present inside a tumour spheroid. Therefore, around a  $P_{\text{crit}}$  of approximately 200 Pa, a stronger change in the enhancement response is observed as the amount of quiescence in the tumour is subject to a drastic increase, for thresholds below this pressure.

In the absence of quiescence, the different effects which lead to a resynchronised proliferation and thus an enhancement peak can be clearly distinguished as was also concluded in section 3.2.5. As shown in figure 3.36, irradiation will lead to a relatively strong redistribution in this case, reducing the proportion of cells in G1, G2 and M-phase, while strongly increasing the proportion of cells in S-phase. After radiation this will lead to a subsequent increase of cells in G2 and a synchronised progression into M-phase.

In summary, a pronounced sensitivity peak and synchronised proliferation will, in the absence of quiescence, develop only as a result of cell cycle redistribution. When quiescence is present, the enhancement will be dampened and a continuous shift of the first peak in enhancement will occur as a result of a switching in the dominant mechanisms for cell cycle changes. The timing of later peaks will remain unaffected.

#### Quiescence resistance factor

The level of quiescence resistance that is applied to cells in G0 will influence the radiation reaction. Typical values for the quiescence resistance factor will be between 1.1 and 1.7 as inferred from [147] in section 2.5.1 (accordingly a factor of 1.5 was chosen as default value). A sample reaction of a tumour spheroid for different levels of quiescence resistance is shown in figure 3.38.

The effects of the chosen quiescence resistance factor on the radiation enhancement development are minor even at a moderate dose of 4 Gy.

A quiescence resistance ratio of 1 will assign the same radiosensitivity to cells in G0 as was measured for cells in G1. Thus an amassment of quiescent cells will not lead to a decrease of overall radiosensitivity or enhancement, but to a slight increase, as the overall number of cells in moderately radiosensitive phases will increase (as the G1-radiosensitivity applied to G0 cells is drastically higher than the sensitivity in S-phase).

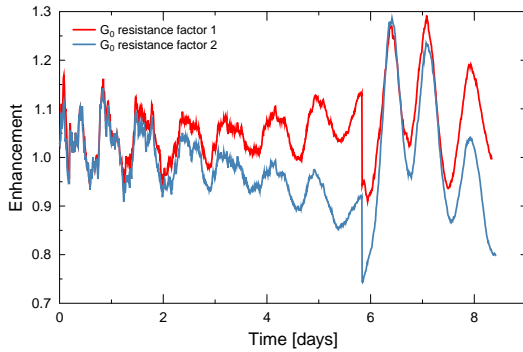


Figure 3.38: Comparison of the tumour reaction to 4Gy of radiation with varied quiescence resistance factors of 2 and 1.

While the magnitude of the enhancement slightly changes with the quiescence resistance factor in use, the quality of the response is conserved. Changes in the magnitude only occur for the enhancement peaks which follow the initial response peak and are accordingly associated with the re-entry of cells into quiescence as a result of the proliferation-induced pressure increase inside the tumour spheroid.

This implies that the exact level of radioresistance of quiescent cells is not required to predict a tumour response. Specific radiation timings to triggered peaks in enhancement are thus possible independently of the QRF, as they are predominantly determined by the cell cycle times and the pressure response of the tumour.

More detailed dose-enhancement curves for varied quiescence resistance factors are also provided in figures 3.25, 3.45(a) and 3.45(b).

### Clearance time of dead cells

As the number of quiescent cells will have a direct influence on the degree of enhancement and on the dynamics of the cell population, the clearance time of dead cells will influence the radio-response indirectly. When a longer time for dissolution of necrotic or apoptotic cells is used, this will lead to a lower amount of release of quiescent cells into the cell cycle. In order to test this assumption, simulations have been performed in which cells either use normal apoptotic and necrotic durations as in the standard parameters in section 4.6 or increased durations of 1440min for apoptosis and 2880min for necrosis.

The results in figure 3.39 show that fast dissolution of dead cells will lead to an efficient clearing of quiescent cells after irradiation, as previously reported. Thus, the associated sensitivity gain is high as a low number of resistant cells are present. The release of quiescence will trigger a transient peak in S-phase, and consequently a larger peak in the sensitive G2-phase quickly after irradiation. Therefore, the observed enhancement reaches a high maximum within a short period of time after irradiation.

If an increased dissolution time for dead cells is in effect, the radioresponse is drastically altered. Only a limited amount of quiescent clearing is achieved within a time frame of about 30 hours. A population of 30% quiescent, resistant cells remains in the tumour at all times, which significantly decreases the enhancement. Even for high radiation doses the absolute enhancement remains low, although a strong relative enhancement can still be induced (raising for example the enhancement from 0.25 to 0.75 after 8 Gy). The slower decrease of pressure will also lead to a slower release of cells from quiescence. Thus, the enhancement peak is drastically shifted to later times. This shifting effect increases with dose, as the clearing of cells and the associated release of cells from quiescence becomes

### 3 Results

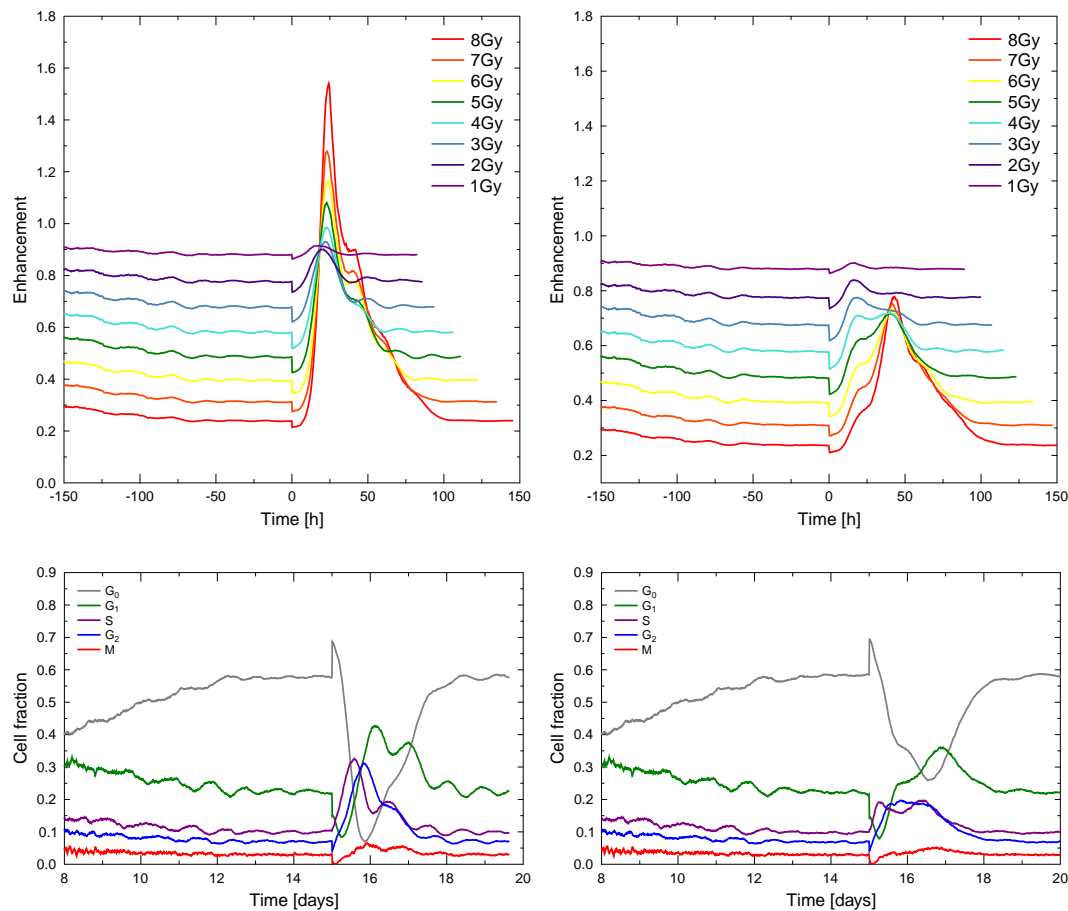


Figure 3.39: Radiation response for normal dead cell clearance (left column) times and slow clearance of apoptotic and necrotic cells (right column, apoptosis and necrosis dissolutions times doubled). The lower row shows a sample development of the viable cell populations after irradiation with 5Gy for both cases. All runs use a quiescence resistance factor of 2.

stronger with dose. At low doses, the direct redistribution of surviving cells as discussed in section 3.2.4 is the main mechanism which dominates the enhancement response. As a result, the time-course of enhancement remains unchanged for low doses, as the change in magnitude will also be lower for small doses.

#### Sensitivity peak timing and tumour size

As the cell cycle distribution within a tumour spheroid changes during growth and reaches a steady state only at the plateau phase of growth, the age and size of a spheroid will influence the observed radiation response.

A systematic investigation of enhancement peak timings has been performed by seeding a small spheroid which was grown to different sizes before an irradiation dose was applied. An alternative investigation was performed by application of a fractionated irradiation scheme as described in section 3.3.7. The repeated irradiation was stopped after different times during the schedule to evaluate the following response of the tumour.

The effects on the peak timing of altered tumour size when irradiation is administered at different times during the growth phase are depicted in figure 3.40.

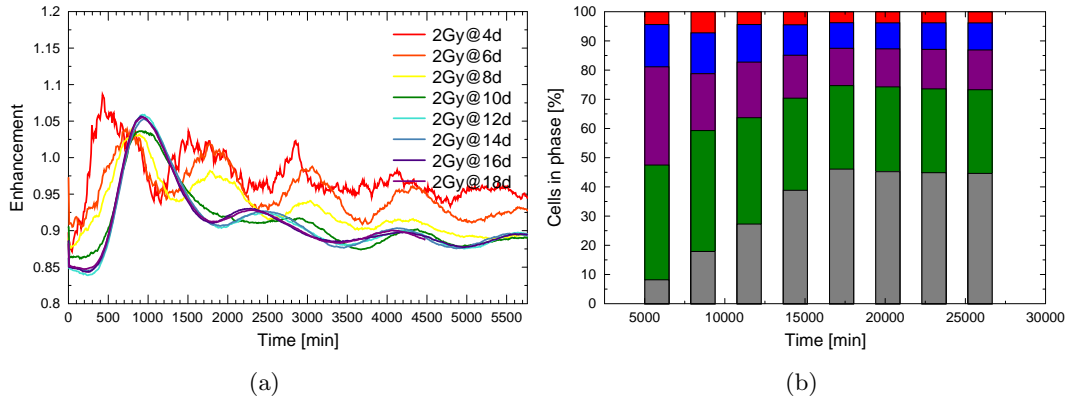


Figure 3.40: **(a)** Sensitivity peak timing after a dose of 2Gy has been delivered to the tumour at different times after seeding of the spheroid during the growth phase. **(b)** The cell cycle distribution inside the tumour exactly before application of radiation.

For a very early administration of radiation, the enhancement will peak significantly faster in response to irradiation. A high fluctuation of enhancement can be observed, which is partially a result of the smaller tumour system (which comprises only about 300 cells at this early stage). Fluctuations persist for multiple days as a cyclic repetition of the initial response is observed with a dampened amplitude.

With increasing tumour age, and thus size, the peak will be shifted further away from the irradiation time and following oscillations in enhancement will be increasingly dampened. This change is associated with the growing proportion of quiescent cells as shown in figure 3.40(b). If irradiation is applied 8 days after seeding, the response will already be a mixture between an exponential growth-phase response and a plateau-phase response.

After about 12 days, the cell cycle distribution of the tumour will remain constant during further growth. Consequently, the enhancement response that is associated with irradiation does not significantly change anymore, if radiation is applied later than day 12.

This confirms that irradiation application after at least 12 days can be used to predict the reaction of a fully grown spheroid at a later time.

Figure 3.41 shows the development of enhancement after a fractionated irradiation regimen has been stopped at different points in time during treatment. In this case, fractionation will apply a dose of 1 Gy which will be followed by a second dose of 3 Gy, timed to be administered at the enhancement peak that was triggered by the first dose (fractionation schedules of this type will be discussed in detail in section 3.3.7).

While the initial 2-dose block of fractionation, which is administered at day 14, will trigger an enhancement response from a plateau-phase tumour, the following blocks will act on a tumour which has a significantly lower quiescent population as can be seen in figure 3.41(b). The second dose of the initial fractionation block will thus exactly hit the maximum of enhancement and trigger a new increase in enhancement itself. For fractionation blocks which are administered at a later point in time in the treatment schedule, the initial response to the trigger dose of 1 Gy has slightly shifted so that the maximum is no longer exactly targeted. A slight systematic shift of the overall enhancement response with treatment time

### 3 Results

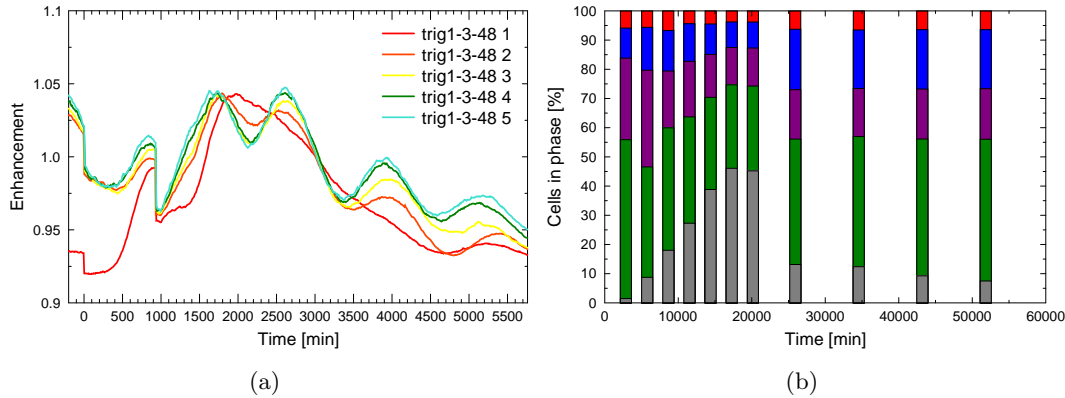


Figure 3.41: **(a)** Sensitivity development during a fractionated treatment regimen which employs blocks of coordinated doses of 1 Gy and 3 Gy. Treatment with the fractionation schedule has been stopped after a last delivery of a 1Gy,3Gy-combination at 20160 (trig1-3 1), 25920 (2), 34560 (3), 43200 (4), or 51840 minutes (5). **(b)** The cell cycle distribution inside the tumour exactly before radiation is applied.

can be observed. Higher enhancement values will be achieved during later times. This is a result of the slightly increasing proportion of cells which are blocked in the radiosensitive G2 phase. Furthermore, the timing of the enhancement peaks continuously shifts to earlier points in time. This effect can be explained by the increased importance of direct cell cycle redistribution over the release of quiescent cells.

In a treatment situation this implies that, for a large, well-structured tumour spheroid, the peak timing will be constant and dampening of enhancement oscillations high. As follow-up irradiations are applied in a coordinated fractionation scheme, the reactivity of the tumour spheroid will change and thus the enhancement timing will systematically be shifted to lower times during the treatment schedule. This effect will be confirmed later in the study of treatment schedules (see section 3.3.7).

#### 3.2.6 Synchronicity and enhancement

The tumour response of enhancement is coupled to a corresponding development of the synchronicity of the cell population. Figure 3.42(a) shows the good correlation between enhancement response and orderedness within the tumour system.

This correlation basically allows for the identification of sensitive phases by a measurement or estimation of the entropy of the tumour cell population.

In order to assess the ability to base the entropy estimation on different measurables, a manual synchronisation test of the tumour population was performed. The phase angle  $\phi$  of all cells was synchronously set to the same position, corresponding to a full synchronisation of the system, which will afterwards decrease as a result of the normal cell cycle dynamics. As indicated in figure 3.43, all different measurables which can be used for the calculation of the system's entropy will lead to a qualitatively equal orderedness.

Thus, a simple classification of cells by DNA content, as is routinely performed in experimental and clinical settings, will be sufficient in order to estimate the entropy with reasonable accuracy. The coarse classifications yield similar results to more advanced methods such as

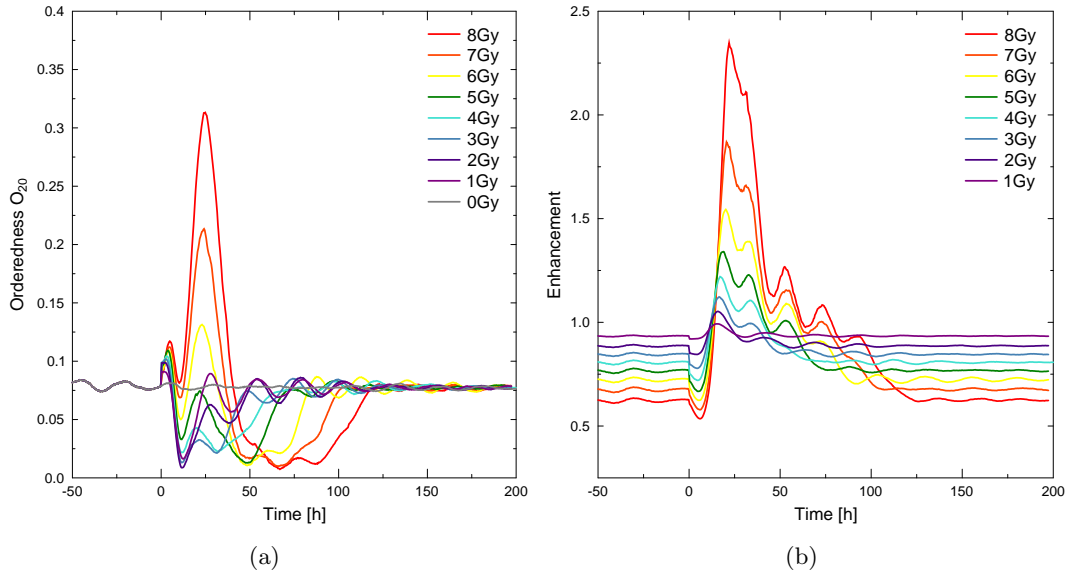


Figure 3.42: The development of entropy for irradiation with varying dose is in good correlation to the enhancement development.

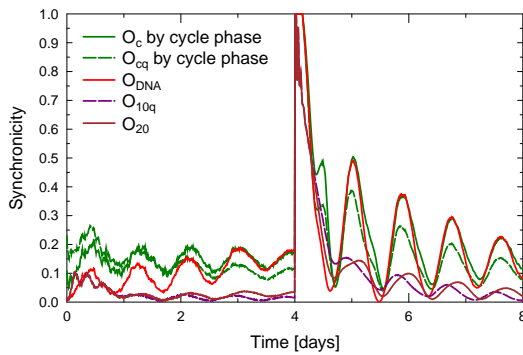


Figure 3.43: The orderedness development in a sample synchronisation test, where a full manual synchronisation is performed at day 4. All possible descriptions of orderedness correspond well even if only the DNA content of cells is used for calculation of the entropy in  $O_{DNA}$ .

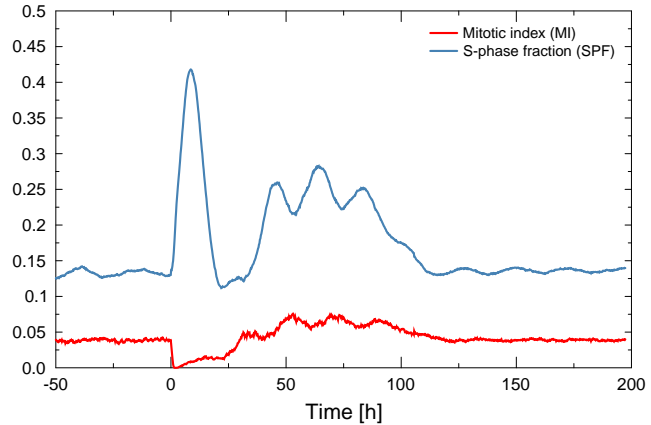
the phase angle-based entropy estimation. Advanced methods however are restricted to a use in the simulation, as long as no frequent immunohistochemical CDK-sorting and according precise determination of the cell cycle position of cells *in vivo* is available.

Different methods for the measurement of proliferation in tumours are established in experimental and clinical settings as described in [18]. This encompasses methods which require tissue samples (such as determination of the mitotic index MI or the S-phase fraction) but also newer techniques which are non-invasive (such as PET scanning with FDG or FLT) which can, to some extent, be used to assess proliferation in tumours under treatment. While the initial method of measuring S-phase fraction (SPF) was by measuring the tritiated thymidine (3HTdR) labelling index (LI), newer methods include flow cytometry measurements (which have been shown to correlate with mitotic counts, histological grades and 3HTdR labelling index).

The S-phase fraction and the mitotic index are readily available within the simulation. As shown in figure 3.44, they show a good correlation with phases of high enhancement.

Due to the longer phase lengths and the relatively higher number of cells in the corresponding phase, the SPF is a more reliable signal which can be immediately seen in the signal to

Figure 3.44: Mitotic index and S-phase fraction can be obtained in experimental settings and through biopsy samples in clinical settings. In response to irradiation with 8 Gy, a strong signal is observed which can be correlated with the corresponding radiosensitivity enhancement.



noise ratio of both observables.

Using a range of observables thus a prediction of radiosensitive tumour states is basically possible in an experimental and, to a limited degree, also in a clinical setting.

However, the correlation between orderedness and enhancement must not be used as the only measure for the prediction of suitable irradiation time points, as a high correlation will also be observed when the tumour is in an especially radio-resistant state. This is obvious in the initial response to irradiation as shown in figure 3.42. While the initial rearrangement of the cell cycle distribution which is triggered by irradiation will cause an increase in S-phase cells and a drop in enhancement, it will also increase the measured orderedness of the system.

A combination of orderedness measurements and predictions with other measurables can allow a robust identification of high enhancement periods.

### Relaxation time for disturbance of the cell cycle distribution

Of special interest for a therapeutic setting is the question of after what time a population of cells will return to an equilibrium state when it has been disturbed e.g. by the administration of a radiation dose. This characteristic relaxation time  $R$  of the tumour can be used to decide if synchronisation effects can or have to be taken into consideration in treatment application. If the relaxation time is larger than the treatment interval  $T > dt_{\text{frac}}$ , a complex interaction between internal tumour dynamics and the external influence of therapy is to be expected.

If the typical treatment interval is longer than the relaxation time of the tumour ( $T < dt_{\text{frac}}$ ), a decoupling of effects between fractions can be expected. The treatment pauses are sufficient for the tumour to reach a steady state again. However, as shown in section 3.2.5, the treatment will still exert a long-term influence which alters the reaction of the tumour system for prolonged schedules.

The relaxation time can be easily identified as the time after which the entropy or orderedness of the tumour returns to a certain interval around the pre-treatment quasi-equilibrium level as for example in figure 3.42. As expected, the relaxation time will depend on the magnitude of the applied dose. The strong and persistent changes which are associated with high radiation doses are also reflected in the level of orderedness development and relaxation.

The relaxation time of a tumour will largely depend on the readiness of cells to commit to quiescence. If a low threshold for quiescence is used, the radiation reaction will be strongly dampened and relax to a pre-radiation state quite quickly. Any other source of quiescence will enhance this effect, as for example hypoxia-induced quiescence.

In later stages of prolonged fractionated irradiation regimens, the relaxation time will be altered with a high probability. The tumour will effectively not return to a steady state anymore, which is normally associated with a typical cell cycle distribution in plateau phase. Thus long-time changes of the overall cell cycle distribution can prove to be a problem in the design of treatment schedules, as discussed in section 3.3.8.

### 3.2.7 Oxygen enhancement

If oxygen enhancement effects are enabled, the cells' radiation survival will depend on the local concentration of  $O_2$  as described in section 2.5.1. For a  $pO_2$  below 4% the resistance of cells to radiation will increase drastically, depending on the LET of the applied radiation as shown in figure 2.30.

The dose-enhancement reaction of a tumour with and without the effects of oxygen enhancement is provided in figure 3.45. The effects of OER are rather subtle. A slight decrease in the first post-radiation enhancement peak can be observed, which increases with the applied dose. The timing of the enhancement peaks remains unaffected.

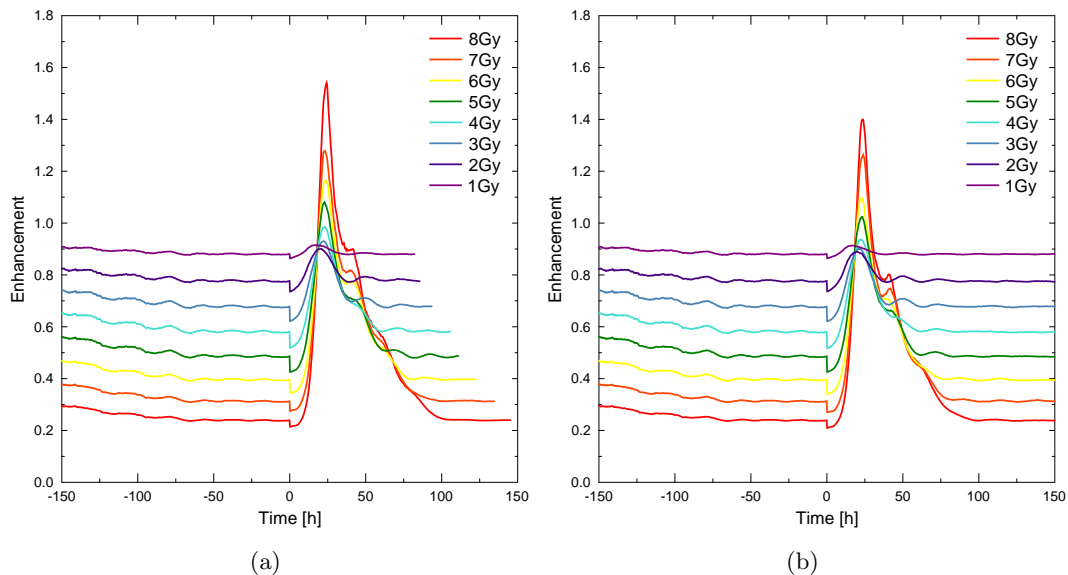


Figure 3.45: Comparison of the oxygen enhancement effects in a sample tumour. An enhanced quiescence resistance factor of 2 is used in both runs. (a) Dose-enhancement without OER (b) with OER according to section 2.5.1.

The radiation enhancement will decrease significantly faster if oxygen enhancement is in effect, especially for runs which employ a higher radiation dose. This is in response to a higher survival of hypoxic cells within the tumour, which are often also quiescent and thus show an increased radiation resistance.

For the given situation, the effects of oxygen enhancement are small. Within the comparison of dose-sensitivity curves, the difference is almost unnoticeable, as is the case in the relative cell cycle phase distributions.

The effect of oxygen enhancement is also shown in the absolute number of viable cells and proportion of hypoxic cells in figure 3.46. As expected, the effects of oxygen enhancement on the survival of cells scale with dose. For lower doses of 2 Gy the difference in absolute

### 3 Results

survival is relatively small, while at a dose of 8 Gy a drastic change in the overall cell survival can be observed.

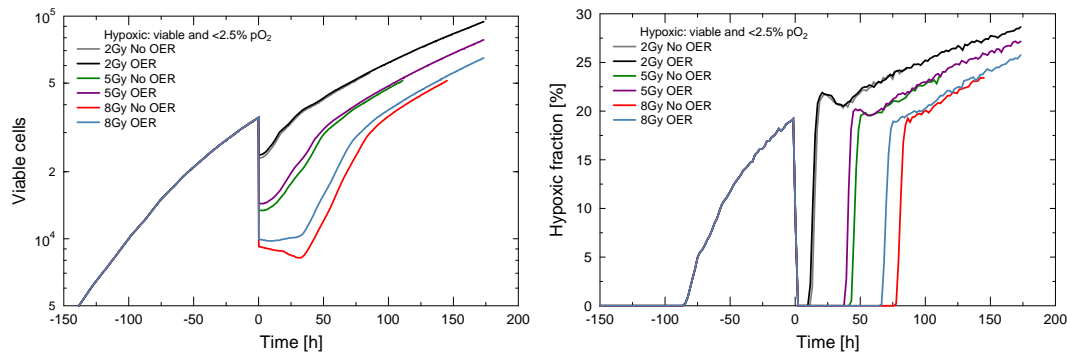


Figure 3.46: Survival of cells will be increased if oxygen enhancement leads to resistance of hypoxic cells in the tumour core. Higher general survival and survival of cells in previously hypoxic regions will lead to the faster reformation of a hypoxic sub-population after irradiation.

After a dose of radiation has been applied, hypoxia can be cleared in response to cell death as discussed in section 3.4. As seen in figure 3.46, a dose of 2 Gy is already sufficient to temporarily clear hypoxia in the sample tumour. The period of time in which hypoxia does not redevelop inside the tumour increases with applied dose. While for a typical clinical dose of 2 Gy the tumour is only void of hypoxic cells for a limited period of about 10 hours, a high dose of 8 Gy can induce a lasting clearing of about 3 days duration.

When oxygen enhancement effects are present, a hypoxic fraction of cells in the tumour is re-established significantly faster than without oxygen enhancement. This effect corresponds to the increased survival of cells in hypoxic regions. These cells are more likely to be affected by hypoxia again, as the tumour regrows after application of radiation.

#### 3.2.8 Split-dose experiments

The overall dynamics of radiosensitivity triggered by irradiation were studied in detail by Elkind et al. [66]. A population of fast-cycling V79-1 Chinese hamster cells was irradiated initially with 8Gy and a follow-up dose of 8Gy was delivered after different time-intervals, ranging from 0 to 10 hours. Figure 3.47(a) shows the original results, where cells were kept at different temperatures during the experiments. This would either allow for a full cell cycle progression and repair at 37°C, only repair at 24°C or drastically impaired repair only at 3°C.

The fraction of surviving cells after split-dose irradiation cannot be directly compared to the survival in the simulation, as the determination of survival is performed with a different approach: while the simulation uses immediate single-cell based survival, within the experiment a colony forming assay is used to determine and score clonogenic survival after the cells have been dissolved and re-seeded. As a result, the survival curves have been normalised to the initial survival level, as was done by Elkind et al. for the original data in figure 3.47(a).

Allowing for a short time-interval between the first and second dose will, initially, strongly enhance the survival of cells when compared to the survival in response to a single dose of 16 Gy. This shows that damage which is only potentially lethal is repaired before the second

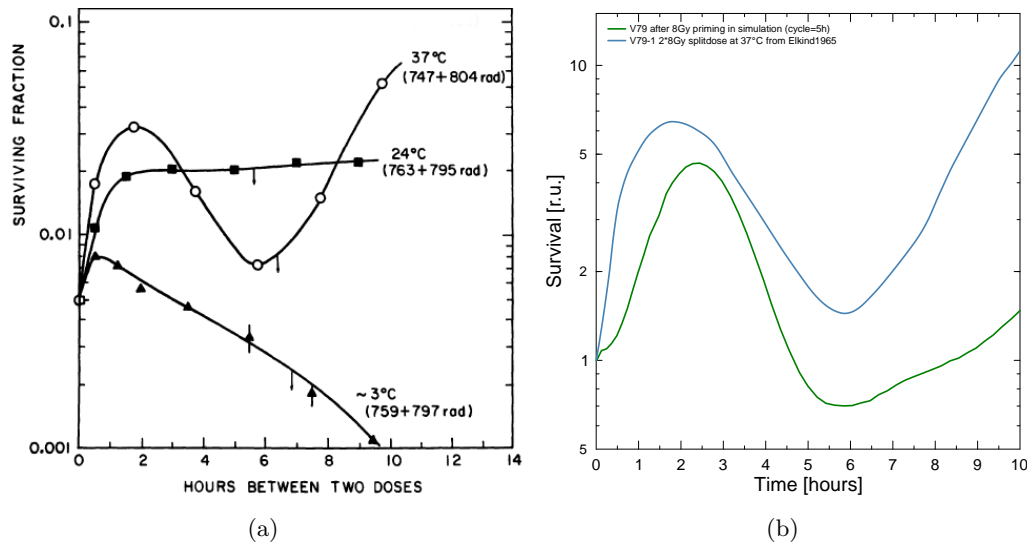


Figure 3.47: (a) Survival of fast-cycling V79-1 cells after split-dose irradiation with 8Gy at 0h followed by a second dose of 8Gy at various time points. Cells at 37°C could continue with cell cycle progression and repair, while cells at 24°C only show repair. From [66]. (b) Normalised cell survival in response to 8Gy of radiation after an initial trigger dose of 8Gy in the experiment of [66] and the simulation. Total cell cycles times of some cells under consideration were different so the time-axis was stretched to visualise the qualitative identity of the response.

dose is applied. The result in increase in total survival reaches a maximum when no cell cycle progression is allowed (24°C), where the saturation marks the point in time when all repairable damage has been removed before a second dose is received. The result in figure 3.47(a) thus demonstrates again the fast rate of repair. In V79 cells, almost all sublethal damage (and probably also PLD) has been repaired within 2 hours post-radiation.

If cell cycle progression is allowed at 37°C, an independent rise in survival can be observed, which is faster than the rise associated with damage repair. The total increase in survival will be higher, due to a large number of cells which progress into the radio-resistant S-phase and because, additionally, the effects of repair are present.

The irradiation model within this simulation does not include any direct damage repair, but the simulation results will nevertheless show an increase in survival, which is just as strong as in the experiment (compare figures 3.47(a) and 3.47(b)). This implies that the importance of sublethal damage repair might be not as high as expected. Specifically, for typical fractionation schedule intervals, which will be well above 2 hours, sublethal damage repair becomes increasingly unimportant (at least in cells which show a fast repair). The progression of cell cycle dynamics will be the largest factor which determines the tumour radiosensitivity.

Elkind states: “Since most of the survivors were in the S phase when irradiated, the initial increase in two-dose survival reflects mainly the repair of damage in these cells.” However, a major contribution to the peak in survival (and within the simulation the only contribution), will be the reactivation of quiescent cells as shown in figure 3.48(b). An immediately progression of quiescent cells into S-phase triggered by the radiation-induced pressure release will thus increase the observed radiation survival.

### 3 Results

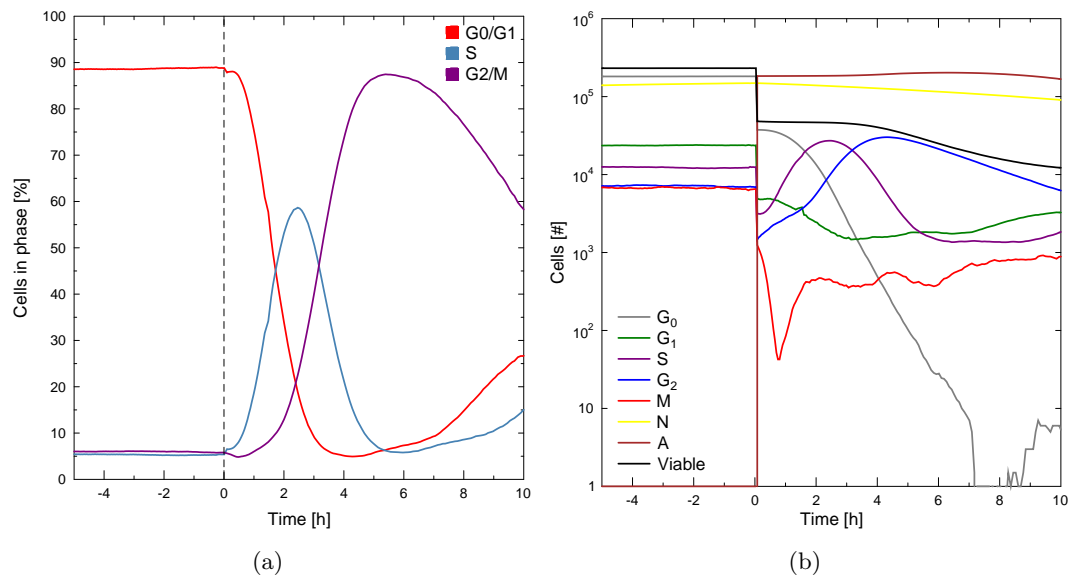


Figure 3.48: Detailed cell cycle progression in response to 8 Gy reveals the origin of the enhancement development reported in [66]. Main determinant for the overall radiosensitivity change is the re-entry of quiescent cells into the cycle in resistant S-phase. Eventual progression into sensitive G2-phase will yield a minimum in survival. Compare also figure 3.47.

The cell cycle progression will eventually advance a majority of cells synchronously into the sensitive G2-phase as shown in figure 3.48(a), which will lead to a transient minimum in overall survival. At this point the total survival in response to two fractions of 8Gy is almost as low as the response to the dose delivered in one fraction of 16Gy in the experiment. This demonstrates the magnitude of the possible enhancing effect, which is a result of the cell cycle progression. Within the simulation, the survival at this point is even lower than the initial survival, which is caused by the absence of repair in cells and which would otherwise add a constant level of survival as seen in figure 3.47(a).

### 3.3 Fractionated irradiation

In the previous section the response of a multicellular tumour spheroid to the administration of radiation as a single fraction or as split-dose was analysed. The standard parameter set, as employed in the simulation, yields an irradiation response which is comparable to experimentally measured developments of the cell cycle distribution. The choice of parameters allows a mixed response to irradiation, which is not purely governed by apoptosis but does also not rely only on G2/M blocking. Within the following section the investigation will be extended to radiation application within prolonged fractionated treatment schedules. As the single response is captured reasonably well by the model, a realistic prediction for the effects which develop in repeated radiation delivery can be expected.

#### 3.3.1 Maximal cell cycle effects during repeated delivery

The current cell cycle phase will largely determine the irradiation response and overall survival as discussed in section 2.5.1. If a population of cells is continuously irradiated in a resistant phase or, alternatively, in a sensitive phase, a total maximum survival difference after fractionated treatment will build up. Assuming an S-phase survival of 70% and an G2-phase survival of 30% after 20 fractions, a theoretical survival difference of factor

$$E = \frac{0.3^{20}}{0.7^{20}} \approx 23000000 \quad (3.2)$$

can build up (as illustrated in figure 3.49).

Introduction of a variation of radiosensitivity and resulting survival between each fraction from either 0.3 to 0.7 or even 0.1 to 0.9 will result in strong differences in overall survival after the full fractionation scheme.

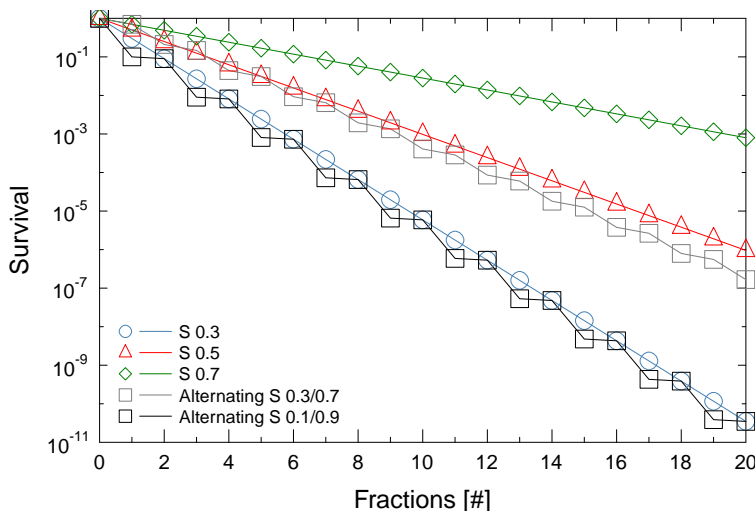


Figure 3.49: Maximum and minimum survival expected due to cell cycle effects after 20 fractions of 2Gy. Each single fractionation will trigger a survival as indicated in the legend. In the alternative schedules, survival will vary between subsequent fractions.

Assuming a typical tumour cell population of  $10^9$  cells, the expected survival for the runs yields a number of surviving cells of either 0 or approx. 800000. This will drastically change the chances of curing the tumour.

While the difference of irradiating either at the least or most radiosensitive point in time is extreme and not realistic for a clinical run, smaller differences in survival probabilities can also result in drastic differences in the outcome. This example illustrates that the cell cycle

### 3 Results

specific survival changes are an important asset in aiming to control a tumour.

If an average cycle time is can be associated with the cell, then a simple strategy to avoid repeated accidental irradiation of a population in a resistant phase is to alter the interval of radiation delivery.

#### 3.3.2 Control dose and fast apoptosis effect

A defining characteristic of a tumour system is the dose per time unit which is needed to stall or even reverse the growth. In order to investigate which dose per time unit is associated with a reduction in tumour size, conventional schedules of 1 fraction per day have been applied to a tumour with a varied dose. Figure 3.50 shows an overview of the effects if the treatment is applied for 14 consecutive days.

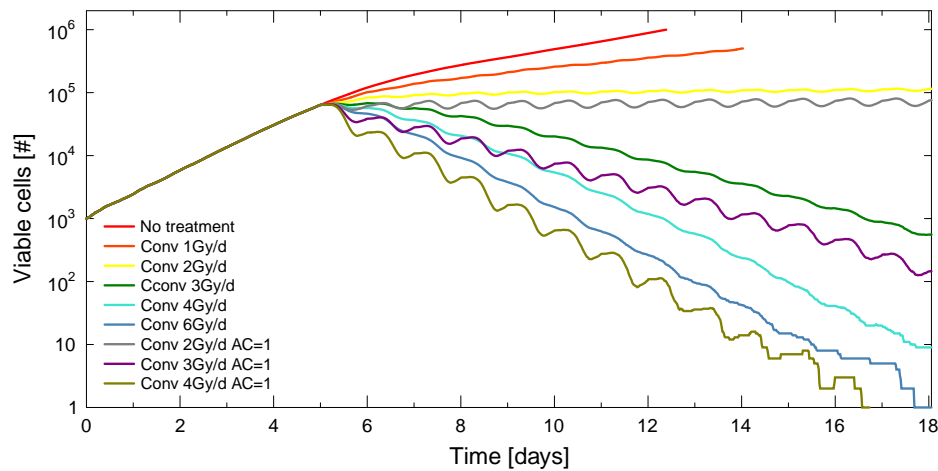


Figure 3.50: Comparison of daily irradiation with different doses reveals which dose per day is needed to control the tumour. If the radiation model is simplified to the fast response via apoptosis only (apoptotic chance set to 1.0) the effectivity of immediate cell killing is enhanced.

A dose per fraction of 2Gy must be applied in order to control the tumour. Application of lower doses per time will not be sufficient to fully counteract the proliferation of the system, resulting in an overall growth of the tumour despite the treatment. Dose rates of more than 2Gy per day will be sufficient to shrink and eventually eliminate the tumour (also, sterilization will, in many cases, only be achieved if the treatment is continued for more than 14 days).

This measurement can act as a basic guideline of the effects that repeated irradiation will have on the model spheroid. As the clonogenic capacity of cells is not bound by a division limit or senescence, the level of possible regrowth in response to treatment within the tumour is very high. Furthermore, the absence of *in vivo* mechanisms, such as immune-mediated cell killing in reaction to radiation or bystander damage, will lead to a higher dose being required to control or shrink the tumour than in a typical clinical setting. This is in agreement with experimental observations on multicellular tumour spheroids, where a much more rapid growth of spheroid cells is observed than for cells in an *in vivo* setting [200].

A simplification of the damage model as discussed in section 2.5.6 has no major effect on the necessary control dose per time unit. If the slow damage pathway of G2/M arrest, loss of control and eventual mitotic catastrophe is disabled, a radiation fraction will induce

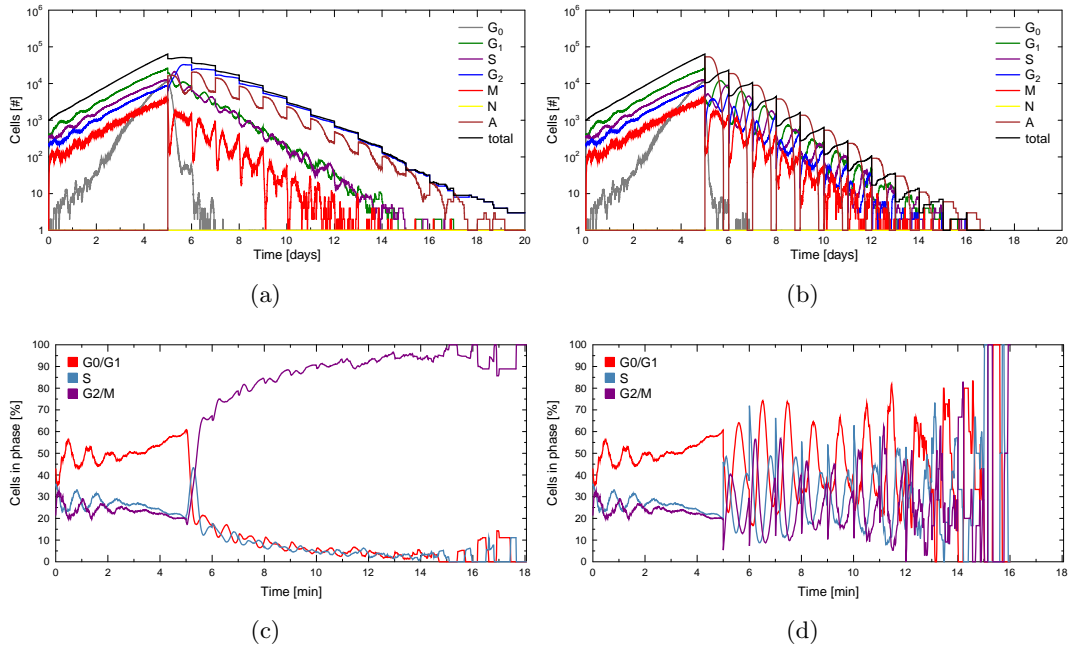


Figure 3.51: **(a-d)** Comparison of tumour reaction if the slow damage reactions via mitotic catastrophe is dominant in **(a)** and **(c)** ( $AC=0.3$ ,  $MM=0.1$ ) or if radiation death is restricted to fast apoptosis only ( $AC=1$ ) in **(b)** and **(d)**.

a stronger immediate decrease in the number of viable cells. This will appear as a greater reduction in tumour burden, as only viable cells are plotted in figure 3.50. However, for runs which use both a dominant fast radio-response and a fraction of cells which are killed via G2/M arrest, a fraction of the cells which are plotted as viable are severely DNA damaged and thus clonogenically dead.

If the radiation model is switched between the two extremes of dominant radiation death via slow mitotic catastrophe (parametrised by  $AC=0.3$  and  $MM=0.1$ ) and fast, direct apoptosis only ( $AC=1$ ), the according cell cycle response changes as shown in figure 3.51.

A fast and persistent increase in damaged cells at the G2/M checkpoint can be observed for the slow damage dynamics. This will lead to an overall high level of apoptosis, as a fraction of cells will constantly die in mitotic catastrophe. The fraction of cells in G2-phase will be extremely high, which will also yield a high radiosensitivity enhancement. If only the fast apoptotic damage pathway is used, a continued oscillation of the cell cycle distribution, which is triggered by the fractionation, will result. After each fraction of radiation, the reaction of the tumour will be similar with transient peaks of S-phase, G2/M-phase and G0/G1-phase cells.

### 3.3.3 Simulation of clinical schedules

A variety of fractionation schemes were tested in the simulation corresponding to the different types of typical clinical schedules as discussed in section 2.5.5. An overview of the according fractionation timings is provided in figure 3.52.

The schedules will deliver an integral dose  $D_i$  of 60 Gy except for CHART treatment which will deliver a total dose of 54 Gy in accordance with its exact clinical implementation. Within

### 3 Results

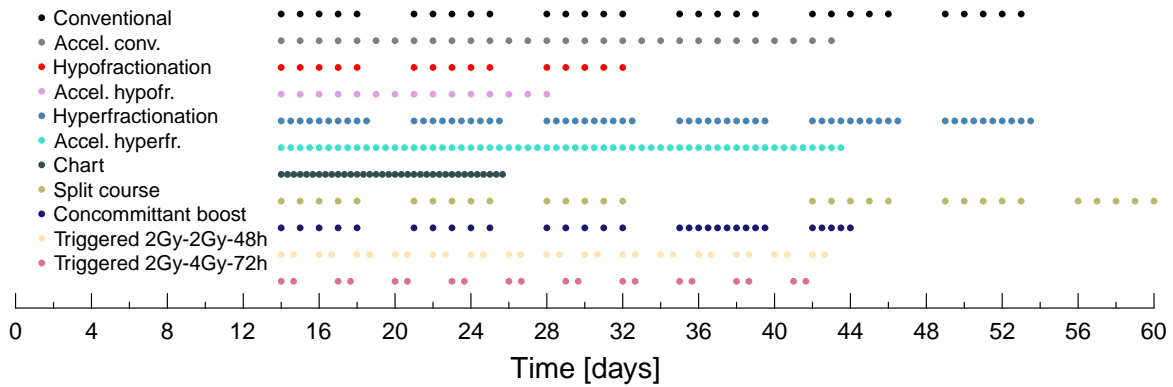


Figure 3.52: A visualisation of the radiation timing in different typical schedules which were used within this investigation.

the conventional schedule, doses of 2 Gy per fraction will be applied, while for hypo- or hyperfractionation, doses of 4 Gy and 1 Gy respectively will be used.

Figure 3.54 provides an overview of the effects of the fractionation schemes from figure 3.52 when applied in the simulation. A high degree of regrowth in response to irradiation can be observed. Reactivated cells will repopulate the tumour and their unlimited replicative potential will lead to a quick reformation of the spheroid even when only a very small number of cells was left alive. This can be seen in the visualisation of the hypofractionated run in figure 3.53). About 3 days after the start of irradiation, the spheroidal histology has been destroyed. In response to the high amount of apoptotic cells which is associated with a fraction dose of 4 Gy, the tumour volume is largely fractured into small aggregates. *In vitro* even a partial dissolution of the spheroid would be possible, as single aggregates are ripped away by stirred culture medium. In an *in vivo* situation, a high external pressure on the boundary would keep the spheroid compact, however local dissolution of apoptotic cells could well lead to an increase in shedding of viable cells or even small aggregates. If in the vicinity of capillaries, this could induce a higher chance of metastasis.

As the hypofractionated schedule continues, the remaining aggregates further decrease in size until the tumour is reduced to a very low number of surviving cells. However, even a single surviving cell is sufficient to restart the formation of a tumour spheroid, so that, in this case, about 20 days after cessation of irradiation the spheroid will have reached its pre-treatment size again.

In an *in vivo* environment, the few remaining cells, as for example left at the end of the hypofractionated or CHART-treatment, would probably be eliminated by immune effects or bystander damage. Within the model, a typical integral dose of 60 Gy will thus not fully sterilize the tumour, even when applied in a short amount of time such as in a hypofractionated schedule.

In terms of a reduction in tumour burden, the high dose-per-time schedules all perform drastically better. They will allow less regrowth of the tumour due to the shortened treatment time and benefit from the quadratic term in the dose-survival relation of the LQ-model due to the high single-doses used. However, larger single doses are more likely to be accompanied by an increase in unwanted side effects, which cannot be assessed in the given model. Conversely, schedules which deliver a dose per fraction below the conventional 2Gy should lead to a slight

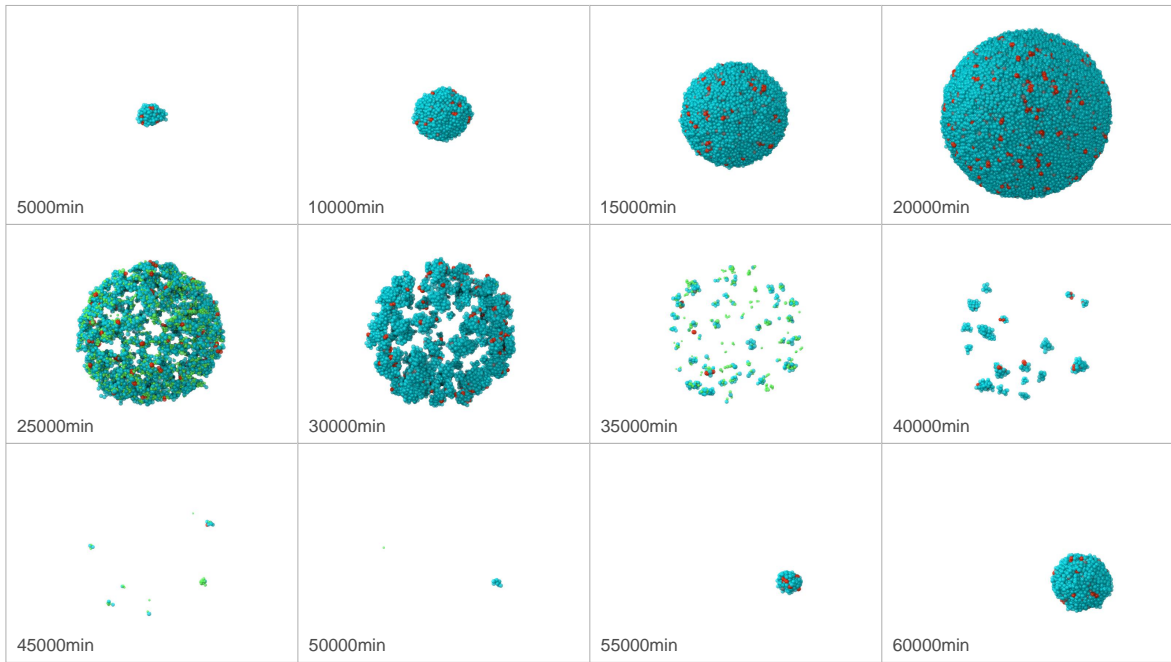


Figure 3.53: Visualisation of the tumour at different times during the hypofractionated irradiation schedule produced with POV-Ray. The high dose per fraction of 4 Gy will lead to the destruction of the tumour integrity and the formation of smaller aggregates.

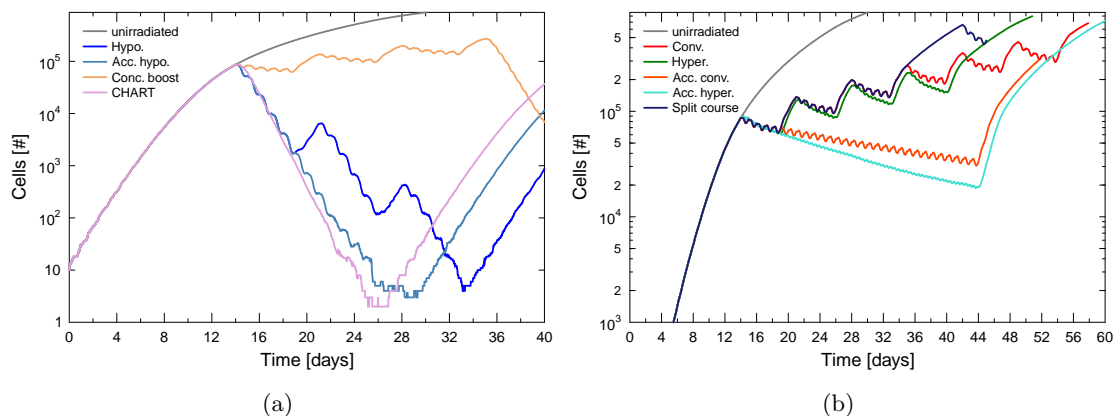


Figure 3.54: Comparison of total tumour size during high dose-per-time scheduling in (a) (runs which apply more than 2Gy/24h) or low dose-per-time scheduling in (b) ( $\leq 2\text{Gy}/24\text{h}$ ).

decrease in side effects and late effects as discussed in section 2.5.5.

Longer treatment pauses as in the conventional, “un-accelerated” schedules will have a drastic negative effect on tumour control in the model. Each pause will allow for an unchecked period of regrowth within the tumour, which will not be stopped if the following doses and the integral dose are not increased. As visible in figure 3.54(b), these pauses can make the difference between the achievement of an overall reduction in tumour load, or a failure to keep the tumour in check, as can be seen for the conventional schedule when compared to the accelerated schedule.

Even so, the CHART-schedule applies lower single doses and yet has a very high effect in

### 3 Results

terms of tumour control. Side effects associated with the low fraction size would be limited, but overall a high dose per time unit is applied with 4.5Gy/24h. Considering the fast repair of sublethal damage in cells, CHART would allow for the repair of most damage in surrounding tissue with a delivery interval of 8 hours. CHART is highly capable of reducing the tumour burden at an overall lower integral dose. The relatively small single doses of 1.5Gy achieve a surprisingly high effect.

Schedules which employ frequent irradiation with a lower dose per fraction, such as the hyperfractionated schedule, will perform better than schedules which deliver the same dose per time unit in medium-sized single fractions. This is not to be expected, as the quadratic survival term in the LQ-model will yield a lower survival for larger doses.

The reason for this effect is the timing of the radiation delivery in conjunction with the development of tumour radiosensitivity as shown in figure 3.55. While the conventional radiation schedule will deliver follow-up doses at a time of low tumour radiosensitivity, within the hyperfractionated schedule follow-up doses will be delivered at a time of high radiosensitivity. Even if the maxima in enhancement are smaller due to the lower doses in the hyperfractionated schedule, a relative decrease in tumour burden will still result.

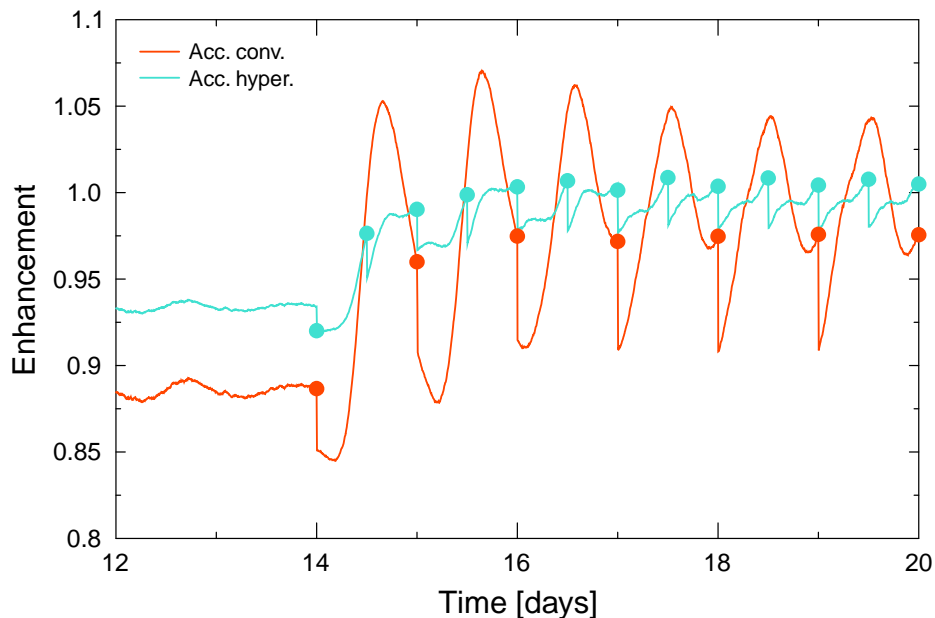


Figure 3.55: Detail of radiosensitivity enhancement during the accelerated conventional schedule and the hyperfractionated schedule in comparison. A delivery interval of 24h (marked by the red dots) will coincide with a region of rather low tumour sensitivity, while an interval of 12h (blue dots) will deliver the follow-up fraction always at a point of high sensitivity.

Dose delivery within the conventional, accelerated conventional or split course treatment occurs in intervals which fail to induce a constant high enhancement within the tumour. In contrast, hyperfractionated schedules succeed at keeping the enhancement in the tumour at a steady high level, which is especially true for the accelerated hyperfractionation schedule. Effectively, the hyperfractionated schedule will drastically suppress the reformation of a resistant quiescent subpopulation. While it therefore allows the tumour to grow exponentially at all times, the frequent delivery of doses will keep the growth in check.

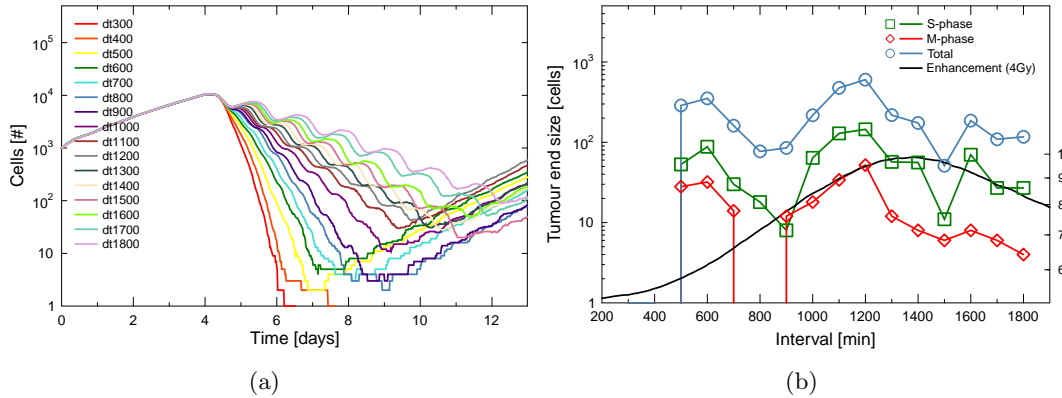


Figure 3.56: **(a)** Effect of repeated irradiation with 4Gy per fraction (using a varying time interval from 300 to 1800 minutes) on the total number of viable cells in the tumour. Integral dose is 21Gy for all runs. **(b)** Final size of tumour after 13 days of growth and irradiation plotted versus the treatment interval (plus 5 days of pre-growth from 10 seed cells to 1000).

### 3.3.4 Optimal radiation delivery interval

In order to systematically study the effects of scheduling on the tumour burden, spheroids were subjected to a fractionated schedule with 4 Gy per dose which uses different time intervals for delivery of an integral dose of 21 Gy. Inter-fractionation times from 300 to 1800 minutes were tested and results of the investigations are shown in figure 3.56(a). Figure 3.56(b) shows the final size of the tumour after 13 days of growth and treatment for different radiation delivery intervals.

A problem for comparison of treatment efficiency arises as a consequence of incomplete sterilisation of the tumour within the time of treatment. Not only regrowth during the actual treatment time is present, but for intermediate radiation delivery intervals, the tumour can re-proliferate as the treatment has ended before the efficiency of the run is assessed. The observation moment of 13 days is accordingly chosen arbitrarily. This can be fixed by irradiation of the tumour with varying inter-fraction times until full sterilisation is reached in all cases, as shown in section 3.3.5.

If only the delivered dose per time unit is important for the control of the tumour, we can expect the degree of tumour control to be higher (and the end-size of the tumour to be lower), when the same integral dose is given in a shorter time. Therefore the end-size in figure 3.56(b) should increase linearly with the treatment interval. However, the interval-endsize relationship is not simply linear. While very short treatment intervals of up to 500 minutes are highly effective and even succeed at a full sterilisation of the tumour, intermediate intervals fail to be effective (especially at around 1200 minutes). The effectivity increases again and shows another maximum at an interval of 1500 minutes.

A very short delivery interval will effectively sterilize the tumour (remaining cells are all dead) but could not be used clinically due to severe side effects. If the treatment interval is made longer, the tumour will no longer be fully sterilized (increase in tumour end size between 500 and 800 minutes). Note the drastic increase in treatment efficiency for an interval of 900 minutes and later on for 1600 minutes. These intervals correspond to the transient periods

### 3 Results

of increased radiosensitivity and should be used for irradiation.

Very short intervals of up to 8 hours, which are efficient in eradicating the tumour burden in the model, are, in reality, prohibitive due to the very severe side effects that will arise as a consequence of the high dose delivered in such a short timespan (more than 8 Gy per 24 hours). For an interval of 10 hours, the effect of enhanced resistance which is introduced by the cell cycle redistribution becomes visible. As, at the same time, the dose rate is not high enough to fully sterilize the tumour, a treatment schedule with this interval will be highly inefficient.

Accordingly, the intermediate region of high efficiency at a treatment interval of 900 minutes corresponds to the transient phase of increased sensitivity that was identified in figure 3.25. This timing is quite interesting as it might offer a trade-off between performance increase and tolerability of side effects while exploiting the increased sensitivity of the tumour.

#### 3.3.5 Sterilisation dose as a function of fraction timing

Comparison of the success of a treatment regimen at an arbitrary endpoint, as was done in section 3.3.4, is problematic, as the choice of the observation time can seemingly alter the outcome. In order to obtain an independent observable for the success of a treatment schedule, the total dose which is needed for complete sterilisation of the tumour can be measured as a function of the time interval in which the dose is applied. Results of an according series, in which a tumour was irradiated with fixed doses of 3 Gy, which were applied with a varying inter-fraction time of 100 minutes to 1800 minutes, are shown in figure 3.57. The according number of fractions which needed to be applied for sterilisation as a function of the fractionation interval is shown in figure 3.58.

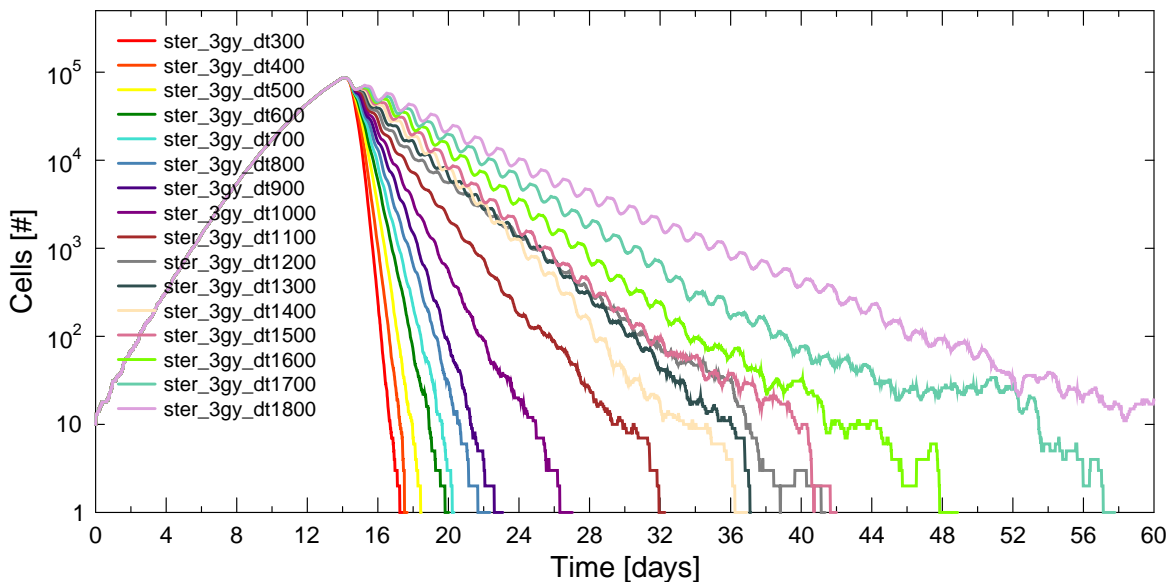


Figure 3.57: Sterilisation trial, in which 3 Gy per dose are applied with a varied inter-fraction time until the tumour has been completely sterilised. The number of fractions needed for sterilisation for different fractionation intervals is shown in figure 3.58.

We can see that the necessary number of fractions does not increase linearly with inter-fractionation time as would be expected if regrowth of the tumour were the only influence on

treatment success that varies with the time-interval of fractionation. Clearly, the development of sensitivity determines the number of fraction which are necessary to sterilize the tumour. For a very fast follow-up fraction interval time of 100-300 minutes, the tumour will require an even higher number of fractions (larger integral dose) to be sterilized when compared with longer fractionation times of 500-700 minutes. The enhancement development in response to a single dose of 3 Gy, which is shown in figure 3.58, can hint at the effect of enhancement. However, the actual development of enhancement within each run will be more involved than for the test. Furthermore, the enhancement development after each fraction will change over the course of the treatment in response to changes in tumour composition as indicated in figure 3.59.

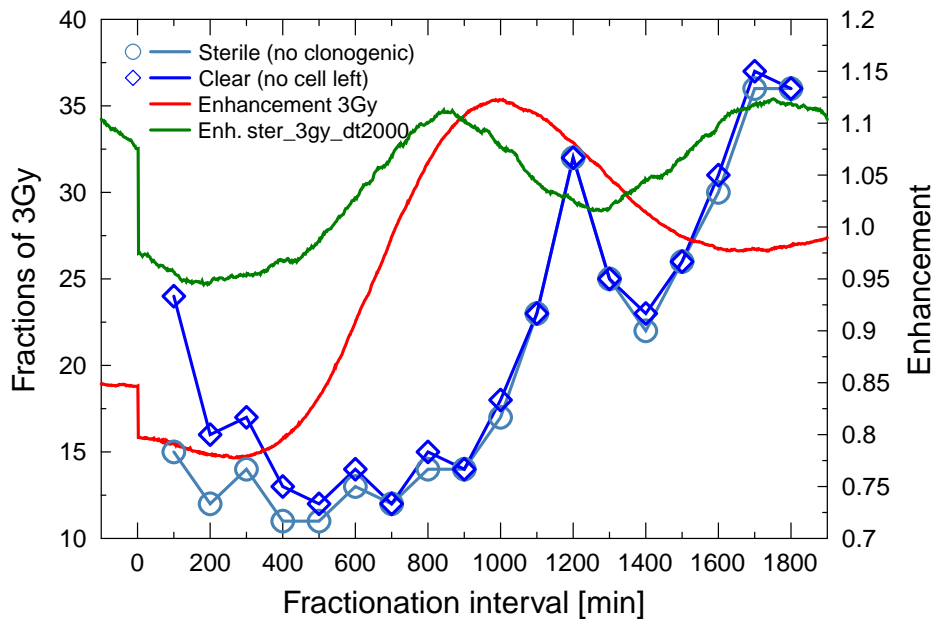


Figure 3.58: Number of fractions of 3 Gy needed to fully sterilize the tumour in the run shown in figure 3.57. Tumour was either sterile when no more clonogenic cells were present or completely cleared, when no more cells were present, that is, apoptotic and necrotic cells had dissolved. The enhancement curve for a single irradiation with 3 Gy is shown for comparison as the enhancement development for continued radiation schedules, as in this case, is more complex than suggested by a single radiation response.

If we analyse the development of enhancement during the continued radiation delivery, we see that the nature of the fractionation curve found in figure 3.58 can be explained by the interval of radiation delivery in relation to the enhancement development in figure 3.59.

A very low fractionation interval time of 100 minutes will be relatively inefficient, requiring 15 fractions of 3 Gy before a sterilisation of the tumour is achieved. This is because a delivery of the follow-up fraction within only 100 minutes will hit the tumour in a region of low enhancement, which was triggered by the cell cycle redistribution of the previous dose. Only as the tumour comes close to sterilisation can an apparent increase in enhancement be observed for this extremely short fraction time. The apparent high number of fractions which are needed to completely clear the tumour is misleading in the cases of extremely short delivery intervals, as the time associated with apoptosis dissolution will be the limiting timescale for clearing.

### 3 Results

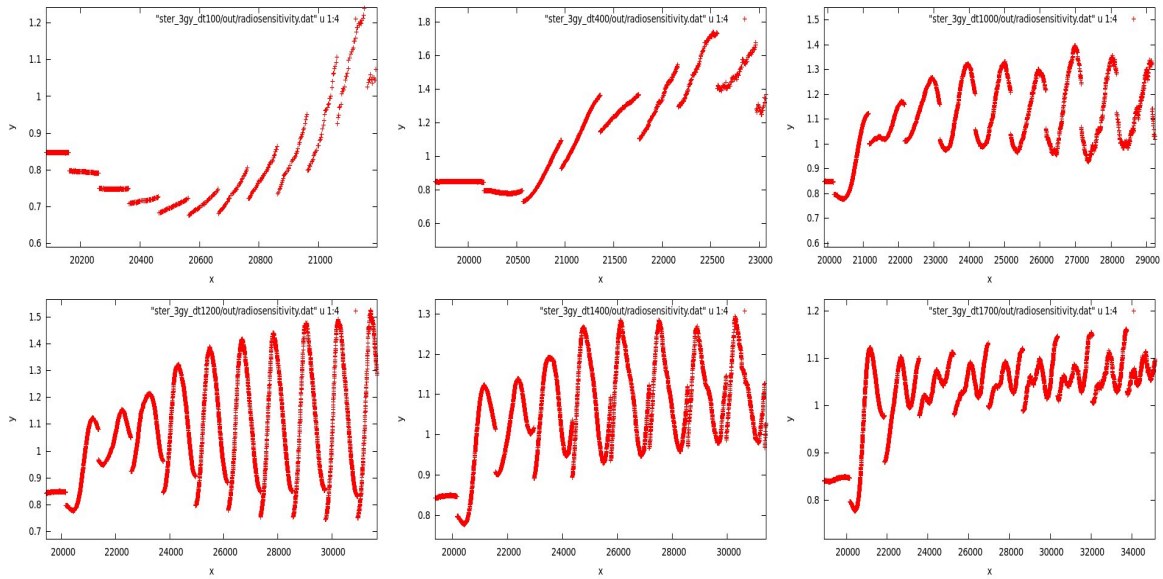


Figure 3.59: A detailed analysis of the sensitivity development during the fractionated irradiation in figure 3.57 reveals the reason for the shape of the fractionation curve. Time on the x-axis in minutes, enhancement on the y-axis.

If the interval is increased to 400 minutes, a small, increasing gain in enhancement can already be achieved with each dose, before its follow-up dose is applied. The gain in enhancement with each fraction increases with inter-fraction time. At an interval of 1000 minutes, each follow-up dose will be repeatedly applied close to the possible maximum in enhancement. If the interval is further increased, a drastic decrease in the triggered enhancement for each follow-up dose will result. This effect is most pronounced for an inter-fraction time of 1200 minutes. This is visible as the peak of fractions required to sterilise the tumour in figure 3.57. A further increase of the fraction time will lead to another window of increased triggered sensitivity, albeit at a lower total enhancement.

The results of the sterilisation trial demonstrate that increased cell killing, which is associated with the higher enhancement of follow-up doses in the case of optimal inter-fraction time, will counterbalance the effect of tumour regrowth, which is also associated with an increase in inter-fraction time.

This means that the tumour can be sterilised with the same number of fractions and thus the same integral dose, even with a drastically increased treatment interval. This can allow repair in surrounding healthy tissue.

#### 3.3.6 Varying interval and dose rate

In order to systematically investigate the reasons for the significantly different performance of some clinical schedules in section 3.3.3, an investigation has been performed in which the same integral dose is applied over the same total time, but with a systematically varied dose rate. The overall dose rate was set to the typical clinical level of 2 Gy per 24 h.

6 h was chosen as the lowest time-interval for fractionation. This should guarantee that sub-lethal damage repair will not play a role. The maximum fractionation interval was set at 48 h. The variation of the dose-rate is accordingly performed around the extremes of a

hyperfractionated schedule with 1 Gy/12 h and a hypofractionated schedule with 4 Gy/48 h.

Figure 3.60 shows the effect of different fractionations for the typical constant dose per time unit of 2 Gy per day.

Larger single fractions will, as usual, have the advantage of inducing a higher amount of cell death compared to the combination of multiple smaller doses, due to the quadratic term in the linear-quadratic model. Still, some runs with smaller doses per fraction are especially effective in reducing the tumour size.

While it is thus not surprising that a run with the largest single doses of 4Gy/48h shows a good performance, it is remarkable that this performance is closely matched by a run with single doses of only 2.5Gy/30h. This fractionation is just above the typical dose of 2Gy/24h which corresponds to the classical accelerated conventional schedule. While single doses of 4Gy may be problematic because of high side-effects, a slightly altered conventional fractionation scheme with a dose per fraction of 2.5Gy will most likely not show this disadvantage. It is clear that the dose-effect does not determine the success of the treatment, as runs with larger single doses of 3 and especially 3.5Gy perform significantly worse.

Even though all runs deliver the same integral dose with the same overall dose-rate, the tumour burden is significantly different for the runs as shown in figure 3.61(a). Despite long inter-fraction pauses and the associated regrowth of the tumour, the lowest tumour burden is achieved by the varied fractionation with 4Gy/48h.

Runs with a positive integral enhancement as depicted in figure 3.61(b) show an overall increased sensitivity in comparison to the ideal exponentially-growing tumour. Negative integral enhancement should be avoided, as the tumour stays in a state where a resistant sub-population or an unsuitable cell cycle distribution result in a decreased radiation sensitivity for most of the time. Overall, the results of integral enhancement and overall tumour burden show a good correlation, where high enhancement will lead to a better treatment outcome and a lower tumour burden.

The drastically altered performance of schedules can be explained by the relationship between their fractionation timing and their development of radiosensitivity enhancement.

The runs with fractionations of 2Gy/24h and 2.5Gy/30h provide an interesting example. Even though their fractionation timings are quite similar, they will lead to a drastically different reduction in tumour burden as shown in figure 3.60(a) or 3.61(a). Their enhancement development is compared in detail in figure 3.60(b) and reveals the reason for their different performance. While the 30h-schedule will induce an increase in enhancement and subsequently delivers each fraction at points of high enhancement, the 24h-schedule will not raise the enhancement above a sub-optimal level of  $E < 1$ . Thus it continuously delivers radiation at points in time at which the tumour will show low radiosensitivity.

This effect is also evident from the integral enhancement values of the runs as shown in figure 3.61(b). While an interval of 24h will yield a negative integral enhancement, 30h will result in a positive integral enhancement, indicating that the tumour was in a sensitive state most of the time.

Thus, while high-dose fractions will have an advantage as a result of the quadratic term in the LQ radiation response, they can be outperformed by some lower-dose schemes due to a better timing of the treatment to the tumour radiosensitivity development (compare also 2.5Gy/30h and 4Gy/48h in figure 3.60(d)).

Also, at comparably high dose-levels, minor variations of the fractionation interval can yield

### 3 Results

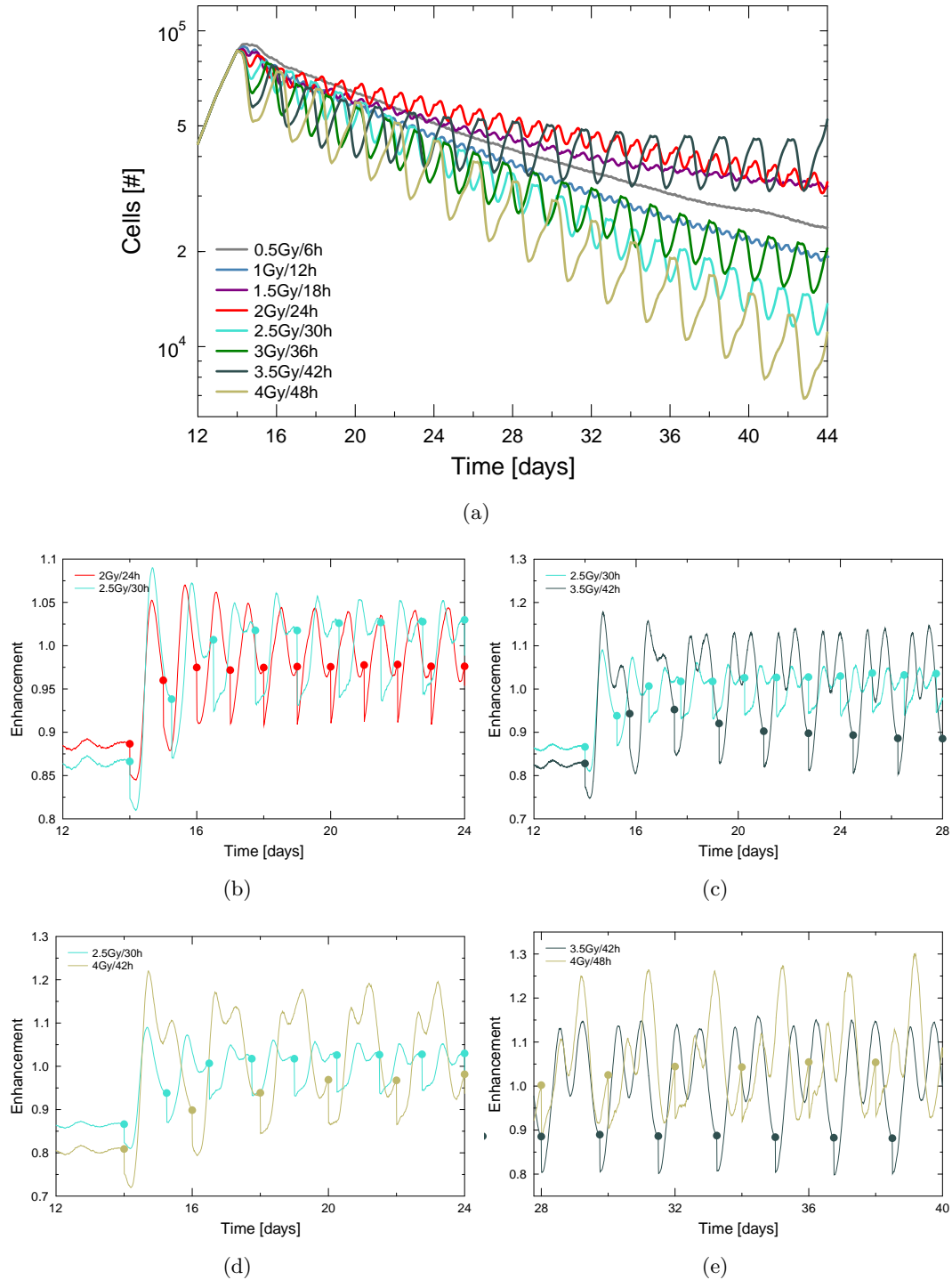


Figure 3.60: (a) Comparison of total tumour size in response to different scheduling of the standard dose of 2Gy/d. Notice that fractionation of the dose will drastically alter the outcome of the regimen. Figures (b-e) shows details of the enhancement development during selected runs with the according radiation delivery times indicated as dots. Full enhancement curves of all runs are provided in figures 3.62 and 3.63.

completely different outcomes in terms of tumour burden. This is evident when the performance of the variable runs with 3.5Gy/42h and 4Gy/48h are compared as in figure 3.60(e).

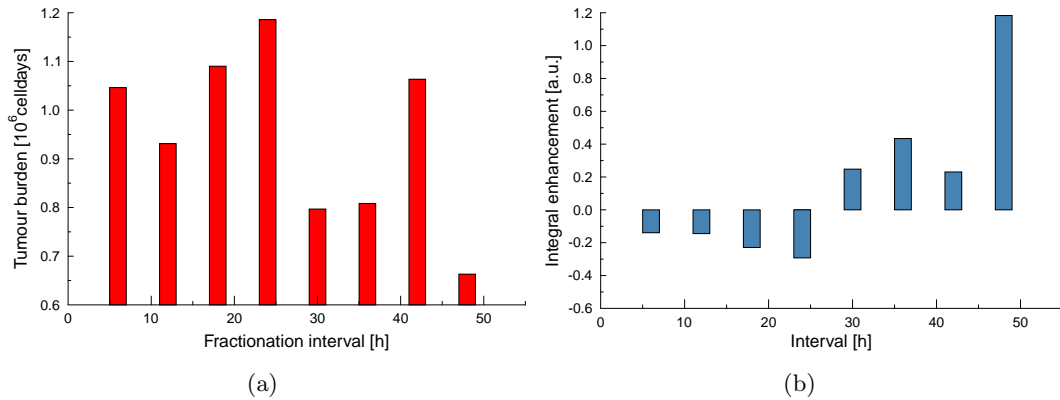


Figure 3.61: The area under the curve of the tumour burden AUC and the sensitivity minus ideal sensitivity of the runs depicted in figure 3.60.

While the fractionation schedule of 4Gy performs reasonably well in terms of enhancement (while not administering follow-ups during the peak in enhancement!), the schedule with 3.5 Gy will deliver radiation continuously at the point of maximum resistance.

Figure 3.63 shows a histogram of the relative frequency of the enhancement during the variable fractionation as depicted in figure 3.62.

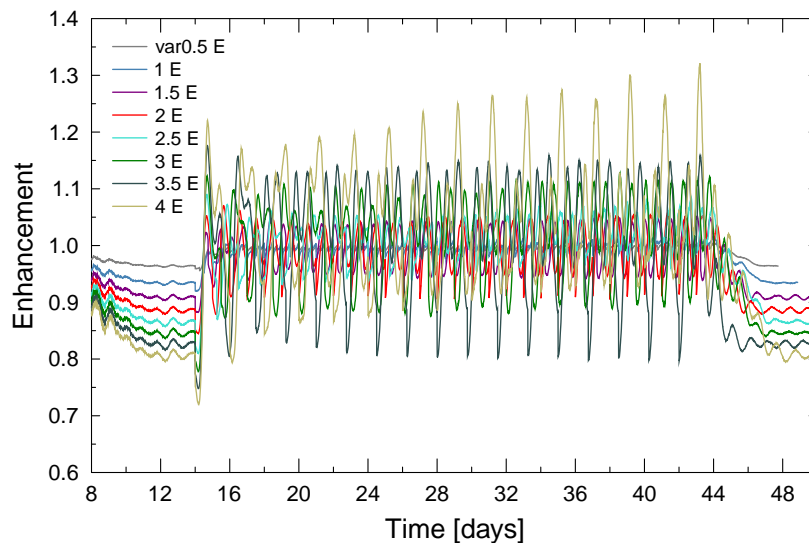


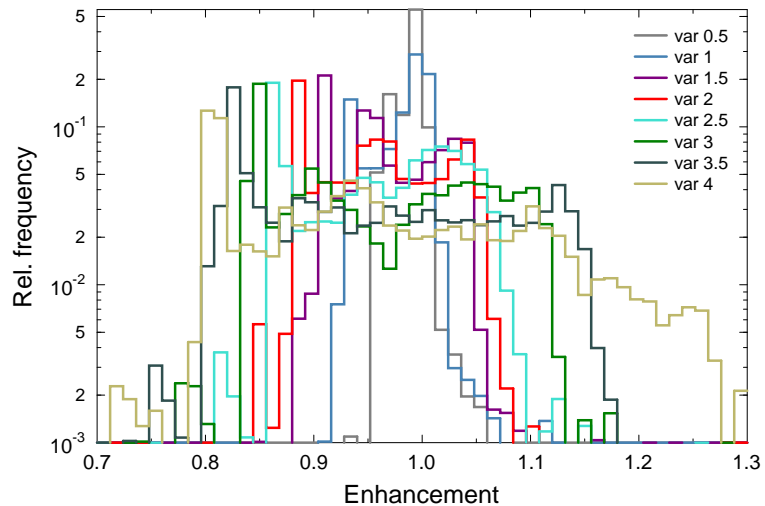
Figure 3.62: Development of enhancement during runs with variable fractionation in figure 3.60. The enhancement can be visualised as histogram to aid interpretation as shown in figure 3.63.

If the according histogram peaks in high-enhancement regions, the run will most likely be very successful.

The maximum possible enhancement will increase with the size of a single dose, but also the minimum possible enhancement. As discussed previously, for larger doses the variance of enhancement is increased (see also figure 3.25).

A peak at lower regions of each histogram indicates the typical enhancement directly after a dose has been applied, that is, when a large number of sensitive cells has been killed. Suc-

Figure 3.63: A histogram of the relative frequency of enhancement which is present in the runs in figure 3.60.



successful schedules will show more weight within the region of the histogram that is associated with enhancements larger than 1.

Note that the 0.5Gy/6h-run has a strong peak at the enhancement of 1, which shows that a continuous irradiation will very effectively control the size of the quiescent subpopulation within the tumour. As small doses of 0.5 Gy will not induce a strong cell cycle redistribution or enhancement reaction, the tumour is thus kept at the expected enhancement which would be typical for an exponentially growing tumour.

### 3.3.7 Triggered optimal delivery

As a dose of radiation will induce dynamic changes in the radiosensitivity enhancement of a tumour, it can be used as a trigger to prepare the tumour into a sensitive state before a follow-up dose is applied. Careful timing of a trigger and follow-up dose can thus be used to achieve an optimal delivery of dose to the tumour.

Figure 3.64 shows the result of tailored radiation protocols which are designed to exploit the induced dynamic changes of radiosensitivity in the tumour. Some of the applied triggered radiation schedules have been visualised for convenience in figure 3.52.

In general, a trigger dose is combined with an effector dose. While the trigger dose will induce a peak in enhancement, the effector dose will be timed to be delivered exactly as the maximum enhancement is reached. After the effector dose, a pause is used to allow the tumour system to settle in order to allow a similar dynamic response to be triggered by the next fraction. An example of a triggered schedule is the application of a 2 Gy trigger dose, followed by a 2 Gy effector dose after an interval of 940 min. This corresponds to the position in time of the first peak in enhancement that is triggered by 2 Gy of radiation (see figure 3.25). After the effector dose is applied, a pause of  $2880 - 940 = 1940$  minutes is observed in order to achieve an overall dose rate of 2 Gy per 24h. In a similar manner, a range of trigger protocols was designed which employ a different weighting of trigger and effector dose and a different fractionation of the overall dose rate.

Protocols which used a smaller triggering dose in combination with a larger follow-up dose are highly successful. The initial dose can induce a synchronisation in the tumour and increase the enhancement which will be most efficiently exploited by a large follow-up dose that is delivered to the tumour while it is in an especially sensitive state.

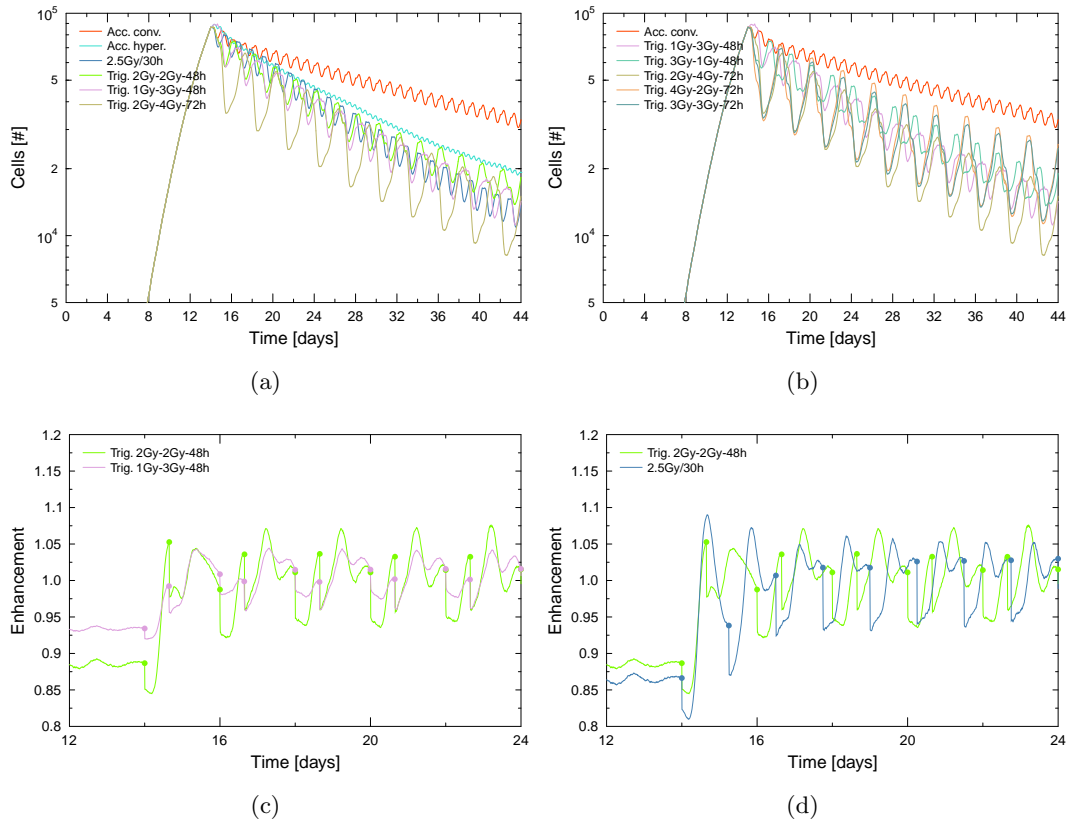


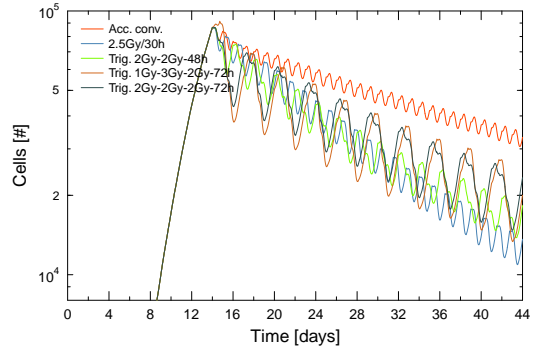
Figure 3.64: Triggered irradiation protocols which were designed to induce a cell cycle response in the tumour which can be exploited in follow-up irradiations. (a) and (b) show a comparison of the overall reduction in tumour size achieved by different conventional and triggered schedules. (c-d): Details of radiosensitivity enhancement development associated with the triggered schedules.

All tailored treatment protocols result in an increase in tumour reduction when compared to the standard accelerated conventional or accelerated hyperfractionated schedule as can be seen in figure 3.64.

A third follow-up sensitivity peak can be found at around 800 min after the second dose has been applied. This allows the design of dose delivery protocols which employ 3 consecutive doses in blocks as shown in figure 3.65. In order to preserve the constant dose rate of 2 Gy per day, a long inter-treatment pause is required when three consecutive doses are coordinated. As the first enhancement peak in the 2Gy-2Gy-2Gy-72h schedule is reached after about 940 minutes and the second triggered peak after another 800 minutes, a pause of almost 2500 minutes is required to fill the 72h until the next fractionation block starts. This long pause is associated with a very high degree of regrowth as can be seen in figure 3.65, so that the performance of the according schedules is weak when compared with alternatives.

In principle, a continuous triggering of enhancement would be possible for dose delivery. However, the peak timing slightly changes during the course of a prolonged treatment regimen, so that targeting of the optimal enhancement point is only possible for permanent recalculation and not in advance. One of the reasons for this alteration is the activation of the tumour out of the steady state. An inter-fraction pause of 48 hours is not sufficient for

Figure 3.65: Triggered irradiation protocols which employ a repeated irradiation block of three consecutive doses.



the tumour to reach a steady state again, so that the response will be altered over time.

The dynamic shift of the optimal treatment time with tumour state and size can be observed when comparing the varied fractionation schedule with 2.5Gy and the triggered 1Gy-3Gy-48h schedule in figure 3.64(a). While initially the triggered schedule will perform better than the varied schedule (which uses one constant inter-fraction time of 30h), this will change after about 24 days of growth. As the tumour decreases in size and changes to its cell cycle distribution are significant, the enhancement peak timing shifts to slightly lower values. Thus the effector dose no longer targets a period of maximum enhancement.

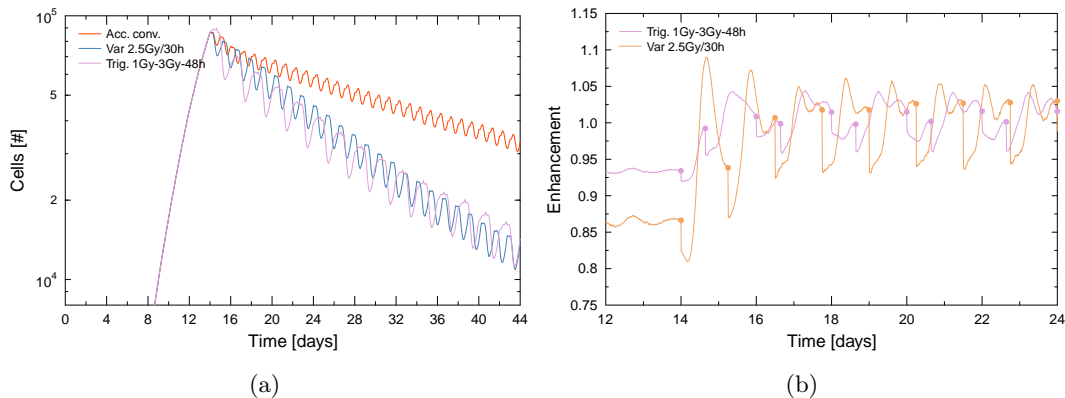


Figure 3.66: (a) Investigation of the triggered schedule 1Gy-3Gy-48h and the variable fractionation schedule 2.5Gy/30h. (b) After an initially successful coordination of trigger and effector dose in the 1Gy-3Gy-48h schedule, instability of the schedule will lead to later effector doses being applied during times of lower enhancement.

Surprisingly, the protocol 2Gy-4Gy-72h, which delivers a trigger dose of 2Gy followed by an effect dose of 4Gy, is able to cancel out the high regrowth which is allowed by the following pause to a treatment interval of 72h. The protocol employs a rather large single dose of 4Gy which could be associated with a slight increase in side-effects and late-effects. Still it is an interesting result, as any measure that could reduce the amount of regrowth (e.g. an adjuvant chemotherapy with proliferation inhibitors) would further improve the performance of the schedule substantially.

However, as can be seen in figure 3.64(a), a simple fractionation protocol of constant 2.5Gy/30h is still the most successful protocol in terms of overall tumour burden. In the case of the 2.5Gy/30h protocol, the timing of the follow-up dose by chance persistently matches the peak in triggered sensitivity over the whole treatment time as can be seen in figure 3.60(b).

Thus an high degree of overall enhancement can be achieved and used.

Figure 3.67 shows the area under the curve of the integral tumour burden and the enhancement (minus the unity-enhancement). In runs with mixed doses such as 3Gy-1Gy-48h, the interpretation of the enhancement is not trivial anymore, since the enhancement is always calculated relative to the first applied dose of the run in order to avoid unsteady changes.

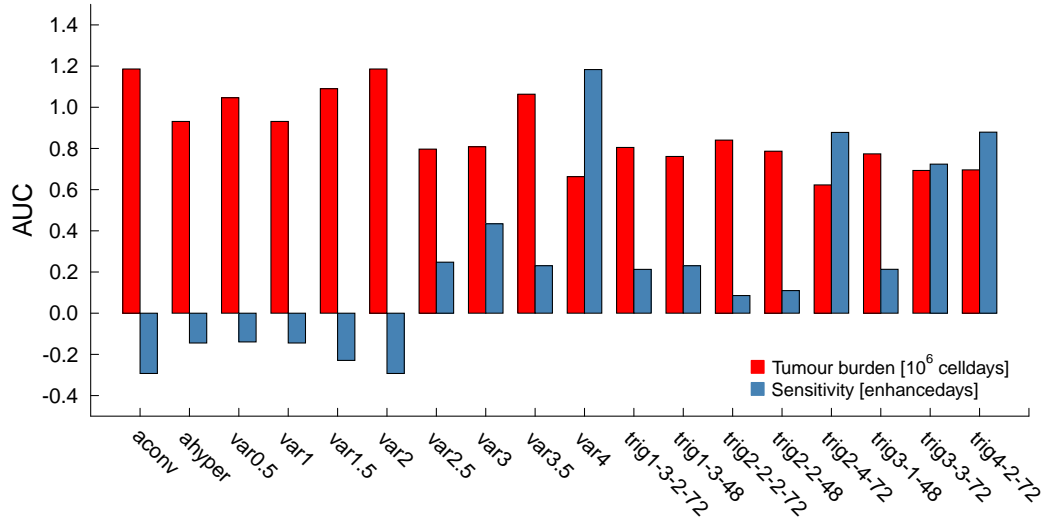


Figure 3.67: Comparison of the tumour burden during different schedules which all deliver an integral dose of 60Gy as 2Gy/24h.

### 3.3.8 Manual optimal scheduling

In order to cope with the typical shifts in sensitivity and enhancement over the course of a treatment regimen, manual radiation triggering at optimal points of enhancement can be used to build an optimal schedule. This requires multiple simulations to be used, where the radiation regimen is stopped after an each increasing number of fractions. The resulting undisturbed development of radiosensitivity can be used to identify the next maximum in radiosensitivity enhancement and trigger radiation accordingly.

Figure 3.69 shows the time to the next peak in enhancement after a dose of 2 Gy has been applied at each previous enhancement points.

Initially, the optimal inter-fraction time will greatly vary in response to optimum-enhancement based triggering (red region in figure 3.69). This variation corresponds to massive changes

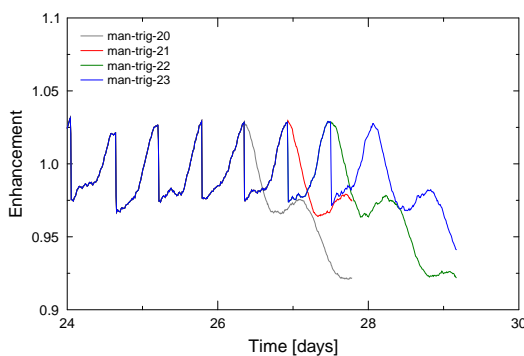


Figure 3.68: Example of manual triggering. Each run adds one more targeted enhancement peak from the previous run to the schedule.

### 3 Results

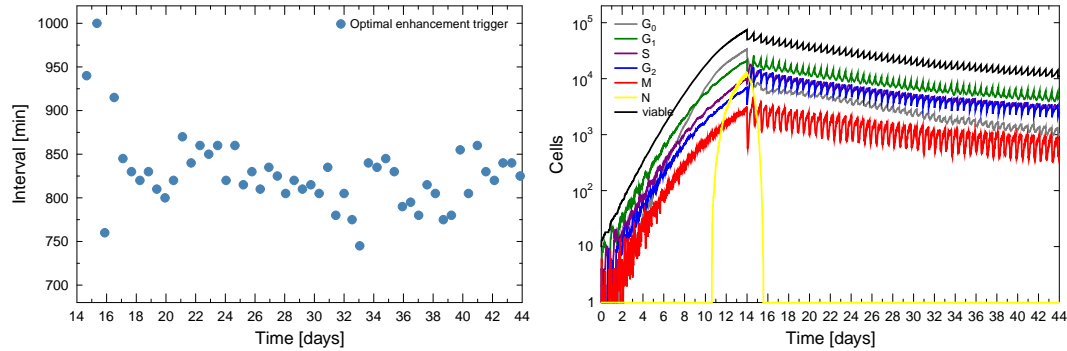


Figure 3.69: Trigger times and cell cycle distribution during an irradiation schedule with optimal manual triggering of irradiation, based on maximum enhancement (apoptotic cells not shown in distribution for reasons of clarity).

in the initially irradiated tumour, such as the release of quiescent cells into the cycle. The optimal fractionation intervals stabilise at about 830 minutes around 3 days after the start of fractionation (green region). While there is still a high degree of variability within this region, the tumour reaction can become stable in this time-frame.

About 17 days after the start of irradiation, a destabilisation of the optimal trigger time is observed in response to small changes in tumour composition or even stochastic effects. A tendency to drastically lowered intervals for optimal delivery of about 770 minutes can be observed, before the optimal trigger time becomes chaotic.

As a constant dose rate of 2 Gy/24h is kept in effect, this means that any change of the inter-fraction time will most likely trigger a self-enhancing destabilising effect: The next dose to be applied will have a different magnitude and thus will trigger a slightly altered effect itself, and so forth.

However, while a schedule developed in this fashion will be able to always trigger at optimal enhancement points, it is not necessarily the most successful global schedule overall, as its optimisation is only local. This is emphasised by the sub-optimal performance of the fully manual schedule as shown in figure 3.70. While the optimal triggered run will initially outperform the best alternative scheduling of 2.5 Gy/30h, it will drop in efficiency at day 32. This corresponds to the point when fluctuations destroy the repeated optimal delivery with an approximately constant time-interval as shown in figure 3.69.

Furthermore, if a constant dose rate of 2 Gy/24h should be used within manual scheduling, there is a degree of freedom to either irradiate always at the first enhancement peak (and consequently use lower single-doses) or to target following peaks in enhancement. Another possibility would be to allow pauses in treatment in order to use larger single dose after the pause. Manual optimisation across all weighting of doses is thus impossible, even if sensible guesses towards the best weighting are possible.

#### 3.3.9 Automatic optimal enhancement-based scheduling

Optimisation using manual triggering at a time of optimal enhancement is partially possible, but the triggering must be dynamically adapted to the tumour changes. A possible solution is an automatic triggering of an adapted dose, which relies on a simple algorithm to identify

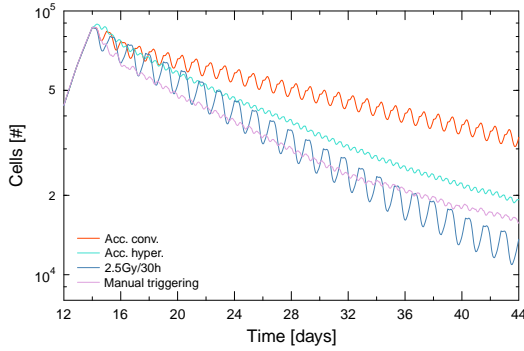


Figure 3.70: Results of fully manual optimisation of the treatment schedule. Dose adapted to 2Gy/24h will be applied at each triggered timepoint of optimal enhancement as shown in figure 3.69.

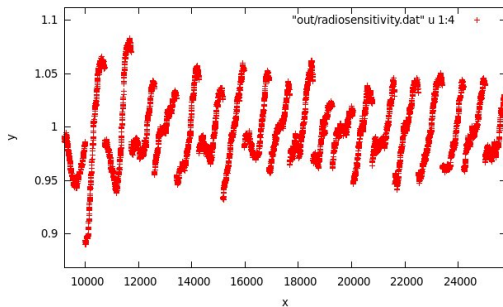


Figure 3.71: An example of maximum-based automatic triggering of irradiation: a dose of radiation is applied whenever no increase in maximum value was found in a moving time window of  $t_m = 50$  minutes and when the triggered dose was at least  $D_m = 1$  Gy (corresponding to an minimum time interval of 720 minutes at a dose rate of 2Gy/24h). X-axis shows time in minutes, y-axis enhancement.

the optimal enhancement point within given constraints (e.g. minimum or maximum delivery intervals).

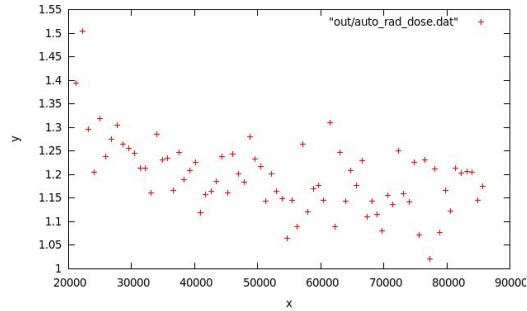
Obviously, the task of finding a maximum within a stochastically fluctuating discrete signal in real time, is non-trivial. Without any further information on the type and typical properties of the signal, a real-time identification of maxima is hard to implement. As a generally valid algorithmic solution to problems of this type is not needed (as this would be beyond the scope of this thesis), but the algorithm will only need to identify enhancement maxima within the provided context, a specialised solution can be developed which is adapted to the specific problem. Thus it is possible to use information on the typical form of the enhancement signal to simplify the triggering.

Multiple approaches for the solution of the automated triggering problem are thus possible: A simple, straightforward approach is to check the enhancement signal for an increase within a given time period. If no new maximum value in enhancement can be found within a predefined time period  $t_m$ , this marks a maximum in enhancement (even though this maximum can naturally only be a local maximum). In combination with a minimum required inter-fraction time (or equivalently a minimum dose  $D_m$ ) this will lead to the only slightly delayed automatic triggering at enhancement peaks as indicated in figure 3.71.

The integration of time-periods where sensitivity has a positive or negative slope and subsequent triggering based on their total value or fraction is another possible method. Valuable information about the development of the enhancement can also be drawn from the slope of a regression, which can be used to define a third targeting method. The according different mechanisms for maximum-based or regression-based triggering have been included in the standard simulation code. By default the maximum-based triggering method is used.

Automatic targeting will frequently irradiate with small doses, slightly above a common

Figure 3.72: Development of the automatic dose during automatic radiation schedule. The tendency to lower doses over time reflects the decreasing time between enhancement maxima. X-axis shows time in minutes, y-axis dose in Gray.



hyperfractionated schedule (see figure 3.72). If the magnitude of automatic doses over the course of a full treatment regime is monitored, a slight tendency for decreasing doses with treatment time is visible, which again confirms the previously discussed shift of enhancement peaks to shorter time intervals.

The delivered dose  $D$  can be automatically adapted in such a way that a fixed dose per time unit  $D_t$  (e.g. 2Gy/24h) will not be exceeded. This is simply achieved by applying a dose equal to  $D = dt \cdot D_t$ , where  $dt$  is the time since the last radiation dose was applied. If a minimum dose is required, this corresponds to a minimum irradiation interval at a fixed dose-rate.

All automatic triggering runs will include a fall-back mechanism, which will trigger irradiation irrespectively of the current enhancement, if no dose has been applied for a critical time (e.g. 2880 minutes). This will ensure that automatic triggering can still continue after an interval in which all maxima were undetected by the triggering mechanisms. Furthermore, it ensures that no dose above a certain size will ever be triggered (e.g. 4Gy at a dose rate of 2Gy/24h and a maximum inter-fraction time of 2880 minutes). Whether or not the fall-back mechanism was used can be considered a good test of the triggering mechanism's suitability to identify present maxima. The accuracy of the targeting has to be evaluated separately.

As shown in figure 3.76, the simple maximum-based automatic triggering mechanism is able to achieve good performance in targeting the periods of maximum enhancement. It significantly outperforms the conventional irradiation schedule and is initially very close to the optimal manually triggered schedule (see chapter on manual triggering).

The fall-back mechanism for dose-delivery is not used, indicating that all according maxima were identified.

Due to the relatively low dose per fraction, the performance of the automatic schedule decreases over time. The variable run with 2.5Gy/30h is able to induce a slightly stronger reduction in quiescent cells and block a higher number of cells in the sensitive G<sub>2</sub>-phase, as shown in figure 3.73 (compare also the amount of G<sub>0</sub> and G<sub>2</sub>-cells in figure 3.31(a)).

### Least squares based triggering

Another approach for optimal triggering employs linear regression of enhancement within a moving time window of interest. A large back-region and a small forward-region within the time window can be defined. If the regression of enhancement in the back-region is positive (or positive above a critical threshold value) and negative in the forward-region, a dose of irradiation can be triggered, as a local maximum was identified.

However, the front region has to be chosen large enough in order not to trigger on small local maxima. As with the other approaches, this will limit the precision of targeting as a

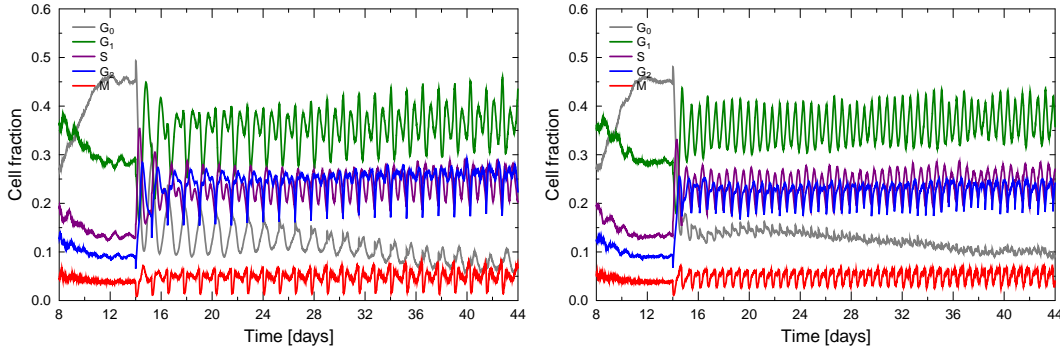


Figure 3.73: Comparison of the relative cell cycle distribution in the 2.5Gy/30h run and the auto-triggered run using maximum triggering and 1Gy minimum dose.

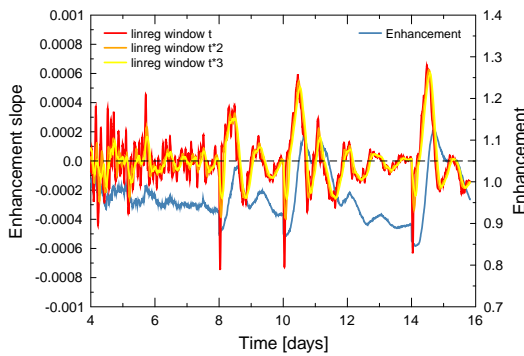


Figure 3.74: A least squares regression of the enhancement in a backward time window of  $t=150$  minutes (or multiples of it) will reveal the characteristic high slope that precedes each maximum in enhancement and can thus be used for triggering. Irradiation doses of 2Gy, 4Gy and 4Gy are applied at 8, 10 and 14 days.

maximum cannot be identified in real-time. An increase in reliability of maximum-finding will cause a decrease of the ability to deliver radiation at the maximum peak.

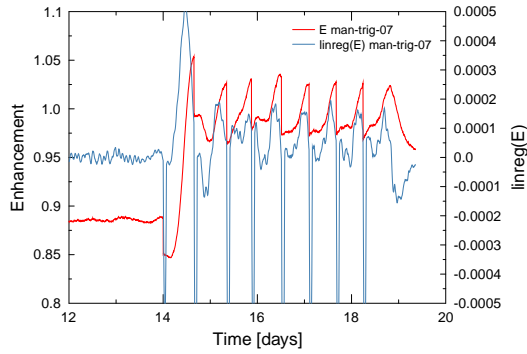
The high positive slope of enhancement which can be observed prior to a maximum is a characteristic feature of the signal and thus can be used to sharpen the response to a sign change in slope, depending on a critical slope threshold in the backward regression (see figure 3.74). The triggering mechanisms will be effectively released each time the system encounters a critically high slope. A subsequent change in the sign of the slope or absence of a new maximal value for enhancement will then trigger radiation.

The time window for the linear regression can be selected to be slightly smaller than the typical time interval that the enhancement will need to rise to a maximum (e.g. 400-500 minutes regression window for a typical 700-900 minutes timing from minimum to maximum sensitivity). Thus high-frequency fluctuations in enhancement which could yield a locally high slope will be filtered out and cannot trigger irradiation.

In all approaches the accuracy of the targeting will be limited by an increase in certainty of maximum-identification. While an increase of the critical time required to trigger will increase the certainty that a maximum was targeted, irradiation will only be triggered after the maximum, and thus with a delay of the critical time window. The same is true for approaches which employ a linear regression, as the size of the (forward) regression window will determine the accuracy of hitting the enhancement maximum.

A reasonably good targeting of maxima is possible with the straightforward approach of defining a critical time-window in which no new maximum enhancement value is found in combination with a minimum inter-fraction time. Least-squares regression-based triggering

Figure 3.75: Enhancement and according linear regression of enhancement (time window 200 min) during a run which uses manual triggering (man-trig-07).



leads to the same triggering. This demonstrates that the characteristics of the enhancement signal allow a simple identification of the maxima, albeit with a slight delay as discussed previously.

Information about the shape and typical timings within the enhancement signal also avoids the release of triggering in negative slope-regions. For more irregular signals, a more involved triggering algorithm would be required.

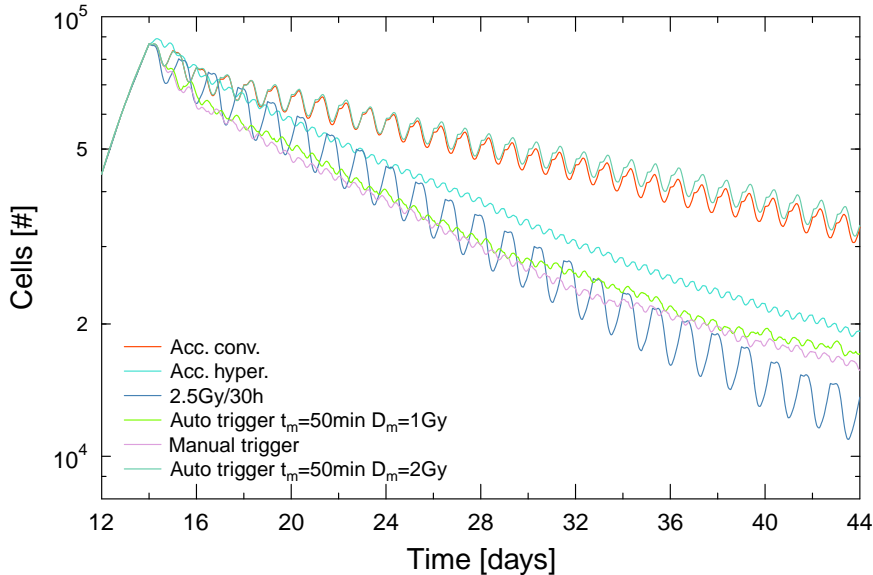


Figure 3.76: Results of simple automatic dose triggering and fully manual optimisation in comparison to typical conventional schedules.

As shown in figure 3.76 for a sample of auto-triggered schedules, automatic triggering will achieve a performance which is equal to manual optimal triggering. The slightly higher tumour burden associated with automatic triggering is a result of the delay in irradiation release relative to the maximum in enhancement, which is necessarily associated with the identification of a local maximum. However, similar to optimal manual triggering, automatic triggering cannot achieve a global optimisation of the treatment plan and thus will not yield optimal results. This is obvious in comparison to the overall most successful simple schedule of 2.5Gy/30h. While it can be temporarily outperformed by manual or automatic triggering, its steady performance will eventually yield a higher reduction in tumour burden.

## 3.4 Hypoxia

### 3.4.1 Formation of a hypoxic cell population

The development and dynamics of hypoxic cells can be studied within the simulation environment. In many tumours, a hypoxic subpopulation of cells is located between the well-oxygenated outer layer of the microtumour and the anoxic tumour core, depending on the actual nutrient consumption of cells. These hypoxic cells are of great interest because of their previously discussed properties which include a high resistance to most therapies and the possibility to target anoxic regions with separate therapeutic approaches (such as hypoxic cytotoxins [185]).

A common way to visualise the oxygen concentration within a tumour is via stained cut-sections. EF5-staining of hypoxic tumour cells is a classical methods as shown in [84] figure 6.12. A sample of a more involved type of staining using immunodetection from [185] is presented in figure 3.77(b) next to an according visualisation from our simulation in figure 3.77(a). The nature of the immunohistochemical staining using anti-pimonidazole does not allow the setting of a clear threshold for detection, however a cell will be stained as hypoxic with high probability if the  $pO_2$  is below 1%.

As a sample of the simulation results, a central cut-section (thickness 40  $\mu\text{m}$ ) of a tumour after 12 days of growth is shown in figure 3.77(a). Cells are stained according to the oxygen concentration at their position either blue (normoxic or slightly hypoxic, that is  $pO_2 > 2.5\%$ ), purple (hypoxic  $pO_2 < 2.5\%$ ), red ( $pO_2 < 0.5\%$ ) or grey (necrotic). Cells show a sustained tolerance to anoxic conditions, so that only total deprivation of glucose will trigger necrosis in cells (followed by swelling up, shrinking and dissolution).

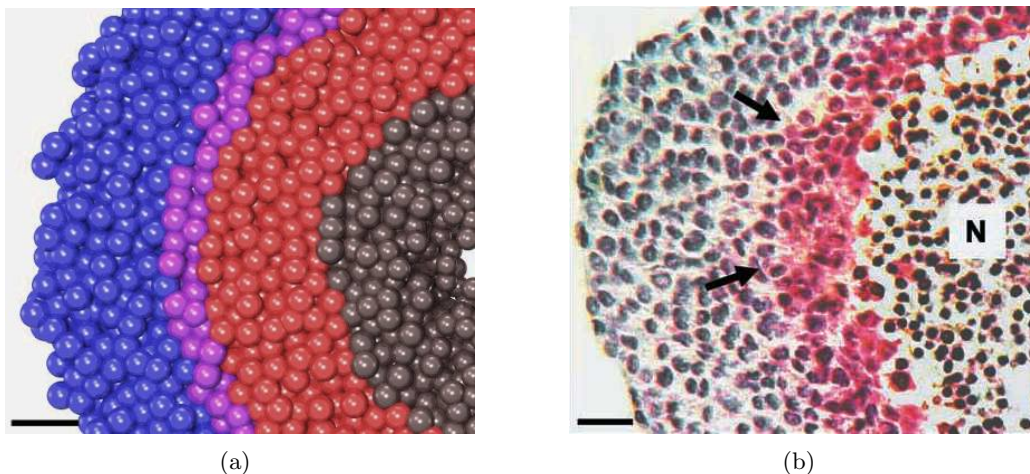
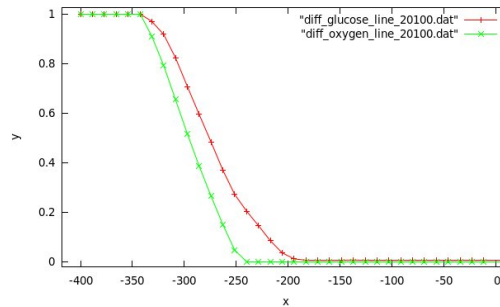


Figure 3.77: Central cut-section through an EMT6 tumour spheroid after 12 days of growth. Normoxic cells ( $pO_2 > 2.5\%$ ) in blue, hypoxic cells below 2.5% partial oxygen tension in purple, below 0.5% in red and necrotic cells in grey (a). Slice thickness is 40  $\mu\text{m}$ . (b) Immunodetection of pimonidazole in hypoxic cells (red) in the peri-necrotic regions of a tumour spheroids (T47D after 10-14 days of growth) from [185] (bar size in both images 50  $\mu\text{m}$ ).

*In vitro* and *in silico* stainings are in good qualitative agreement even though the standard simulation conditions were used and no fitting to the conditions in [185] has been performed.

Figure 3.78: Section from a lateral concentration profile of glucose and oxygen. The higher reach of survival-promoting glucose will lead to the formation of an anoxic region. See also figure 2.11(b).



As the spheroids in the experiment were grown under normal oxygen conditions (20.9%  $pO_2$ ), whereas capillary blood was used in the simulation conditions (13%  $pO_2$ ), the outer layer of normoxic cells is slightly thicker. The apparent greater width of the layer of severely hypoxic cells in the simulation results can be explained by the inaccuracy of the immunochemical hypoxia marker. It is also likely that the tolerance of T47D cells to anoxia in the experiment is only transient, so that anoxic regions will be partially filled by necrotic cells.

In either case, it is clear that the width of the viable, oxygenated rim of cells depends on the surrounding nutrient concentration, cell size and nutrient uptake. As discussed in section 2.2, diffusion lengths of oxygen through viable tissue have been measured to range from 100 to 300  $\mu\text{m}$ . Figure 3.78 illustrates the origin of the anoxic region: the diffusion length of glucose through the active tissue is longer than the length of oxygen. As glucose is the critical nutrient for survival, a region develops in which cells can exist under anoxic conditions, while still being sufficiently supplied with glucose.

Over time the hypoxic fraction of cells in the tumour will reach a steady state as indicated in figure 3.79(e). Hypoxic fractions of about 20% for head and neck squamous cell carcinoma xenograft tumours in a mouse model (FaDu) are reported in [91], but higher fractions of up to more than 50% are common [214, 161]. [38] reports typical hypoxic fractions of 80-90% in FSA and 9L tumors in Fischer 344 rats. Thus it is clear that the number of hypoxic cells varies strongly depending on the parameters of the cell line and the setting.

For the parameters in use, the tumour develops a steady hypoxic fraction of about 40% cells below 1.25%  $pO_2$  as shown in figure 3.79(e). This demonstrates that a large quantity of cells is below a level where oxygen enhancement effects play a role during irradiation. Larger fractions are subject to a slightly hypoxic milieu, which will, however, not directly influence the radiation response (but could do so indirectly, e.g. via production of lactate).

This equilibrium population of hypoxic cells will be disturbed with a characteristic timescale as shown in the next section.

### 3.4.2 Spatial and temporal dynamics of reoxygenation

Every treatment will affect the number of viable cells, their cycle phase distribution (and therefore also consumption of nutrients), density of the tissue and a number of further aspects. Consequently, the proportion of hypoxic cells will change in response to treatment. This treatment-induced change in the oxygenation of the tumour is of high interest for treatment planning as discussed for example in [7] and [183]. As further problematic behaviours such as metastasis [17], angiogenesis [59] and collective behaviour [115] are linked to hypoxia, the necessity to predict the oxygenation of tumours during treatment becomes increasingly important.

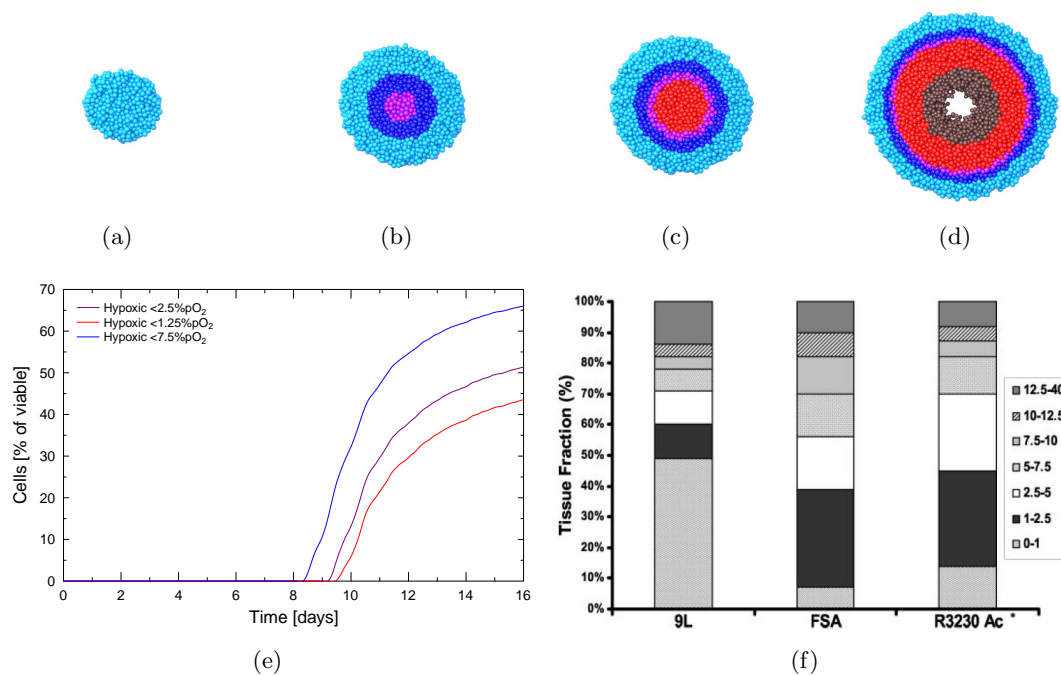


Figure 3.79: **(a)** Visualisation of the partial oxygen pressure  $pO_2$  in a tumour after approx. 7 days, 9.4 **(b)**, 10.1 **(c)**, and 12.2 days **(d)**. Colouring according to legend in **(e)**, normoxic cells ( $pO_2 > 5\%$  in turquoise). **(e)** Fraction of cells at different  $pO_2$  within the simulation during tumour growth. **(f)** Tissue fraction at  $pO_2$  (in mmHg) in advanced FSA and 9L tumors xenografted in Fischer 344 rats from [38].

In order to assess the amount and time scale of the change in hypoxia which is introduced by irradiation of the tumour, a sample spheroid was treated with 4Gy of x-ray radiation after 14 days of growth. The oxygen concentration was closely monitored and the resulting reoxygenation dynamics are shown in figure 3.80.

Within the microvolume that is affected by diffusion-limit-induced hypoxia (usually referred to as chronic hypoxia e.g. in [86]), the reoxygenation is very fast (on the scale of a few minutes). This is to be expected from the typical associated diffusion time  $t = \frac{L^2}{4D}$  which is about 6 seconds for 200  $\mu\text{m}$  diffusion distance (neglecting tissue breathing).

The immediate increase of the oxygen concentration is due to a halt in nutrient consumption by lethally damaged cells that committed to apoptosis. This effect will immediately increase the availability of oxygen for all surviving cells. In conjunction with the pressure release that is associated with slowly shrinking and dissolving apoptotic cells, the reactivation of previously quiescent cells will limit this immediate concentration rise. This can be seen in figure 3.81 where a detail from the oxygen-development in the tumour centre is plotted.

A few hours post-radiation, the concentration of oxygen will again increase significantly almost to the level of the outer spheroid layer. This is in response to an increase in the diffusion coefficient as apoptotic cells steadily dissolve. A corresponding rise in the diffusion coefficient will provide a better oxygen and glucose support to the tumour bulk (see figure 3.82).

Reactivation of cells and accelerated regrowth will lead to a surprisingly fast re-depletion of the oxygen within the tumour (see figure 3.80(b)). After only 39 hours oxygen in the core

### 3 Results

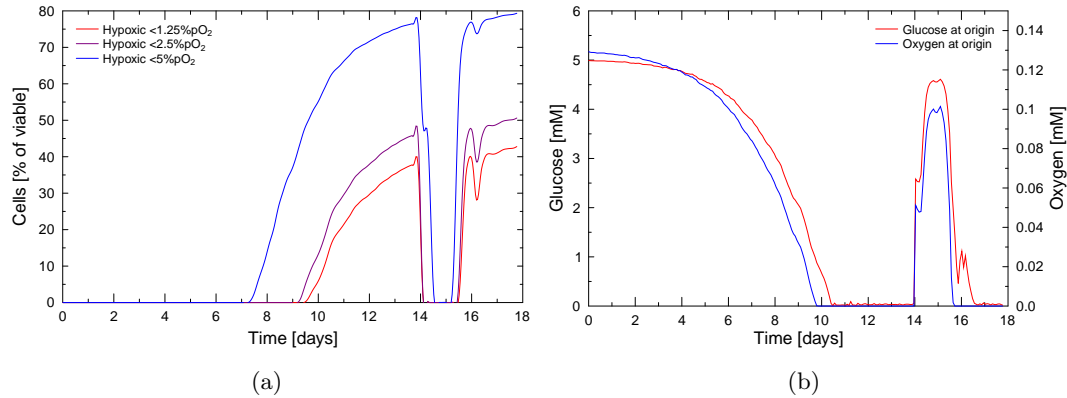
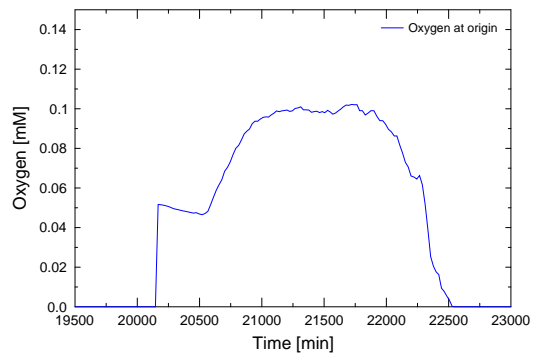


Figure 3.80: **(a)** Fraction of cells at different  $p\text{O}_2$  within the simulation during tumour growth and single radiation with 4Gy of x-rays at 14 days. **(b)** Oxygen and glucose concentration in the centre of the tumour during the corresponding run.

Figure 3.81: Detailed response of oxygen concentration in the tumour centre to irradiation with 4Gy x-rays at 20160 minutes.



of the tumour is again fully depleted. A transient peak in oxygen concentration is found between 16 and 29 hours post-radiation. This implies that follow-up irradiation should be applied within this time interval in order to exploit the reoxygenation effects. While longer treatment pauses will allow tissue regeneration, they will permit not only tumour regrowth but also a re-hypoxigenation of the tumour volume as expected in [245].

Within a multifractionated radiation schedule the re-oxygenation is repeatable as shown in figure 3.83. Longer pauses between fractions will allow for a re-depletion of oxygen and will trigger a similar response as the initial irradiation. As the average density (and thus the diffusion coefficient) will still be lower, the initial response of cell death overlaps with the diffusion enhancing dissolution of cells in follow-up irradiation (see second re-oxygenation pulse after 16 days in figure 3.83(a)).

If a lower dose is applied, the tumour might re-oxygenate only partially or with a delay. This has been demonstrated in figure 3.83(b). Small fractions of about 1Gy have been applied following a manual optimal triggered schedule as discussed in section 3.3.7. Since oxygen is severely depleted, the initial killing of cells will not be sufficient to re-oxygenate the tumour core but only to increase the availability of glucose. However the effects of small fractions will add up to a persistent increase in glucose and oxygen up to the optimal concentrations. This is an ideal situation in terms of oxygen enhancement, as all cells in the tumour mass will be sufficiently oxygenated to allow damage fixation.

Macroscopic, perfusion-induced hypoxia should be released in correspondence to the pres-

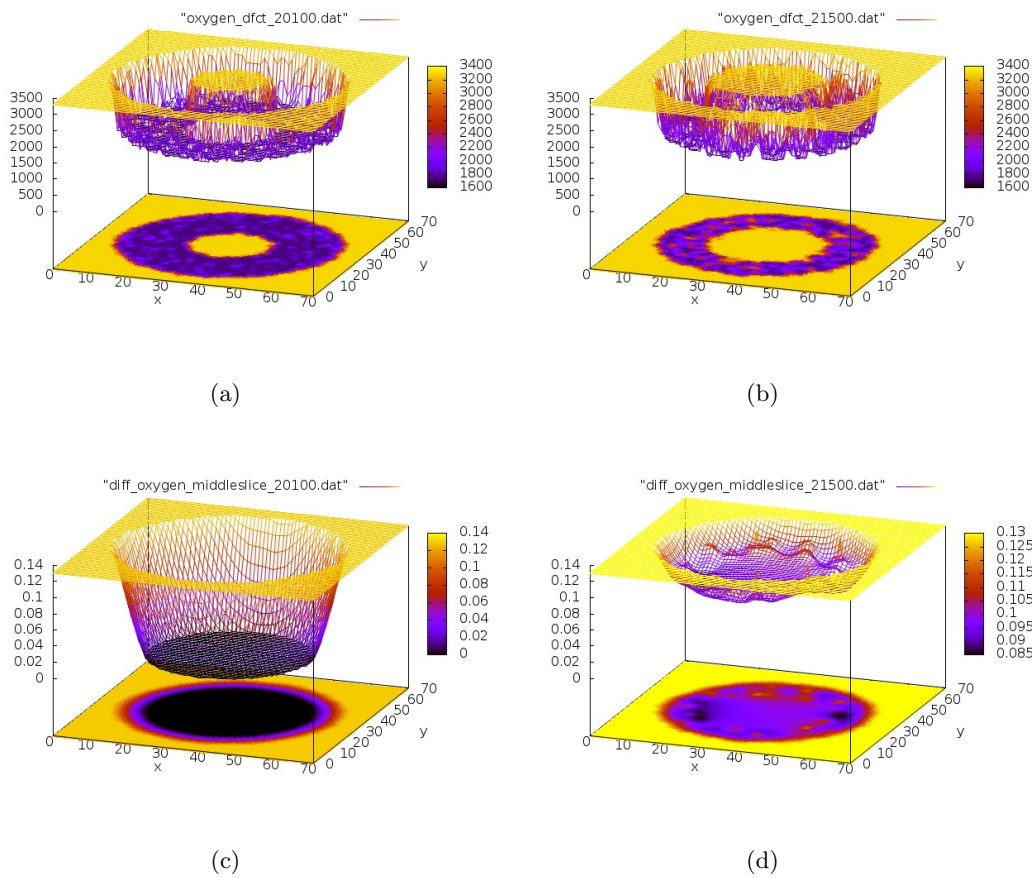


Figure 3.82: Local density-dependent diffusion coefficient for oxygen pre- and post-irradiation (top left and right). The dissolution of apoptotic cells will lead to a significant rise in oxygen diffusion into the tumour bulk. The bottom row visualises the corresponding oxygen concentrations.

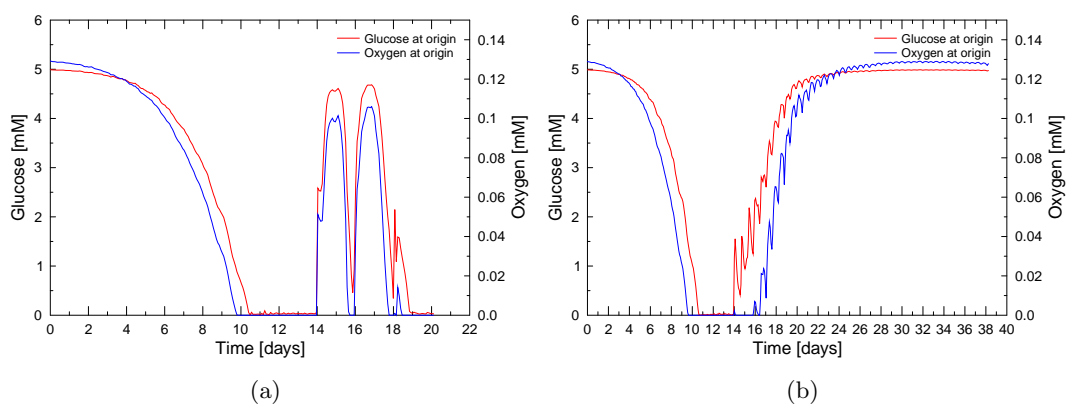
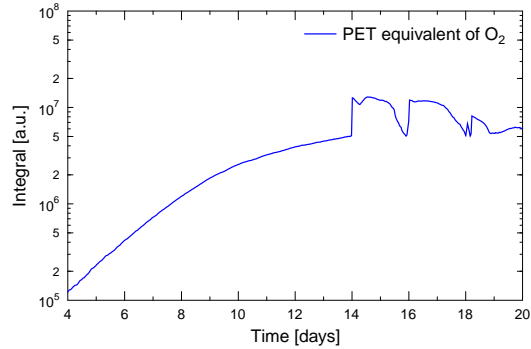


Figure 3.83: Persistence and stability of the reoxygenation response during multiple fractions and in a prolonged irradiation regime.

sure decrease within the model tumour spheroid. As the main mechanism of lifting transient

Figure 3.84: Integral oxygen  $P(t)$  in the tumour spheroid after initial growth period and subsequent irradiation with 4Gy xrays at 14 and 16 days.



vessel occlusions will be the dissolution of apoptotic cells, which frees up space in the tissue. This effect can be modelled indirectly via temporal variations in the boundary concentration which correspond to the changes in blood flow and oxygen availability.

Reaction to increases in oxygen availability can also be paradoxical as reported in [38]. Switching the breathing of rats to pure oxygen and, thus, increasing oxygen availability actually *decreased* the average oxygen concentration in some of the tumour xenografts. This illustrates that the oxygen support of tumours is an extremely complicated phenomenon so that the current model can only be a crude approximation.

### 3.4.3 Comparison to PET-results

Assuming the structural analogy between small microtumours and large macrotumours discussed in section 2.2.3, the relative oxygen content inside a macroscopic large tumour volume can be modelled using tumour spheroids. As a major factor of reoxygenation during treatment is the fast diffusion-based reoxygenation discussed in the previous sections, the oxygen content in a macroscopic tumour should follow the predictions from this model.

Effects may overlap with others such as the release of vascular occlusions and other sources of temporal variation of oxygen (see also [38]).

If the oxygen concentration is integrated throughout the volume of the tumour spheroid

$$P(t) = \int_{\text{Tumor}} C(\mathbf{x}, t) d^3\mathbf{x} \quad (3.3)$$

the total concentration will saturate over time as the growth of the spheroid is bound. The observable  $P(t)$  should be directly proportional to the signal measured in experimental positron emission tomography (PET) used for oxygen detection. Figure 3.84 shows a sample of the integral oxygen content within a tumour spheroid. After an exponential growth phase, the effects of growth saturation and the internal depletion of oxygen will lead to a saturation of the total oxygen content. As irradiation triggers a re-oxygenation in the tumour, as previously discussed, this can be seen as a fast jump in the integral oxygen and should reflect PET-based measurements with high temporal resolution.

Regrowth will lower the integral oxygen level as observed for the local concentration in the previous section. Follow-up irradiations will cause a similar response, while after the end of treatment strong regrowth will cause a wave of necrosis. This can be seen as the third spike in the oxygen concentration at day 18, 2 days after the second radiation dose was applied.

The possibility to relate the oxygen dynamics from a small tumour spheroid or a spheroid simulation to macroscopic tumours is of great interest as it could allow the prediction and

modelling of oxygen distributions in patients undergoing radiation treatment. This will be discussed in section [4.1.4](#)

## 3.5 Synergies in radiochemotherapy

In order to investigate the possible beneficial combination of radio- and chemotherapy, the irradiation response of a tumour treated with hydroxycarbamide/hydroxyurea has been simulated.

As discussed in section 2.6.2, hydroxyurea (HU) will have multiple effects which make it interesting for combination with irradiation: If applied directly before irradiation it will kill radioresistant S-phase cells and thus increase the overall sensitivity of the tumour. When HU is applied for a longer time period it will synchronise the cell cycle progression for cells in the tumour.

While the first effect of S-phase killing will yield just an additional effect to irradiation without real synergy, the clearing of resistant S-phase cells can still be of great interest for radiotherapy. The latter effect of synchronisation can be employed in order to prepare the tumour into a sensitive state, if the timing is chosen correctly.

### 3.5.1 Synchronisation using Hydroxyurea

When a dose of hydroxycarbamide is administered in the simulation it will instantly kill the S-phase cell population, as expected from the drug action. Cells which are not in S-phase at the time of treatment will be marked as being affected by hydroxycarbamide. This will prohibit their transition past the G1/S-checkpoint once reached during their advancement in the cell cycle. Thus, if the drug is administered for a timespan which is bigger than the average time for a cell to pass through G2-, M- and G1-phase, all cells will be halted at the G1/S checkpoint, leading to a perfect synchronisation.

Hydroxyurea effects persist in the simulation until a removal function is called (assuming an unlimited supply of hydroxyurea in the medium which surrounds the spheroid). Removal of hydroxyurea itself is instantaneous which corresponds to a complete exchange of the nutrient medium in experimental settings.

This basic effect of administration, synchronisation and release is shown in figure 3.85 both as schematic and in central cutslices from a tumour spheroid in the corresponding states. Hydroxyurea was applied at day 14 after seeding of the tumour and kept at high concentration for 24 h. After removal, cells could react to the released G1/S block with a scaling factor  $\rho$  of 0.5 as discussed in section 2.6.2.

The left cutslice in figure 3.85 shows the tumour state directly after hydroxyurea has been applied to the system. Cells which were in S-phase have committed to apoptosis in response to the drug. A large quiescent population and a necrotic core are still present within the tumour. As the cells are exposed to HU for a time period longer than their typical cell cycle, all active cells will be gathered in G1 phase, as HU prohibits their entry into synthesis phase.

One of the effects induced by a dose of hydroxyurea is an equilibration of the pressure within the tumour. If the drug is present over a sufficiently long period of time, both proliferation and cell growth within the tumour cease. Furthermore, the dissolution of apoptotic cells will provide free space within the tumour. Passive rearrangement of cells will thus lead to a slight drop in pressure. As cells equilibrate into a dense organisation due to their adhesion, the drop in pressure remains limited. However, the reduction in pressure is sufficient to significantly decrease the amount of quiescent cells within the tumour.

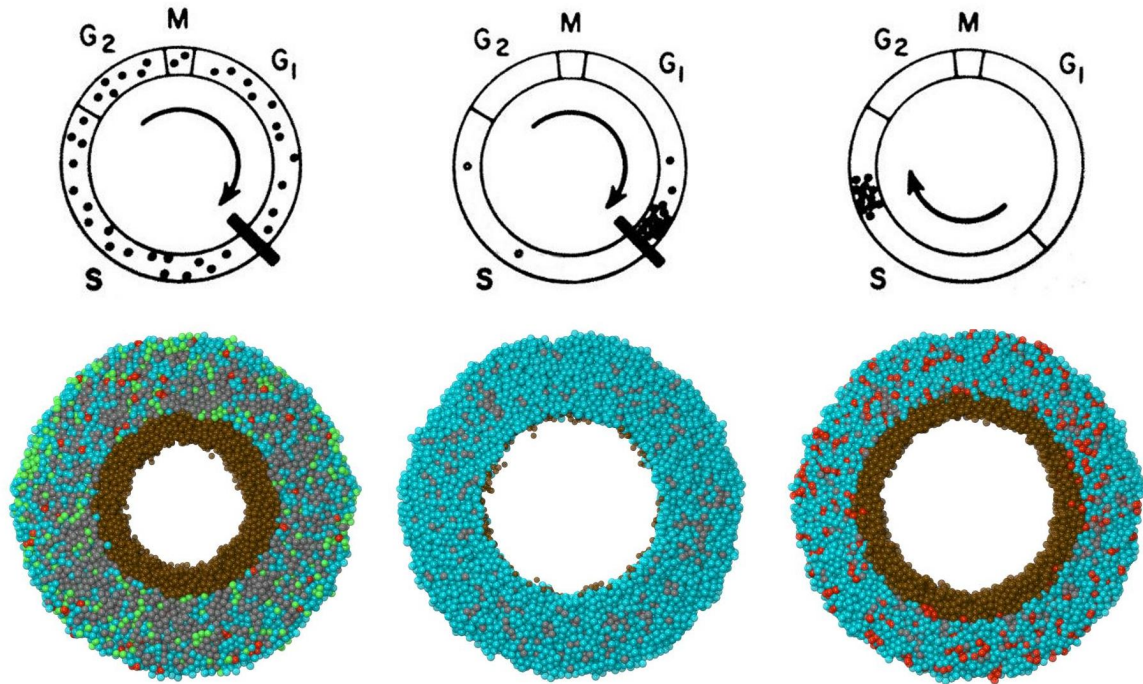


Figure 3.85: Effects of prolonged hydroxyurea administration for 24 hours and subsequent removal as schematic and visualised in according cutsections from the simulation. Cells can react to the release of HU with a medium scaling factor for the G1-phase lengths of  $\rho=0.5$ .

While this release of quiescent cells corresponds to a reactivation of a dormant tumour, the radiobiological effect is a drastic reduction of the resistant population within the tumour. This phenomenon further increases the potential of HU to be useful in combination with radiotherapy.

As S-phase cells were killed and are dissolving, the nutrient availability in the spheroid is increased, so that necrosis will vanish and remaining necrotic cells dissolve (compare also figure 3.87).

Within less than 24 hours, all cells are either in G1 phase or remain in quiescence, as is visible in figure 3.86.

Upon the release of HU, a wave of synchronised cell cycle progression is triggered, which can be seen as a drastic increase in mitotic cells within the right cutsection of figure 3.85. The increase in cell number associated with proliferation will quickly reduce the nutrient availability below a critical level and trigger a new central necrosis.

The synchronisation which was achieved by HU persists for a period of 3-4 days after release of the drug as can be seen in figure 3.86 and as quantified in figure 3.87. Depending on the distribution width of the cell cycle phase durations, this synchronicity will vanish over the course of multiple cycles. This effect is similar to the desynchronisation of an exponentially growing population from only a few seeder cells or to desynchronisation after radiation-induced synchronisation. However, even when an extreme degree of variability of the normal distribution for cell cycle durations is assumed, the initial synchronisation within 24 h post-treatment will be high.

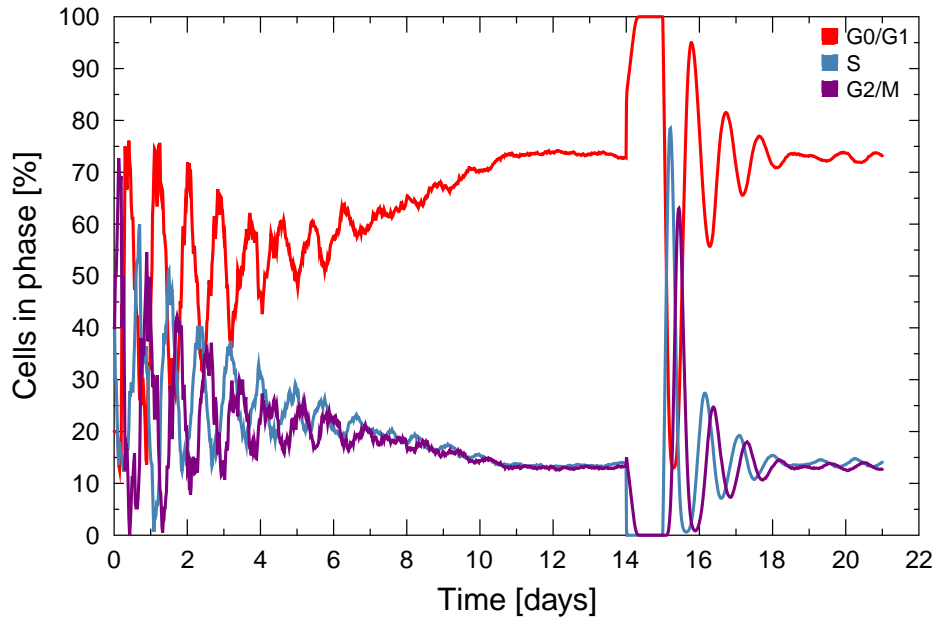


Figure 3.86: Cell cycle distribution by DNA content during tumour spheroid growth and in response to a dose of hydroxyurea as described in figure 3.85.

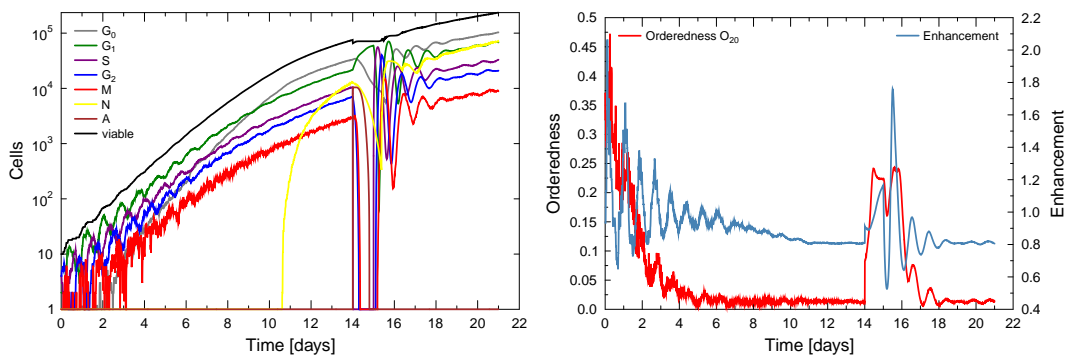


Figure 3.87: Cell cycle distribution and synchronicity after application of hydroxyurea for 24 h with a release factor  $\rho$  of 0.5.

### 3.5.2 Effect of release reaction factor $\rho$

If the population is completely synchronised after sufficiently long exposure to hydroxyurea, the release from the G1/S block will not be completely synchronous. While being marked as G1/S-blocked a cell will draw a new G1-phase length upon reaching the G1/S checkpoint and prolong its stay in G1-phase accordingly. This G1-phase length is modified by the release factor  $\rho$  as described in section 2.6.2, so that  $\rho$  effectively describes the responsiveness of cells to removal of hydroxyurea. If  $\rho$  is chosen to be very small, cell agents can instantly adapt to changes in HU-concentration, while for  $\rho = 1$  cells will use the normally distributed G1-phase length in order to be delayed due to a G1/S-block.

Figure 3.88 shows a comparison of the reaction that is induced by administration of HU for a period of 24h if different scaling factors for the release of cells are assumed. This can

also be used in order to approximate the response to incomplete removal of the drugs. This would be common for *in vivo* application as no simple medium exchange can be used to remove the drug. However, assuming that the cells can show a fast reaction to the removal of hydroxyurea but that the actual decrease of local drug concentration varies, then there will be a corresponding variation of the cells' reaction capability.

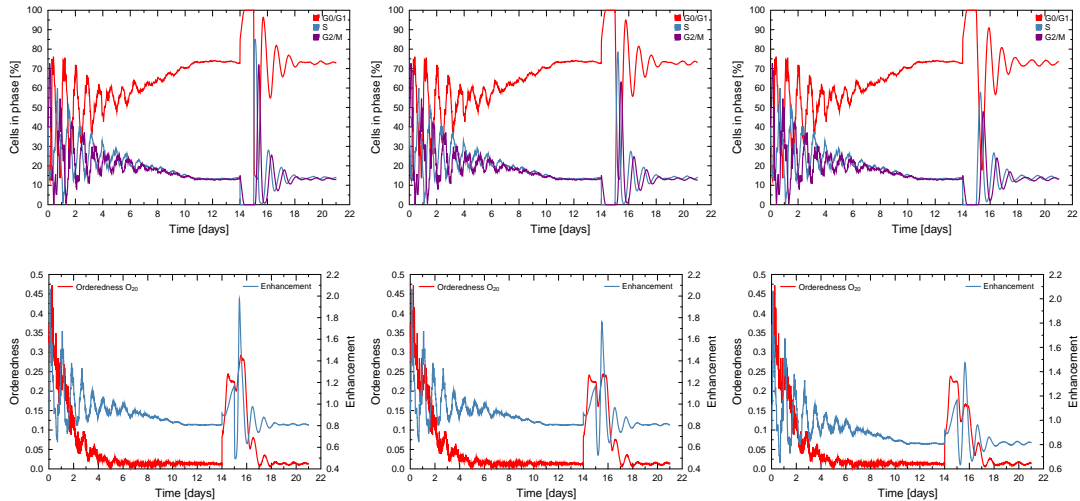


Figure 3.88: Cell cycle distribution and synchronicity after application of hydroxyurea for 24h with varied  $\rho$  of 0.1 (left column), 0.5 (middle) and 1 (right column).

As expected, the strongest synchronisation, which is associated with the highest radiosensitivity enhancement, will be achieved if cells show a fast reaction to HU removal with  $\rho=0.1$  (left column in figure 3.88). After the release of the G1/S block, the orderedness will decrease slightly but then immediately rise to a new peak when the majority of cells divide and thus effectively double the number of cells in G1-phase. The post-release drop in radiosensitivity that is associated with the synchronous progression of cells into S-phase will persist for the typical duration of S-phase. After that, a radiobiologically interesting peak in enhancement is present over a time of about 5 hours which corresponds to the average time for a cell to complete G2 and M phase. For a medium release potential of  $\rho=0.5$  a similar response can be observed.

Even when  $rho$  is set to 1, meaning that cells under the effect of hydroxyurea can only react to the removal of the drug over the timespan of a normal G1-phase length, the post-release synchronisation is still very high (as seen in the right column of figure 3.88). The peak of orderedness will now be the highest during the G1/S block of cells. A smaller, second peak of orderedness can be observed again after release, however the ratio of the peaks is now switched when compared to the fast-reaction case of  $\rho=0.1$ .

This confirms that even when the potential to remove hydroxyurea from the system is limited (as would be the case in a clinical setting), a radiobiologically highly relevant synchronisation and the corresponding enhancement can be achieved.

### 3.5.3 Short application of HU

If hydroxyurea is administered even for a short time, synchronising effects can be observed, as shown in figure 3.89. As the tumour will, depending on the cell cycle distribution, contain about 30% of cells in S-phase, their apoptotic death in response to hydroxyurea alone is sufficient to raise the synchronicity.

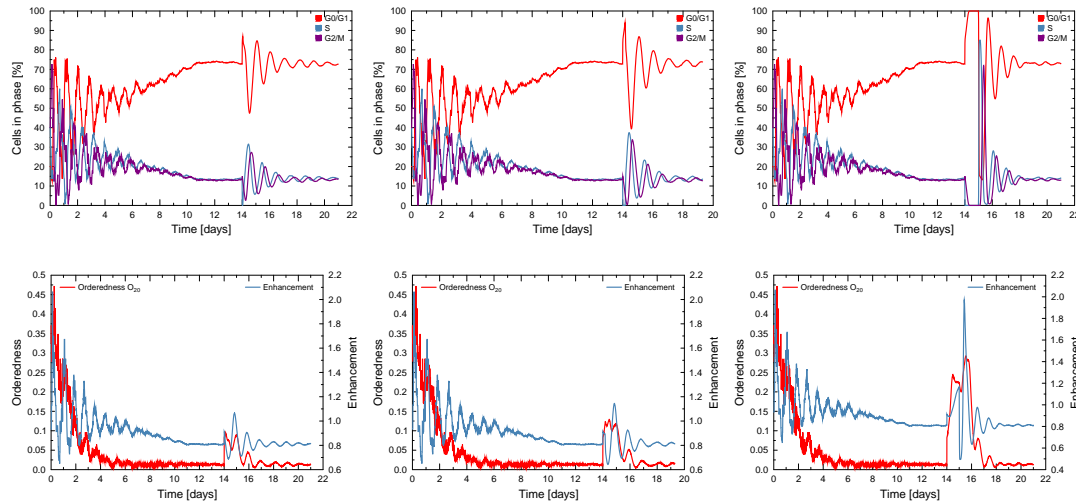


Figure 3.89: Cell cycle distribution and synchronicity after application of hydroxyurea for a varied period of time (1h, 4h, and 24h from left to right) with a constant  $\rho$  of 0.1.

With an increase of treatment time the synchronicity will reach saturation as all cells are halted at the restriction point. A 1h administration of HU will achieve a radiobiologically relevant activation of the tumour. Apart from the removal of S-phase cells, this activation is due to the associated pressure release which re-enters quiescent cells into the active cycle.

Prolonged exposure to HU for 4h will only slightly increase the response of the tumour. For an exposure duration of 8h (not shown) a full synchronisation into G0/G1 phase is achieved. However, the pressure decrease due to equilibration of the system which will result in release of quiescent cells is still not fully achieved, so that radiation enhancement will be limited to a factor of 1.4. A linear scaling of the response with exposure time is observed, with a maximum effect at 24h exposure.

### 3.5.4 Combination of hydroxyurea and radiotherapy

After the capability of hydroxyurea to induce a strong synchronisation has been demonstrated, it is of interest to examine which effect this synchronisation can have on the outcome of radiation therapy.

Similar to experiments performed by Sinclair et al. [205], a significant increase in efficiency can be observed if HU is administered at the appropriate time before applying irradiation. In the case of asynchronous CHO-cells as in [205], a time-interval of 4 hours between HU and irradiation was most efficient. If HU was not removed immediately but only after irradiation, the survival of cells in response to irradiation decreased significantly.

A further increase in treatment efficiency is possible if hydroxyurea is kept at high levels for a prolonged period and then neutralised (possibly using an inhibiting drug). The cell

population will respond to this sudden drop in hydroxyurea concentration by a continued synchronous advancement into synthesis phase. Even if synchronisation will slightly decrease again in response to the cell advancement, the fact that cells will still be largely synchronised when they reach the sensitive G2/M phase yields a tremendous increase in radiosensitivity.

Hydroxyurea can also be used in adjuvant drugs administered after radiotherapy. As irradiation will leave a population which contains a high level of resistant S-phase cells, a dose of HU can be effective in removing cells which survived the radiation dose.

Another possible combination can be achieved by using hydroxyurea with the right timing: if cells have been synchronised by a prolonged hydroxyurea block, a largely synchronous advancement into synthesis phase will be the result of removing the drug. If a second high dose of HU is delivered at this timepoint, it will result in a massive killing of cells in S-phase via inhibition of DNA synthesis. However, this approach would show systemic effects and thus kill a large proportion of cells everywhere in the body which have been previously synchronised, unless the hydroxyurea availability can be somehow restricted to the tumour region (e.g. by using a hypoxia-based delivery mechanism or any other form of targeted delivery).

A combination of HU with a localised therapy, such as precise radiation delivery, will work in any case and thus is to be preferred.

Whenever hydroxyurea is applied, the timing effects of synchronicity and enhancement should be respected. Even when applied as a post-irradiation drug, the synchronising effects of hydroxyurea could lead to the follow-up irradiation being delivered at an induced peak in radiosensitivity if the cell cycle progression alteration due to HU is not taken into account. Similar effects can be expected in other chemotherapeutic drugs, which affect cells in specific cycle phases or prohibit cell cycle progression.

### 3.5.5 Countering accelerated repopulation

Proliferation inhibitors or cytostatica open up the possibility of halting the growth of tumours by preventing the cells from completing the cell cycle or even keeping them fixed in one cycle phase, as discussed in section 2.6.3. However, due to the development of cellular drug resistance, this mechanism cannot be kept in effect indefinitely.

A typical response to the treatment of tumours is the so called accelerated repopulation, which will lead to a very fast regrowth of some tumours. After treatment, the surviving cells in the tumour will start to divide under the effect of improved environmental conditions. This is one of the reasons why treatment should not be paused but finished as fast as possible regarding the side effects. In a common approach, a level of regrowth is considered when the initial treatment plan is developed and enters in the form of additional fractions or an increased dose per fraction [86]. One alternative approach is to combine a prolonged irradiation regimen with an increasing dose of proliferation inhibitors in order to counterbalance the accelerated repopulation of the tumour. This schedule can limit the dose increase that is needed in order to cancel out the regrowth of the tumour.

While clinically accelerated repopulation is usually only considered to be an effect that is significant on the timescale of weeks, a high degree of fast local repopulation is observed in response to irradiation within the simulation. During fractionated radiotherapy regimens, periods of regrowth are common since, within the conventional irradiation schedule, cells in the tumour have 24 hours between fractions in which they can divide. For typical cell cycles

### 3 Results

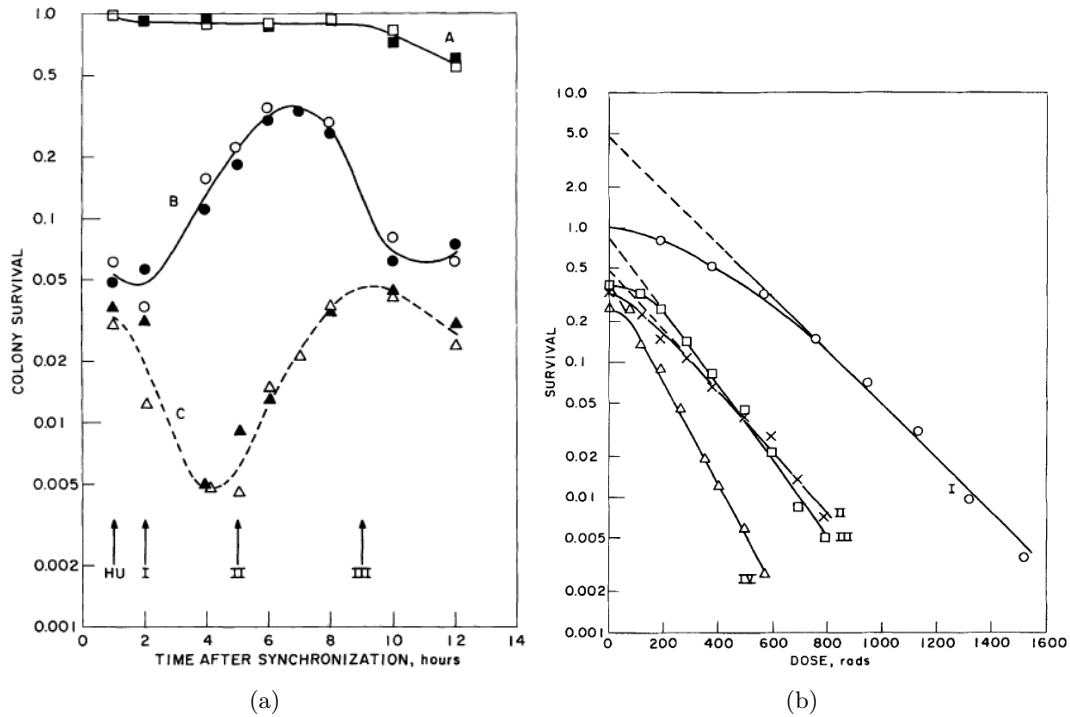


Figure 3.90: (a) Survival curve of CHO cells in response to irradiation, hydroxyurea or a combination depending on time between hydroxyurea treatment and irradiation. (b) Response of an initially asynchronous population of CHO cells to irradiation (curve I), radiation followed by hydroxyurea (II), hydroxyurea pre-treatment followed by irradiation (III) and pre- and post-treatment with HU combined with irradiation (IV). From [205].

this can result in a doubling of the cell count. Even if the limited clonogenicity of the cells in response to irradiation is taken into account, a considerable amount of regrowth can be expected. This effect is more severe for treatment schedules which allow longer pauses, but even in hyperfractionated schedules a baseline of regrowth is present.

An interesting approach is to counter the rapid regrowth which is triggered by a radiation dose by immediate administration of a proliferation inhibiting drug. If done correctly, this would lead to a great increase in treatment efficiency or could, alternatively, allow for risk-less pauses in the treatment schedule. Such pauses could be either motivated economically, by irradiation modalities, socially, to allow the patient to rest, or biologically, in order to allow for an increased amount of damage repair within the benign tissue in the entry channels of irradiation.

Within the simulation, time intervals after a radiation dose can be identified in which the relative amount of cells in mitosis (experimentally known as Mitotic Index MI) is drastically increased, as shown in figure 3.91. Even greater increases are observed for S-phase which is also easily targeted by drugs (as was shown for the example of hydroxyurea).

If the concentration of a proliferation inhibiting drug is timed to peak during these periods, a substantial amount of regrowth in the tumour can be cancelled. Especially therapies which require longer treatment pauses in response to larger doses of radiation could profit from the synergistic use of proliferation inhibiting drugs. An example of these is the highly successful 2.5Gy/30h schedule.

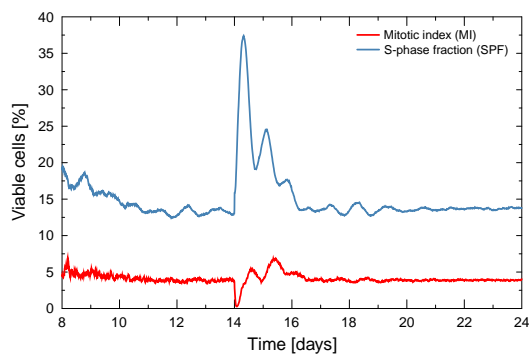


Figure 3.91: Mitotic index and S-phase fraction in a sample tumour in response to irradiation with 4Gy at day 14.

## 4 Discussion

Within the preceding chapters, a model for agent-based tumour spheroid growth was developed and tested, tuned to physiological parameters and employed in order to study the dynamic reaction of the spheroid to therapeutic approaches. With emphasis on the tumour response to radiation, the investigations were expanded onto the fractionated treatment of tumours.

### 4.1 Implication of main results

#### 4.1.1 Cell behaviour and tumour growth

As expected, the growth of tumour spheroids could be described reasonably well within the model. Under matching *in vitro* nutrient conditions, the model can qualitatively and quantitatively describe the growth of EMT6/Ro spheroids for different nutrient conditions. The structuring of spheroid and measured quantities, like the typical width of the viable rim, which are obtained in the *in silico* growth, correspond well to reported *in vitro* values from the literature. While for the limited dataset from [72] a critical product of glucose and oxygen concentration could successfully be used to trigger necrosis, as described in section 2.1.2 and [194], the growth dynamics can be captured using only glucose as critical nutrient. Strong experimental evidence as discussed in section 2.1.2 suggests that nutrient-induced necrosis will usually depend on glucose alone. Anoxic cells can survive for prolonged periods of time [235]. They can be subject to an increased level of metabolic stress which can trigger spontaneous apoptosis or induce quiescence. It is clear that critical thresholds must be examined carefully and are most likely not a good approximation of nature. Different cell types have been reported to exhibit a widely varying spectrum of behaviour from quick anoxia-induced cell death to a singular dependence on glucose for survival. However, the wide variability also suggests that a rather “generic” cell can be used to capture the most important facets of cell behaviour.

In the initial growth phase *in vivo*, a microtumour will develop from only one malignant cell. It is safe to assume that a typical tissue is slightly oversupplied with nutrients, as can be inferred from typical capillary distances (see [124]). Furthermore, a nutrient reserve induced by oversupply is of great use in times of stress or increased nutrient demands. This implies that there is an initial nutrient capacity left which can be used by the growing tumour nodule. Depending on the nutrient reserve at the tumour cell location, a fast induction of vessel growth or a high tolerance to adverse nutrient conditions is required from tumour cells in order to allow proliferation. A high tolerance for low conditions would allow effective starvation of surrounding benign cells. As the surrounding space is filled with viable cells, these will limit the amount of nutrients that arrive at a tumour seed cell. The initial position of the cancer cell within the intercapillary region will thus determine the availability of nutrients. Furthermore, it can be argued the tendency for oncogenic mutations is increased based on the

location, e.g. with a higher probability associated with cell stress induced by low nutrient conditions. This would imply an increased probability for cancer cells to develop under adverse nutrient conditions and further emphasise the importance of early vascularisation or metabolic adaptation.

The cell cycle distribution of the *in silico* spheroids in the initial exponential growth and the following plateau phase was comparable to experimentally measured distributions as confirmed in figure 3.8. A steady state in the evolution of the cell cycle distribution and the tumour histology is reached after about 12 days of growth. While beyond this point in time the necrotic core will still increase in size, the relative cell cycle distribution is constant as, for example, shown in figure 3.37. Histograms of the cell phase-angle as in figure 3.9 provide a good method to visualise the cell-age distribution. They correspond to experimentally obtainable cell-age curves or visualisations of dependencies on cell age, as the measured radiosensitivity curves in figure 2.28.

Further factors affecting tumour spheroid growth, such as possible mechanisms for growth saturation or the radial velocity distribution profile, have been studied. In a limited test setting, increased cell-cell adhesion was not sufficient to induce a full growth saturation. It is possible that, for even higher levels of adhesion or the additional use of adhesion mechanisms such as ICAM adhesion, saturation can be induced, comparable to the pseudo-saturation reported for high adhesion in [194]. However, within the main experimental dataset which was used for growth comparison [72], a full growth saturation is not obtained within 24 days of growth, except for the case of drastically low nutrient support with 0.8 mM glucose and 0.07 mM oxygen. For this extreme case of low-nutrients, a growth saturation is also obtained in the simulation, as shown in figure 3.1.

A range of possible mechanisms for the induction of growth saturation has been discussed in section 3.1.3. A common hypothesis is that toxic by-products of the central necrosis will further limit the viability of cells within the inner region of the viable rim. External pressure on the surface cells of the spheroid can lead to a significant increase of pressure inside the spheroid. In extreme cases, this can induce quiescence in all internal cells of the spheroid, which drastically limits growth as division is restricted to the outermost layer of free cells, as shown in figure 3.11. As a consequence of the extreme growth restriction and the lower nutrient consumption which is associated with quiescence, spheroids under the effect of external pressure will not develop a central necrosis within a period of 21 days. For a longer growth time, a full saturation can be expected, as proliferation will only be present in a very restricted thin surface layer, while necrosis will be related to the inner volume of the spheroid.

The radial velocity profile of cells confirms a flux of cells from the inner shell of the viable rim into the necrotic core, as well as an inverse outflux of cells which are in the outer regions of the viable rim. An interesting observation is the inversion of this flow profile in a limited time frame following irradiation, as indicated in figure 3.13. This implies that, in response to treatment, a compactification of the tissue will occur. The radiation-induced shrinkage of the tumour spheroid is accordingly limited, as inner cells show a strong outwards velocity component. While this flux can be observed in tumour spheroids, *in vivo* interaction with the surrounding microenvironment will induce a shrinkage of the tumour. This shows that, in order to make the model fully applicable to the *in vivo* behaviour of a small microtumour nodule, an external inwards force on the boundary cells (as has been implemented and tested)

or a specific inclusion of the microenvironment via a surrounding layer of benign cells would be useful. As the inclusion of benign surrounding cells implies that the spheroid must be growing inside a significantly larger spheroid of benign cells, this would pose a very high computational demand on the system, which is likely to exceed the typically available computational power. An interesting approach for this problem could be the agent-based modelling of only the viable rim of the spheroid (or even only the outer proliferating cell layers) and a restricted layer of surrounding benign cells. Inner parts of the spheroid and outer parts of the benign tissue must be handled in a continuous representation. This solution could yield a realistic, agent-based description of effects at the tumour-tissue interface, while restricting to fluid-like dynamics in the regions of lower importance. However, the connection of an agent-based simulation to a continuous model would be involved.

Shedding of the cells from the spheroid surface has been implemented and studied, as it is reported to be one of the main mechanisms which could induce a growth saturation. In contrast to experimental predictions, it has been demonstrated that a constant shedding rate cannot be present independently of the spheroid size. If the assumption of a constant shedding rate at an experimentally measured level is tested, it will effectively prohibit the formation of a tumour spheroid from small aggregates below a critical size. A high shedding rate will lead to an effective dissolution of the cell aggregates as a consequence of its surface to volume ratio. With increasing aggregate size, a higher shedding rate can be tolerated as the surface to volume ratio will be reduced. The formation of a necrotic core will be of importance, as it leads to a drastic increase in the surface to volume ratio. The shedding of cells can be limited to mitotic surface cells as suggested by experimental evidence. If this limitation is applied, it will act as a bounding mechanism for shedding. That is, within the simulation, a lower availability of mitotic surface cells was observed than required by the shedding rate. This implies that shedding is either not complete restricted to mitosis-induced contact loss, or that the typical time scale of mitosis differs between the experiments and the simulation.

A most interesting observation is the critical dependence of spheroid growth on the shedding rate of surface cells as depicted in figure 3.18. For an initial aggregate size of 100 cells, variation of the shedding rate across a physiological range revealed that the formation or dissolution of the spheroid is critically determined by the shedding rate. Small variations of the rate at a critical point will either lead to the subsequent development of a macroscopic tumour spheroid or to the dissolution of the aggregate. This implies that cell shedding can be of great interest in the context of tumour therapy. A therapeutic increase of the shedding-rate might lead to the dissolution of developing or remaining small tumour nodules. This could be achieved by targeted inhibition of adhesion molecules which are over-expressed in tumour cells and required for the maintenance of cell-cell contact during mitosis. *In vivo* shedding is not necessarily a beneficial mechanism. While it will reduce the size of the primary tumour, it can lead to an increase in local reseeded and metastasis. However, a majority of shed cells will probably die because of anoikis, although tumour cells have been reported to be independent of according adhesion-related survival signals. Furthermore, the immune surveillance is highly likely to dispose of single tumour cells, and most treatment approaches show a higher efficiency on smaller aggregates, so that overall the effects of shedding will be beneficial.

A synchronised progression of the cell cycle can influence shedding via an associated surface change due to synchronised proliferation. This effect can also induce an oscillatory behaviour,

as the amount of shedding and the tumour size interact, as discussed in section 3.1.5. Oscillations in the size of tumour spheroids in response to treatment have been reported e.g. by Staab et al. after X-ray of HI-irradiation as shown in figure 4.1 [213]. While Staab et al. conclude that the oscillations are most likely not caused simply by cellular synchronisation and shedding, their conclusion is based on the observed oscillation frequency in relation to the typical cell cycle time. However, as the oscillatory effects would be a result of the coupling of cell cycle effects and shedding rate via the tumour surface to volume ratio, the observed frequency is not necessarily simply the inverse cell cycle time. A radiation-induced alteration of the expression of adhesion molecules is also likely [10]. Furthermore, the observed changes in the post-treatment radial cell flux will lead to further alterations in the surface to volume ratio and thus the effect of cell shedding.

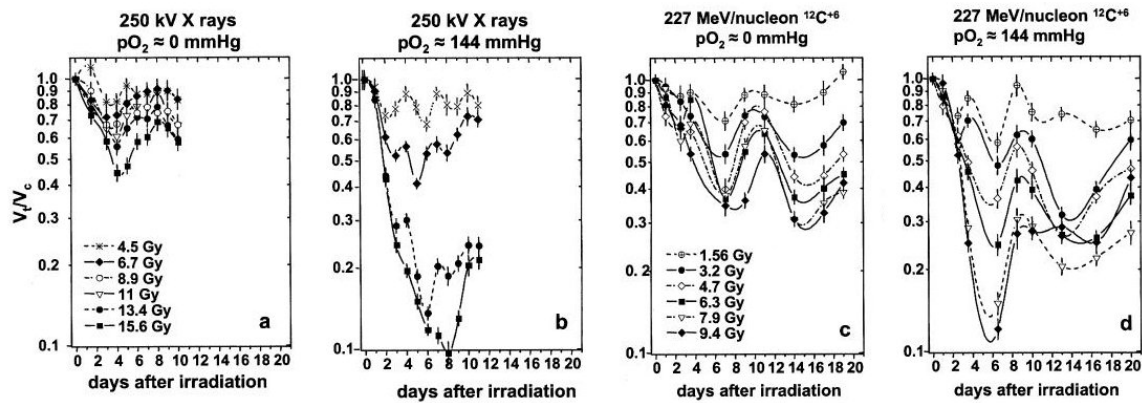


Figure 4.1: Oscillations in V79 spheroids after X-ray or carbon-irradiation under anoxic or oxygenated conditions. Adapted from [213].

With regards to treatment approaches, an increase in shedding after therapy can be expected. A possible synchronous cell cycle progression and the associated mitosis will increase the number of available mitotic surface cells for shedding. Furthermore, an increased loss of cell-cell contact due to apoptotic cells can be expected. If shedding is highly correlated with mitotic cells, this also implies that shedding can be temporarily diminished by the use of drugs which act on cells in mitosis or synthesis phase. An expected, therapy-induced increase in shedding could thus be either increased or decreased by the timed delivery of appropriate drugs.

#### 4.1.2 Irradiation response

Cell cycle synchronisation can lead to drastically altered results of radiation therapy. Using a range of sample tumours with altered cell cycle distributions which correspond to different tumour phenotypes, variations of the single cell survival of up to 50% can be confirmed. The cell cycle effects will be especially important in the typical therapeutic range of doses from 1 Gy to 4 Gy.

Within tumour spheroids that were subjected to irradiation treatment in the model, a range of coupled dynamic changes could be studied, which correspond to the basic mechanisms that are employed in fractionated irradiation as described by Withers [245]. A radiation dose will induce a high degree of synchronisation within the tumours' cell cycle progression. This

effect could be quantitatively described with the help of different synchronisation observables. The radiation response in terms of cell cycle distribution was compared to experimentally measured data. A good agreement between the development *in vivo* and the predictions of the simulation was observed. However, in many cases, the temporal resolution of available experimental data on the radiation response was poor.

Results of the simulation imply that tumours will show an oscillatory cell cycle response to irradiation with a characteristic timing that is in the order of magnitude of the typical cell cycle duration. Measurements need to be performed with a minimal temporal resolution which is less than half the typical cell cycle time, as discussed in section 3.2.2. If a lower temporal resolution is used, interpolation may lead to misleading interpretations of the obtained data. In extreme cases, as in clinical modelling, this can result in completely wrong treatment timing, as interpolation can effectively hide periods of high or low radiosensitivity.

The treatment-induced resynchronisation within tumour spheroids was found to mainly rely on three processes. A direct redistribution of cells is the result of their different radiosensitivity based on cell cycle phase. As irradiation will induce cell death, especially fast apoptosis will also lead to a significant amount of resynchronisation which stems from the re-entry of quiescent cells into the active cell cycle. The third mechanism is the blocking of cells at the G2/M checkpoint which will further synchronise the population.

Depending on the radiation quality, or more precisely, on the branching of fast versus slow cell death in the model, the magnitude and timing of resynchronisation will change. A high degree of slow death will induce a stronger synchronisation with a lower amount of oscillation. Conversely, a high degree of fast cell death will induce a stronger immediate resynchronisation, followed by pronounced oscillations. The strength of the synchronisation effect also depends on the variability of the radiosensitivity of the cells under consideration. If the variability that is associated with the cell cycle phase is high, the observed synchronisation will be stronger, while the mechanism of direct redistribution will lose importance for cells which show a uniform sensitivity to radiation.

The synchronous radiation-induced advancement of cells in the cycle will lead to macroscopic variations in the overall radiation sensitivity of the tumour. These variations were described and quantified using the measurable of radiosensitivity enhancement as in figure 3.25. Administration of radiation will immediately lead to a fast decrease in overall radiosensitivity, which defines an interval in which follow-up doses should not be applied. After the initial decrease, a strong, dose-dependent rise in enhancement is observed in the model that is qualitatively independent of any parameter or mechanism. A sequence of following oscillations in enhancement are observed as the tumour will return to a baseline of enhancement.

A synchronous progression of cells will typically be present within a time-frame of 24-48 hours post-radiation. The readiness of cells to commit to quiescence was identified as the main mechanism which will dampen the oscillatory response. If quiescence of cells is decreased or disabled in the model, oscillations can persist for a longer time. Higher doses of radiation will induce a stronger clearing of cells and, consequently, a more persistent absence of quiescence. A stronger and longer lasting oscillatory response is also observed for higher doses. The natural variation in length of cell cycle duration will be another dampening effect, which is also present in the absence of quiescence (compare figure 3.35). A variation of the average cell cycle phase length for cells in the simulation led to predictable shifts in the enhancement response. Assuming a lower width in the normal distribution of cell cycle durations would

increase synchronisation effects and their persistence. For this reason the variability of cell cycle durations becomes interesting as a target in therapeutic approaches.

While variation of the model parameters for irradiation will shift the enhancement response, the quality of the response will be conserved within a wide range of parameters, indicating that the effect of synchronisation will be universal and thus can be used in treatment planning of tumours. The strongest dependence on the branching of fast and slow damage was observed for the primary enhancement peak in response to irradiation which is related to the shift of the main mechanism of resynchronisation, as discussed in section 3.2.4. Timing of the following peaks in enhancement was demonstrated to be mainly determined by the cell cycle time and largely independent of the radiation model.

The importance of the mechanisms of quiescence resistance and oxygen enhancement to the radiation response was investigated. The resistance factor assigned to quiescent cells will drastically alter the radiosensitivity of the population, as a large fraction of cells will become radioresistant. However, the timing of the irradiation response remains unaffected by the level of radioresistance that is attributed to quiescent cells, as demonstrated in figure 3.38. While oxygen enhancement will play a role in cell survival, its effect on the quality of the irradiation response is also limited.

A surprisingly strong influence on the radiation response was confirmed for the characteristic time which was associated with the clearing of dead cells from the tumour. A doubling of the times for necrosis and apoptosis leads to a drastic decrease of radiation-induced enhancement in the tumour spheroid. Furthermore, the timing of the enhancement response will be altered, with a shift to later times. This effect is a direct result of the slower dissolution of cells, which will decrease the number of cells which can re-enter the active cycle from quiescence. This observation implies that an alteration of the clearing of cells can have a beneficial effect in radiotherapy. Faster clearing will not only increase the post-radiation enhancement for radiosensitivity, but will also lead to a more defined synchronisation of cells, which could be targeted with the appropriate drugs (e.g. antimetabolite compounds to target S-phase cells). The results imply that if the induction of apoptosis as radiation-induced death pathway can be stimulated *in vivo*, this could yield a number of beneficial effects. However, with regards to the immunogenicity of cell death, a high level of necrosis will be useful in order to stimulate an immune response against the tumour. Also, the level of bystander damage will be higher if cells die via necrosis. Thus, an active control over the branching of radiation-induced cell death into apoptosis or necrosis could prove to be of therapeutic relevance. A possibility to influence the mode of cell death is given with the LET-dependence of cell death as discussed in section 2.5.3. Thus, a further factor in the decision to either apply conventional radiation therapy with X-rays or particle therapy could be if immune-effects are suspected to be high (thus calling for necrosis as favoured mode of death) or if a stronger synchronisation and clearing of the cells is to be employed (which would be associated with increased apoptosis).

The variation of the treatment response, which is connected with the spheroid size at the time of irradiation, demonstrates that a rising level of quiescence in the spheroid is connected to a later and more stable radio-enhancement response as shown in figure 3.40. At the same time, the preliminary cessation of fractionated treatment revealed that this shift can be of relevance to the exact timing in radiation schedules.

The range of observables which were developed in order to assess the synchronicity of

the tumour population in response to treatment, was shown to be in good correlation with enhancement effects. Even if only a limited basis for the calculation of synchronicity is available, such as the ratio of cells with different DNA content, the orderedness will yield reliable results. As synchronicity can be both connected to a high or low enhancement, further measurables, such as the S-phase fraction, need to be assessed in order to decide if the tumour is in a radiosensitive or radioresistant state.

In connection to the synchronicity of the population, a typical relaxation time for tumours could be identified. In response to irradiation treatment, this relaxation time will increase with dose size, as the deregulating effects on the tumour increase. For high doses of 8 Gy, it was demonstrated that the tumour will only return to a steady state about 120 hours after treatment. Within the range of typical clinical doses, a relaxation time of about 40 hours is characteristic. This relaxation time can be used as guideline to decide if cell cycle effects need to be considered in a treatment plan.

As a major effect in radiation damage, oxygen enhancement effects were implemented in the model using a flexible LET-dependent parametrisation as discussed in section 2.5.1. Especially at higher doses, oxygen enhancement can significantly alter the overall performance of irradiation as demonstrated in figure 3.46. Higher survival rates of cells in hypoxic regions will also lead to a faster reformation of hypoxia in response to irradiation. However, hypoxia has only a very limited influence on the development of the overall enhancement response to radiation. This implies that the use of response predictions in therapeutic schedules would be largely independent from the oxygenation status of tumours. If a connection between severe and persistent hypoxia and quiescence were to be implemented in the model, this limited effect would become more important. As reoxygenation in response to radiation would also lead to a reactivation of hypoxia-induced quiescence, a strong alteration of the enhancement response could result.

Predictions of the enhancement in split-dose experiments demonstrate that the importance of sublethal damage repair for the overall development of the radiosensitivity is drastically lower than the associated cell cycle effects. Even without an implemented mechanism for the repair dynamics of DNA damage, the radiation model was able to predict the according development of the radiosensitivity as observed in experiments using V79 spheroids as discussed in section 3.2.8.

The importance of cell cycle effects for irradiation is very high. While for particle irradiation, an independence of cell killing from the current cycle phase is usually assumed, this is only true in the region of the Bragg peak. Within the plateau region of the entry channel and the low-LET regions of the spread out Bragg peak, a high dependence on the cell cycle will be present, as will be discussed in more detail later [64].

Quiescence plays a central and multifaceted role in the radiation response of tumours. It partially determines the overall radiosensitivity via the radioresistance of the quiescent population, it determines the initial development of the treatment response to a large degree and it affects the dampening of the oscillations in enhancement.

The tumour response to irradiation revealed a stable and largely parameter-independent evolution of the overall radiosensitivity. Within time windows of opportunity, a trigger dose of radiation will induce an enhancement which can be employed by a second dose that is applied with the right timing.

The similarity of tumour spheroids to micro-regions inside macroscopic tumours, as dis-

cussed in section 2.2.3, implies that results of the spheroid simulations under *in vivo* boundary conditions can be expanded to *in vivo* tumours within certain limits. Sham and Durand state that “since spheroids show tumour-like growth properties as well as cellular and microenvironmental heterogeneity, the changes occurring during multifraction irradiations should be comparable to those in human tumours undergoing therapy.” [200].

### 4.1.3 Fractionated irradiation

The theoretical gain or loss which is associated with cell cycle effects in even a short regimen of fractionated irradiation is extreme, as was demonstrated in section 3.3.1. Consequently, the use of triggered enhancement periods in radiotherapy seems mandatory. As within common clinical schedules no cell cycle effects are considered, a range of simulations could show that the associated performance of conventional schedules is rather poor when compared to optimised schedules.

Also, for typical clinical schedules, the differences in performance could be traced back to their timing in relation to the enhancement response. Hyperfractionated schedules showed a higher performance and a persistently higher level of enhancement. It is reported that hyperfractionated schedules are associated with a number of other beneficial effects, such as a reduction in late effects [246].

Treatment pauses proved to have a drastic adverse effect on the performance of radiation schedules. The associated high amount of regrowth would render a range of clinical schedules incapable of achieving a reduction in tumour size. An overview of the radiation reaction in terms of classical radiobiological observables like potential doubling time, labelling index and so forth can be found in [201]. Sham and Durand could observe a strongly accelerated repopulation, which is proposed to be countered by fast treatment, in agreement with the conclusions from this simulation. While it is often argued that longer treatment pauses can increase reoxygenation, this is not true, at least on a microscopic level of reoxygenation as was demonstrated in section 3.4.2.

An interesting effect is the possible dissolution of larger spheroids into smaller aggregates in response to a high-dose schedule as illustrated in figure 3.53. Radiation-induced apoptosis could lead to a loss of contact between cells and an associated degradation of the tissue. This would drastically affect the tumour properties. An increase in drug-penetration is to be expected as well as a higher efficiency of drugs on the smaller tumour aggregates. If shedding effects are present, as previously discussed this would imply that a high dose schedule could disturb the tumour integrity and distribute the remaining cells into aggregates below critical size which can be effectively dissolved. However, while the mechanism of shedding is of importance *in vivo*, the results of the current implementation cannot be simply transferred to the *in vivo* level. The presence of a microenvironment would probably drastically alter the observed shedding effects.

Cell cycle synchronisation can induce immense effects in a prolonged radiation regimen. This was demonstrated in the integral dose which is needed for complete sterilisation of a spheroid in dependence of the radiation timing. Longer fractionation pauses, which allow for a higher degree of regrowth, can be employed without a negative effect, as the associated regrowth is cancelled by the enhancement in radiosensitivity. These pauses can allow a higher degree of repair in surrounding benign tissue while the same control can be achieved in the tumour region under treatment. The timing of fractionation intervals which were especially

successful, as depicted in figure 3.58, could be directly linked to the enhancement development in response to a single radiation dose. Also, in prolonged schedules, the enhancement development from fraction to fraction was a clear determinant of the overall performance of the according schedule.

The test of fractionation schedules which deliver the same dose per time unit with varied fraction size demonstrated the strong change which an optimal sensitivity development between doses can yield in the overall performance of the schedule. A simple and optimal schedule for the tumour under investigation could be identified. A repeated dose of 2.5Gy every 30 hours will yield an optimal reduction in tumour size over time. While initially this schedule is outperformed by hypofractionated low-dose schedules, it retains its performance even over a long time and eventually shows a better total performance. The large degree of regrowth associated with the inter-fraction time of 30 hours could yield a high synergy of this schedule if employed together with a proliferation-inhibiting drug-regimen. For the assessment of treatment performance, the tumour burden and the integral enhancement proved to be useful observables, which are in good correlation to each other and the result of the assessed schedules.

As investigated earlier in section 3.2.5, the enhancement response will be subject to a slight shift in time, as the tumour composition changes during prolonged treatment regimens. This effect partially prohibits the straightforward definition of triggered radiation schedules. Still, the variations are within a range that allows for a targeting of sensitive time frames, while it is not possible to trigger at optimal points in time during the whole schedule. For single high-dose irradiation, an optimal calculation is possible and highly advisable as the enhancement effects can be drastic, especially if high single doses are to be employed as discussed later. If the tumour system does return to its quasi steady state, the exact response can also be predicted for prolonged treatment schedules. This will require long treatment pauses. The question of the time scale and dynamics which the tumour takes on its path to the steady state is of interest itself, as it is possible that resonances between fractionation and oscillatory changes in the tumour dynamics are possible.

While the performance of schedules which employed a well-timed combination of trigger and effector doses was significantly better than other schedules, the effect of most timings was lost with a shift of the enhancement response over treatment, as was discussed above. A combination of a 2 Gy trigger dose with a 4 Gy effector dose proved to have a very strong effect in terms of a reduction of the tumour burden. The very long treatment pause which is kept in between two blocks of trigger and effector dose, is highly suitable for a combination of the schedule with proliferation-inhibiting drugs. If the immense regrowth which is associated with the reactivated tumour in the treatment pauses can be reduced, this treatment schedule could be the most successful overall schedule in the investigation. The long treatment pause in the schedule can also explain its lasting performance over the course of the complete regimen, as it will allow the tumour system to relax and thus trigger a predictable enhancement as discussed above.

The investigation of a manual optimal triggering schedule provides an example of the fact that the treatment optimisation is a global phenomenon and cannot be optimised locally. In order to obtain a high overall enhancement during a prolonged treatment regimen it is thus not sufficient to target the next enhancement peak. As effects within the tumour change over time, the success of a treatment can only be evaluated after it has been performed, or

after it has been completely simulated. However, it is possible to derive general guidelines for successful radiation delivery and even locally optimised schedules show a drastically enhanced performance when compared with un-optimised clinical schedules.

A tumour corresponds to a dynamically reacting system, with a complicated or even non-linear response function. When an optimal schedule is to be enforced, the tumour is supposed to be repeatedly prepared into a specific state of enhancement. This analogous to an external force which is applied to a pendulum with a given eigenfrequency. Repeated external excitation can thus lead to beats in the tumour system, when the treatment frequency and the response frequency of the tumour are within the appropriate range.

Simple automatic triggering algorithms can achieve a significant advantage in tumour size reduction when compared to the conventional 2Gy/24h schedule. Even if triggering is not perfectly tuned to the enhancement peaks and will also only perform a local optimisation, the scheduling is still superior to conventional planning and to simple hyperfractionated schedules.

A monitoring of synchronisation and enhancement, as would be required for automatic triggering, would be difficult, if not impossible, to implement in a clinical setting. A range of possible observables which can be used for the prediction of enhancement has been discussed. However, the clinical workload of such a schedule would still be extremely high as patients would need to receive radiotreatment whenever an optimum in enhancement is reached.

Experimentally and clinically different observables can be used as predictors of the synchronicity within the cell population. Candidates include the mitotic fraction, S-phase fraction or characteristic changes in the doubling time. These can be obtained either from biopsy samples or non-invasive measurements such as the PET-measurements of oxygen or glucose consumption. FACS-sorting of cells from biopsies by DNA or by their specific CDK-content can yield a good approximation of the population synchronicity as shown in section 3.2.6.

Possibilities to closely monitor the cell cycle progression *in vitro* with high resolution are steadily increasing. Even single-cell monitoring of cycle progression via staining has been developed as shown in figure 4.2 [188]. A continuous cell-cycle specific tracking of cells *in vivo* could yield an unprecedented possibility to monitor the cycle kinetics in tumours.

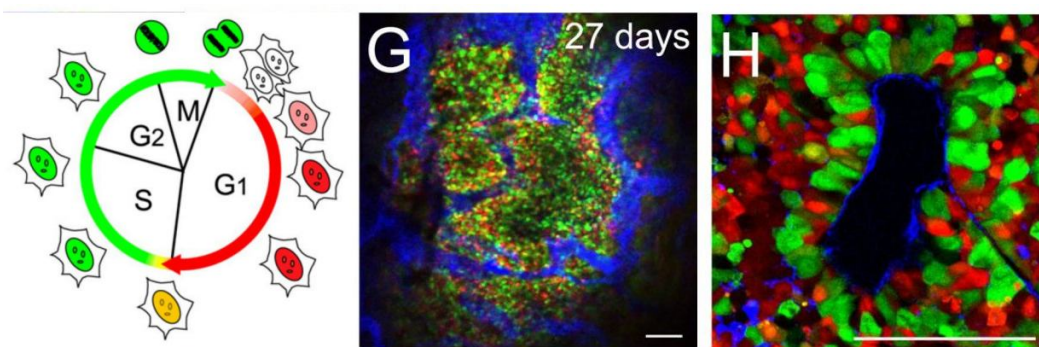


Figure 4.2: High-resolution cell-cycle specific staining of HeLa tumour cells *in vivo* from [187]. Continuous cell-cycle specific tracking of cells *in vivo* could yield an unprecedented possibility to monitor the cycle kinetics in tumours during treatment.

#### 4.1.4 Hypoxia

A number of different reasons for hypoxia in tumours has been discussed, with a discrimination between micro- and macroscopic phenomena and an acute or chronic timescale in section 2.2.2. The development of a hypoxic cell population within tumour spheroids was studied in the model, with special emphasis on the spatial and temporal dynamics of reoxygenation, which are induced by treatment. A microscopic, local increase in diffusion length, as a result of cell killing and a decrease of tissue density, could be identified as main effect for fast reoxygenation in tumours in response to treatment.

Within the literature ([84] being the most prominent example) it is often illustrated that fractionated radiation therapy will lead to a layer-wise reoxygenation of a large tumour mass. However, this is only partially true as the fast response of reoxygenation is a purely diffusion-based effect and, therefore, microscopic in its nature. While on a larger timescale vessel occlusions will also be released by a decrease in pressure, the immediate response will rely on diffusion, and, as a result, do not show any macroscopic layering. Instead, reoxygenation on the microscopic level will occur simultaneously in the microscopic volumes of the tumour which surround the capillaries. This effect of the microtumour structure, as discussed in section 2.2.3, opens up the possibility to directly compare the predicted reoxygenation from the model with clinical data.

Most experimental results measure the long-term effects of hypoxia or its release days after irradiation, but do not include the fast, diffusion-based dynamics of oxygen. Results of the model, as in figure 3.80, indicate that a fast and transient reoxygenation will be present in the tumour in response to irradiation. This oxygenation is lost within a time frame of 24-48h due to regrowth in the tumour and the associated high uptake of nutrients.

As the observed timescale of reoxygenation concurs with typical fractionation intervals, it is expected that the microscopic reoxygenation will be of importance for treatment. Longer pauses in schedules seem prohibitive if oxygen enhancement effects are to be employed, at least for reoxygenation on the microscopic scale. While treatment pauses could allow for an increase of oxygenation in the tumour as a result of macroscopic effects, the microscopic diffusion-based reoxygenation will be lost even within moderate treatment pauses. Reoxygenation effects on larger scales, such as the pressure-related release of vessel obstructions, cannot be directly studied in the model. However, a correlation between tumour pressure and the overall probability for vessel occlusion could be established. Thus, the decay of tissue and the following regrowth dynamics in the model could be used to obtain an estimate of more macroscopic phenomena of reoxygenation.

The effects of hypoxic resistance and quiescent resistance are experimentally hard to separate. In many cases, quiescent cells will reside within hypoxic regions of the tumour and thus be subject to a mixture of quiescence- and oxygenation-mediated radiosensitivity. Within a model the factors could be separated and their according influence studied more systematically.

The formation of new blood vessels will be of importance for the oxygenation of the tumour. While this will influence the availability of oxygen in the tumour, this effect will be on a macroscopic scale and thus most likely independent of the observed microscopic effects. Even if the formation of new vessels is stimulated, this effect will be stimulated by hypoxic cells. Thus, a population of hypoxic or anoxic cells will most likely always be present inside the tumour.

Histologically the distribution of hypoxic cells could be qualitatively compared to experimental results for tumour spheroids as in figure 3.77. For the reoxygenation response of the tumour, the hypoxic fraction as well as the integral oxygen in the tumour are useful observables. The first measurable can be compared to experimental results in biopsies, the latter observable should be directly comparable with the signals obtained in PET-scanning.

In vivo monitoring of oxygen concentration with high time resolution, as it is progressively also available in clinical settings, will make inclusion of these fast oxygen dynamics into treatment plans possible [91]. As hypoxia dose-painting is commonly employed to adapt the applied dose in accordance to the oxygenation, a continued prediction of the oxygenation at all points in time in the tumour would be of great value for the optimisation of the treatment [210]. This could be achieved with a reliable simulation of the oxygen dynamics in the tumour, which is initialised with data obtained at the beginning of treatment. Predictions of how the oxygenation will change in response to the first doses can be included in the treatment plan. After a given number of fractions, the simulation predictions are corrected using new data obtained from the patient. In this manner the number of necessary PET-scans can be decreased and the inter-scanning dose-painting according to the oxygenation is optimised.

As stated in [7]: “For clinical applications, the appropriate combination of hypoxia detection for patient selection with a hypoxia-specific treatment is essential.”. If hypoxia-specific treatment will not be limited to a binary classification of the tumour as hypoxic/normoxic, but a spatiotemporal estimation of hypoxia can be used to optimise the prescribed dose, this could yield large enhancements in the efficiency of the therapy.

#### 4.1.5 Radiochemotherapy

A range of possible synergistic uses for a concomitant chemotherapy regimen was identified within the model. Irradiation-induced regrowth within tumours can yield time windows for the efficient application of cytostatic drugs. These points in time can be identified using clinical observables such as the doubling time, the S-phase fraction, or the mitotic index, which proved to be good estimators within the model.

While no full investigation of a possible combination of radiotherapy treatment schedules with chemotherapeutic schedules has been performed, the possibility to model adjuvant therapies with drugs in the simulation, and thus within the context of cell cycle dynamics, has been demonstrated. Gains from a combined therapy using hydroxycarbamide and radiation have been quantified in terms of the enhancement measure.

Whether hydroxycarbamide is suited to be used as adjuvant treatment for radiotherapy cannot be decided on the basis of this investigation alone. However, it was demonstrated that the induced synchronisation of cells can be of great use in radiotherapy. The basic mode of action of hydroxycarbamide alone, namely the induction of severe DNA damage at replication forks, is of great interest for the use in cancer treatment and the combination with radiotherapy. As the cancerous cell population will be highly active, it will be also very susceptible to S-phase killing, such as induced by hydroxycarbamide. It is an added bonus that killing cells in S-phase eradicates the most radioresistant cells in the tumour population at the same time, which yields a great synergy with radiotherapy (see also [84]). Effects of hydroxyurea will depend on the relative cell cycle distribution, so that in a cell line with a relatively longer S-phase and thus an increased S-phase-fraction (SPF) of cells, the immediate

effects might be stronger.

While it is easy to remove a drug from an *in vitro* setting, it is almost impossible to achieve this in an *in vivo* setting. Thus, the amount to which a post-drug-treatment synchronisation will be seen is not clear. However, the synchronisation of cells in G1-phase through the suppression of G1/S-advancement can still be exploited in order to control the treatment outcome when using it in combination with irradiation treatment. Even if a very poor ability of cells to react to a drop in hydroxyurea concentration was assumed, or if hydroxyurea concentration decreases with local variations, a pronounced synchronisation and radiosensitivity enhancement could be observed.

To the knowledge of the author, there exists no study of the synchronising effects of hydroxycarbamide *in vivo*. While it seems technically possible to assess the degree of synchronisation in response to different doses of hydroxycarbamide over time by using small biopsies, this has unfortunately not been done. Considering the huge beneficial effect to be seen in the simulation, this investigation would seem to be very worthwhile.

Hydroxyurea effects can be improved by considering rates instead of fixed one-time probabilities. That is, as long as the drug is present, S-phase cells will be killed with a probability which is derived from the time-step and a (possibly concentration-dependent) rate of killing. The same reasoning would be applied at the G1/S-checkpoint, where cells are subject to a probability to shake off the drug's effects which is determined by a rate of escaping cells and the passed time  $dt$ . For this approach, more detailed information on the kinetics of hydroxyurea needs to be available, which is not the case, to the author's knowledge. With an extended model of hydroxyurea, other chemoradiotherapy scenarios could also be investigated.

Radiosensitisers and radioprotectors are a further class of drugs which are of interest for investigation within the model. If a localisation of both is possible e.g. via delivery or activation of radiosensitisers specifically in hypoxic regions, an increase in treatment efficiency would be possible.

As hypoxia has already been included and studied in the model, hypoxic cytotoxins are a further class of drugs which is suitable for modelling. Their ability to affect specifically hypoxic regions would yield a high synergy with radiation as a consequence of the oxygen enhancement effects which limit the effectiveness of radiotherapy in hypoxic regions.

### 4.1.6 Particle irradiation

Because therapy with linear accelerator-generated X-rays remains the *de facto* standard in treatment, investigations in the thesis have been focused on the modelling of X-ray effects, or a general radiation response. At the moment, only a vanishing minority of cancer patients will receive particle irradiation.

The parameters of apoptotic chance and mitotic mismatch roughly characterise the radiation quality and thus can be used to tune the model to reflect the effects of different radiation types (apart from the use of radiation-specific linear-quadratic survival parameters as discussed in section 2.5.6). While a high affinity for clustered lesions, as in high-LET radiation, would most likely lead to a high degree of fast apoptosis, low LET radiation will predominantly induce a G2/M block. If heavy-ion irradiation will accordingly induce a fast effect of cell death, this also implies that the oscillations in the perturbed cell population should be strong and the associated enhancement high.

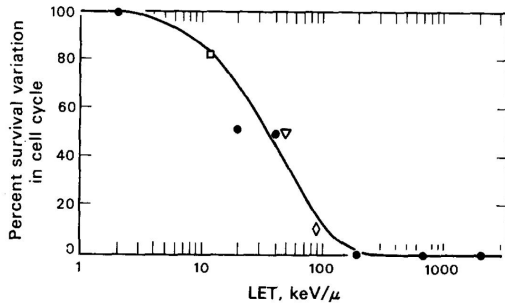


Figure 4.3: Variation of the cell-cycle dependent survival in V79 cells as a function of the radiation LET shows the decrease of cell cycle effects with increasing LET (survival variation calculated only between late S-phase and G1 phase, not M-phase). Adapted from [25]

The cell cycle dependence of radiosensitivity is considered to decrease linearly with an increase in LET of the applied radiation (see figure 4.3). This observation often leads to the assumption that cell cycle effects and oxygen enhancement are of lower significance in heavy ion irradiation.

However, within the entry channel particle irradiation will be in the so called plateau region, which is associated with a high radiation energy and a low LET. Carbon ions in the plateau region thus are radiobiologically comparable to X-rays [136]. This implies a high OER of about 3 and a very high cell cycle dependence [64]. Within the spread-out Bragg peak region, which is normally used for therapy, the average LET will be around 70 keV/μm, so a pronounced cell cycle effect and oxygen enhancement effects are to be expected (compare figure 2.30). Consequently, cell cycle effects, as well as oxygen enhancement, were concluded to be of great importance also in particle irradiation [25].

Side effects within the entry channel of radiation could be drastically reduced if cells can be selected to be in a radioresistant phase of the cycle. This protective approach for benign tissue can be further combined with enhancing approaches for the target region.

An increase of alternative modes of radiation death in cells, such as autophagy and premature senescence, is supposed to be in effect in HI irradiation [87]. These phenomena can be implemented in a straightforward manner in an open expandable agent-based model, as opposed to specialised models for radiation effects.

## 4.2 Critical model review and expansion

A range of critical points concerning the model needs to be discussed. In general, the model performed drastic simplifications of many involved mechanisms. This is a necessity of the inherent complexity of cancer as a multifaceted disease which involves a range of processes. In order to achieve a reduction of parameters, simplifications have to be performed.

Extreme simplifications will rather result in a very general model. Such a universal model can be used to scan the system under investigation for interesting effects which are of a general nature. One such example is the studied enhancement as a result of cell cycle dynamics, which can be observed virtually independently of all parameters. Effects which have been discovered and studied with a generic model can act as starting point for studies in more specifically tuned models, which must be employed in order to verify and further describe the effects. Ultimately, an experimental verification is required.

Large parts of the *in vivo* response of tumours to therapy were neglected within the model, such as immune effects, repair kinetics or bystander damage. While many of the neglected phenomena will not be present in the *in vitro* system of tumour spheroids, this neglect can

limit the transferability of results to *in vivo* cases.

### 4.2.1 Cell behaviour and interaction

Active cell motility was neglected in accordance with the modelling of tumour spheroids as structures which are governed by passive cell rearrangement. However, the model is suited to study cell motility in detail, especially in regards to tissue invasion and metastasis. As cell motility has also been discussed as being involved in growth saturation in tumour spheroids, the inclusion of active motility becomes even more relevant. Furthermore, the epithelial–mesenchymal transition, which is associated with a downregulation of cell interaction and increase in motility, is of importance for the metastatic potential, which could be integrated into the model [6].

An expansion of the cell-cell and cell-ECM interaction model could be of high interest in order to capture further effects of the cytoskeleton on the cellular radiosensitivity and yield a more realistic microenvironmental interaction [220]. Bystander effects in irradiation and necrosis could be directly implemented. Sprung et al. conclude in their analysis of cell reactions to irradiation: “the bystander effect has been shown to function through a number of mechanisms including via soluble factors, such as chemokines and cytokines, which can act over longer distances, or signalling via gap junctions, which occurs between adjacent cells” [212]. A Voronoi/Delaunay model is thus especially suited to also study the effects of bystander damage, as cell contact via gap junctions can be easily described. In combination with the implemented diffusion solver soluble factors for the mediation of bystander damage can also be investigated.

Cellular adhesion molecules (CAM) and gap junctions have been demonstrated to be of importance in radioresistance [164] and in targeted therapy [10]. Therefore, the implementation of a realistic model for the regulation of expression of according adhesion molecules would be necessary to refine the radiation response on a level of cell-cell contact.

In general, the use of critical thresholds for cell behaviour is questionable. A continuous, steady mechanism of growth retardation depending on nutrient concentration would be preferable to discrete thresholds as it could better reflect the nature of the biological system.

As quiescence was shown to be a central mechanism for the response of tumour spheroids to irradiation, a more realistic implementation of quiescence seems mandatory. This can include other pathways which can lead to quiescence, such as environmental stress in the form of low oxygen or nutrient concentrations. Especially hypoxia should be coupled to quiescence, as low oxygen levels should increase the probability of cells to become quiescent. Furthermore, a mechanism for stress-induced apoptosis in response to prolonged quiescence should be used. The latter mechanism is already implemented in the simulation environment and has been loosely fitted to yield a baseline level of apoptosis, which increases with distance from the tumour surface, as observed in [172]

Furthermore, hypoxia could lead to a vascularisation of the tumour which could induce alterations in the oxygenation. However, as reasoned earlier, a population of hypoxic cells will always be present in tumours as a result of the regulation of vessel growth.

### 4.2.2 Radiation model

The radiation model is a strong simplification of actual radiation-induced processes on a cellular level. Due to the immense complexity of the radiation response in cells, simplifications will be unavoidable. The use of the linear-quadratic model for cell survival with cell cycle dependent radiosensitivity parameters  $\alpha_p$  and  $\beta_p$  guarantees that the overall radiation killing in the model will eventually correspond to experimental measurements.

The damage model is problematic, as it can not capture the true behaviour of non-lethally damaged cells at the G2/M-checkpoint, since their delay has not been quantified experimentally and thus is, by default, neglected in the model. The underlying assumption is that the damage of surviving cells will be eliminated in fast repair, and thus is without effect in the delivery of a following fraction. However, the delay of non-lethally damaged cells will probably alter the radiation response of tumours, even if no qualitative change is to be expected. The according neglect of damage repair mechanisms seems justified, as in most fractionated schedules the doses were separated in time in order to allow for an almost complete repair of sublethal damage (according to its typical half-life [51]). However, damage kinetics can be of great interest within the radiation model. Especially for closely-timed trigger and follow-up doses, a significant change in survival could be the result of unrepaired damage. If repair rates can be derived from the literature, damage accumulation in healthy tissue during fractionated irradiation would be an interesting target of investigation. This could be achieved by using two populations of cells with an altered repair potential (which can further depend on nutrient availability or other spatial effects).

In general, the radiation model will either be a top-down model, which uses an overall measured survival rate, or a bottom-up model, which weights a range of physiological processes in order to yield a survival which corresponds to measured data (as shown in figure 2.38). Agent-based models are especially suited for the use of a bottom-up model, as a range of regulating processes can be realistically implemented directly on the single-cell level. However, a bottom-up approach will require drastically more parameters, such as measured rates for the single processes, and the resulting fitting process can be very involved.

An alternative to a bottom-up approach is to neglect the final fit of observed survival to experimental data in the model. While this sacrifices any possibility to quantitatively transfer results to the experimental system, it can offer the possibility to focus more directly on the qualitatively effects which mechanisms in the model will introduce.

As a further extension, the radiation model could distinguish between early and late S-phase cells instead of using an average S-phase radiosensitivity. This is easily possible using the pre-determined cell cycle length which is stored in each cellular agent in order to decide if cells are in early or late S phase. This would further increase the difference in radiosensitivity between S-phase and G2-phase, depending on the cell-age sensitivity.

Different cell-age sensitivity profiles should be included and studied for systematically altered effects. Hahnfeldt and Hlatky demonstrated that the functional form of the cell radiosensitivity across its cycle phases can drastically alter observed development in the overall radiosensitivity of a cell population [83].

It is not entirely clear if the measurable of enhancement can be related to the efficiency of a schedule. While simulations show a good correlation between the induced integrated enhancement and the performance of schedule, a low enhancement will also be a temporary characteristic of highly efficient schedules.

### 4.2.3 Cell metabolism

The cell metabolism should be refined in order to exhibit a variety of metabolic modes based on intracellular decisions and extracellular conditions. At the moment, only the metabolic switch which is associated with quiescence of cells (and which can be thus quantified in experiments) is implemented. A key problem in refinement is the limited availability of a quantitative metabolic investigation of single cells or small cell populations. If a lack of quantitative data further prohibits the implementation of a more realistic metabolic model, an educated guess in combination with the according investigation of the results it yields could be employed to expand the model.

In direct connection to a refinement of the cell metabolism is the acidification of tissue in association with the production of lactate. The radiobiological action of lactate has become a growing field of research as described in [191]. Lactate has also been reported to induce migration of cells and cell clusters and has a strong connection to immune escape [100]. These phenomena can add further realism to the redistribution of cells, guide active motility and alter the observed radiation response in the simulation. As a result, a direct inclusion of lactate effects is of high interest for further investigations. An implementation can be performed in a straightforward manner by expansion of the existing metabolism model.

### 4.2.4 Diffusion and drugs

The effects of chemotherapeutica have been extremely simplified for the initial investigation of effects. While the high-dose approximation as discussed in section 2.6.3 seems applicable in the investigated case, for a more realistic approach the inclusion of a dedicated pharmacokinetics/pharmacodynamics model is mandatory. However, this depends on the availability of appropriate parameters, which would also include rates for the reaction of cells to hydroxyurea.

Effects of hydroxyurea were demonstrated to be largely independent of the actual time that is needed for a decrease of concentration, so that for typical *in vivo* half-life of hydroxyurea a significant effect can still be observed. This might not be the case for drugs which induce more differentiated effects or which have a significantly higher half-life *in vivo*.

The applied steady state approximation of diffusion could be limited during reoxygenation dynamics. However, the performance of the diffusion solver would allow for an explicit solution of the problem in cases where the approximation could lead to invalid results. Variable diffusion coefficients based on the tissue density might not be the correct approach for the description of porous, partially dissolving tumour tissue. It should be investigated if anomalous diffusion or other methods could be more suitable mechanisms which should be accordingly used for the simulation of diffusion [2].

### 4.2.5 Voronoi

A future expansion of Delaunay-Voronoi models is the use of graphical processing units for computation. The computational power which is available for highly specific tasks, such as the maintenance of triangulations, within GPUs is extremely high, in fact, orders of magnitude higher than in normal CPUs. While a development of a Delaunay object dynamics code on a GPU language is beyond the scope of this thesis, it seems that this is a worthwhile task. Similarly, the possibility for fast inversion of tri-diagonal diffusion matrices on GPUs should be

checked. If these significant processes can be efficiently executed on GPU hardware, this could yield a drastic performance increase. Eventually, this could allow for the single-cell based simulation of tumours of clinical size. While it is not clear if this amount of precision is needed in clinical simulations, an improvement in performance could also mean that simulations can be performed fast enough in order to allow real-time optimisations during treatments.

The Voronoi/Delaunay model could benefit from an expansion to the use of piecewise spherical contact surfaces. This can be achieved by using a quotient method instead of a difference method for the calculation of the weight in the generalized Voronoi tessellation as described in [26]. Figure 4.4 provides an overview of the construction method and the corresponding results in comparison to a staining of keratinocytes in monolayer culture from [141]. It is expected that a switch to the quotient method within this simulation would only yield minor changes. If a more complex tissue interaction model is to be used in future investigations, an optional upgrade to include the quotient method seems advisable.

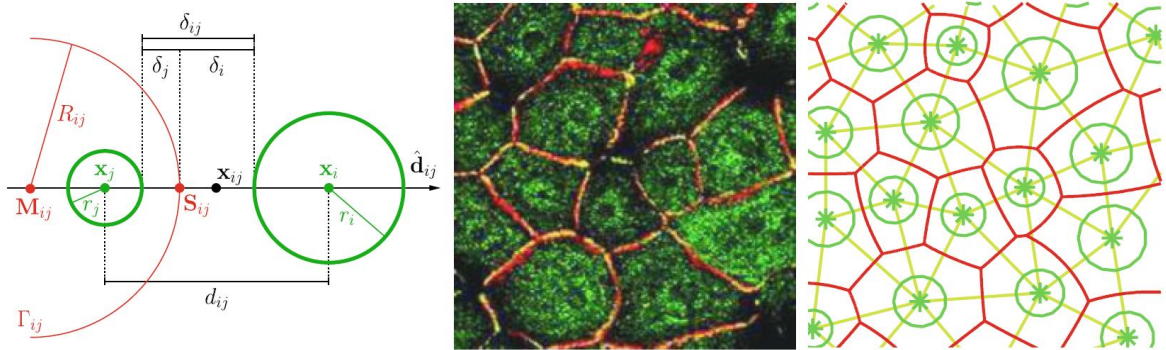


Figure 4.4: Illustration of the generation of Voronoi contact surfaces using the quotient method instead of the difference method. Some contact faces of cells in vitro show a piecewise spherical geometry which can be reproduced using this model. From [26].

#### 4.2.6 Model type and mechanisms

For some parts, a simplified, stochastic population-based model (without advanced spatial representation or diffusion solution) might be of interest to model the irradiation response, especially when comparing to monolayer cultures, in which no gradients arise. Such a simplified model could still be used in order to estimate the redistribution and cell cycle dynamics in response to irradiation in monolayer cultures.

Coarse graining approach would be needed to expand the model to a larger scale, e.g. as described in [62]. Experimental mechanisms for the runtime-reduction were tested, including movement or growth-thresholds, a freezing of quiescent cells or cells in the core region. As quiescent cells will make up a large fraction of plateau-phase tumours, a coarse graining approach that targets them might be able to achieve a significant runtime improvement. However, the reactivation of quiescent cells is of vital importance for many treatment approaches, so that any optimisation would be lost, as soon as quiescent cells are reactivated.

An interesting approach in this context is a hybrid microscopic-macroscopic model as, for example, discussed in [57]. In this case, only selected regions, such as the proliferating, viable boundary of a tumour node, will be simulated with an agent-based model, while other

regions (such as the necrotic core) will be replaced e.g. by a viscoelastic continuum model. The challenge within hybrid approaches, of course, is the correct linking of both approaches.

Surprisingly, few quantitative data is available on the reaction of tumour spheroids to irradiation. Most research on spheroids is of a basic nature, which proves to be insightful but neglects the potential of spheroids to be also used as an excellent model system for more complex scheduling-reaction. It has been argued that tumour spheroids are a realistic model of *in vivo* tumour growth and furthermore that they can also be used to realistically predict the treatment response in multifractionated irradiation regimens [68] [200].

Without dedicated experiments which provide experimental data of specific cells, the limited availability of cell data and explicit measurements within the literature complicates the fitting procedure. An open database for cell parameters which are of interest for modelling could significantly improve the visibility and availability of data within the modelling community. Furthermore, an increase in communication between modellers and experimentalists could be achieved via the interface of a database.

### 4.3 Further investigations

#### 4.3.1 Tumour control

A senescent cell will be clonogenically dead to the tumour, but still consumes nutrients and is part of the microenvironment. If terminal differentiation of cells and senescence can be enforced, this would convey a range of beneficial developments in the tumour, which could be first studied in a model system. An approach in which a majority of the tumour is not killed, but instead hamstrunged, would not allow a rapid repopulation of the tumour and avoid selection of resistant phenotypes.

A similar reasoning is the use of insights from ecology and pest control in cancer treatment. Instead of trying to eradicate a tumour at possible high cost for the patient, it might be beneficial to just keep cancer in check, allowing some degree of regrowth in order to avoid a phenotypic switch of cancer cells to a more resistant and aggressive type. A review about this reasoning can be found in [78, 77]. Overall, the search for a magic bullet to target cancer might be futile, while an ecologic approach could possibly benefit a large number of patients [79]. Such a control scenario is very suited for modelling with agent-based techniques.

Evolutionary dynamics in cancers can be taken into account by modelling them as a collection of diverse, mutable subpopulations which can react and adapt to external selection factors. Depending on the treatment combination, a model could predict suitable combinations in order to avoid a development of especially aggressive, invasive and resistant cells to take over as a result of treatment. All cancer therapy approaches which focus on evolutionary dynamics are of special interest for treatment with spatially resolved agent-based models. Not only can mutations on a single-cell level be implemented in a straightforward manner in these models, but also their ability to feature spatial heterogeneities in selective pressure (hypoxic areas, local acidosis, drug distribution) is unparalleled.

#### 4.3.2 Effects of the immune system

The reaction of the immune system would introduce a further level of complexity to the radiation response. This could be achieved via the explicit inclusion of immune agents (e.g.

macrophages or cytotoxic lymphocytes) into the simulation. The feasibility of modelling fast-moving immune cells with the present model framework has been demonstrated in [22]. Especially in regards to the immunogenicity of different cell death modes (apoptosis vs. necrosis), it can be of high interest to predict which schedule will trigger or suppress a beneficial immune response. The possibility to enforce an immunogenic death in tumours could have far-reaching consequences on the treatment outcome and especially the probability of relapses [139].

The study of immune reactions is especially problematic in experiments, as common *in vitro* systems cannot be used, or are at least likely to produce a reliable result. As a large fraction of *in vivo* xenograft tumour studies is performed using severely immunocompromised or immunodeficient mice (e.g. SCID or NOG), the reaction of the immune system can not be studied in these animal models. Simulations of the effects might provide a way to improve knowledge of the immune effects in cancer.

### 4.3.3 Influence of the circadian rhythm

The natural circadian rhythm influences the metabolism and the synchronised progression of cells through the cycle phases [133]. This regulation is of interest for cancer treatment, as the high dependency of therapeutic approaches on the cell cycle phase has been demonstrated.

If the synchronisation is present in healthy tissue but not in a deregulated malignant tissue, it could be used to deliver irradiation at points in time when a majority of cells in the healthy tissue is in insensitive cycle phases. Thus healthy tissue can be spared, while malignant tissue is targeted. If the synchronisation is still present in the tumour tissue and in the healthy tissue, radiation should, if it is possible to deposit it precisely, be targeted at the sensitive phases, as this will increase the efficiency of treatment. Since it is shown that therapy will redistribute or even resynchronise the cells in the malignant tissue, a combination of artificial synchronisation and circadian synchronisation can be used. Thus, healthy tissue will be in a insensitive cycle phase, while the malignant tissue is triggered into a sensitive state.

### 4.3.4 Cancer stem cells and selection

The cancer stem cell hypothesis has developed within recent years from a hypothesis to a well-documented fact [89]. As phenotypically different cell populations exist in tumours, some of them can be identified as having the attributes commonly associated with cancer stem cells [6]. These will include limitless replicative potential (which is within the cancer stem cell hypothesis not associated with normal tumour cells) and a high resistance to treatments, which makes cancer stem cells a prime target in cancer therapy [60].

While no definite universal marker for “stemness” has been agreed upon yet, a key step in the cancerogenesis might be the transition from a regular stem cell or stem-like cell, which already possesses some attributes of cancer cells (like a limitless replicative potential) into a CSC by the acquisition of key mutations which convey the undesired properties of cancer. Mutation and phenotypical selection of populations inside the tumour need to be modelled in an agent-based approach, since they are highly individual events. The change in growth characteristics, under the assumption that a population of CSCs is present in a tumour, can be predicted using agent-based models.

A question of interest in regards to stem cells is which treatment schedules select CSCs or other resistant subpopulations due to their typically higher resistance. Efficient combination of different therapeutic approaches might limit the positive selection of unwanted cells.

### 4.3.5 High single-dose delivery

The use of multiple entry channels and other technical improvements have made it possible to deliver doses of up to 20 Gy X-rays without severe side effects [184]. Very high single doses have been used extracranially, e.g. in the treatment of metastatic lung cancer [116] or liver metastases [196]. The application of high doses in stereotactic radiosurgery is becoming a standard tool in clinics, which can replace operative treatment in a number of cases [51].

For typical doses in stereotactic body radiotherapy (SBRT) within the range of 6 Gy to 20 Gy, a very high radiosensitivity enhancement as a result of cell cycle synchronisation has been confirmed in this work (within the range of 6 Gy to 10 Gy). As only a single fraction is delivered, this opens up the possibility to precede the high dose with a trigger dose of 2 Gy in order to induce a cell cycle synchronisation in the target volume prior to delivery of the main dose. Alternatively, an initial measuring dose could be applied in order to trigger a response, whose exact time scale can be accordingly determined, in order to apply the later combination of trigger- and effector dose with perfect timing. It seems mandatory to employ the cell cycle effects in this setting as cell survival will vary up to an order of magnitude in response to synchronisation and timing and the use of a single dose opens up the possibility to exactly predict the enhancement response of the tumour.

# Appendix

## 4.4 Summary of the model and growth of sample spheroids

As described in detail in section 2, a model for the description of multicellular tumour growth and the according treatment reactions has been developed. The simulation was implemented in C++ in order to allow for easy portability to different computational environments and simple expansion. Code for a dynamic and kinetic Delaunay triangulation was employed as described in [23].

Within the simulation system cell cycle progression and dynamics, nutrient diffusion and uptake, cell-cell interaction and radiation or drug effects are coupled to represent the complex environment of a multicellular tumour spheroid.

The system is subject to updates with a dynamic timestep width which will advance each agents cell cycle according to regulation, handle nutrient consumption and results of local concentration changes, perform cell-cell interaction and associated movement and necessary updates of the Delaunay triangulation amongst other functions. The global timestep is determined in an adaptive stepsize approach in order to result in a maximum cell displacement of  $0.5\ \mu\text{m}$  which is well below the cell radius. Fast cells are pre-treated with an adiabatic approach for their movement as described in [114].

Handling of cell cytokinesis is implemented as shown in figure 4.6 and described in [114].

For the growth of sample spheroids, physiological concentrations of glucose and oxygen as found in typical capillary blood are assumed as described in section 2.2.4. A cubic diffusion system of 1.4mm edge length with 71 nodes per dimension is used with according Dirichlet boundary conditions on all faces. A CNS-type solver is employed where the solution is calculated using the biconjugate gradient method [169]. A quasi steady-state approximation of the diffusion solution results in recalculation of a steady state within typical intervals of

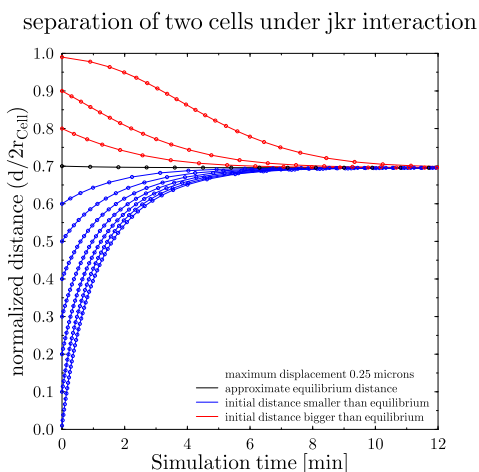


Figure 4.5: Simulation of two cells with different initial distances separating due to JKR interaction. Cells move into the JKR equilibrium distance, where the resulting force between them is zero. Note the markers which show the global adaptive timestep algorithm at work, limiting the displacement to  $dx_{\text{max}} = 0.25\ \mu\text{m}$  per timestep. Therefore in regions with higher slope the marker density is increased on the same curve corresponding to a smaller timestep.

## 4 Discussion

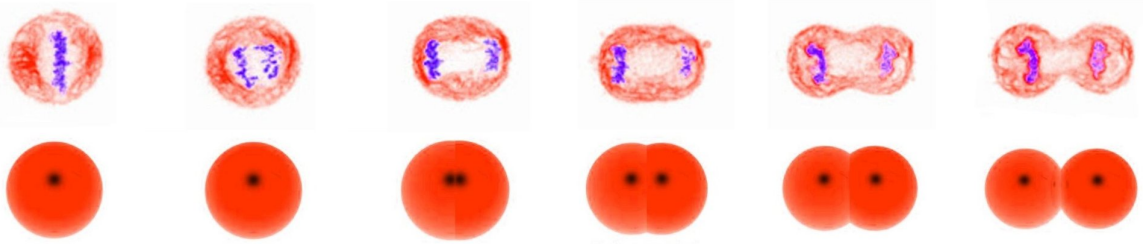


Figure 4.6: Comparison of cytokinesis of cells during mitosis within the model (bottom row) and *in vitro* (top row). Cytokinesis handling is described in detail in [114].

10 minutes. Cell consumption and local density-dependent diffusion coefficients are updated before each steady-state solution.

For a sample run, as used for the investigation of the radiation reaction, a small number of usually 10 tumour cells is seeded at the centre of the system and starts proliferation. After 14 days of growth a tumour spheroid with a diameter of about 700  $\mu\text{m}$  has developed which shows a steady cycle distribution and all histologically relevant areas (viable rim, quiescent population, necrotic core). Spheroids will contain about 100000 cells at day 14. Computation up to day 14 will take about 5 hours runtime on a single Intel i7 CPU M 620 @ 2670MHz.

### 4.5 Runtime of simulations

Most simulations were performed on a single core of a computing server equipped with two AMD Opteron processors 2218 HE @ 2600MHz. Alternatively simulations were run on an Intel Core i7 CPU M 620 @ 2670MHz. An according plot of the simulation runtime for the Opteron processor can be seen in figure 4.7. The plot shows the runtime needed to advance the in-simulation time for 100 minutes over the simulated time in days. An accurate runtime is obtained using the `MPI:Wtime()` function of the MPI runtime environment for parallel execution. The added runtime closely matches the accurate runtime, but is only composed of measurements within the function-calls that are shown in the plot. Difference between according MPI runtime and added runtime is due to other processes which were not measured directly.

It is obvious that the parts of the simulation which directly depend on the number of cells (e.g. calculating a cell velocity from interaction or updating the triangulation) have an execution time which is drastically growing with increasing tumour cell count in the beginning. Once the growth of the tumour is slowing down, this will have an according effect on the runtime. The increase in runtime for the triangulation update is however below exponential, as expected from the scaling of the triangulation update time.

The update of the diffusion system in the background is almost constant in terms of runtime as the only contribution which varies with time is the addition or removal of sinks at cell positions. Depending on the type of solver employed, the diffusion runtime will also scale with the tumour size. However the major determining factor for the diffusion is simply the chosen resolution of the diffusion grid.

Since the triangulator in use is ready for parallel execution with an almost optimal scaling (as shown in [23]), it becomes possible to parallelise the whole simulation environment for

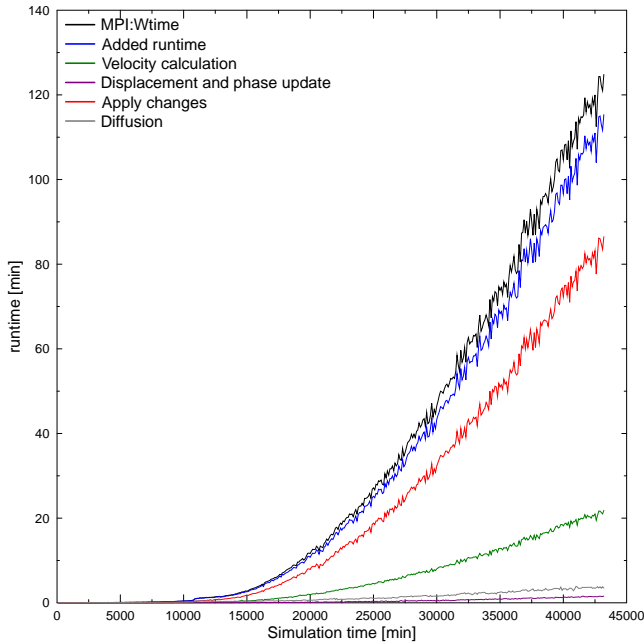


Figure 4.7: Sample runtime of a simulation run. Runtime needed per 100 minute step is plotted over the simulated time in days. As expected, the growth-dependent parts such as update of the triangulation or calculation of interaction grow exponentially in runtime. However the total runtime is still well manageable on a single CPU.

execution in a distributed computing environment. So far only tests for this parallelisation were run because the simulation runtime was still easily manageable on a single CPU. However for future applications such as simulation of macroscopic tumour volumes, it seems reasonable to run the simulation in a parallelised version which would reduce the total runtime by a constant factor.

## 4.6 Parameters

Parameters for the simulation have been compiled or derived from a range of publications as cited in the according sections of the model description. A selection of important sources is [81], [130], [71], [40], [41], [180], [97], [140], [11], [241], [127], [82], [47], [104], and [76].

A similar compilation of parameters for agent-based growth of EMT6 spheroids can be found in [194], [193], and [113]. A set of parameters for the cycle durations for EMT6 cells can also be found in [104] (unfortunately, Zacharaki et al. do not cite their source).

The simulation does not critically depend on any parameter in use. Furthermore, a high natural variability of parameters which are associated with cells can be assumed, due to the nature of the biological system and due to measuring accuracy. A wide variation of parameters has been observed in cell lines, even among subcultures of the same cell line (see also section 2.1.1).

A listing of model parameters as they have been used to simulate the irradiation response is provided in tables 4.1 for cell parameters, 4.2 for diffusion parameters, and 4.3 for radiation and miscellaneous parameters.

For a range of publications which can be used as parameter source for radiation mechanisms see also table 2.8.

Cycle phase specific single cell survival measured for V79 cells for irradiation with 250 kV X-rays at a dose rate of 1.1 Gy/min in [206] and [204] is used within the simulations as discussed in section 2.5.6. Survival is weighted with EMT6 cell cycle times to obtain an expected average Survival  $S_{\text{exp}}$  for the active cycle phases. An active, exponentially growing

Parameter	Value
G1 phase length	480 min
S phase length	360 min
G2 phase length	270 min
M phase length	60 min
Apoptosis duration	700 min
Necrosis duration	1440 min
Rel. width of phase length normal $\sigma$	0.3
Rel. cutoff for phase length	0.6
Necrosis dependence	Glucose
Critical glucose level	0 mM
Quiescence induction	Pressure
Critical pressure	200 Pa
Hypoxia threshold	0.0135 mM
Active glucose consumption	180amol cell <sup>-1</sup> s <sup>-1</sup>
Quiescent glucose consumption	130amol cell <sup>-1</sup> s <sup>-1</sup>
Active oxygen consumption	83amol cell <sup>-1</sup> s <sup>-1</sup>
Quiescent oxygen consumption	49amol cell <sup>-1</sup> s <sup>-1</sup>
Initial cell radius (start G1)	7.94 $\mu\text{m}$
Division cell radius (end G2)	10 $\mu\text{m}$
ECM viscosity (dampening)	0.005kg $\mu\text{m}^{-1}$ s <sup>-1</sup>
Poisson number	0.5
Elastic modulus	1 nN/ $\mu\text{m}^2$
Surface energy	0.1 nN/ $\mu\text{m}$

Table 4.1: Listing of typical cell parameters. Details and sources in table 2.1, table 2.2, [70][69][121][175][91].

tumour without a quiescent population will show this average sensitivity which can be used for normalisation of enhancement effects. Quiescent cells will usually show an increased radioresistance [142], which can be included by scaling their effectively received dose with a reducing factor. A sample of survival data is provided in table 4.4.

Parameter	Value
Diffusion nodes per dimension	71
System size	1400 $\mu\text{m}$
Glucose boundary conc.	5 mM
Oxygen boundary conc.	0.13 mM
Update intervall	10 min
Glucose diffusion coefficient water	690 $\mu\text{m}^2/\text{s}$ [219]
Glucose diffusion coefficient tissue	105 $\mu\text{m}^2/\text{s}$ [40]
Oxygen diffusion coefficient water	3300 $\mu\text{m}^2/\text{s}$ [81]
Oxygen diffusion coefficient tissue	1750 $\mu\text{m}^2/\text{s}$ [81]

Table 4.2: Listing of diffusion parameters. Details and sources in section 2.2.4, table 2.5.

Parameter	Range
Apoptotic death chance AC	0.66
Mitotic mismatch prob. MM	0.3
Quiescence resistance factor QRF	1.5
Number of seeder cells	10
Default time step	5 min
Typ. adaptive time step	1.5 min

Table 4.3: Listing of radiation and miscellaneous parameters. Details and sources in section 2.5.6, [142].

Dose [Gy]	$S(G_0)$	$S(G_1)$	$S(S)$	$S(G_2)$	$S(M)$	$S_{\text{exp}} (G1-M)$
0.25	0.91393	0.91393	0.96932	0.81996	0.81996	0.90447
0.5	0.83110	0.83110	0.93601	0.67233	0.67233	0.81860
1	0.67705	0.67705	0.86286	0.45203	0.45203	0.67076
2	0.42316	0.42316	0.70047	0.20433	0.20433	0.44676
3	0.24414	0.24414	0.53499	0.09236	0.09236	0.29082
4	0.13002	0.13002	0.38442	0.04175	0.04175	0.18340
5	0.06392	0.06392	0.25988	0.01887	0.01887	0.11151
6	0.02901	0.02901	0.16529	0.00853	0.00853	0.06517
7	0.01215	0.01215	0.09891	0.00385	0.00385	0.03650
8	0.00470	0.00470	0.05568	0.00174	0.00174	0.01955
9	0.00167	0.00167	0.02949	0.00078	0.00078	0.00998
10	0.00055	0.00055	0.01469	0.00035	0.00035	0.00485

Table 4.4: Cycle phase specific single cell survival measured for V79 cells in [206] and [204].

## 4.7 Integrity tests of the diffusion solvers

It is of vital importance to test any numerical solver for its stability and accuracy. In order to test any implementation, sanity checks such as conservation of substances under no-flux conditions should be applied.

Furthermore an elegant solution is the comparison of a numerical solution to an analytic solution, which allows to check the accumulation and propagation of errors. A possible approach is also the initialisation of the solver using an invariant solution (such as a composition of sine-waves). If the solver is sane and implemented correctly, the solution should be stable.

### 4.7.1 Conservation of substances

As a basic test the conservation of substances should be monitored when using no-flux boundary conditions. The initial total of substance in the system is calculated and then tracked over time. If the substance was distributed unequally in the beginning, an equilibration should be observed, however the total amount of the substance should not change.

An example of this test is shown in figure 4.8, where a non-zero concentration was initially set in a single point. Subsequent evolution of the system will eventually lead to the equal distribution of the concentration throughout the total system.

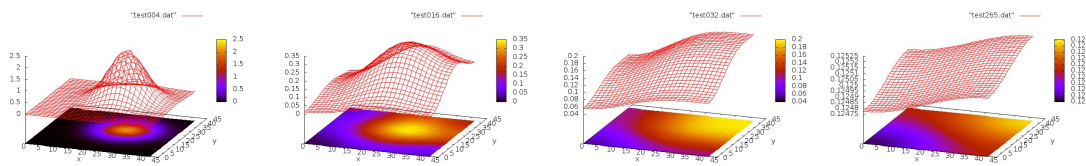


Figure 4.8: Evolution of the concentration for a point concentration and no-flux boundary conditions can be used to test conservation. Note that a uniform distribution will not be reached in finite time due to numerical accuracy, but the numerical solution can get arbitrary close to the analytical.

The integral concentration in the total system should not change. This test is even reasonable for non von-Neumann boundary conditions if the evolution time is short enough to prevent interaction with the boundary.

If all rates in the system  $Q(\mathbf{x}, t)$  are well defined, the total amount of substance in the system at all times analytically using

$$C(t) = C(0) + \int_0^t \left[ \int_V Q(\mathbf{x}, t') d^3\mathbf{x} \right] dt', \quad (4.1)$$

which becomes trivial for a single point-source and thus is a good test for the conservation within the numerical solver.

### 4.7.2 Stability of sinusoidal solutions

When calculating an initial solution for the Laplace equation

$$\Delta\phi = f \quad (4.2)$$

a sinusoid test function can be used to distribute a concentration which should be stable for Dirichlet boundary conditions. This test relies on the eigenfunctions of the Laplacian operator to obtain a stable solution:

$$\phi = \sin\left(\frac{2\pi x}{n_x}\right)\sin\left(\frac{2\pi y}{n_y}\right)\sin\left(\frac{2\pi z}{n_z}\right) \quad (4.3)$$

$$f = -4\pi^2\left(\frac{1}{(n_x)^2} + \frac{1}{(n_y)^2} + \frac{1}{(n_z)^2}\right)\sin\left(\frac{2\pi x}{n_x}\right)\sin\left(\frac{2\pi y}{n_y}\right)\sin\left(\frac{2\pi z}{n_z}\right) \quad (4.4)$$

The results of this test are visualised in figure 4.9 and illustrate the required stability.

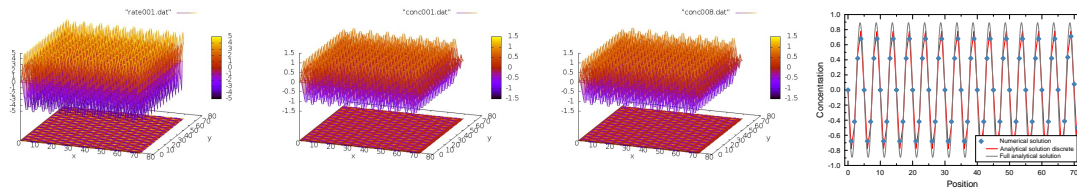


Figure 4.9: Stability of a sinusoid concentration according to equation 4.4 for  $n_x = 10$ ,  $n_y = 5$ ,  $n_z = 10$ .

## 4.8 Further applications of the simulation framework

The model which was developed within this thesis was also in parts or wholly employed in the investigation of multiple experiments apart from tumour growth or treatment reactions. A sample of further applications is provided in this chapter.

### 4.8.1 Dynamics of T-cells in a fibroblastic reticular network

A combination of a Delaunay network with an agent-based approach was used to investigate the possible mechanisms for T-cell movement inside the stromal network provided by fibroblastic reticular cells in lymphoid tissue [151]. Cells in the model moved either attached to the fibres (represented by network edges) or freely in space.

Different movement mechanisms were implemented for a cell in order to decide which edge to follow when confronted with choices at network intersections.

Basis for movement was an isotropic random choice between all possible fibres which were connected to a node of the stromal network. Other movement influences were chemokine-oriented movement towards a source and a preference for frontal movement imposed by the restructuring of the microtubule organisation center (MTOC inertia). The according

## 4 Discussion

movement mechanisms were weighted with factors  $\alpha$  for random movement,  $\beta$  for chemokine-directed movement and  $\gamma$  for MTOC-related inertia of the cell. Free movement of cells included also the development of a model for collisions with FRC fibres and the associated probabilities to detach from or attach to a fibre during movement. The investigation included furthermore an analysis of the properties of the underlying Delaunay network in order to assess the influence of the distribution of possible turning angles, which is an intrinsic property of the network, on the movement of the cell. The efficiency of the T cell to scan the network for a dendritic cell was measured by comparison to optimal pathes on the network between two random points [156].

Investigations included the question how a T cell will move under the influence of the different available mechanisms in order to produce a turning angle distribution and a mean square displacement which corresponded to experimental measurements [150]. A further question involved the degree of success that a T cell can achieve in locating and scanning dendritic cells on the same network in dependence of the used movement mechanisms.

As shown in figure 4.10(b) a mixture of frontal and chemotactic orientation for the movement decisions of the cell on the Delaunay network could reproduce the experimentally measured turning angle distribution and yield a high probability to find a dendritic cell on the network.

Further important information on the system that was modelled can be found in references [15], [8], [16], [151].

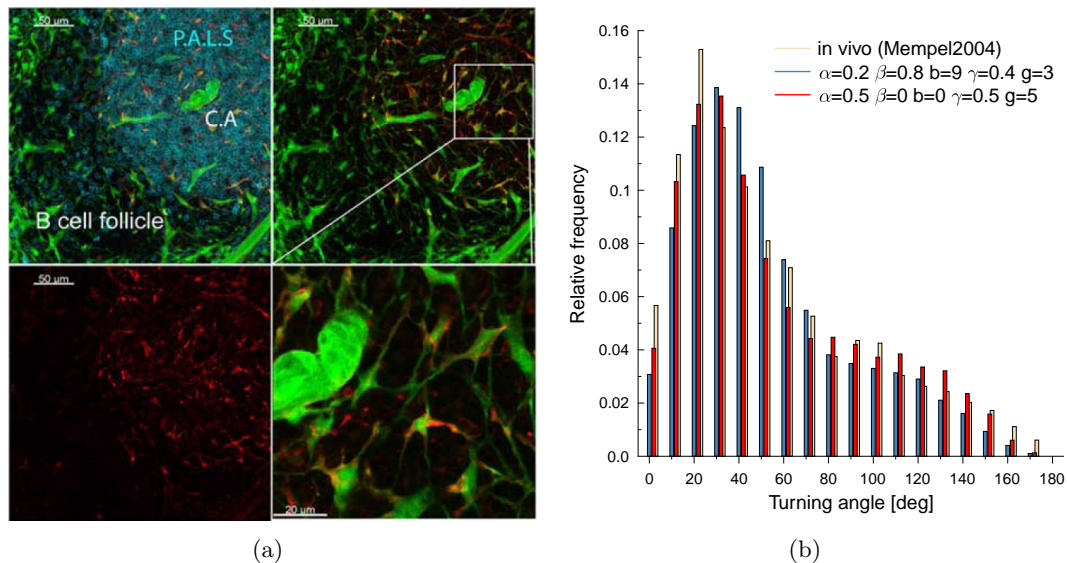


Figure 4.10: **(a)** Snapshot of the FRC-network reveals the Delaunay-like structure of fibres between reticular cells. T cells migrate preferentially attached to these fibres while scanning the space for dendritic cells. **(b)** A mixture random, chemotactic and MTOC movement can reproduce the experimental turning angle distribution as well as yield a high chance to successfully establish a contact with a dendritic cell.

### 4.8.2 Interpretation of $2\gamma$ -tracking data

[16], In correlation to the investigation of T cell movement in the FRC network, an analysis

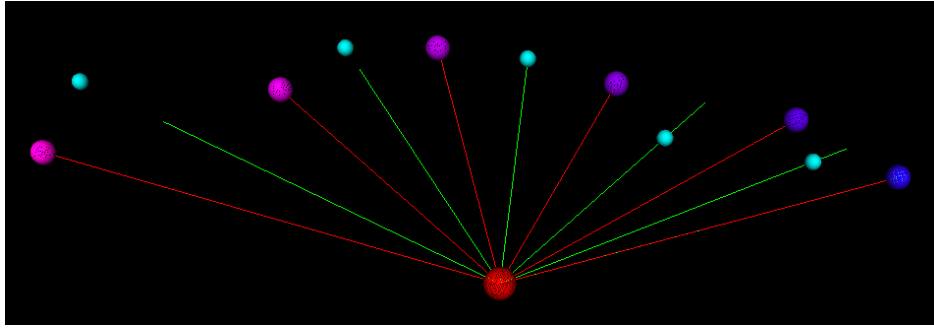


Figure 4.11: Averages between cell positions over time. Red sphere: source point, blue to purple spheres: next tracking positions, green lines: average between two tracking positions, turquoise spheres: closest point of projection of next position onto average line.

of the possible interpretation of cell movement data obtained by  $2\gamma$ -imaging was performed.

Within the method, linear segments in a dataset from optical cell tracking should be identified. Assuming, that the cells move attached to a network of linear fibres, they will be localised on straight path segments with a random jitter due to the finite cell and fibre size. Naive interpretation of each datapoint in a tracking set as a turning will yield a large amount of small “turning” angles. However, these apparent turns are in many cases an artefact of the measurement. Observed angles depend strongly on the time-interval of measurement and are not correlated to the real turning decisions of the cell at fibre crossings within the case of T cell movement in the FRC network.

If the time interval between measurements is significantly smaller than the movement time of a cell on a single fibre segment, it is possible to identify the real turning angles of the cell, and the topology of the underlying network, by identification of linear movement segments and subsequent calculating of turning angles in between these segments. In order to identify these segments, a dataset of points in space was used, which was classified by commercial tracking software as resulting from the movement of one single cell.

One approach involved an incremental algorithm, that processed points in a regression until two consecutive points exhibited a deviation from the regression which was above a tolerance threshold. At this point the connection line between the start point of the algorithm and the end point was identified as a real linear segment of cell movement. The algorithm then continued to identify linear segments, using the last point of the previous segment as start-point. Finally the turning angles between all identified linear segments could be calculated and analysed.

If cells require a significant amount of time due to the restructuring of their MTOC at turning points, this results in an increased density of cell tracks in the vicinity of true turning points. Identification of high-density regions can thus yield the nodes in an underlying FRC network.

Based on this principle an algorithm was designed which can identify true turning points in a dataset of cell movement data as illustrated in figure 4.12.

### 4.8.3 Development of space-filling mosaics in the avian retina

The different types of cones which are present in the bird retina each form an independent sub-mosaic which is close to a perfect Voronoi tessellation of hexagons [122]. Although being

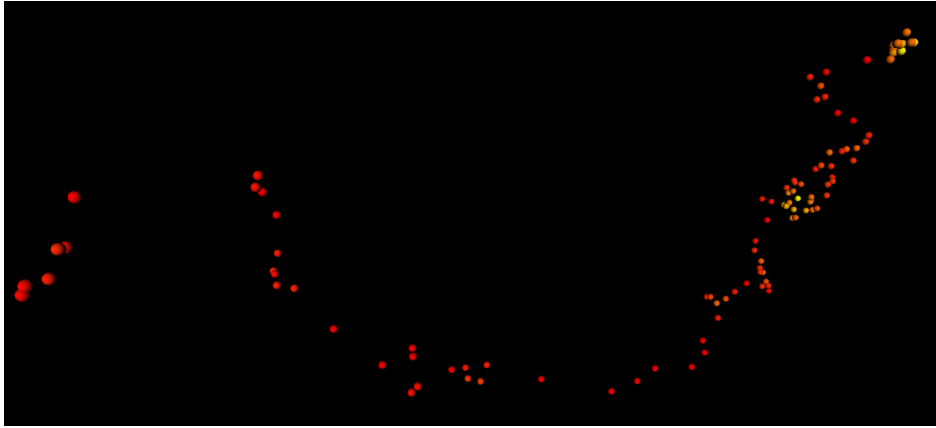


Figure 4.12: Principal function of the density threshold algorithm which can identify true turning points in  $2\gamma$ -tracking data of cell movement.

close to an optimal tiling, these mosaics are still disturbed in a sense that they are not completely perfect. The mechanisms which lead to this efficient tiling of the retina during organogenesis are however not known.

The bird retina consists of 5 different cone types known as double, red, green, blue and violet cones. The four colour cones mediate tetrachromatic vision while the double cones are used in motion detection. At the same time rods are present in the retina in order to mediate grey-scale vision under low light conditions.

An agent-based simulation approach was employed in order to investigate possible interaction mechanisms for the system of cone types, which would lead to the *in vivo* tiling of the retina. Fundamental properties of the Voronoi tessellation were used as observables to compare results to experimental measurements. Different scenarios in regard to interaction mechanisms, cone differentiation and timescale were investigated. For the most likely interaction, system simulated knock outs of key chemokines were used in order to study possible disorders of the retinal development.

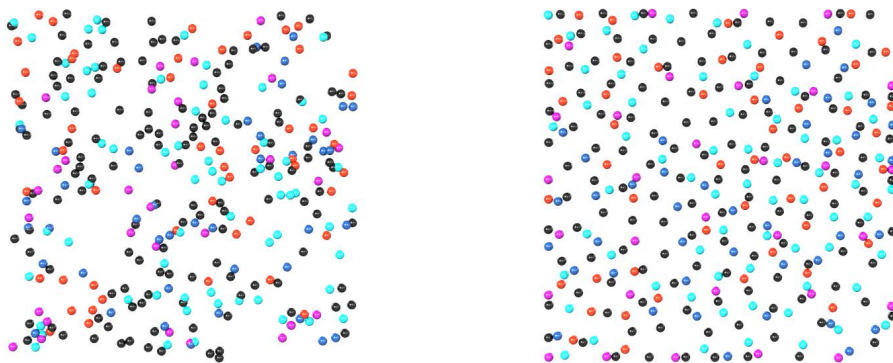


Figure 4.13: A small segment of retina with a random distribution of different cones can develop a regular pattern as a consequence of the underlying interaction mechanisms.

to dynamic heterogeneities found in particulate systems as they become more crowded

and approach a glass transition. In addition we find a diminishing self-diffusivity of short-wavelength motions within the cell layer, and growing peaks in the vibrational density of states associated with cooperative cell-shape fluctuations. Both of these observations are also intriguingly reminiscent of a glass transition. Thus, these results provide a broad and suggestive analogy between cell motion within a confluent layer and the dynamics of super-cooled colloidal and molecular fluids approaching a glass transition.

#### 4.8.4 Motility and invasion of glioblastoma cells

Peterziel, Harter and Mittelbronn compared the invasive potential of LN308 cells with and without knock-down of PDPN in mouse orthotopic brain slices [92, 167]. A small tumour spheroid comprised of 400 cells, half of them with knock-down of the mucin-like glycoprotein podoplanin (PDPN) half of the WT, was implanted in 300  $\mu\text{m}$  brain slices. The invasive growth was analysed after 0, 24 and 72 hours using confocal laser microscopy (see figure 4.14). A main result was that reduced PDPN expression will lead to lower migration and proliferation, while overexpression will increase both, which is in striking agreement with popular “go or grow” models for tumour invasion [94].

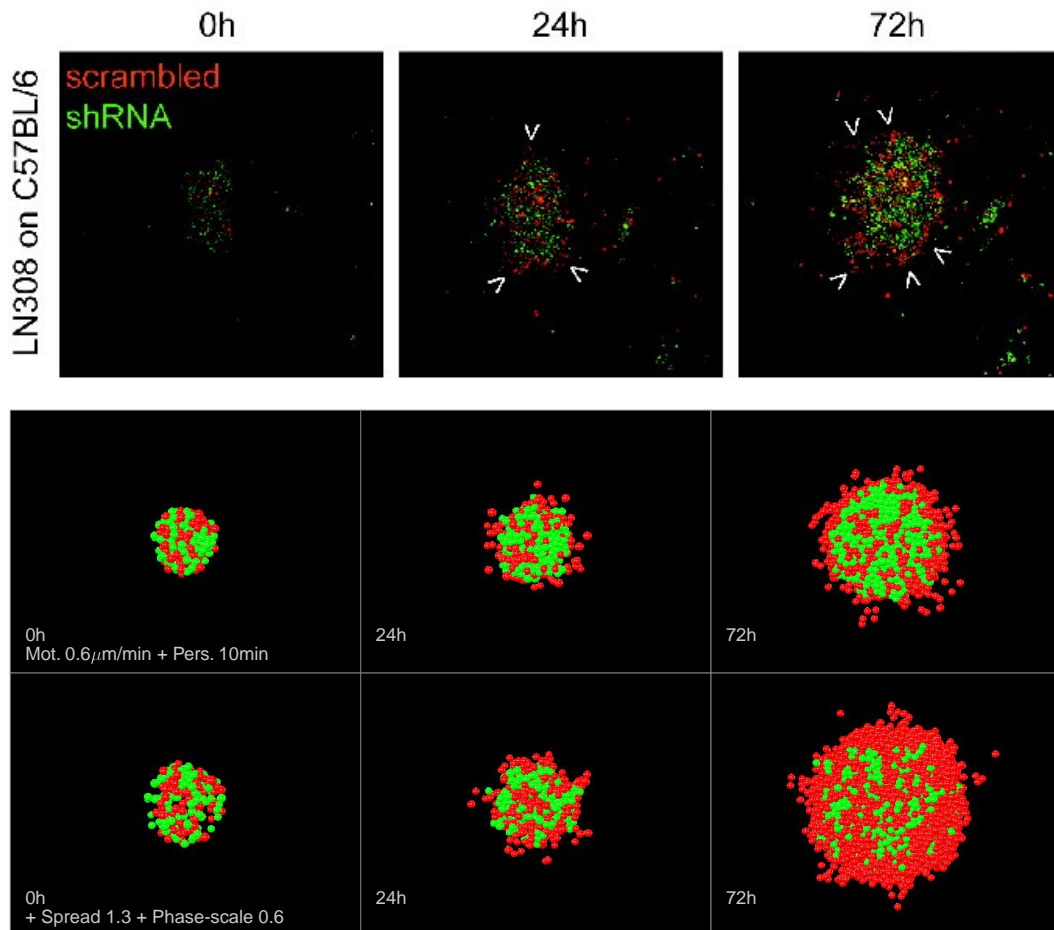


Figure 4.14: Invasive growth of LN308 cells with and without knock-down of PDPN in mouse orthotopic brain slices (from [167]). Bottom rows show comparison in agent-based simulation.

Using a cell-based model, this behaviour was investigated, assuming possible differences

between the PDPN-overexpressing cell type and the PNP-WT cells. Variation in parameters included a decreased overall phase length, a higher velocity during random migration, an increased persistence time for migration and preferential migration into sparsely populated areas. Figure 4.14 provides a sample of glioma invasion under different sets of parameters using the agent-based model of this thesis.

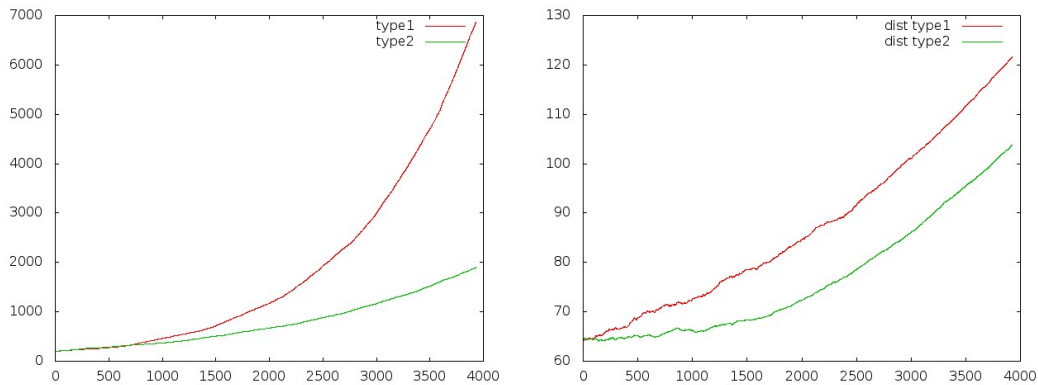


Figure 4.15: Different proliferation speed and average distance from centre in a run with motility 0.6, persistence time 10min and phase-scale of 0.6 for type1 cells.

Motility of the cells needs to be compared to the spread of the tumour front which arises as a consequence of cell division.

The persistence time plays a very important role for cell spread. In order to detach in the model, a cell must overcome the adhesive force which binds it to its neighbours. The typical detachment force which is needed can be estimated by taking an average of the binding force for cells in the tumour surface. This individual binding force can be calculated by summation of the force-components which act on a surface cell as a result of JKR interaction with its neighbours.

In reality motile or invasive phenotypes will probably downregulate the expression of ICAMs or other adhesion molecules and thus reduce their stickiness. This can be achieved via a differential adhesion in the model. In general for studying invasive potential also setups which use a differential adhesion between different cell types are of great interest (as has been demonstrated for the modelling of cell-demixing).

## 4.9 Copyright terms / Urheberrechte

All citation and excerpts used within this thesis have been marked accordingly.

The use of minor copyrighted material is considered to be legal within the “fair use” doctrine according to certain limitations found in sections 107 through 118 of the Copyright Act (title 17, U. S. Code). Section 107 explicitly lists research as one of the various purposes for which the reproduction of a particular work may be considered “fair”.

Within the German jurisdiction, the use of excerpts is considered to be legal within the “Zitatrecht” of §51 UrhG.

If the use of any picture within this thesis is not considered to be “fair use” by its current copyright holder or user, please contact the author [kempf@fias.uni-frankfurt.de](mailto:kempf@fias.uni-frankfurt.de) for a

resolution of the conflict.

## 4.10 Technical terms

Abbreviation	Meaning
<sup>3</sup> HTdR	Tritiated thymidine
BrdU	Bromodeoxyuridine, nucleoside analogue incorporated in S-phase for staining
CCR	Cell cycle dependent radiosensitivity
CDK	Cyclin-Dependent kinase
CT	Computed tomography
DSB	Double strand break of the DNA
FACS	Fluorescence-activated cell sorting
FCM	Flow cytometry
H2AX	Gene encoding histone H2A, becomes phosphorylated to $\gamma$ H2AX in the presence of DNA DSBs
HeLa	Immortal human cell line of cervical cancer
HI	Heavy ion
HIF	Hypoxia-inducible factors (e.g. HIF-1 $\alpha$ )
HR	Homologous recombination
HSATT	High Specific-Activity Tritiated Thymidine
Hydroxyurea	Hydroxycarbamide, antineoplastic drug
IMRT	Intensity-modulated radiation therapy
IGRT	Image-guided radiation therapy
LET	linear energy transfer
LQ/LQM	Linear quadratic (model)
MCTS	Multicellular tumour spheroid
MI	Mitotic index
MMEJ	Microhomology-mediated end joining
MRI	Magnetic resonance imaging
MRT	Magnetic resonance tomography or microbeam radiation therapy
MLC	Multileaf collimator
NHEJ	Non-homologous end joining
NOG (NOD/Shi-scid/IL-2R $\gamma$ null)	severely immunodeficient mouse
ODE	Ordinary differential equation
OER	Oxygen enhancement ratio
PDE	Partial differential equation
Pharmacokinetics	PK, absorption, distribution, metabolisms, duration of an administered drug
Pharmacodynamics	PD, relationship between drug concentration and effect (e.g. receptor-ligand reaction dynamics)

<b>Abbreviation</b>	<b>Meaning</b>
<b>PLD/PLDR</b>	Potentially lethal damage (repair)
<b>Restriction point</b>	G1/S checkpoint in the cell cycle; restricts further cell growth and can lead to quiescence
<b>PBS</b>	Phosphate buffered saline
<b>PET</b>	Positron emission tomography
<b>QRF</b>	Quiescence resistance factor (used to scale down effective dose received by quiescent cells)
<b>SBRT</b>	Stereotactic body radiotherapy
<b>SCID mice</b>	Severe combined immunodeficiency mice
<b>Senescence</b>	Cell which entered a terminal state of quiescence
<b>SLD/SLDR</b>	Sub-lethal damage (repair)
<b>SOBP</b>	Spread-out Bragg peak
<b>SPF</b>	S-phase fraction
<b>Temozolomide</b>	DNA methylating agent
<b>PI</b>	Propidium iodide - a dye used for DNA staining

Table 4.5: Listing of technical terms and abbreviations used in this work.

## 4.11 Cell lines

A listing of cell lines which are mentioned within this work is presented in table 4.6. An incomplete list of cell lines and information sources can also be found at [http://en.wikipedia.org/wiki/Cell\\_culture#List\\_of\\_cell\\_lines](http://en.wikipedia.org/wiki/Cell_culture#List_of_cell_lines). A valuable source for information and parameters of the according cells are supplier databases such as <http://www.lgcstandards-atcc.org/> or <http://www.dsmz.de/>.

Table 4.6: Listing of cell lines mentioned in this work and corresponding sources

Cell line	Description and sources
<b>67NR</b>	Non-metastatic murine mammary carcinoma cells (ATCC) [43]
<b>A549</b>	Human lung [148]
<b>AG1522</b>	Fibroblast [247]
<b>BT474</b>	Breast cancer, can form spheroidal aggregates [172], [216]
<b>CHO</b>	Chinese hamster ovarian (immortalized non-tumour cell line) [204]
<b>CHO-XRS</b>	Hamster fibroblasts [69]
<b>EMT6</b>	Mouse mammary carcinoma/sarcoma; radio-resistant [241], (subline Ro) [72], [69], ATCC-Number: CRL-2755
<b>HX117</b>	Xenografted human melanoma [242]
<b>HX118</b>	Xenografted human melanoma [242]
<b>MCC26</b>	Mouse colon carcinoma [69]
<b>LN229</b>	Glioblastoma [27]
<b>MCF7</b>	Human breast [148]
<b>ME/MAR</b>	Human small cell carcinoma of the lung [242]
<b>RIF-1</b>	Radiation-induced fibrosarcoma; radioresponsive tumor [241]
<b>SCC VII</b>	Squamous cell carcinoma [146]
<b>U87</b>	Glioblastoma [27]
<b>V79</b>	Chinese hamster fibroblast cells derived from lung tissue [242]; sublines: V79-1 and V79-379-A [66], 285B [204], [69], [213], 171b
<b>WiDr</b>	Human colon adenocarcinoma spheroid [159]

# Bibliography

- [1] Altinok, A., Lévi, F., and Goldbeter, A., 2007. A cell cycle automaton model for probing circadian patterns of anticancer drug delivery. *Advanced drug delivery reviews*, **59**(9-10):1036–53. doi: [10.1016/j.addr.2006.09.022](https://doi.org/10.1016/j.addr.2006.09.022).
- [2] Alvarez-Ramírez, J., Nieves-Mendoza, S., and González-Trejo, J., 1996. Calculation of the effective diffusivity of heterogeneous media using the lattice-Boltzmann method. *Physical review. E, Statistical physics, plasmas, fluids, and related interdisciplinary topics*, **53**(3):2298–2303.
- [3] Athanassiou, H., Synodinou, M., Maragoudakis, E., Paraskevaidis, M., Verigos, C., Misailidou, D., Antonadou, D., Saris, G., Beroukas, K., and Karageorgis, P., 2005. Randomized phase II study of temozolomide and radiotherapy compared with radiotherapy alone in newly diagnosed glioblastoma multiforme. *Journal of clinical oncology : official journal of the American Society of Clinical Oncology*, **23**(10):2372–7. doi: [10.1200/JCO.2005.00.331](https://doi.org/10.1200/JCO.2005.00.331).
- [4] Aurenhammer, F., 1991. Voronoi Diagrams — A Survey of a Fundamental Data Structure. *ACM Computing Surveys (CSUR)*, **23**(3).
- [5] Awwad, H. K., Lotayef, M., Shouman, T., Begg, A. C., Wilson, G., Bentzen, S. M., Abd El-Moneim, H., and Eissa, S., 2002. Accelerated hyperfractionation (AHF) compared to conventional fractionation (CF) in the postoperative radiotherapy of locally advanced head and neck cancer: influence of proliferation. *British journal of cancer*, **86**(4):517–23. doi: [10.1038/sj.bjc.6600119](https://doi.org/10.1038/sj.bjc.6600119).
- [6] Baccelli, I. and Trumpp, A., 2012. The evolving concept of cancer and metastasis stem cells. *The Journal of Cell Biology*, **198**(3):281–293. doi: [10.1083/jcb.201202014](https://doi.org/10.1083/jcb.201202014).
- [7] Bache, M., Kappler, M., Said, H. M., Staab, A., and Vordermark, D., 2008. Detection and specific targeting of hypoxic regions within solid tumors: current preclinical and clinical strategies. *Current medicinal chemistry*, **15**(4):322–38.
- [8] Bajénoff, M., Glaichenhaus, N., and Germain, R. N., 2008. Fibroblastic reticular cells guide T lymphocyte entry into and migration within the splenic T cell zone. *Journal of immunology (Baltimore, Md. : 1950)*, **181**(6):3947–54.
- [9] Ballarini, F., 2010. From DNA radiation damage to cell death: theoretical approaches. *Journal of nucleic acids*, **2010**(1):350608. doi: [10.4061/2010/350608](https://doi.org/10.4061/2010/350608).
- [10] Baluna, R. G., Eng, T. Y., and Thomas, C. R., 2006. Adhesion molecules in radiotherapy. *Radiation research*, **166**(6):819–31. doi: [10.1667/RR0380.1](https://doi.org/10.1667/RR0380.1).
- [11] Baranov, V. I., Belichenko, V. M., and Shoshenko, C. A., 2000. Oxygen Diffusion Coefficient in Isolated Chicken Red and White Skeletal Muscle Fibers in Ontogenesis. *Microvascular Research*, **60**(2):168–176.
- [12] Bauman, G. S., MacDonald, W., Moore, E., Ramsey, D. a., Fisher, B. J., Amberger, V. R., and Del Maestro, R. M., 1999. Effects of radiation on a model of malignant glioma invasion. *Journal of neuro-oncology*, **44**(3):223–31.
- [13] Bautch, V. L., 2010. Cancer: Tumour stem cells switch sides. *Nature*, **468**(7325):770–1. doi: [10.1038/468770a](https://doi.org/10.1038/468770a).
- [14] Beckloff, G. L., Lerner, H. J., Frost, D., Russo-Alesi, F. M., and Gitomer, S., 1965. Hydroxyurea (NSC-32065) in biologic fluids: dose-concentration relationship. *Cancer chemotherapy reports. Part 1*, **48**:57–8.

- [15] Beltman, J. B., Marée, A. F. M., and de Boer, R. J., 2007. Spatial modelling of brief and long interactions between T cells and dendritic cells. *Immunology and cell biology*, **85**(4):306–14. doi: [10.1038/sj.icb.7100054](https://doi.org/10.1038/sj.icb.7100054).
- [16] Beltman, J. B., Marée, A. F. M., and de Boer, R. J., 2009. Analysing immune cell migration. *Nature reviews. Immunology*, **9**(11):789–98. doi: [10.1038/nri2638](https://doi.org/10.1038/nri2638).
- [17] Bennewith, K. L. and Dedhar, S., 2011. Targeting hypoxic tumour cells to overcome metastasis. *BMC cancer*, **11**(1):504. doi: [10.1186/1471-2407-11-504](https://doi.org/10.1186/1471-2407-11-504).
- [18] Beresford, M. J., Wilson, G. D., and Makris, A., 2006. Measuring proliferation in breast cancer: practicalities and applications. *Breast cancer research : BCR*, **8**(6):216. doi: [10.1186/bcr1618](https://doi.org/10.1186/bcr1618).
- [19] Bethe, H., 1930. Zur Theorie des Durchgangs schneller Korpuskularstrahlen durch Materie. *Annalen der Physik*, **397**(3):325–400.
- [20] Beyer, T., 2007. *Spatio-Temporal Dynamics of Primary Lymphoid Follicles During Organogenesis and Lymphneogenesis*. Ph.D. thesis, Johann Wolfgang Goethe-Universität, Frankfurt am Main.
- [21] Beyer, T. and Meyer-Hermann, M., 2007. Modeling emergent tissue organization involving high-speed migrating cells in a flow equilibrium. *Physical review. E, Statistical, nonlinear, and soft matter physics*, **76**(2 Pt 1):021929.
- [22] Beyer, T. and Meyer-Hermann, M., 2008. Mechanisms of organogenesis of primary lymphoid follicles. *International immunology*, **20**(4):615–23. doi: [10.1093/intimm/dxn020](https://doi.org/10.1093/intimm/dxn020).
- [23] Beyer, T., Schaller, G., Deutsch, A., and Meyer-Hermann, M., 2005. Parallel dynamic and kinetic regular triangulation in three dimensions. *Computer Physics Communications*, **172**(2):86–108. doi: [10.1016/j.cpc.2005.06.009](https://doi.org/10.1016/j.cpc.2005.06.009).
- [24] Bibby, S. R. S. and Urban, J. P. G., 2004. Effect of nutrient deprivation on the viability of intervertebral disc cells. *European spine journal : official publication of the European Spine Society, the European Spinal Deformity Society, and the European Section of the Cervical Spine Research Society*, **13**(8):695–701. doi: [10.1007/s00586-003-0616-x](https://doi.org/10.1007/s00586-003-0616-x).
- [25] Bird, R. P. and Burki, H. J., 1975. Survival of synchronized Chinese hamster cells exposed to radiation of different linear-energy transfer. *International journal of radiation biology and related studies in physics, chemistry, and medicine*, **27**(2):105–20.
- [26] Bock, M., Tyagi, A. K., Kreft, J.-U., and Alt, W., 2010. Generalized voronoi tessellation as a model of two-dimensional cell tissue dynamics. *Bulletin of mathematical biology*, **72**(7):1696–731. doi: [10.1007/s11538-009-9498-3](https://doi.org/10.1007/s11538-009-9498-3).
- [27] Bohl, J., 2006. *Charakterisierung von zwei Glioblastomzelllinien zur Vorbereitung für die Tumorthherapie mit schweren Ionen in Kombination mit Chemotherapie*. Diplomarbeit, TU Darmstadt.
- [28] Bourhis, J., Overgaard, J., Audry, H., Ang, K. K., Saunders, M., Bernier, J., Horiot, J.-C., Le Maître, A., Pajak, T. F., Poulsen, M. G., O’Sullivan, B., Dobrowsky, W., Hliniak, A., Skladowski, K., Hay, J. H., Pinto, L. H. J., Fallai, C., Fu, K. K., Sylvester, R., and Pignon, J.-P., 2006. Hyperfractionated or accelerated radiotherapy in head and neck cancer: a meta-analysis. *Lancet*, **368**(9538):843–54. doi: [10.1016/S0140-6736\(06\)69121-6](https://doi.org/10.1016/S0140-6736(06)69121-6).
- [29] Brahme, A., 2004. Recent advances in light ion radiation therapy. *International journal of radiation oncology, biology, physics*, **58**(2):603–16. doi: [10.1016/j.ijrobp.2003.09.034](https://doi.org/10.1016/j.ijrobp.2003.09.034).
- [30] Brahme, A., 2011. Accurate description of the cell survival and biological effect at low and high doses and LET’s. *Journal of radiation research*, **52**(4):389–407. doi: [10.1269/jrr.10129](https://doi.org/10.1269/jrr.10129).
- [31] Brahme, A. and Lind, B. K., 2010. A systems biology approach to radiation therapy optimization. *Radiation and environmental biophysics*, **49**(2):111–24. doi: [10.1007/s00411-010-0268-2](https://doi.org/10.1007/s00411-010-0268-2).

## Bibliography

- [32] Brenner, D. J., 2008. The linear-quadratic model is an appropriate methodology for determining isoeffective doses at large doses per fraction. *Seminars in radiation oncology*, **18**(4):234–9. doi: [10.1016/j.semradonc.2008.04.004](https://doi.org/10.1016/j.semradonc.2008.04.004).
- [33] Brenner, D. J., Hlatky, L. R., Hahnfeldt, P. J., Hall, E. J., and Sachs, R. K., 1995. A convenient extension of the linear-quadratic model to include redistribution and reoxygenation. *International journal of radiation oncology, biology, physics*, **32**(2):379–90.
- [34] Brenner, D. J., Hlatky, L. R., Hahnfeldt, P. J., Huang, Y., and Sachs, R. K., 1998. The linear-quadratic model and most other common radiobiological models result in similar predictions of time-dose relationships. *Radiation research*, **150**(1):83–91.
- [35] Brown, J. M., 2002. Tumor microenvironment and the response to anticancer therapy. *Cancer biology & therapy*, **1**(5):453–8.
- [36] Brown, J. M. and Giaccia, A. J., 1998. The unique physiology of solid tumors: opportunities (and problems) for cancer therapy. *Cancer research*, **58**(7):1408–16.
- [37] Byrne, H. and Drasdo, D., 2009. Individual-based and continuum models of growing cell populations: a comparison. *Journal of mathematical biology*, **58**(4-5):657–87. doi: [10.1007/s00285-008-0212-0](https://doi.org/10.1007/s00285-008-0212-0).
- [38] Cárdenas-Navia, L. I., Yu, D., Braun, R. D., Brizel, D. M., Secomb, T. W., and Dewhirst, M. W., 2004. Tumor-dependent kinetics of partial pressure of oxygen fluctuations during air and oxygen breathing. *Cancer research*, **64**(17):6010–7. doi: [10.1158/0008-5472.CAN-03-0947](https://doi.org/10.1158/0008-5472.CAN-03-0947).
- [39] Cargill, R. W., 1976. Solubility of oxygen in some water + alcohol systems. *Journal of the Chemical Society, Faraday Transactions 1*, **72**:2296. doi: [10.1039/f19767202296](https://doi.org/10.1039/f19767202296).
- [40] Casciari, J. J., Sotirchos, S. V., and Sutherland, R. M., 1988. Glucose Diffusivity in Multicellular Tumor Spheroids. *Cancer Research*, **48**(14):3905–3909.
- [41] Casciari, J. J., Sotirchos, S. V., and Sutherland, R. M., 1992. Variations in tumor cell growth rates and metabolism with oxygen concentration, glucose concentration, and extracellular pH. *Journal of Cellular Physiology*, **151**(2):386–394.
- [42] Chamberlain, M. C., 2012. Hydroxyurea for recurrent surgery and radiation refractory high-grade meningioma. *Journal of neuro-oncology*, **107**(2):315–21. doi: [10.1007/s11060-011-0741-z](https://doi.org/10.1007/s11060-011-0741-z).
- [43] Cheng, G., Tse, J., Jain, R. K., and Munn, L. L., 2009. Micro-environmental mechanical stress controls tumor spheroid size and morphology by suppressing proliferation and inducing apoptosis in cancer cells. *PloS one*, **4**(2):e4632. doi: [10.1371/journal.pone.0004632](https://doi.org/10.1371/journal.pone.0004632).
- [44] Choi, K. S., 2012. Autophagy and Cancer. *Experimental & molecular medicine*.
- [45] Chris Wang, C.-K. and Zhang, X., 2006. A nanodosimetry-based linear-quadratic model of cell survival for mixed-LET radiations. *Physics in medicine and biology*, **51**(23):6087–98. doi: [10.1088/0031-9155/51/23/010](https://doi.org/10.1088/0031-9155/51/23/010).
- [46] Chu, Y.-S., Dufour, S., Thiery, J. P., Perez, E., and Pincet, F., 2005. Johnson-Kendall-Roberts theory applied to living cells. *Physical review letters*, **94**(2):28102.
- [47] Chu, Y.-S., Thomas, W. A., Eder, O., Pincet, F., Perez, E., Thiery, J. P., and Dufour, S., 2004. Force measurements in E-cadherin-mediated cell doublets reveal rapid adhesion strengthened by actin cytoskeleton remodeling through Rac and Cdc42. *The Journal of cell biology*, **167**(6):1183–94. doi: [10.1083/jcb.200403043](https://doi.org/10.1083/jcb.200403043).
- [48] Cignoni, P., Montani, C., and Porego, R., 1993. Parallel 3D Delaunay Triangulation Delaunay Triangulations: definition and algorithms. **12**(3).
- [49] Cobb, J. P., Hotchkiss, R. S., Karl, I. E., and Buchman, T. G., 1996. Mechanisms of cell injury and death. *British journal of anaesthesia*, **77**(1):3–10. doi: [10.1093/bja/77.1.3](https://doi.org/10.1093/bja/77.1.3).

- [50] Coelho Neto, J., Agero, U., Gazzinelli, R. T., and Mesquita, O. N., 2006. Measuring optical and mechanical properties of a living cell with defocusing microscopy. *Biophysical journal*, **91**(3):1108–15. doi: [10.1529/biophysj.105.073783](https://doi.org/10.1529/biophysj.105.073783).
- [51] Connell, P. P. and Hellman, S., 2009. Advances in radiotherapy and implications for the next century: a historical perspective. *Cancer research*, **69**(2):383–92. doi: [10.1158/0008-5472.CAN-07-6871](https://doi.org/10.1158/0008-5472.CAN-07-6871).
- [52] Cornelissen, B., Kersemans, V., Darbar, S., Thompson, J., Shah, K., Sleeth, K., Hill, M. a., and Vallis, K. a., 2011. Imaging DNA damage in vivo using gammaH2AX-targeted immunoconjugates. *Cancer research*, **71**(13):4539–49. doi: [10.1158/0008-5472.CAN-10-4587](https://doi.org/10.1158/0008-5472.CAN-10-4587).
- [53] Cotran, R. S., Kumar, V., Collins, T., and Robbins, S. L., 1999. *Robbins pathologic basis of disease*. Robbins Pathology Series. Saunders, 6th edition.
- [54] Crank, J. and Nicolson, P., 1996. A practical method for numerical evaluation of solutions of partial differential equations of the heat-conduction type. *Advances in Computational Mathematics*, **6**(1):207–226. doi: [10.1007/BF02127704](https://doi.org/10.1007/BF02127704).
- [55] Dallon, J. C. and Othmer, H. G., 2004. How cellular movement determines the collective force generated by the Dictyostelium discoideum slug. *Journal of theoretical biology*, **231**(2):203–22. doi: [10.1016/j.jtbi.2004.06.015](https://doi.org/10.1016/j.jtbi.2004.06.015).
- [56] Davis, P. K., Ho, A., and Dowdy, S. F., 2001. Biological methods for cell-cycle synchronization of mammalian cells. *BioTechniques*, **30**(6):1322–6, 1328, 1330–1.
- [57] Deisboeck, T. S., Wang, Z., Macklin, P., and Cristini, V., 2011. *Multiscale cancer modeling.*, volume 13. doi: [10.1146/annurev-bioeng-071910-124729](https://doi.org/10.1146/annurev-bioeng-071910-124729).
- [58] Demaria, S., Ng, B., Devitt, M. L., Babb, J. S., Kawashima, N., Liebes, L., and Formenti, S. C., 2004. Ionizing radiation inhibition of distant untreated tumors (abscopal effect) is immune mediated. *International journal of radiation oncology, biology, physics*, **58**(3):862–70. doi: [10.1016/j.ijrobp.2003.09.012](https://doi.org/10.1016/j.ijrobp.2003.09.012).
- [59] Dewhirst, M. W., Cao, Y., and Moeller, B., 2008. Cycling hypoxia and free radicals regulate angiogenesis and radiotherapy response. *Nature reviews. Cancer*, **8**(6):425–37. doi: [10.1038/nrc2397](https://doi.org/10.1038/nrc2397).
- [60] Dingli, D. and Michor, F., 2006. Successful therapy must eradicate cancer stem cells. *Stem Cells*, **24**(12):2603–2610. doi: [10.1634/stemcells.2006-0136](https://doi.org/10.1634/stemcells.2006-0136).
- [61] Douglas, J., 1962. Alternating direction methods for three space variables. *Numerische Mathematik*, **4**(1):41–63. doi: [10.1007/BF01386295](https://doi.org/10.1007/BF01386295).
- [62] Drasdo, D., 2005. Coarse graining in simulated cell populations. *Advances in Complex Systems (ACS)*, **8**(3):319–363.
- [63] Dulla, K. and Santamaria, A., 2011. Large-scale mitotic cell synchronization. *Methods in molecular biology (Clifton, N.J.)*, **761**:65–74. doi: [10.1007/978-1-61779-182-6\\_4](https://doi.org/10.1007/978-1-61779-182-6_4).
- [64] Durante, M. and Loeffler, J. S., 2010. Charged particles in radiation oncology. *Nature reviews. Clinical oncology*, **7**(1):37–43. doi: [10.1038/nrclinonc.2009.183](https://doi.org/10.1038/nrclinonc.2009.183).
- [65] El Naqa, I., Pater, P., and Seuntjens, J., 2012. Monte Carlo role in radiobiological modelling of radiotherapy outcomes. *Physics in medicine and biology*, **57**(11):R75–97. doi: [10.1088/0031-9155/57/11/R75](https://doi.org/10.1088/0031-9155/57/11/R75).
- [66] Elkind, M. M., Sutton-Gilbert, H., Moses, W. B., Alescio, T., and Swain, R. W., 1965. Radiation Response of Mammalian Cells Grown in Culture. V. Temperature Dependence of the Repair of X-Ray Damage in Surviving Cells (Aerobic and Hypoxic). *Radiation research*, **25**(2):359–76.
- [67] Ferrez, J. J.-A., 2001. *Dynamic triangulations for efficient 3D simulation of granular materials*. Ph.D. thesis, Ecole Polytechnique Federal de Lausanne.
- [68] Franko, a. J. and Koch, C. J., 1983. The radiation response of hypoxic cells in EMT6 spheroids in suspension culture does model data from EMT6 tumors. *Radiation research*, **96**(3):497–504.

## Bibliography

- [69] Freyer, J. P., 1988. Role of necrosis in regulating the growth saturation of multicellular spheroids. *Cancer research*, **48**(9):2432–9.
- [70] Freyer, J. P. and Sutherland, R. M., 1985. A reduction in the in situ rates of oxygen and glucose consumption of cells in EMT6/Ro spheroids during growth. *J Cell Physiol*, **124**(3):516–524. doi: [10.1002/jcp.1041240323](https://doi.org/10.1002/jcp.1041240323).
- [71] Freyer, J. P. and Sutherland, R. M., 1986. Proliferative and clonogenic heterogeneity of cells from EMT6/Ro multicellular spheroids induced by the glucose and oxygen supply. *Cancer research*, **46**(7):3513–20.
- [72] Freyer, J. P. and Sutherland, R. M., 1986. Regulation of growth saturation and development of necrosis in EMT6/Ro multicellular spheroids by the glucose and oxygen supply. *Cancer research*, **46**(7):3504–12.
- [73] Freyer, J. P., Tustanoff, E., Franko, A. J., and Sutherland, R. M., 1984. In situ oxygen consumption rates of cells in V-79 multicellular spheroids during growth. *Journal of cellular physiology*, **118**(1):53–61. doi: [10.1002/jcp.1041180111](https://doi.org/10.1002/jcp.1041180111).
- [74] Fritz, P., Weber, K. J., Frank, C., and Flentje, M., 1996. Differential effects of dose rate and superfractionation on survival and cell cycle of V79 cells from spheroid and monolayer culture. *Radiotherapy and oncology : journal of the European Society for Therapeutic Radiology and Oncology*, **39**(1):73–9.
- [75] Fu, K. K., Pajak, T. F., Trotti, A., Jones, C. U., Spencer, S. a., Phillips, T. L., Garden, A. S., Ridge, J. a., Cooper, J. S., and Ang, K. K., 2000. A Radiation Therapy Oncology Group (RTOG) phase III randomized study to compare hyperfractionation and two variants of accelerated fractionation to standard fractionation radiotherapy for head and neck squamous cell carcinomas: first report of RTOG 9003. *International journal of radiation oncology, biology, physics*, **48**(1):7–16. doi: [10.1016/S0360-3016\(00\)00663-5](https://doi.org/10.1016/S0360-3016(00)00663-5).
- [76] Galle, J. J., Loeffler, M., and Drasdo, D., 2005. Modeling the Effect of Deregulated Proliferation and Apoptosis on the Growth Dynamics of Epithelial Cell Populations In Vitro. *Biophysical journal*, **88**(1):62–75. doi: [10.1529/biophysj.104.041459](https://doi.org/10.1529/biophysj.104.041459).
- [77] Gatenby, R. A., 2009. A change of strategy in the war on cancer. *Nature*, **459**(7246):508–9. doi: [10.1038/459508a](https://doi.org/10.1038/459508a).
- [78] Gatenby, R. a., Brown, J., and Vincent, T., 2009. Lessons from applied ecology: cancer control using an evolutionary double bind. *Cancer research*, **69**(19):7499–502. doi: [10.1158/0008-5472.CAN-09-1354](https://doi.org/10.1158/0008-5472.CAN-09-1354).
- [79] Gillies, R. J., Verduzco, D., and Gatenby, R. A., 2012. Evolutionary dynamics of carcinogenesis and why targeted therapy does not work. *Nature reviews. Cancer*, **12**(7):487–93. doi: [10.1038/nrc3298](https://doi.org/10.1038/nrc3298).
- [80] Groebe, K. and Mueller-Klieser, W., 1991. Distributions of oxygen, nutrient, and metabolic waste concentrations in multicellular spheroids and their dependence on spheroid parameters. *European biophysics journal : EBJ*, **19**(4):169–81.
- [81] Grote, J., Süsskind, R., and Vaupel, P., 1977. Oxygen diffusivity in tumor tissue (DS-carcinosarcoma) under temperature conditions within the range of 20–40 degrees C. *Pflügers Archiv : European journal of physiology*, **372**(1):37–42.
- [82] Guck, J., Ananthakrishnan, R., Mahmood, H., Moon, T. J., Cunningham, C. C., and Käs, J., 2001. The optical stretcher: a novel laser tool to micromanipulate cells. *Biophysical journal*, **81**(2):767–84. doi: [10.1016/S0006-3495\(01\)75740-2](https://doi.org/10.1016/S0006-3495(01)75740-2).
- [83] Hahnfeldt, P. and Hlatky, L., 1996. Resensitization due to redistribution of cells in the phases of the cell cycle during arbitrary radiation protocols. *Radiation research*, **145**(2):134–43.
- [84] Hall, E. J., 1993. *Radiobiology for the Radiologist*. Lippincott Williams & Wilkins, 4th edition.
- [85] Hall, E. J., 2003. The Bystander Effect. *Health Physics*, **85**(1).

- [86] Hall, E. J. and Giaccia, A. J., 2005. *Radiobiology For The Radiologist*. Lippincott Williams & Wilkins, 6th edition.
- [87] Hamada, N., Imaoka, T., Masunaga, S.-i., Ogata, T., Okayasu, R., Takahashi, A., Kato, T. a., Kobayashi, Y., Ohnishi, T., Ono, K., Shimada, Y., and Teshima, T., 2010. Recent advances in the biology of heavy-ion cancer therapy. *Journal of radiation research*, **51**(4):365–83. doi: [10.1269/jrr.09137](https://doi.org/10.1269/jrr.09137).
- [88] Hanahan, D. and Weinberg, R. A., 2000. The hallmarks of cancer. *Cell*, **100**(1):57–70.
- [89] Hanahan, D. and Weinberg, R. A., 2011. Hallmarks of cancer: the next generation. *Cell*, **144**(5):646–74. doi: [10.1016/j.cell.2011.02.013](https://doi.org/10.1016/j.cell.2011.02.013).
- [90] Haraf, D. J., Rosen, F. R., Stenson, K., Argiris, A., Mittal, B. B., Witt, M. E., Brockstein, B. E., List, M. A., Portugal, L., Pelzer, H., Weichselbaum, R. R., and Vokes, E. E., 2003. Induction chemotherapy followed by concomitant TFHX chemoradiotherapy with reduced dose radiation in advanced head and neck cancer. *Clinical cancer research : an official journal of the American Association for Cancer Research*, **9**(16 Pt 1):5936–43.
- [91] Harriss, W., Bezak, E., Yeoh, E., and Hermans, M., 2010. Measurement of reoxygenation during fractionated radiotherapy in head and neck squamous cell carcinoma xenografts. *Australasian physical & engineering sciences in medicine / supported by the Australasian College of Physical Scientists in Medicine and the Australasian Association of Physical Sciences in Medicine*, **33**(3):251–63. doi: [10.1007/s13246-010-0032-6](https://doi.org/10.1007/s13246-010-0032-6).
- [92] Harter, P., Caspary, L., Momma, S., Meister, J., Zinke, J., Dützmänn, S., Weissenberger, J., Copanaki, E., Steinbach, J., Plate, K., and Mittelbronn, M., 2010. Limitations and perspectives of glioma cell migration and invasion assays. In *International Brain Tumor Research Conference*. Seeheim-Jugenheim, Germany.
- [93] Harting, C., Peschke, P., Borkenstein, K., and Karger, C. P., 2007. Single-cell-based computer simulation of the oxygen-dependent tumour response to irradiation. *Physics in medicine and biology*, **52**(16):4775–89. doi: [10.1088/0031-9155/52/16/005](https://doi.org/10.1088/0031-9155/52/16/005).
- [94] Hatzikirou, H., Basanta, D., Simon, M., Schaller, K., and Deutsch, A., 2012. 'Go or grow': the key to the emergence of invasion in tumour progression? *Mathematical medicine and biology : a journal of the IMA*, **29**(1):49–65. doi: [10.1093/imammb/dqq011](https://doi.org/10.1093/imammb/dqq011).
- [95] Hawkins, R. B., 2000. Survival of a mixture of cells of variable linear-quadratic sensitivity to radiation. *Radiation research*, **153**(6):840–3.
- [96] Hei, T. K., Zhou, H., Ivanov, V. N., Hong, M., Lieberman, H. B., Brenner, D. J., Amundson, S. A., and Geard, C. R., 2008. Mechanism of radiation-induced bystander effects: a unifying model. *The Journal of pharmacy and pharmacology*, **60**(8):943–50. doi: [10.1211/jpp.60.8.0001](https://doi.org/10.1211/jpp.60.8.0001).
- [97] Helmlinger, G., Netti, P. A., Lichtenbeld, H. C., Melder, R. J., and Jain, R. K., 1997. Solid stress inhibits the growth of multicellular tumor spheroids. *Nature biotechnology*, **15**(8):778–83. doi: [10.1038/nbt0897-778](https://doi.org/10.1038/nbt0897-778).
- [98] Helmlinger, G., Yuan, F., Dellian, M., and Jain, R. K., 1997. Interstitial pH and pO<sub>2</sub> gradients in solid tumors in vivo: high-resolution measurements reveal a lack of correlation. *Nature medicine*, **3**(2):177–82.
- [99] Hirschhaeuser, F., Menne, H., Dittfeld, C., West, J., Mueller-Klieser, W., and Kunz-Schughart, L. a., 2010. Multicellular tumor spheroids: an underestimated tool is catching up again. *Journal of biotechnology*, **148**(1):3–15. doi: [10.1016/j.jbiotec.2010.01.012](https://doi.org/10.1016/j.jbiotec.2010.01.012).
- [100] Hirschhaeuser, F., Sattler, U. G. A., and Mueller-Klieser, W., 2011. Lactate: a metabolic key player in cancer. *Cancer research*, **71**(22):6921–5. doi: [10.1158/0008-5472.CAN-11-1457](https://doi.org/10.1158/0008-5472.CAN-11-1457).
- [101] Hoffman, B. D., Massiera, G., Citters, K. M. V., and Crocker, J. C., 2006. The consensus mechanics of cultured mammalian cells. *Proc Natl Acad Sci U S A*, **103**(27):10259–10264. doi: [10.1073/pnas.0510348103](https://doi.org/10.1073/pnas.0510348103).

## Bibliography

- [102] Höring, E., Harter, P. N., Seznec, J., Schittenhelm, J., Bühring, H.-J., Bhattacharyya, S., von Hattingen, E., Zachskorn, C., Mittelbronn, M., and Naumann, U., 2012. The "go or grow" potential of gliomas is linked to the neuropeptide processing enzyme carboxypeptidase E and mediated by metabolic stress. *Acta neuropathologica*, **124**(1):83–97. doi: [10.1007/s00401-011-0940-x](https://doi.org/10.1007/s00401-011-0940-x).
- [103] Horiot, J. C., Le Fur, R., N'Guyen, T., Chenal, C., Schraub, S., Alfonsi, S., Gardani, G., Van Den Bogaert, W., Danczak, S., and Bolla, M., 1992. Hyperfractionation versus conventional fractionation in oropharyngeal carcinoma: final analysis of a randomized trial of the EORTC cooperative group of radiotherapy. *Radiotherapy and oncology : journal of the European Society for Therapeutic Radiology and Oncology*, **25**(4):231–41.
- [104] I. Zacharaki, E., S. Stamatakos, G., S. Nikita, K., K. Uzunoglu, N., Zacharaki, E. I., Stamatakos, G. S., Nikita, K. S., and Uzunoglu, N. K., 2004. Simulating growth dynamics and radiation response of avascular tumour spheroids-model validation in the case of an EMT6/Ro multicellular spheroid. *Computer methods and programs in biomedicine*, **76**(3):193–206. doi: [10.1016/j.cmpb.2004.07.003](https://doi.org/10.1016/j.cmpb.2004.07.003).
- [105] Indovina, P., Rainaldi, G., and Santini, M. T., 2007. Three-dimensional cell organization leads to a different type of ionizing radiation-induced cell death: MG-63 monolayer cells undergo mitotic catastrophe while spheroids die of apoptosis. *International journal of oncology*, **31**(6):1473–83.
- [106] Izuishi, K., Kato, K., Ogura, T., Kinoshita, T., and Esumi, H., 2000. Remarkable tolerance of tumor cells to nutrient deprivation: possible new biochemical target for cancer therapy. *Cancer research*, **60**(21):6201–7.
- [107] Jain, R. K., 1987. Transport of molecules across tumor vasculature. *Cancer metastasis reviews*, **6**(4):559–93.
- [108] Jain, R. K. and Stylianopoulos, T., 2010. Delivering nanomedicine to solid tumors. *Nature reviews. Clinical oncology*, **7**(11):653–64. doi: [10.1038/nrclinonc.2010.139](https://doi.org/10.1038/nrclinonc.2010.139).
- [109] Johnson, K. L., Kendall, K., and Roberts, a. D., 1971. Surface Energy and the Contact of Elastic Solids. *Proceedings of the Royal Society A: Mathematical, Physical and Engineering Sciences*, **324**(1558):301–313. doi: [10.1098/rspa.1971.0141](https://doi.org/10.1098/rspa.1971.0141).
- [110] Jorgensen, P. and Tyers, M., 2004. How cells coordinate growth and division. *Current biology : CB*, **14**(23):R1014–27. doi: [10.1016/j.cub.2004.11.027](https://doi.org/10.1016/j.cub.2004.11.027).
- [111] Kaelin, W. G. and Thompson, C. B., 2010. Q&A: Cancer: clues from cell metabolism. *Nature*, **465**(7298):562–4. doi: [10.1038/465562a](https://doi.org/10.1038/465562a).
- [112] Kaur, B., Tan, C., Brat, D. J., Post, D. E., and Van Meir, E. G., 2004. Genetic and hypoxic regulation of angiogenesis in gliomas. *Journal of neuro-oncology*, **70**(2):229–43. doi: [10.1007/s11060-004-2752-5](https://doi.org/10.1007/s11060-004-2752-5).
- [113] Kempf, H., 2008. *Agent-based modelling of tumour spheroid growth and treatment*. Diploma thesis, Johann Wolfgang Goethe-Universität, Frankfurt.
- [114] Kempf, H., Bleicher, M., and Meyer-Hermann, M., 2010. Spatio-temporal cell dynamics in tumour spheroid irradiation. *The European Physical Journal D*, **60**(1):177–193. doi: [10.1140/epjd/e2010-00178-4](https://doi.org/10.1140/epjd/e2010-00178-4).
- [115] Khain, E., Katakowski, M., Hopkins, S., and Szalad, A., 2011. Collective behavior of brain tumor cells: The role of hypoxia. *Physical Review E*, **031920**:1–6. doi: [10.1103/PhysRevE.83.031920](https://doi.org/10.1103/PhysRevE.83.031920).
- [116] Kim, H., Ahn, Y. C., Park, H. C., Lim, D. H., and Nam, H., 2010. Results and prognostic factors of hypofractionated stereotactic radiation therapy for primary or metastatic lung cancer. *Journal of thoracic oncology : official publication of the International Association for the Study of Lung Cancer*, **5**(4):526–32. doi: [10.1097/JTO.0b013e3181cbf622](https://doi.org/10.1097/JTO.0b013e3181cbf622).
- [117] Kimmelman, a. C., 2011. The dynamic nature of autophagy in cancer. *Genes & Development*, **25**(19):1999–2010. doi: [10.1101/gad.17558811](https://doi.org/10.1101/gad.17558811).

- [118] Kirkpatrick, J. P., Meyer, J. J., and Marks, L. B., 2008. The linear-quadratic model is inappropriate to model high dose per fraction effects in radiosurgery. *Seminars in radiation oncology*, **18**(4):240–3. doi: [10.1016/j.semradonc.2008.04.005](https://doi.org/10.1016/j.semradonc.2008.04.005).
- [119] Korff, T. and Augustin, H. G., 1998. Integration of endothelial cells in multicellular spheroids prevents apoptosis and induces differentiation. *The Journal of cell biology*, **143**(5):1341–52.
- [120] Kraft, G., Scholz, M., and Bechthold, U., 1999. Tumor therapy and track structure. *Radiation and Environmental Biophysics*, **38**(4):229–237.
- [121] Krahenbuhl, J. L., 1980. Effects of activated macrophages on tumor target cells in discrete phases of the cell cycle. *Cancer research*, **40**(12):4622–7.
- [122] Kram, Y. A., Mantey, S., and Corbo, J. C., 2010. Avian cone photoreceptors tile the retina as five independent, self-organizing mosaics. *PLoS one*, **5**(2):e8992. doi: [10.1371/journal.pone.0008992](https://doi.org/10.1371/journal.pone.0008992).
- [123] Krause, B. J., Beck, R., Souvatzoglou, M., and Piert, M., 2006. PET and PET/CT studies of tumor tissue oxygenation. *The quarterly journal of nuclear medicine and molecular imaging : official publication of the Italian Association of Nuclear Medicine (AIMN) [and] the International Association of Radiopharmacology (IAR), [and] Section of the Society of Radiopharmaceutica*, **50**(1):28–43.
- [124] Krogh, A., 1919. The number and distribution of capillaries in muscles with calculations of the oxygen pressure head necessary for supplying the tissue. *The Journal of physiology*, **52**(6):409–15.
- [125] Krogh, A., 1919. The supply of oxygen to the tissues and the regulation of the capillary circulation. *The Journal of physiology*, **52**(6):457–74.
- [126] Kumei, Y., Nakajima, T., Sato, a., Kamata, N., and Enomoto, S., 1989. Reduction of G1 phase duration and enhancement of c-myc gene expression in HeLa cells at hypergravity. *Journal of cell science*, **93** (Pt 2):221–6.
- [127] Kunz-Schughart, L. A., Doetsch, J., Mueller-Klieser, W., and Groebe, K., 2000. Proliferative activity and tumorigenic conversion: impact on cellular metabolism in 3-D culture. *American journal of physiology. Cell physiology*, **278**(4):C765–80.
- [128] Kuszyk, B. S., Corl, F. M., Franano, F. N., Bluemke, D. A., Hofmann, L. V., Fortman, B. J., and Fishman, E. K., 2001. Tumor transport physiology: implications for imaging and imaging-guided therapy. *AJR. American journal of roentgenology*, **177**(4):747–53.
- [129] Landau, L. D. and Lifshitz, E. M., 1959. *Theory of Elasticity*. Pergamon Press, London.
- [130] Landry, J., Freyer, J. P., and Sutherland, R. M., 1981. Shedding of mitotic cells from the surface of multi-cell spheroids during growth. *Journal of cellular physiology*, **106**(1):23–32. doi: [10.1002/jcp.1041060104](https://doi.org/10.1002/jcp.1041060104).
- [131] Langley, R. E., Bump, E. a., Quartuccio, S. G., Medeiros, D., and Brauhut, S. J., 1997. Radiation-induced apoptosis in microvascular endothelial cells. *British journal of cancer*, **75**(5):666–72.
- [132] Lankelma, J., 2002. Tissue transport of anti-cancer drugs. *Current pharmaceutical design*, **8**(22):1987–93.
- [133] Lévi, F. and Levi, F., 2001. Circadian chronotherapy for human cancers. *The lancet oncology*, **2**(5):307. doi: [10.1016/S1470-2045\(00\)00326-0](https://doi.org/10.1016/S1470-2045(00)00326-0).
- [134] Levine, A. J. and Puzio-Kuter, A. M., 2010. The control of the metabolic switch in cancers by oncogenes and tumor suppressor genes. *Science (New York, N.Y.)*, **330**(6009):1340–4. doi: [10.1126/science.1193494](https://doi.org/10.1126/science.1193494).
- [135] Lind, B. K., Persson, L. M., Edgren, M. R., Hedlöf, I., and Brahme, a., 2003. Repairable-conditionally repairable damage model based on dual Poisson processes. *Radiation research*, **160**(3):366–75.

## Bibliography

- [136] Lücke-Huhle, C., Blakely, E. a., Ngo, F. Q., Chang, P. Y., and Tobias, C. a., 1980. Survival and kinetic response of V79-spheroids after exposure to heavy ion beams. *International journal of radiation biology and related studies in physics, chemistry, and medicine*, **37**(5):483–92.
- [137] Lunt, S. J., Kalliomaki, T. M., Brown, A., Yang, V. X., Milosevic, M., and Hill, R. P., 2008. Interstitial fluid pressure, vascularity and metastasis in ectopic, orthotopic and spontaneous tumours. *BMC cancer*, **8**:2. doi: [10.1186/1471-2407-8-2](https://doi.org/10.1186/1471-2407-8-2).
- [138] Lyng, H., SundfØr, K., and Rofstad, E. K., 1997. Oxygen tension in human tumours measured with polarographic needle electrodes and its relationship to vascular density, necrosis and hypoxia. *Radiotherapy and oncology : journal of the European Society for Therapeutic Radiology and Oncology*, **44**(2):163–9.
- [139] Ma, Y., Conforti, R., Aymeric, L., Locher, C., Kepp, O., Kroemer, G., and Zitvogel, L., 2011. How to improve the immunogenicity of chemotherapy and radiotherapy. *Cancer metastasis reviews*, pp. 71–82. doi: [10.1007/s10555-011-9283-2](https://doi.org/10.1007/s10555-011-9283-2).
- [140] Maniotis, A. J., Chen, C. S., and Ingber, D. E., 1997. Demonstration of mechanical connections between integrins, cytoskeletal filaments, and nucleoplasm that stabilize nuclear structure. *Proceedings of the National Academy of Sciences of the United States of America*, **94**(3):849–54.
- [141] Marie, H., Pratt, S. J., Betson, M., Epple, H., Kittler, J. T., Meek, L., Moss, S. J., Troyanovsky, S., Attwell, D., Longmore, G. D., and Braga, V. M. M., 2003. The LIM protein Ajuba is recruited to cadherin-dependent cell junctions through an association with alpha-catenin. *The Journal of biological chemistry*, **278**(2):1220–8. doi: [10.1074/jbc.M205391200](https://doi.org/10.1074/jbc.M205391200).
- [142] Masunaga, S., Ono, K., and Abe, M., 1991. A method for the selective measurement of the radiosensitivity of quiescent cells in solid tumors—combination of immunofluorescence staining to BrdU and micronucleus assay. *Radiation research*, **125**(3):243–7.
- [143] Masunaga, S., Ono, K., Mitsumori, M., and Abe, M., 1993. Alteration of radiosensitivity of quiescent cell populations in solid tumors irradiated with X-rays twice at various intervals. *Japanese journal of cancer research : Gann*, **84**(11):1130–5.
- [144] Masunaga, S., Ono, K., Wandl, E. O., Fushiki, M., and Abe, M., 1990. Use of the micronucleus assay for the selective detection of radiosensitivity in BUdR-unincorporated cells after pulse-labelling of exponentially growing tumour cells. *International journal of radiation biology*, **58**(2):303–11.
- [145] Masunaga, S.-I., Ando, K., Uzawa, A., Hirayama, R., Furusawa, Y., Koike, S., and Ono, K., 2008. Responses of total and quiescent cell populations in solid tumors to carbon ion beam irradiation (290 MeV/u) in vivo. *Radiation medicine*, **26**(5):270–7. doi: [10.1007/s11604-008-0227-x](https://doi.org/10.1007/s11604-008-0227-x).
- [146] Masunaga, S.-i., Ando, K., Uzawa, A., Hirayama, R., Furusawa, Y., Koike, S., and Ono, K., 2008. The radiosensitivity of total and quiescent cell populations in solid tumors to 290 MeV/u carbon ion beam irradiation in vivo. *Acta oncologica (Stockholm, Sweden)*, **47**(6):1087–93. doi: [10.1080/02841860701821999](https://doi.org/10.1080/02841860701821999).
- [147] Masunaga, S.-i. and Ono, K., 2002. Significance of the response of quiescent cell populations within solid tumors in cancer therapy. *Journal of radiation research*, **43**(1):11–25.
- [148] Matthews, J. H., Meeker, B. E., and Chapman, J. D., 1989. Response of human tumor cell lines in vitro to fractionated irradiation. *International journal of radiation oncology, biology, physics*, **16**(1):133–8.
- [149] Mauro, F. and Elkind, M. M., 1968. Differences in survival variations during the growth cycle of cultured Chinese hamster cells treated with sulfur mustard and x-rays. *Cancer research*, **28**(6):1150–5.
- [150] Mempel, T. R., Henrickson, S. E., and Von Andrian, U. H., 2004. T-cell priming by dendritic cells in lymph nodes occurs in three distinct phases. *Nature*, **427**(6970):154–9. doi: [10.1038/nature02238](https://doi.org/10.1038/nature02238).
- [151] Mempel, T. R., Junt, T., and von Andrian, U. H., 2006. Rulers over randomness: stroma cells guide lymphocyte migration in lymph nodes. *Immunity*, **25**(6):867–9. doi: [10.1016/j.immuni.2006.11.002](https://doi.org/10.1016/j.immuni.2006.11.002).
- [152] Merrill, G. F., 1998. Cell synchronization. *Methods in cell biology*, **57**:229–49.

- [153] Minchinton, A. I. and Tannock, I. F., 2006. Drug penetration in solid tumours. *Nature reviews. Cancer*, **6**(8):583–92. doi: [10.1038/nrc1893](https://doi.org/10.1038/nrc1893).
- [154] Minohara, S., Fukuda, S., Kanematsu, N., Takei, Y., Furukawa, T., Inaniwa, T., Matsufuji, N., Mori, S., and Noda, K., 2010. Recent innovations in carbon-ion radiotherapy. *Journal of radiation research*, **51**(4):385–92. doi: [10.1269/jrr.10028](https://doi.org/10.1269/jrr.10028).
- [155] Misra, N., Singh, H., and Hnizdo, V., 2010. Nearest Neighbor Estimates of Entropy for Multivariate Circular Distributions. *Entropy*, **12**(5):1125–1144. doi: [10.3390/e12051125](https://doi.org/10.3390/e12051125).
- [156] Muche, L., 1996. Distributional properties of the three-dimensional Poisson Delaunay cell. *Journal of Statistical Physics*, **84**(1-2):147–167. doi: [10.1007/BF02179580](https://doi.org/10.1007/BF02179580).
- [157] Mueller-Klieser, W., 2000. Tumor biology and experimental therapeutics. *Critical reviews in oncology/hematology*, **36**(2-3):123–39.
- [158] Mueller-Klieser, W., Schreiber-Klais, S., Walenta, S., and Kreuter, M. H., 2002. Bioactivity of well-defined green tea extracts in multicellular tumor spheroids. *International journal of oncology*, **21**(6):1307–15.
- [159] Mueller-Klieser, W. F. and Sutherland, R. M., 1982. Oxygen tensions in multicell spheroids of two cell lines. *British journal of cancer*, **45**(2):256–64.
- [160] Nguyen, L. N. and Ang, K. K., 2002. Radiotherapy for cancer of the head and neck: altered fractionation regimens. *The lancet oncology*, **3**(11):693–701.
- [161] Nordsmark, M., Bentzen, S. r. M., Rudat, V., Brizel, D., Lartigau, E., Stadler, P., Becker, A., Adam, M., Molls, M., Dunst, J., Terris, D. J., and Overgaard, J., 2005. Prognostic value of tumor oxygenation in 397 head and neck tumors after primary radiation therapy. An international multi-center study. *Radiotherapy and oncology : journal of the European Society for Therapeutic Radiology and Oncology*, **77**(1):18–24. doi: [10.1016/j.radonc.2005.06.038](https://doi.org/10.1016/j.radonc.2005.06.038).
- [162] Okabe, A., Boots, B., Sugihara, K., and Chiu, S. N., 2000. *Spatial Tessellations*. Wiley Series in Probability and Statistics. John Wiley & Sons, Inc., Hoboken, NJ, USA, 2nd edition. doi: [10.1002/9780470317013](https://doi.org/10.1002/9780470317013).
- [163] Okada, T., Kamada, T., Tsuji, H., Mizoe, J.-e., Baba, M., Kato, S., Yamada, S., Sugahara, S., Yasuda, S., Yamamoto, N., Imai, R., Hasegawa, A., Imada, H., Kiyohara, H., Jingu, K., Shinoto, M., and Tsujii, H., 2010. Carbon ion radiotherapy: clinical experiences at National Institute of Radiological Science (NIRS). *Journal of radiation research*, **51**(4):355–64. doi: [10.1269/jrr.10016](https://doi.org/10.1269/jrr.10016).
- [164] Olive, P. L. and Durand, R. E., 1994. Drug and radiation resistance in spheroids: cell contact and kinetics. *Cancer metastasis reviews*, **13**(2):121–38.
- [165] Oloumi, A., Lam, W., Banáth, J. P., and Olive, P. L., 2002. Identification of genes differentially expressed in V79 cells grown as multicell spheroids. *International journal of radiation biology*, **78**(6):483–92. doi: [10.1080/09553000210122299](https://doi.org/10.1080/09553000210122299).
- [166] Pederson, A. W., Salama, J. K., Haraf, D. J., Witt, M. E., Stenson, K. M., Portugal, L., Seiwert, T., Villalor, V. M., Cohen, E. E. W., Vokes, E. E., and Blair, E. a., 2011. Adjuvant chemoradiotherapy for locoregionally advanced and high-risk salivary gland malignancies. *Head & neck oncology*, **3**(1):31. doi: [10.1186/1758-3284-3-31](https://doi.org/10.1186/1758-3284-3-31).
- [167] Peterziel, H., Pfenning, P., Harter, P., Mittelbronn, M., Weiler, M., Wick, W., Hess, J., and Angel, P., 2011. Function of the mucin-like glycoprotein podoplanin in glioma. In *Brain Tumor 2011*. Berlin, Germany.
- [168] Phung, Y. T., Barbone, D., Broaddus, V. C., and Ho, M., 2011. Rapid generation of in vitro multicellular spheroids for the study of monoclonal antibody therapy. *Journal of Cancer*, **2**:507–14.

## Bibliography

- [169] Press, W. H., Teukolsky, S. A., Vetterling, W. T., and Flannery, B. P., 1992. *Numerical recipes in C (2nd ed.): the art of scientific computing*. Cambridge University Press, New York, NY, USA, 2nd edition.
- [170] Primeau, A. J., Rendon, A., Hedley, D., Lilge, L., and Tannock, I. F., 2005. The distribution of the anticancer drug Doxorubicin in relation to blood vessels in solid tumors. *Clinical cancer research : an official journal of the American Association for Cancer Research*, **11**(24 Pt 1):8782–8. doi: [10.1158/1078-0432.CCR-05-1664](https://doi.org/10.1158/1078-0432.CCR-05-1664).
- [171] Pshenichnov, I., Mishustin, I., and Greiner, W., 2005. Neutrons from fragmentation of light nuclei in tissue-like media: a study with the GEANT4 toolkit. *Physics in medicine and biology*, **50**(23):5493–507. doi: [10.1088/0031-9155/50/23/005](https://doi.org/10.1088/0031-9155/50/23/005).
- [172] Qvarnström, O. F., Simonsson, M., Eriksson, V., Turesson, I., and Carlsson, J., 2009. gammaH2AX and cleaved PARP-1 as apoptotic markers in irradiated breast cancer BT474 cellular spheroids. *International journal of oncology*, **35**(1):41–7. doi: [10.3892/ijo](https://doi.org/10.3892/ijo).
- [173] Radszuweit, M., Block, M., Hengstler, J., Schöll, E., and Drasdo, D., 2009. Comparing the growth kinetics of cell populations in two and three dimensions. *Physical Review E*, **79**(5):1–12. doi: [10.1103/PhysRevE.79.051907](https://doi.org/10.1103/PhysRevE.79.051907).
- [174] Rasey, J. S. and Nelson, N. J., 1980. Effect of tumor disaggregation on results of in vitro cell survival assay after in vivo treatment of the EMT-6 tumor: x-rays, cyclophosphamide, and bleomycin. *In vitro*, **16**(7):547–53.
- [175] Rasey, J. S. and Nelson, N. J., 1981. Repair of potentially lethal damage following irradiation with X rays or cyclotron neutrons: response of the EMT-6/uw tumor system treated under various growth conditions in vitro and in vivo. *Radiation research*, **85**(1):69–84.
- [176] Ricci-Vitiani, L., Pallini, R., Biffoni, M., Todaro, M., Invernici, G., Cenci, T., Maira, G., Parati, E. A., Stassi, G., Larocca, L. M., and De Maria, R., 2010. Tumour vascularization via endothelial differentiation of glioblastoma stem-like cells. *Nature*, **468**(7325):824–8. doi: [10.1038/nature09557](https://doi.org/10.1038/nature09557).
- [177] van Rijn, J., Heimans, J. J., van den Berg, J., van der Valk, P., and Slotman, B. J., 2000. Survival of human glioma cells treated with various combination of temozolomide and X-rays. *International journal of radiation oncology, biology, physics*, **47**(3):779–84.
- [178] Rischin, D., Peters, L. J., O’Sullivan, B., Giralt, J., Fisher, R., Yuen, K., Trotti, A., Bernier, J., Bourhis, J., Ringash, J., Henke, M., and Kenny, L., 2010. Tirapazamine, cisplatin, and radiation versus cisplatin and radiation for advanced squamous cell carcinoma of the head and neck (TROG 02.02, HeadSTART): a phase III trial of the Trans-Tasman Radiation Oncology Group. *Journal of clinical oncology : official journal of the American Society of Clinical Oncology*, **28**(18):2989–95. doi: [10.1200/JCO.2009.27.4449](https://doi.org/10.1200/JCO.2009.27.4449).
- [179] Robinson, J. and Cooper, J. M., 1970. Method of determining oxygen concentrations in biological media, suitable for calibration of the oxygen electrode. *Analytical biochemistry*, **33**(2):390–9.
- [180] Rofstad, E. K., Eide, K., Skøyum, R., Hystad, M. E., and Lyng, H., 1996. Apoptosis, energy metabolism, and fraction of radiobiologically hypoxic cells: a study of human melanoma multicellular spheroids. *International journal of radiation biology*, **70**(3):241–9.
- [181] Roose, T., Chapman, S. J., and Maini, P. K., 2007. Mathematical Models of Avascular Tumor Growth. *SIAM Rev.*, **49**(2):179–208. doi: [10.1137/S0036144504446291](https://doi.org/10.1137/S0036144504446291).
- [182] Roose, T., Netti, P. a., Munn, L. L., Boucher, Y., and Jain, R. K., 2003. Solid stress generated by spheroid growth estimated using a linear poroelasticity model small star, filled. *Microvascular research*, **66**(3):204–12. doi: [10.1016/S0026-2862\(03\)00057-8](https://doi.org/10.1016/S0026-2862(03)00057-8).
- [183] Ruggieri, R., Naccarato, S., and Nahum, A. E., 2010. Severe hypofractionation: Non-homogeneous tumour dose delivery can counteract tumour hypoxia. *Acta oncologica (Stockholm, Sweden)*, (December 2009):1304–1314. doi: [10.3109/0284186X.2010.486796](https://doi.org/10.3109/0284186X.2010.486796).

- [184] Rusthoven, K. E., Kavanagh, B. D., Cardenes, H., Stieber, V. W., Burri, S. H., Feigenberg, S. J., Chidel, M. a., Pugh, T. J., Franklin, W., Kane, M., Gaspar, L. E., and Schefter, T. E., 2009. Multi-institutional phase I/II trial of stereotactic body radiation therapy for liver metastases. *Journal of clinical oncology : official journal of the American Society of Clinical Oncology*, **27**(10):1572–8. doi: [10.1200/JCO.2008.19.6329](https://doi.org/10.1200/JCO.2008.19.6329).
- [185] Ryan, R. M., Green, J., Williams, P. J., Tazzyman, S., Hunt, S., Harmey, J. H., Kehoe, S. C., and Lewis, C. E., 2009. Bacterial delivery of a novel cytotoxin to hypoxic areas of solid tumors. *Gene therapy*, **16**(3):329–39. doi: [10.1038/gt.2008.188](https://doi.org/10.1038/gt.2008.188).
- [186] Sakaue-Sawano, A., Kobayashi, T., Ohtawa, K., and Miyawaki, A., 2011. Drug-induced cell cycle modulation leading to cell-cycle arrest, nuclear mis-segregation, or endoreplication. *BMC cell biology*, **12**(1):2. doi: [10.1186/1471-2121-12-2](https://doi.org/10.1186/1471-2121-12-2).
- [187] Sakaue-Sawano, A., Kurokawa, H., Morimura, T., Hanyu, A., Hama, H., Osawa, H., Kashiwagi, S., Fukami, K., Miyata, T., Miyoshi, H., Imamura, T., Ogawa, M., Masai, H., and Miyawaki, A., 2008. Visualizing spatiotemporal dynamics of multicellular cell-cycle progression. *Cell*, **132**(3):487–98. doi: [10.1016/j.cell.2007.12.033](https://doi.org/10.1016/j.cell.2007.12.033).
- [188] Sakaue-Sawano, A., Ohtawa, K., Hama, H., Kawano, M., Ogawa, M., and Miyawaki, A., 2008. Tracing the silhouette of individual cells in S/G2/M phases with fluorescence. *Chemistry & biology*, **15**(12):1243–8. doi: [10.1016/j.chembiol.2008.10.015](https://doi.org/10.1016/j.chembiol.2008.10.015).
- [189] Sancar, A., Lindsey-Boltz, L. a., Unsal-Kaçmaz, K., and Linn, S., 2004. Molecular mechanisms of mammalian DNA repair and the DNA damage checkpoints. *Annual review of biochemistry*, **73**:39–85. doi: [10.1146/annurev.biochem.73.011303.073723](https://doi.org/10.1146/annurev.biochem.73.011303.073723).
- [190] Santini, M. T. and Rainaldi, G., 2008. Three-dimensional spheroid model in tumor biology. *Pathobiology : journal of immunopathology, molecular and cellular biology*, **67**(3):148–57.
- [191] Sattler, U. G. a., Meyer, S. S., Quennet, V., Hoerner, C., Knoerzer, H., Fabian, C., Yaromina, A., Zips, D., Walenta, S., Baumann, M., and Mueller-Klieser, W., 2010. Glycolytic metabolism and tumour response to fractionated irradiation. *Radiotherapy and oncology : journal of the European Society for Therapeutic Radiology and Oncology*, **94**(1):102–9. doi: [10.1016/j.radonc.2009.11.007](https://doi.org/10.1016/j.radonc.2009.11.007).
- [192] Saunders, M., Dische, S., Barrett, A., Harvey, A., Griffiths, G., and Palmar, M., 1999. Continuous, hyperfractionated, accelerated radiotherapy (CHART) versus conventional radiotherapy in non-small cell lung cancer: mature data from the randomised multicentre trial. CHART Steering committee. *Radiotherapy and oncology : journal of the European Society for Therapeutic Radiology and Oncology*, **52**(2):137–48.
- [193] Schaller, G., 2005. *On selected numerical approaches to Cellular Tissue*. Phd thesis, Johann Wolfgang Goethe–Universität, Frankfurt.
- [194] Schaller, G. and Meyer-Hermann, M., 2005. Multicellular tumor spheroid in an off-lattice Voronoi-Delaunay cell model. *Physical Review E*, **71**(5):51910–51916. doi: [10.1103/PhysRevE.71.051910](https://doi.org/10.1103/PhysRevE.71.051910).
- [195] Schaller, G. and Meyer-Hermann, M., 2006. Continuum versus discrete model: a comparison for multicellular tumour spheroids. *Philosophical transactions. Series A, Mathematical, physical, and engineering sciences*, **364**(1843):1443–64. doi: [10.1098/rsta.2006.1780](https://doi.org/10.1098/rsta.2006.1780).
- [196] Schefter, T. E., Kavanagh, B. D., Timmerman, R. D., Cardenes, H. R., Baron, A., and Gaspar, L. E., 2005. A phase I trial of stereotactic body radiation therapy (SBRT) for liver metastases. *International journal of radiation oncology, biology, physics*, **62**(5):1371–8. doi: [10.1016/j.ijrobp.2005.01.002](https://doi.org/10.1016/j.ijrobp.2005.01.002).
- [197] Scholz, M. and Elsässer, T., 2007. Biophysical models in ion beam radiotherapy. *Advances in Space Research*, **40**(9):1381–1391. doi: [10.1016/j.asr.2007.02.066](https://doi.org/10.1016/j.asr.2007.02.066).
- [198] Scholz, M. and Kraft, G., 1996. Track structure and the calculation of biological effects of heavy charged particles. *Advances in space research : the official journal of the Committee on Space Research (COSPAR)*, **18**(1-2):5–14.

## Bibliography

- [199] Scifoni, E., Krämer, M., and Durante, M., 2011. Towards an oxygen effect implementation of TRiP98. *GSI Sci. Rep.*, **5**(228436):228436.
- [200] Sham, E. and Durand, R. E., 1998. Cell kinetics and repopulation mechanisms during multifraction irradiation of spheroids. *Radiotherapy and oncology : journal of the European Society for Therapeutic Radiology and Oncology*, **46**(2):201–7.
- [201] Sham, E. and Durand, R. E., 1999. Repopulation characteristics and cell kinetic parameters resulting from multi-fraction irradiation of xenograft tumors in SCID mice. *International journal of radiation oncology, biology, physics*, **43**(3):617–22.
- [202] Siggaard-Andersen, O., Wimberley, P. D., Göthgen, I., and Siggaard-Andersen, M., 1984. A mathematical model of the hemoglobin-oxygen dissociation curve of human blood and of the oxygen partial pressure as a function of temperature. *Clinical chemistry*, **30**(10):1646–51.
- [203] Simon, W., 1986. *Mathematical techniques for biology and medicine*. Dover Books on Biology, Psychology and Medicine. Dover Publications.
- [204] Sinclair, W. K., 1968. Cyclic x-ray responses in mammalian cells in vitro. *Radiation research*, **33**(3):620–43.
- [205] Sinclair, W. K., 1968. The combined effect of hydroxyurea and x-rays on Chinese hamster cells in vitro. *Cancer research*, **28**(2):198–206.
- [206] Sinclair, W. K. and Morton, R. A., 1966. X-ray sensitivity during the cell generation cycle of cultured Chinese hamster cells. *Radiation research*, **29**(3):450–74.
- [207] Smallbone, K., Gavaghan, D. J., Gatenby, R. a., and Maini, P. K., 2005. The role of acidity in solid tumour growth and invasion. *Journal of theoretical biology*, **235**(4):476–84. doi: [10.1016/j.jtbi.2005.02.001](https://doi.org/10.1016/j.jtbi.2005.02.001).
- [208] Solov'yov, A. V., Surdutovich, E., Scifoni, E., Mishustin, I., and Greiner, W., 2009. Physics of ion beam cancer therapy: a multiscale approach. *Physical review. E, Statistical, nonlinear, and soft matter physics*, **79**(1 Pt 1):011909.
- [209] Song, C., Wang, P., and Makse, H. a., 2008. A phase diagram for jammed matter. *Nature*, **453**(7195):629–32. doi: [10.1038/nature06981](https://doi.org/10.1038/nature06981).
- [210] South, C. P., Evans, P. M., and Partridge, M., 2009. Dose prescription complexity versus tumor control probability in biologically conformal radiotherapy. *Medical Physics*, **36**(10):4379. doi: [10.1118/1.3213519](https://doi.org/10.1118/1.3213519).
- [211] Spivak, J. L. and Hasselbalch, H., 2011. Hydroxycarbamide: a user's guide for chronic myeloproliferative disorders. *Expert review of anticancer therapy*, **11**(3):403–14. doi: [10.1586/era.11.10](https://doi.org/10.1586/era.11.10).
- [212] Sprung, C. N., Cholewa, M., Usami, N., Kobayashi, K., and Crosbie, J. C., 2011. DNA damage and repair kinetics after microbeam radiation therapy emulation in living cells using monoenergetic synchrotron X-ray microbeams. *Journal of synchrotron radiation*, **18**(Pt 4):630–6. doi: [10.1107/S0909049511011836](https://doi.org/10.1107/S0909049511011836).
- [213] Staab, A., Zukowski, D., Walenta, S., Scholz, M., and Mueller-Klieser, W., 2004. Response of Chinese hamster v79 multicellular spheroids exposed to high-energy carbon ions. *Radiation research*, **161**(2):219–27.
- [214] Stadler, P., Feldmann, H. J., Creighton, C., Kau, R., and Molls, M., 1998. Changes in tumor oxygenation during combined treatment with split-course radiotherapy and chemotherapy in patients with head and neck cancer. *Radiotherapy and oncology : journal of the European Society for Therapeutic Radiology and Oncology*, **48**(2):157–64.
- [215] Steel, G. G., McMillan, T. J., and Peacock, J. H., 1989. The 5Rs of radiobiology. *International journal of radiation biology*, **56**(6):1045–8.

- [216] Steffen, A.-C., Göström, L., Tolmachev, V., Palm, S., Stenerlöv, B., and Carlsson, J., 2008. Differences in radiosensitivity between three HER2 overexpressing cell lines. *European journal of nuclear medicine and molecular imaging*, **35**(6):1179–91. doi: [10.1007/s00259-007-0713-x](https://doi.org/10.1007/s00259-007-0713-x).
- [217] Stehman, F. B., 1992. Experience with hydroxyurea as a radiosensitizer in carcinoma of the cervix. *Seminars in oncology*, **19**(3 Suppl 9):48–52.
- [218] Stehman, F. B., Bundy, B. N., Thomas, G., Keys, H. M., D’Ablaing, G., Fowler, W. C., Mortel, R., and Creasman, W. T., 1993. Hydroxyurea versus misonidazole with radiation in cervical carcinoma: long-term follow-up of a Gynecologic Oncology Group trial. *Journal of clinical oncology : official journal of the American Society of Clinical Oncology*, **11**(8):1523–8.
- [219] Stein, W. D., 1990. *Channels, carriers, and pumps: An introduction to membrane transport*. Academic Press (San Diego).
- [220] Stevenson, A. F. and Lange, C. S., 1997. Extracellular matrix (ECM) and cytoskeletal modulation of cellular radiosensitivity. *Acta oncologica (Stockholm, Sweden)*, **36**(6):599–606.
- [221] Surdutovich, E., Obolensky, O. I., Scifoni, E., Pshenichnov, I., Mishustin, I., Solov’yov, A. V., and Greiner, W., 2008. Ion-induced electron production in tissue-like media and DNA damage mechanisms. doi: [10.1140/epjd/e2008-00207-y](https://doi.org/10.1140/epjd/e2008-00207-y).
- [222] Swanson, K. R., Alvord, E. C., and Murray, J. D., 2000. A quantitative model for differential motility of gliomas in grey and white matter. *Cell proliferation*, **33**(5):317–29.
- [223] Takahashi, A., Matsumoto, H., Yuki, K., Yasumoto, J.-I., Kajiwara, A., Aoki, M., Furusawa, Y., Ohnishi, K., and Ohnishi, T., 2004. High-LET radiation enhanced apoptosis but not necrosis regardless of p53 status. *International journal of radiation oncology, biology, physics*, **60**(2):591–7. doi: [10.1016/j.ijrobp.2004.05.062](https://doi.org/10.1016/j.ijrobp.2004.05.062).
- [224] Taubock, G., 2011. A maximum entropy theorem for complex-valued random vectors, with implications on capacity. *Information Theory Workshop (ITW), 2011 IEEE*, pp. 375–379.
- [225] Tesniere, a., Panaretakis, T., Kepp, O., Apetoh, L., Ghiringhelli, F., Zitvogel, L., and Kroemer, G., 2008. Molecular characteristics of immunogenic cancer cell death. *Cell death and differentiation*, **15**(1):3–12. doi: [10.1038/sj.cdd.4402269](https://doi.org/10.1038/sj.cdd.4402269).
- [226] Titz, B. and Jeraj, R., 2008. An imaging-based tumour growth and treatment response model: investigating the effect of tumour oxygenation on radiation therapy response. *Physics in medicine and biology*, **53**(17):4471–88. doi: [10.1088/0031-9155/53/17/001](https://doi.org/10.1088/0031-9155/53/17/001).
- [227] Topsch, J., Scholz, M., and Mueller-Klieser, W., 2007. Radiobiological characterization of human tumor cell multilayers after conventional and particle irradiation. *Radiation research*, **167**(6):645–54. doi: [10.1667/RR0775.1](https://doi.org/10.1667/RR0775.1).
- [228] Travis, E. L. and Tucker, S. L., 1987. Isoeffect models and fractionated radiation therapy. *International journal of radiation oncology, biology, physics*, **13**(2):283–7.
- [229] Tuckwell, W., Bezak, E., Yeoh, E., and Marcu, L., 2008. Efficient Monte Carlo modelling of individual tumour cell propagation for hypoxic head and neck cancer. *Physics in medicine and biology*, **53**(17):4489–507. doi: [10.1088/0031-9155/53/17/002](https://doi.org/10.1088/0031-9155/53/17/002).
- [230] Tung, Y.-C., Hsiao, A. Y., Allen, S. G., Torisawa, Y.-s., Ho, M., and Takayama, S., 2011. High-throughput 3D spheroid culture and drug testing using a 384 hanging drop array. *The Analyst*, **136**(3):473–8. doi: [10.1039/c0an00609b](https://doi.org/10.1039/c0an00609b).
- [231] Turner, J. J., Ewald, J. C., and Skotheim, J. M., 2012. Cell size control in yeast. *Current biology : CB*, **22**(9):R350–9. doi: [10.1016/j.cub.2012.02.041](https://doi.org/10.1016/j.cub.2012.02.041).

## Bibliography

- [232] Vander Heiden, M. G., Cantley, L. C., and Thompson, C. B., 2009. Understanding the Warburg effect: the metabolic requirements of cell proliferation. *Science (New York, N.Y.)*, **324**(5930):1029–33. doi: [10.1126/science.1160809](https://doi.org/10.1126/science.1160809).
- [233] Vaupel, P., 2004. Tumor microenvironmental physiology and its implications for radiation oncology. *Seminars in radiation oncology*, **14**(3):198–206. doi: [10.1016/j.semradonc.2004.04.008](https://doi.org/10.1016/j.semradonc.2004.04.008).
- [234] Vokes, E. E., Crawford, J., Bogart, J., Socinski, M. A., Clamon, G., and Green, M. R., 2005. Concurrent chemoradiotherapy for unresectable stage III non-small cell lung cancer. *Clinical cancer research : an official journal of the American Association for Cancer Research*, **11**(13 Pt 2):5045s–5050s. doi: [10.1158/1078-0432.CCR-05-9008](https://doi.org/10.1158/1078-0432.CCR-05-9008).
- [235] Walenta, S., Doetsch, J., Mueller-Klieser, W., and Kunz-Schughart, L. a., 2000. Metabolic Imaging in Multicellular Spheroids of Oncogene-transfected Fibroblasts. *Journal of Histochemistry & Cytochemistry*, **48**(4):509–522. doi: [10.1177/002215540004800409](https://doi.org/10.1177/002215540004800409).
- [236] Wang, C.-K. C., 2010. The progress of radiobiological models in modern radiotherapy with emphasis on the uncertainty issue. *Mutation research*, **704**(1-3):175–81. doi: [10.1016/j.mrrev.2010.02.001](https://doi.org/10.1016/j.mrrev.2010.02.001).
- [237] Wang, R., Chadalavada, K., Wilshire, J., Kowalik, U., Hovinga, K. E., Geber, A., Fligelman, B., Leversha, M., Brennan, C., and Tabar, V., 2010. Glioblastoma stem-like cells give rise to tumour endothelium. *Nature*, **468**(7325):829–33. doi: [10.1038/nature09624](https://doi.org/10.1038/nature09624).
- [238] Wang, R., Xu, J., Juliette, L., Castilleja, A., Love, J., Sung, S.-Y., Zhau, H. E., Goodwin, T. J., and Chung, L. W. K., 2005. Three-dimensional co-culture models to study prostate cancer growth, progression, and metastasis to bone. *Seminars in cancer biology*, **15**(5):353–64. doi: [10.1016/j.semcancer.2005.05.005](https://doi.org/10.1016/j.semcancer.2005.05.005).
- [239] Ward, J. P. and King, J. R., 1997. Mathematical modelling of avascular-tumour growth. *IMA journal of mathematics applied in medicine and biology*, **14**(1):39–69.
- [240] Wedenberg, M., Lind, B. K., Toma-Dașu, I., Rehbinder, H., and Brahme, A., 2010. Analytical description of the LET dependence of cell survival using the repairable-conditionally repairable damage model. *Radiation research*, **174**(4):517–25. doi: [10.1667/RR2045.1](https://doi.org/10.1667/RR2045.1).
- [241] Wehrle, J. P., Ng, C. E., McGovern, K. A., Aiken, N. R., Shungu, D. C., Chance, E. M., and Glickson, J. D., 2000. Metabolism of alternative substrates and the bioenergetic status of EMT6 tumor cell spheroids. *NMR in biomedicine*, **13**(6):349–60.
- [242] West, C. M., Sandhu, R. R., and Stratford, I. J., 1984. The radiation response of V79 and human tumour multicellular spheroids—cell survival and growth delay studies. *British journal of cancer*, **50**(2):143–51.
- [243] White, E., Karp, C., Strohecker, A. M., Guo, Y., and Mathew, R., 2010. Role of autophagy in suppression of inflammation and cancer. *Current opinion in cell biology*, **22**(2):212–7. doi: [10.1016/j.ceb.2009.12.008](https://doi.org/10.1016/j.ceb.2009.12.008).
- [244] Williams, J. R., Zhang, Y. G., and Dillehay, L. E., 1992. Sensitization processes in human tumor cells during protracted irradiation: possible exploitation in the clinic. *International journal of radiation oncology, biology, physics*, **24**(4):699–704.
- [245] Withers, H. R., 1985. Biologic basis for altered fractionation schemes. *Cancer*, **55**(9 Suppl):2086–95.
- [246] Zackrisson, B., Mercke, C., Strander, H., Wennerberg, J., and Cavallin-Ståhl, E., 2003. A systematic overview of radiation therapy effects in head and neck cancer. *Acta oncologica (Stockholm, Sweden)*, **42**(5-6):443–61. doi: [10.1080/02841860310014886](https://doi.org/10.1080/02841860310014886).
- [247] Zahnreich, S., Melnikova, L., Winter, M., Nasonova, E., Durante, M., Ritter, S., and Fournier, C., 2010. Radiation-induced premature senescence is associated with specific cytogenetic changes. *Mutation research*, **701**(1):60–6. doi: [10.1016/j.mrgentox.2010.03.010](https://doi.org/10.1016/j.mrgentox.2010.03.010).
- [248] Zhang, H. and Liu, K.-K., 2008. Optical tweezers for single cells. *Journal of the Royal Society, Interface / the Royal Society*, **5**(24):671–90. doi: [10.1098/rsif.2008.0052](https://doi.org/10.1098/rsif.2008.0052).

# Curriculum Vitae

## Address

Harald Kempf  
Westring 18  
63500 Seligenstadt, Germany  
kempf@fias.uni-frankfurt.de



## Personal details

Name: Harald Christoph Kempf  
Nationality: German  
Date of birth: 29.08.1984  
Place of birth: Hanau

## Education and career

<b>2003</b>	German A-Levels at the public school “Franziskanergymnasium Kreuzburg”, Großkrotzenburg, numerus clausus 1.5
<b>2003–2009</b>	Studies in physics at the “Goethe-University”, Frankfurt (as university scholarship holder from 2007–2008)
<b>2005</b>	Predegree in physics, minor subjects: geophysics, catastrophe theory, overall average grade: “outstanding”
<b>2007–2008</b>	Diploma thesis at the “Frankfurt Institute for Advanced Studies (FIAS)”, Frankfurt, Germany Supervisors: Prof. Dr. M. Bleicher, Prof. Dr. M. Meyer-Hermann, <i>average grade: “outstanding with distinction”</i>
<b>2008–2011</b>	Scholarship holder of a “MainCampus doctus” Ph.D. scholarship of the “Stiftung Polytechnische Gesellschaft”, Frankfurt
<b>2009</b>	Diploma in physics, minor subjects: cognitive neuroscience, computational biophysics, overall average grade: “outstanding with distinction”
<b>Since 2009</b>	Ph.D. student at the “Goethe-University”, Frankfurt, the Frankfurt Institute for Advanced Studies (FIAS), Frankfurt and at the Helmholtz Centre for Infection Research, Braunschweig Supervisors: Prof. Dr. M. Bleicher, Prof. Dr. M. Meyer-Hermann
<b>2009</b>	“Philipp Siedler” science award of the “Physikalische Verein”, Frankfurt